Microscopic Investigations on various Silicon Materials Irradiated with different Particles with the DLTS Method

Dissertation

zur Erlangung des Doktorgrades
des Fachbereichs Physik
der Universität Hamburg

vorgelegt von
Martin Kuhnke
aus Buchholz/Nordheide

Hamburg
2001

Gutachter der Dissertation	: Prof. Dr. Dr. hc. G. Lindström
	: Prof. Dr. K. Wick
Gutachter der Disputation	: Dr. E. Fretwurst
	: Prof. Dr. W. Scobel
Datum der Disputation	: 28.02.2001
Dekan des Fachbereichs Physik und Vorsitzender des Promotionsausschusses	: Prof. Dr. F.-W. Büßer

Abstract

During irradiation of crystalline silicon with high energy particles silicon atoms are displaced out of their lattice sites and the primary defects silicon interstitials and vacancies form defects with the impurities oxygen and carbon. The radiation induced defects change the macroscopic parameters of silicon detectors, the leakage current and the full depletion voltage. The item of this thesis is to study the microscopic properties of radiation induced defects with the DLTS method and to understand the change of the macroscopic parameters of silicon detectors after particle irradiation.

Various silicon materials were irradiated with low and high energy protons, high energy pions, neutrons and ^{60}Co γ-photons to investigate the dependence of the introduction rates of the radiation induced defects on particle and material type. The varied parameters of the silicon material are the shallow doping concentration phosphorous and the concentrations of the impurities oxygen and carbon.

The introduction rates of isolated point defects VO_i, C_iC_s and C_iO_i are higher for charged particle irradiations in comparison to neutron irradiation, because more isolated single displacements are produced due to Coulomb scattering. The defect kinetic of point defects is influenced by the impurities oxygen and carbon. The defect VO_i is created near the cascade collision regions during neutron irradiation and more homogeneously in the sample volume during charged particle irradiation. The defect V_2O is assumed to be responsible for the radiation hardness of oxygen enriched silicon. The generation of the acceptor V_2O is suppressed in oxygen rich silicon. The introduction rate of the cluster defects $VV+?$ is independent on the particle and material type. Divacancies are mainly generated in the terminal cluster regions after particle irradiation. But also a broad signal E4a on the left hand side and a signal E4b on the right hand side of the cluster signal $VV^{-/0}+?$ is observed. The carbon defects C_iO_i and C_iC_s are created in the environment of the terminal clusters. Also the generation of C_iC_s at the terminal cluster peripheries is assumed to occur. No clusters are created during ^{60}Co γ-photon irradiation. The leak of silicon interstitial related defects after particle and ^{60}Co γ-photon irradiation is explained with the surface annihilation of silicon interstitials.

The exponential annealing of the current related damage rate is correlated with the annealing of the defect E4b. The logarithmic annealing of the current related damage rate and the short term annealing of the effective space charge density is not understood. The donor removal is explained with the creation of VP_s defects. The stable acceptor damage is explained with the acceptor V_2O and negative charged divacancies in the terminal clusters due to inter-centre-charge-transfer. The reverse annealing of the effective space charge density is suggested to be due to higher order carbon defects which envelope the terminal clusters after high fluence irradiation.

Kurzfassung

Während der Bestrahlung von kristallinen Silizium mit hochenergetischen Teilchen werden Siliziumatome aus ihren Gitterplätzen versetzt und die primären Defekte, Zwischengitteratome und Leerstellen, bilden Defekte mit den Fremdatomen Sauerstoff und Kohlenstoff. Die strahleninduzierten Defekte ändern die makroskopischen Eigenschaften von Siliziumdetektoren, den Leckstrom und die Verarmungsspannung. In dieser Arbeit wurden die mikroskopischen Eigenschaften von strahleninduzierten Defekten mit der DLTS Methode untersucht, um die Änderung der makroskopischen Parameter von Siliziumdetektoren nach Teilchenbestrahlung zu verstehen.

Verschiedene Siliziummaterialen wurden mit nieder- und hochenergetischen Protonen, hochenergetischen Pionen, Neutronen und ^{60}Co γ-Photonen bestrahlt, um die Abängigkeit der Defektgeneration von Teilchen- und Materialtyp zu untersuchen. Die variierten Parameter der Siliziummaterialen sind die Konzentrationen der flachen Dotierung Phosphor und der Fremdatome Sauerstoff und Kohlenstoff.

Die Generationsraten von isolierten Punktdefekten VO_i, C_iC_s and C_iO_i sind höher für geladene Teilchenbestrahlungen verglichen mit Neutronenbestrahlungen, weil mehr isolierte Einzelversetzungen aufgrund von Coloumbstreuung vorkommen. Die Defektkinetik der Punktdefekte wird durch die Verunreinigungen Sauerstoff und Kohlenstoff beeinflußt. Der Defekt VO_i wird während Neutronenbestrahlung in der Nähe der Kollisionskaskaden erzeugt und während geladener Teilchenbestrahlung mehr homogen im Strukturvolumen. Es wird angenohmen, daß der Defekt V_2O mit der Strahlenresistenz von sauerstoffangereicherten Silizium zu tun hat. Die Generation von V_2O ist unterdrückt in sauerstoffreichen Silizium. Die Generationsrate der Clusterdefekte $VV+?$ ist unabhängig von Teilchen- und Materialtyp. Die Doppelleerstellen entstehen hauptsächlich in den Clustergebieten nach Teilchenbestrahlung. Zusätzlich wird ein breites Signal E4a auf der linken Seite und ein Signal E4b auf der rechten Seite des Signals $VV^{-/0}+?$ beobachtet. Die Kohlenstoffdefekte C_iO_i und C_iC_s entstehen in der Umgebung der Cluster. Auch eine Erzeugung von C_iC_s an den Rändern der Cluster ist möglich. Es werden keine Cluster während ^{60}Co γ-Photonenbestrahlung erzeugt. Das Fehlen von Zwischenstellendefekten wird durch die Oberflächenannihilation von Zwischengitteratomen erklärt.

Die exponentielle Stromausheilung wird durch den Defekt E4b verursacht. Die logarithmische Stromausheilung und die Kurzzeitausheilung der effektiven Raumladungsdichte ist nicht verstanden. Die Abnahme der flachen Donatorkonzentration wird durch die Erzeugung von VP_s Defekten erklärt. Die stabile akzeptorartige Schädigung wird durch den Akzeptor V_2O und durch negativ geladene Doppelleerstellen in den Clustern erklärt. Die Langzeitausheilung der effektiven Raumladungsdichte wird möglicher Weise durch eine Kohlenstoffdefektschale um die Cluster verursacht.

Contents

1 Introduction **1**

2 Basic Features of Silicon detectors **3**

2.1 Basic principle of semiconductor physics 3

2.1.1 Bulk properties of silicon crystals 3

2.1.2 pn junction 11

2.1.3 Metal semiconductor contact - Schottky diode 16

2.1.4 Ohmic contact - Back side contact 17

2.2 Manufacturing of the silicon material and processing 17

2.2.1 Czochralski silicon 18

2.2.2 Floatzone silicon 18

2.2.3 Epitaxial silicon 19

2.2.4 Oxygen diffusion 20

2.2.5 Planar processing 20

2.3 Operation of silicon detectors 21

2.3.1 Properties of silicon detectors 21

3 Radiation induced damage in silicon **24**

3.1 Damage mechanism of particles 24

3.1.1 Surface damage 25

3.1.2 Bulk damage 26

3.2 Non Ionising Energy Loss 28

3.2.1 Displacement damage cross section 29

3.2.2 Hardness factor 30

3.2.3 Experimental determination of the hardness factor . . 30

3.2.4 Particle dependence 32

3.3 Radiation induced defects . . . 35
3.3.1 Interstitial-carbon Substitutional-carbon complex . . . 35
3.3.2 Divacancy . . . 37
3.4 Electrical properties of defect centers . . . 38
3.4.1 Capture rate . . . 39
3.4.2 Isolated point defects - Shockley Read Hall statistics . 39
3.4.3 Inter-center-charge-transfer . . . 43
3.5 Defect kinetics . . . 44
3.5.1 Defect formation and annealing . . . 45

4 Experimental Methods 49
4.1 Material . . . 49
4.2 Irradiations . . . 49
4.2.1 Be(d,n) neutron irradiation . . . 50
4.2.2 Reactor neutron irradiation . . . 51
4.2.3 23 GeV proton irradiation . . . 52
4.2.4 27 MeV proton irradiation . . . 53
4.2.5 7-10 MeV proton irradiation . . . 53
4.2.6 192 MeV pion irradiation . . . 53
4.2.7 ^{60}Co γ-photon irradiation . . . 53
4.3 Macroscopic methods for damage characterisation . . . 54
4.3.1 CV and IV setup . . . 55
4.4 Microscopic methods for damage characterisation . . . 55
4.4.1 Deep Level Transient Spectroscopy . . . 56
4.4.2 DLTS setup . . . 70

5 Macroscopic studies 76
5.1 Volume generation current . . . 76
5.2 Effective doping concentration . . . 76

6 Microscopic studies 83
6.1 Process induced defects . . . 83
6.2 Introduction rates of radiation induced defects . . . 86
6.2.1 Particle and material dependence . . . 87
6.2.2 ^{60}Co γ-photon irradiation . . . 93
6.3 Capture measurements . . . 97

6.3.1 Electrical filling of VO_i and C_iC_s 98
6.3.2 Configurational switching of C_iC_s 106
6.3.3 Electrical filling of C_iO_i 106
6.3.4 Electrical filling of VV 107
6.3.5 Electrical filling of C_i 110
6.3.6 Optical filling of C_i and C_iO_i 110
6.3.7 Optical filling of VO_i 114
6.4 Ratios of defect concentrations 114
6.4.1 ^{60}Co γ-photon irradiation 115
6.4.2 Particle dependence 116
6.4.3 Material dependence 118
6.4.4 Low energy protons 120
6.4.5 Ratio $[VV^{=/-}]/[VV^{-/0}]$ 120
6.5 Annealing studies 122
6.5.1 Annealing of C_i 123
6.5.2 Annealing of $VO_i + C_iC_s$ 125
6.5.3 Annealing of VV+? 125
6.5.4 Annealing of $[VV^{=/-}]/[VV^{-/0}$+?] 129
6.6 Correlation with macroscopic results 130
6.6.1 Volume generation current 130
6.6.2 Effective space charge density 132

7 Summary **136**

A Properties of crystalline silicon **142**

B Emission parameters of radiation induced defects **144**

C Majority charge carrier capture characteristic **145**

D Minority charge carrier capture characteristic **148**

E Divacancy cluster with a Gaussian distribution **150**

F Irradiated samples **153**

Chapter 1

Introduction

Silicon detectors are used in the inner tracking region of High Energy Physic (HEP) experiments, because a high spatial resolution and a fast readout are needed to track the particles. In future experiments the collisions of particles with high energy and luminosity will lead to intense radiation fields. Hence radiation damage in silicon detectors is a main issue of future HEP experiments [Lin99]. An increase of the leakage current, a change of the depletion voltage [Mol99] and a decrease of the charge collection efficiency [Bro00] are well known effects after hadron irradiation. It was shown that oxygen enrichment of silicon has a beneficial effect on the depletion voltage after charged hadron irradiation, but not after neutron irradiation [Ros00].

However, microscopic characterization of radiation induced defects could help to explain the macroscopic results on the scale of defect formation during irradiation and defect evolution after irradiation. The displacement damage in the crystal lattice produced by γ-photons and high energetic particles is different. In γ-photon irradiated silicon only isolated point defects are produced. In particle irradiated silicon also clusters of defects are created. Because only the defect kinetic of point defects depends on the impurity content, the radiation damage due to point defects is different in oxygen enriched silicon compared to standard silicon.

The Deep Level Transient Spectroscopy (DLTS) is used to investigate the defect properties after irradiation with neutrons, high and low energy protons, high energy pions and ^{60}Co γ-photons. Silicon materials with different concentrations of oxygen and carbon are investigated to study the effect of the impurities on defect formation. The correlation with macroscopic parameters is difficult, because no simple model exits to explain the complicated behaviour of cluster damage.

As mentioned previously the radiation hardness of silicon detectors depends on the particle type. Therefore irradiations with particles were performed, which mainly contribute to the LHC environment that is shown in figure 1.1. The pion spectrum is centered around 200 MeV and the neutrons have an almost homogeneous energy distribution between 0.1 and 100 MeV.

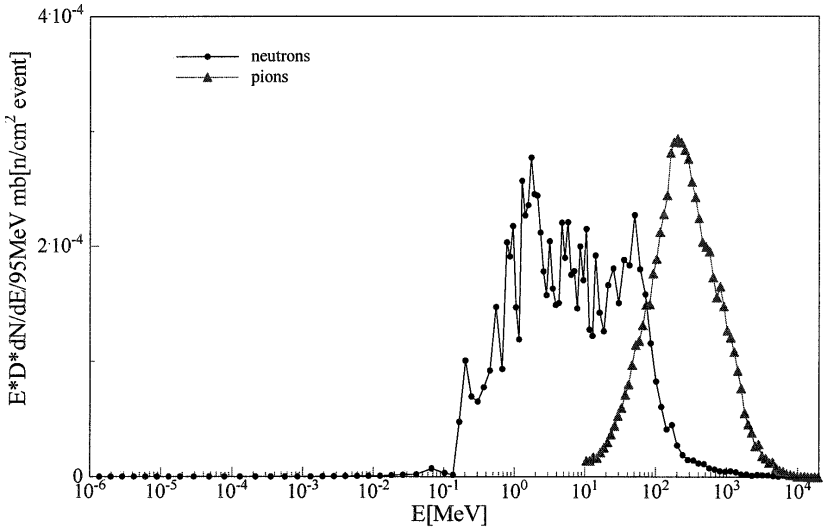

Figure 1.1: *The main contributions to the energy spectra present in the inner detector of the ATLAS experiment are shown. The neutron and pion energy spectra are folded with the appropriate damage efficiency* [Ros00].

However, experiments with high energy neutrons have not been performed yet. But the nuclear reactions of high energy neutrons and protons are not very different and therefore the created damage is assumed to be identical.

The chapter 2 consists of an introduction to the basis principles of semiconductor physics, a description of the manufacturing of silicon crystals, the processing of silicon wafers and a short review of detector operation. Chapter 3 describes the radiation damage in silicon produced by different types of particles and the Non Ionising Energy Loss (NIEL) hypothesis is discussed. Also the Shockley Read Hall statistics for isolated defect centers and the theory to describe the electrical properties of clustered defects are included. Briefly the defect kinetic is described. In chapter 4 the investigated materials and their processing histories are listed. An overview of the different irradiation sources is given. The DLTS method is explained. The macroscopic characterisation is only shortly mentioned. In chapter 5 and 6 the experimental results of the macroscopic and microscopic studies are compiled and discussed. The last chapter contains the summary of the thesis.

Chapter 2

Basic Features of Silicon detectors

2.1 Basic principle of semiconductor physics

A short introduction of semiconductor physics that are relevant for the study of silicon detectors and understanding the principle of the DLTS[1] method is presented. For a detailed introduction in semiconductor physics and solid state physics refer the well known textbooks [Sze85, Ash76, Kit93, Iba93].

2.1.1 Bulk properties of silicon crystals

Crystal structure

Silicon belongs to the Group IV in the periodical system and its electron configuration is $1s^2\ 2s^2\ 2p^6\ 3s^2\ 3p^2$. The electron configuration of silicon atoms constituting a crystal is changed to lower the total energy of the system. One electron of the 3s-shell is excited to the 3p-shell. A new linear combination of the $3s$, $3p_x$, $3p_y$ and $3p_z$ orbital wave functions results in an electron distribution, which fits into a tetrahedron. The electron distribution is shown on the right hand side of figure 2.1. Hence silicon have four valence electrons. This configuration is named sp^3-hybrid. In a crystalline solid the silicon atoms form a diamond lattice as shown on the left hand side of figure 2.1. In further detail the crystal structure of diamond consists of a face-centered cubic lattice (fcc) and a basis with two identical atoms at $(0,0,0)$ and $(\frac{1}{4}a, \frac{1}{4}a, \frac{1}{4}a)$. The axes of the Cartesian coordinate system coincide with the edges of the cube. The lattice constant of silicon is a = 5.43 Å. The four nearest neighbours of a silicon atom which is centered in a tetrahedron are attached to the corners of the tetrahedron. The bounds between the atoms are covalent and the electron distribution between two atoms is symmetric. Thus silicon is a non polar semiconductor.

[1] **D**eep **L**evel **T**ransient **S**pectroscopy

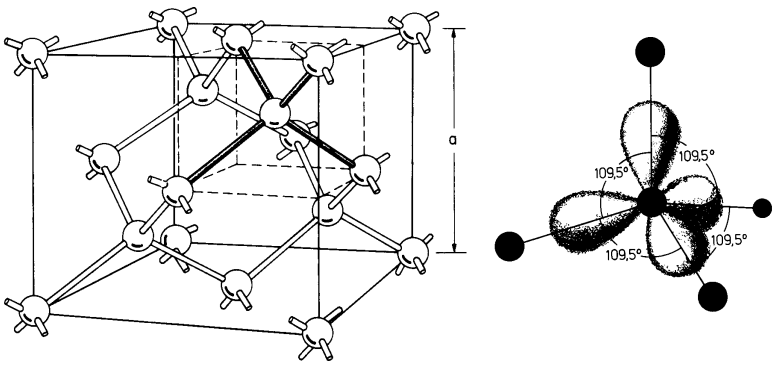

Figure 2.1: *Diamond crystal structure of silicon is shown on the left hand side* [Sze85] *and the electron distribution of the* sp^3*-hybrid is shown on the right hand side* [Iba93].

Energy bands

The energy band structure of crystalline silicon has been calculated using quantum mechanics. The periodicity of the electronic potential of the lattice constricts the complete translation invariance of the Hamilton operator. The solution of this problem are the Bloch wave functions

$$\Psi_k(\vec{r}) = u_k(\vec{r}) \cdot e^{i\vec{k}\cdot\vec{r}} \tag{2.1}$$

where $u_k(\vec{r})$ is a periodic function of the space vector $\vec{r}$ and the wave vector $\vec{k}$ is the crystal momentum. The function $u_k(\vec{r})$ has the same periodicity as the electronic potential. The wave vector $\vec{k}$ is a quantum number. Two types of particles exit in a semiconductor, electrons and holes, which are described by the wave function $\Psi_k(\vec{r})$. An energy band shows the dependence of the particle energy on the crystal momentum $\vec{k}$. The function $E(\vec{k})$ has the periodicity of a body-centered cubic lattice (bcc). The bcc lattice is the reciprocal of the fcc lattice. But there are various energy states for a quantum number $\vec{k}$. The different energy states are labeled by a further quantum number n. Thus there are different energy bands. In the special case of a semiconductor the two main bands are separated by an forbidden energy gap, or band gap E_g. The upper band is called conduction band, the lower is called valence band. A simplified energy band structure of silicon for two different directions in the first brillouin zone of the fcc lattice is shown in figure 2.2. The first brillouin zone is the primitive Wigner-Seitz cell of the reciprocal of the fcc lattice. The small spacing of the discrete energy levels in the $\vec{k}$-space make a continuous energy spectrum useful. The mobile particles in the conduction band are electrons and in the valence band holes. However, holes are generated by excitation of an electron from a valence band state into a conduction band state. The minimal energy of this process is given by the band gap and it is about 1.12 eV at room temperature. A transition is not possible with out changing the crystal momentum. Thus silicon is a member of the group of indirect semiconductors. This is accomplished by

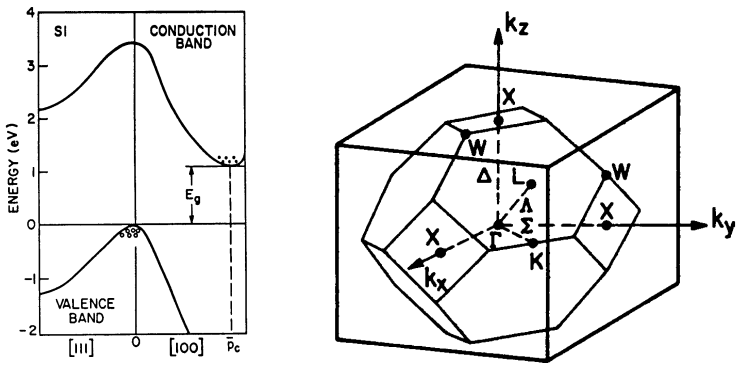

Figure 2.2: *Simplified energy band structure of silicon is shown on the left hand side* [Sze85]. *The conduction band and one of three valence bands are shown. The first brillouin zone of the face-centered cubic lattice is shown on the right hand side [Sze81]. In the band structure presentation the reduce wave vector* $\vec{\zeta} = \vec{k}/(2\pi/a)$ *is used.* It is clear that the crystal momentum at the conduction band minimum is $\vec{k} \neq 0$, but $E_{kin}(\vec{k}) = 0$.

an additional absorption of a phonon which has a large crystal momentum, but a small energy. A phonon dispersion spectrum is shown in figure 2.3.

Density of states

The parabolic approximation of the band structure near the minimum of the conduction or the maximum of valence band suggests the same mathematical formalism as for a free particle in a constant potential

$$\Psi_{\vec{k}} = \frac{1}{\sqrt{V}} \, e^{i\vec{k}\cdot\vec{r}} \tag{2.2}$$

where V is the crystal volume to normalize the wave function and the kinetic energy is

$$E(\vec{k}) = \frac{\hbar^2 k_1^2}{2m_1^*} + \frac{\hbar^2 k_2^2}{2m_2^*} + \frac{\hbar^2 k_3^2}{2m_3^*} \tag{2.3}$$

where m_1^*, m_2^*, m_3^* are the three different effective masses, $\{k_1, k_2, k_3\}$ are the three components of $\vec{k}$ and $\hbar$ the Planck constant. Because of the periodicity of the electronic potential the effective masses are different from the electron rest mass. The effective density of states is the number of states per unit volume and energy interval. The effective density of states, taking into account the volume of the momentum space for an energy state is h^3, is

$$D(E) = \frac{(m_1^* m_2^* m_3^*)^{1/2}}{2\pi^2\hbar^3} E^{1/2} \tag{2.4}$$

The conduction band is a non-spherical parabolic band and the effective density of states is

$$D_C(E) = \frac{(m_l^* m_t^* m_t^*)^{1/2}}{2\pi^2\hbar^3} E^{1/2} \tag{2.5}$$

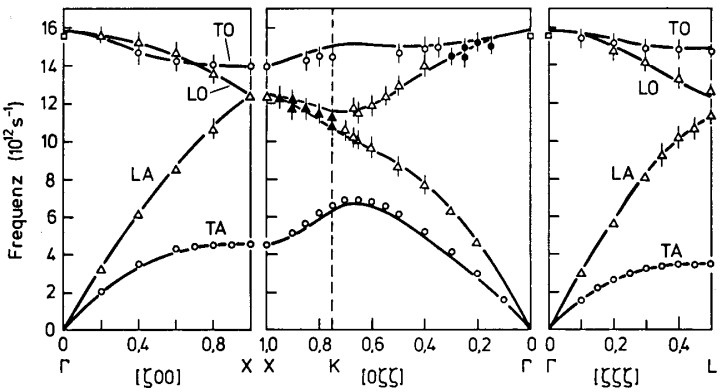

Figure 2.3: *The phonon frequency spectrum for three different path in the first brillouin zone are shown. The circles and triangles are measurements and the solid line are the results of a calculation. The different vibration modes of the lattice are TA (transverse acoustic mode), LA (longitudinal acoustic modes), TO (transverse optical mode) and LO (longitudinal optical mode). The reduce wave vector* $\vec{\zeta} = \vec{k}/(2\pi/a)$ *is used. The phonon energy is* $E_{ph} = h\nu$ [Iba93].

where m_l^* and m_t^* are the longitudinal and transverse effective masses of the non-spherical band. However, experimental work suggests a relative weak temperature dependence of m_t^* and theoretical considerations suggest an even weaker temperature dependence of m_l^* [Gre90]. The valence band is approximated by three spherical parabolic bands, the heavy and light hole bands and the split-off band, which degenerate at $\vec{k} = 0$. The effective density of states is

$$D_V(E) = \frac{m_{hh}^{*3/2} + m_{lh}^{*3/2} + m_{SO}^{*3/2}\, e^{-\beta\Delta}}{2\pi^2\hbar^3} E^{1/2} \tag{2.6}$$

where m_{hh}^*, m_{lh}^* and m_{SO}^* are effective masses[2] of the three spherical valence bands and Δ is the split-off energy. However, it is more accurate to treat the valence bands as non-spherical non-parabolic bands and the energy equation has the form

$$k^2 = \frac{2m_0}{\hbar^2}\,\gamma(E, \hat{k}) \tag{2.7}$$

where m_0 is the electron rest mass and $\hat{k}$ is the unit vector in the direction of the wave vector $\vec{k}$. This dependence makes the effective masses of the spherical parabolic bands in Equation 2.6 temperature dependent. A numerical calculation of the masses is done by [Mad81].

[2] **h**eavy **h**ole, **l**ight **h**ole bands and **S**plit-**O**ff band

Intrinsic carrier concentration

An semiconductor without any contamination of foreign atoms is called intrinsic. Thermal agitation results in an excitation of electrons from the valence band states into the conduction band states and leaves the equal number of holes in the valence band. The thermal equilibrium condition of a system of fermions is given by the Fermi-Dirac distribution

$$f_{Dirac}(E) = \frac{1}{1 + e^{\beta(E-\mu)}} \tag{2.8}$$

with

$$\beta = \frac{1}{k_B T} \tag{2.9}$$

where k_B is the Boltzmann constant, T the temperature and μ the chemical potential. For T = 0 K the chemical potential is called the Fermi level. In semiconductor physics the term Fermi level E_F is also used for T > 0 K. The density of charge carriers in the conduction band is

$$\begin{aligned} n &= \int_{E_C}^{E_{top}} D_C(E^{'})\ f_{Dirac}(E^{'})\ dE^{'} \\ &\approx \frac{m_n^{*3/2}}{2^{1/2}\,\pi^{3/2}\,\hbar^3}\ (1/\beta)^{3/2}\ e^{-\beta(E_C - E_F)} \end{aligned} \tag{2.10}$$

with

$$m_n^* = (m_l^*\ m_t^*\ m_t^*)^{1/3} \tag{2.11}$$

where m_n^* is the effective mass of conduction band state density, m_l^* and m_t^* the longitudinal and transverse masses of the non-spherical conduction band, E_C and E_F the energies of the conduction band edge and Fermi level. For the calculation of the hole density three valence bands have to be taken into account

$$\begin{aligned} p &= \int_{E_{bottom}}^{E_V} D_V(E^{'})\ (1 - f_{Dirac}(E^{'}))\ dE^{'} \\ &\approx \frac{m_p^{*3/2}}{2^{1/2}\,\pi^{3/2}\,\hbar^3}\ (1/\beta)^{3/2}\ e^{-\beta(E_F - E_V)} \end{aligned} \tag{2.12}$$

with

$$m_p^* = (m_{hh}^{3/2} + m_{lh}^{3/2} + m_{SO}^{3/2}\, e^{-\beta\Delta})^{2/3} \tag{2.13}$$

where m_p^* is the effective mass of valence band state density, m_{hh}^*, m_{lh}^* and m_{SO}^* the effective masses of the three spherical valence bands, E_V and E_F the energies of the valence band edge and Fermi level, Δ the split-off energy. It is more convenient to write the density of electrons as

$$n = N_C\ e^{-\beta(E_C - E_F)} \tag{2.14}$$

with the effective density of conduction band states

$$N_C = 2\left(\frac{2\pi m_n^* k_B T}{h^2}\right)^{3/2} \tag{2.15}$$

and the density of holes as

$$p = N_V \; e^{-\beta(E_F - E_V)} \tag{2.16}$$

with the effective density of valence band states

$$N_V = 2 \left(\frac{2\pi m_p^* k_B T}{h^2} \right)^{3/2} \tag{2.17}$$

For an intrinsic semiconductor the condition $n = p = n_i$ is valid, where n_i is the intrinsic carrier density. The intrinsic Fermi level E_i is obtained from equating Eqs. 2.14 and 2.16

$$\begin{aligned} E_i &= \frac{E_C + E_V}{2} + \frac{k_B T}{2} \ln\left(\frac{N_V}{N_C}\right) \\ &= \frac{E_C + E_V}{2} + \frac{3 k_B T}{4} \ln\left(\frac{m_p^*}{m_n^*}\right) \end{aligned} \tag{2.18}$$

The intrinsic carrier density is also obtained from Eqs. 2.14 and 2.16:

$$n_i = \sqrt{n \cdot p} = \sqrt{N_C N_V} \; e^{-\beta E_g / 2} \tag{2.19}$$

where $E_g = E_C - E_V$ is the energy of the band gap. This equation is called the mass action law, which is valid for both intrinsic and extrinsic (i.e. doped with impurities) semiconductors under thermal equilibrium condition. A compilation of the effective masses of state density, the intrinsic carrier concentrations and the band gap energy can be found in appendix A.

Effective thermal mass

The effective thermal mass of charge carriers is related to their thermal velocity. However, using the approximation of a free particle in a constant potential the velocity of the particle is

$$\vec{v} = \frac{1}{\hbar} \; \nabla_{\vec{k}} \cdot E(\vec{k}) \tag{2.20}$$

where $E(\vec{k})$ is the kinetic energy of the particle. The thermal velocity v_{th} is used in the capture rate equations. For further details see chapter 3.4.1. The thermal velocity of electrons and holes is

$$\begin{aligned} v_{th,n,p} &= \frac{\int_E |\vec{v}_{n,p}| \; \{f_{Dirac}, [1 - f_{Dirac}]\} \; D_{C,V} \; dE}{\int_E \{f_{Dirac}, [1 - f_{Dirac}]\} \; D_{C,V} \; dE} \\ &\approx \frac{\int_{\vec{k}} |\vec{v}_{n,p}| \; e^{-\beta \cdot E(\vec{k})} \; d\vec{k}}{\int_{\vec{k}} e^{-\beta \cdot E(\vec{k})} \; d\vec{k}} \end{aligned} \tag{2.21}$$

In the case of a spherical energy band the evaluation of Equation 2.21 gives

$$\bar{v}_{th} = \sqrt{\frac{8 k_B T}{\pi m^*}} \tag{2.22}$$

where m^* is the effective mass of the energy band. Equation 2.22 is used to define the effective thermal mass by setting $m^* = m^*_{th}$. The effective thermal mass for the non-spherical conduction band is

$$\begin{aligned} m^*_{th,n} &= \frac{4\, m^*_l\, \delta^2}{\left(\delta + \sqrt{\frac{m^*_l}{m^*_t}} \arcsin \delta\right)^2} \\ \delta &= \sqrt{\frac{m^*_l - m^*_t}{m^*_l}} \end{aligned} \tag{2.23}$$

The effective thermal mass for three spherical valence bands is

$$m^*_{th,p} = \left(\frac{m^{*3/2}_{hh} + m^{*3/2}_{lh} + m^{*3/2}_{SO}\, e^{-\beta\Delta}}{m^*_{hh} + m^*_{lh} + m^*_{SO}\, e^{-\beta\Delta}} \right)^2 \tag{2.24}$$

But it is more accurate for the calculation of the effective thermal mass of holes to take into account the non-parabolic shape of the bands. In this case Equation 2.24 is not valid. The effective thermal masses of both charge carriers are compiled in appendix A.

Doping of semiconductors - Donors and Acceptors

When a semiconductor is doped with impurities, which introduces shallow energy levels, the semiconductor becomes extrinsic. If a silicon atom is

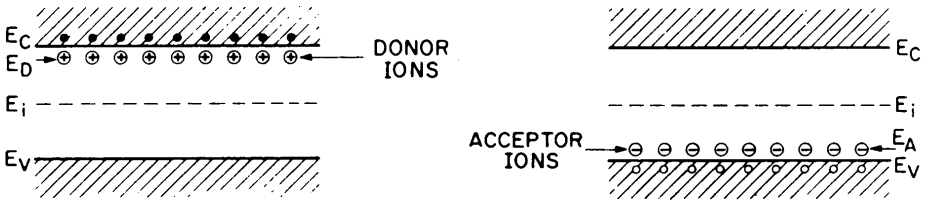

Figure 2.4: *Schematic bands with shallow energy levels are shown. On the left hand side n-type silicon with positive ionized donors and on the right hand side p-type silicon with negative ionized acceptors are shown* [Sze85].

replaced by a phosphorous atom with five valence electrons, the fifth electron is not needed to form the four covalent bonds around the phosphorous, and an electron is released to the conduction band. The phosphorous sites are positively charged, as shown on the left hand side of 2.4. The silicon becomes n-type, because the free charge carriers are negatively charged. The phosphorous atom is a donor. Under complete ionisation condition at room temperature the electron density in the conduction band is

$$n = N_D \tag{2.25}$$

where N_D is the donor concentration. Electrons are in an n-type semiconductor the majority charge carriers and holes the minority charge carriers. From Eqs. 2.14 and 2.25 one obtains the Fermi level in terms of the effective density of states N_C and the donor concentration N_D

$$E_C - E_F = k_B T \ln\left(\frac{N_C}{N_D}\right) \tag{2.26}$$

Similarly when a boron atom with three valence electrons substitutes a silicon atom, an additional electron is needed to form the four covalent bonds around the boron, and a hole is created in the valence band. The boron sites are negatively charged, as shown on the right hand side of 2.4. The silicon becomes p-type, because the free charge carriers are positively charged. The boron atom is an acceptor. Under complete ionisation condition at room temperature the concentration of holes in the valence band is

$$p = N_A \tag{2.27}$$

where N_A is the acceptor concentration. Holes in a p-type semiconductor are the majority charge carriers and electrons the minority charge carriers. Again one obtains the Fermi level from Eqs. 2.16 and 2.27

$$E_F - E_V = k_B T \ln\left(\frac{N_V}{N_A}\right) \tag{2.28}$$

It is often useful to express both charge carrier concentrations in terms of the intrinsic carrier density and the intrinsic Fermi level. From Eqs. 2.14 and 2.16 one obtains

$$\begin{aligned} n &= N_C \, e^{-\beta(E_C - E_F)} \\ &= n_i \, e^{\beta(E_F - E_i)} \end{aligned} \tag{2.29}$$

and

$$\begin{aligned} p &= N_V \, e^{-\beta(E_F - E_V)} \\ &= n_i \, e^{\beta(E_i - E_F)} \end{aligned} \tag{2.30}$$

The mass action law $n \cdot p = n_i^2$ can be easily verified by multiplying Eqs. 2.29 and 2.30.

It have to be mentioned that a semiconductor can be doped with both donors and acceptors and the free charge carrier concentration at room temperature is equal to effective doping concentration

$$N_{eff} = N_D - N_A \tag{2.31}$$

For example a partion of negative charge carriers are captured into the acceptor states and thus the electron density is reduced.

2.1.2 pn junction

The pn junction is the basic device structure in semiconductor physics. Its behaviour under applied voltage is elementary for understanding other semiconductor devices. Silicon detectors are in principle asymmetric p^+n junctions and for the DLTS studies also p^+n junctions are employed. The measured quantities of a p^+n junction, capacitance and current, are explained.

Formation of a pn junction

On the left hand side of figure 2.5 a p-type and n-type semiconductor together with the schematic energy band diagrams are shown. If the two semiconductors are joined together the thermal equilibrium condition is perturbed[3]. The holes of the p-type region diffuse into the n-type region and the electrons of the n-type region diffuse into the p-type region. Hence the diffusing charge carriers become minority charge carriers and recombine with majority charge carriers. Due to the depletion of charge carriers a space charge region (SCR) is formed containing the fixed charged atoms of the doping species. The donors are positively charged and the acceptors are negatively charged. The space charge region creates a potential barrier. The potential difference is called the built-in voltage V_{bi}. The additional electric field induces a drift current J_{drift} which cancel the diffusion current J_{diff} under thermal equilibrium condition, as shown on the right hand side of figure 2.5. The current densities of electrons and holes are

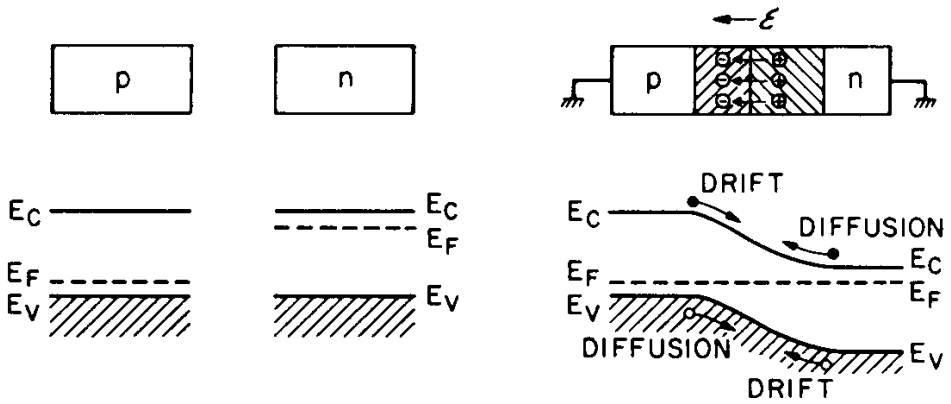

Figure 2.5: *On the left hand side the physically separated p-type and n-type semiconductors together with the schematic energy band diagrams are shown. On the right hand side the formation process of the junction and the junction under thermal equilibrium are shown* [Sze85].

[3]Also indicated by the different positions of the Fermi levels of the two separated semiconductors. The Fermi level is constant, if the thermal equilibrium condition is reached.

$$
\begin{aligned}
J_n &= J_{n,drift} + J_{n,diff} \\
&= q_0\,\mu_n\,n\,|\vec{E}| - q_0\,D_n\,\frac{dn}{dx} \\
J_p &= J_{p,drift} + J_{p,diff} \\
&= q_0\,\mu_p\,p\,|\vec{E}| + q_0\,D_p\,\frac{dp}{dx}
\end{aligned} \tag{2.32}
$$

where q_0 is the charge unit of a charge carrier, $\mu_{n,p}$ the mobility[4] of a charge carrier type, n and p the charge carrier concentrations, E the electric field in the space charge region and $D_{n,p}$ the diffusion constants. If the Einstein relation $D = \mu \cdot \frac{k_B T}{q}$ and Eqs. 2.29 and 2.30 are used, Equation 2.32 reduce to

$$
\begin{aligned}
J_n &= \mu_n\,n\,\frac{dE_F}{dx} = 0 \\
J_p &= \mu_p\,p\,\frac{dE_F}{dx} = 0
\end{aligned} \tag{2.33}
$$

Hence the Fermi level is constant, if the current densities are zero. It should be mentioned that the gradient of the potential energy is equal the gradient of the intrinsic Fermi level, because the intrinsic Fermi level is parallel to the energy bands.

Space charge region

The biasing of the pn junction with an external voltage source changes the width of the space charge region and the free charge carrier distributions near the edges of the space charge region, as shown in figure 2.6. In the forward bias case the applied voltage at the p-type side is positive to the n-type side. Thus majority charge carriers are injected on both sides and the space charge region shrinks. In the reverse bias case the applied voltage at the n-type side is positive to the p-type side. This results in a further depletion of free charge carriers on both sides and hence the space charge region grows. The gradient of the electric field in the space charge region is[5]

$$
\left|\frac{dE}{dx}\right| = \frac{q_0 \cdot N_{eff}}{\epsilon_s} \tag{2.34}
$$

where q_0 is the charge unit of a ionized impurity atom, N_{eff} the effective doping concentration and ϵ_s the permeability of silicon which is the product of the permeability in vacuum ϵ_0 and the dielectric constant of silicon. For a homogeneously doped semiconductor the electric field gradient is constant. The potential difference between the begin and end of the space charge region is obtained from two fold integration of Equation 2.34. Neglecting the voltage drop across the resistance of the undepleted bulk, it follows for a reverse biased junction

$$
V_R + V_{bi} = \frac{q_0 N_A}{2\epsilon_s}\,W_p^2 \;+\; \frac{q_0 N_D}{2\epsilon_s}\,W_n^2 \tag{2.35}
$$

[4] The drift velocity of a charge carrier in a semiconductor is $\vec{v}_{n,p,drift} = \mu_{n,p} \cdot \vec{E}$

[5] This can be easily verified with Gauss law.

where W_p and W_n are the widths of the space charge layers in the p-type and n-type regions. $W = W_n + W_p$ is the total width of the space charge region. The charge neutrality requires

$$N_A \cdot W_p = N_D \cdot W_n \tag{2.36}$$

It can be easily verified for a p^+n junction that the width of the p-type region $W_p \ll W_n$ and the width of the n-type region is

$$W_n = \sqrt{\frac{2\epsilon_s \, (V_R + V_{bi})}{q_0 \, N_D}} \tag{2.37}$$

Often N_{eff}, which is net space charge density from different doping species, is used instead of N_D.

The electric field distribution on the n-type side of a pn junction is obtained by integration of Eq. 2.34

$$\begin{aligned} E(x) &= E_{max} \left(1 - \frac{x}{W_n}\right) \\ E_{max} &= \frac{q_0 \, N_{eff}}{\epsilon_s} \cdot W_n \end{aligned} \tag{2.38}$$

where E_{max} is the maximal electric field at boundary to the p-side. The space coordinate at the boundary is zero and is positive on the n-type side, as shown in figure 2.6. The electric field distribution has a triangular shape. In the case of a p^+n junction the voltage drop across p^+ side of the junction is negligible, as mentioned above. Hence the maximal electric field is

$$E_{max} = \frac{2 \cdot (V_R + V_{bi})}{W_n} \tag{2.39}$$

employing Equations 2.37 and 2.38.

Depletion capacitance

A measured quantity of a pn junction is the small signal capacitance. It depends on the applied voltage. The depletion capacitance of a reverse biased p^+n junction is

$$C_R \equiv \frac{dQ}{dV} = \frac{dQ}{dW}\frac{dW}{dV} = \sqrt{\frac{q_0 \, \epsilon_s \, N_D}{2(V_R + V_{bi})}} = \frac{\epsilon_s}{W} \tag{2.40}$$

The capacitance is inverse proportional to the width of the depletion region and therefore used to determine the depletion width. A reordering of Eq. 2.40 results in

$$\frac{1}{C_R^2} = \frac{2 \, (V_R + V_{bi})}{q_0 \, \epsilon_s \, N_D} \tag{2.41}$$

It is clear from Eq. 2.41 that a plot of $1/C_R^2$ versus V_R produces a straight line for a homogeneously doped p^+n junction. The slope gives the doping concentration of the n-type region and from extrapolation to $1/C_R^2 = 0$ the built-in voltage V_{bi} is obtained. Again often N_{eff} is used instead of N_D.

Current

The current flow through a pn junction depends on the applied bias. The net current is the sum of the drift and diffusion currents of each charge carrier type. The drift current is independent on the applied bias, because it depends only on the conditions at the boundaries of the space charge region, which are not changed for a homogeneously doped semiconductor. On the other hand the diffusion current depends strongly on the height of the potential barrier across the the space charge region. The thermal agitation on the charge carriers in the electrical neutral bulk (ENB) is described by the Boltzmann distribution function[6]. Therefore the diffusion current density is

$$J_{diff} \propto e^{-\frac{q_0(V_R+V_{bi})}{k_B T}} \tag{2.42}$$

where V_R is the applied reverse voltage. The addition of both current components gives

$$J(V) = J_s \left(e^{\frac{q_0 V}{k_B T}} - 1 \right) \tag{2.43}$$

where J_s is the saturation current density and V the applied voltage. In this equation the applied voltage is negative for the reverse biasing case. The reverse current for large voltages is dominated by the drift currents which are independent on the applied voltage. The saturation current density is the sum of hole and electron drift current densities

$$J_S = \frac{q_0 D_p p_{no}}{L_p} + \frac{q_0 D_n n_{po}}{L_n} \tag{2.44}$$

where $L_{n,p} = \sqrt{D_{n,p}\tau_{n,p}}$ are the diffusion lengths of the charge carriers, $\tau_{n,p}$ the minority lifetimes of the charge carriers, p_{no} and n_{po} the minority charge carrier densities in n-type and p-type silicon under thermal equilibrium condition. Equation 2.43 can also be employed for the forward bias case with low current levels. In this case the polarity of the voltage source is changed and the space charge region shrinks and therefore the potential height. The current is dominated by the diffusion currents. However, the ideal diode equation is often modified by an ideality factor η

$$J(V) = J_s \left(e^{\frac{qV}{\eta k_B T}} - 1 \right) \tag{2.45}$$

At high current densities the injected minority carrier density is comparable to the majority concentration on the n-side of a p^+n junction [Mol58]. This is the high injection condition and $\eta \approx 2$. Also recombination or generation of charge carriers in the space charge region modify η.

In irradiated asymmetric p^+n junctions or silicon detectors the reverse or leakage current is dominated by the current generated by radiation induced

[6] It is the common employed approximation of the tail of the Fermi-Dirac distribution.

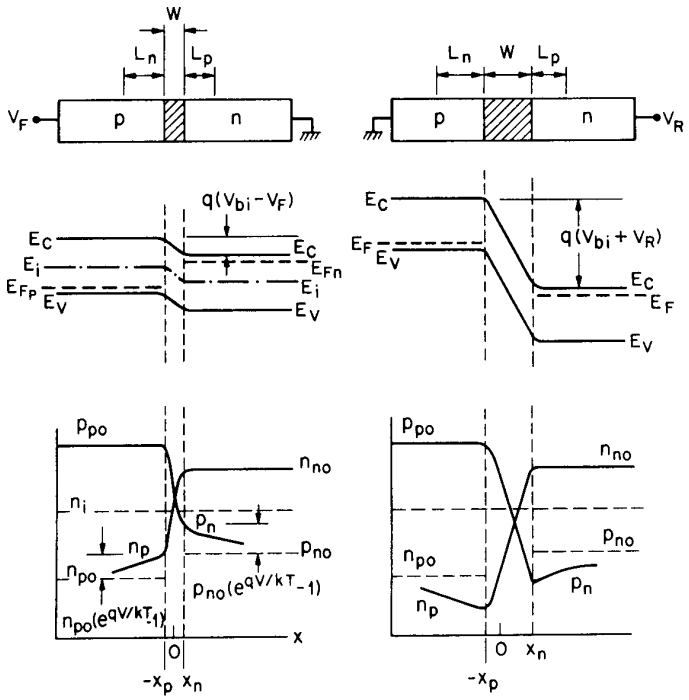

Figure 2.6: *Depletion region, energy bands and charge carrier distributions of a biased pn junction are shown. On the left hand side the forward bias case and on the right hand side the reverse bias case are shown* [Sze85].

defect centers near the intrinsic Fermi level. The generation rate of electron-hole pairs per unit volume is defined by

$$G = \frac{n_i}{\tau_g} \tag{2.46}$$

where n_i is the intrinsic carrier density and τ_g the generation lifetime. Thus the volume generation current is

$$J_{Vol} = q_0 \cdot \frac{n_i}{\tau_g} \cdot W \tag{2.47}$$

where $W \approx W_n$ for a reverse biased p^+n junction. A combination of Eqs. 2.37 and 2.47 gives $J_{Vol} \propto \sqrt{V_R + V_{bi}} \approx \sqrt{V_R}$. The generation lifetime of a defect center with one energy level in the band gap is

$$\tau_g = \frac{c_T \cdot N_T}{2 \cdot \cosh(\beta(E_T - E_i))} \tag{2.48}$$

where c_T is the capture coefficient, N_T the defect concentration and E_T the energy of the defect state. The simplification $c_T = c_n = c_p$ is employed. For further details see chapter 3.4.2. The temperature dependence of the volume generation current is mainly due to the temperature dependence of

the intrinsic carrier density. An empirical formula of the intrinsic carrier concentration in the temperature range from 275 to 375 K [Spr91] is

$$n_i(T) = 9.15 \cdot 10^{19}\ \mathrm{cm}^{-3} \left(\frac{T}{300\mathrm{K}}\right)^2 \exp\left(-\frac{6880\mathrm{K}}{T}\right) \tag{2.49}$$

The change of the volume generation current due to the change in the generation time constant divided by the change due to the change in the intrinsic carrier concentration is

$$\frac{\frac{dJ_{vol}}{d\tau_g}\frac{d\tau_g}{dT}}{\frac{dJ_{vol}}{dn_i}\frac{dn_i}{dT}} = \frac{\tanh(\beta(E_T - E_i)) \cdot \beta(E_T - E_i)}{2 + 6880\mathrm{K}/T}$$

The ratio is small for small values of $\beta(E_T - E_i)$ at room temperature. Therefore the assumption of a temperature independence of τ_g is in good approximation valid. The factor to calculate the volume generation current at a reference temperature T_R from the leakage current measured at a temperature T is

$$R(T) = \left(\frac{T_R}{T}\right)^2 \exp\left(-6880\mathrm{K}\left[\frac{1}{T_R} - \frac{1}{T}\right]\right) \tag{2.50}$$

The correction factor used in [Mol99] is

$$R(T) = \left(\frac{T_R}{T}\right)^2 \exp\left(-6498\mathrm{K}\left[\frac{1}{T_R} - \frac{1}{T}\right]\right) \tag{2.51}$$

The difference between the two correction factors in the temperature range from 18°C to 22°C for a reference temperature 20°C is smaller than 1%.

2.1.3 Metal semiconductor contact - Schottky diode

A metal semiconductor contact has as a p^+n junction a depleted zone or space charge region. The width of the space charge region depends on the applied voltage. A clear difference is that the current flow is furnished only by majority charge carriers of the semiconductor. Figure 2.7 shows the energy band diagram of a metal layer adjacent to a n-type semiconductor. The work functions of the metal $q \cdot \Phi_m$ and of the semiconductor $q \cdot \Phi_s$ are different. The work function is the difference between the Fermi level and the vacuum level. Also shown is the electron affinity $q \cdot \chi$, which is the energy difference between the conduction band edge of the semiconductor and the vacuum level. For a metal the work function and the electron affinity are equal. When the metal is in contact with the semiconductor, electrons migrate to the metal side, because the energy of the charge carriers is higher in the n-type semiconductor. Thus the metal semiconductor contact is going into a state with a lower energy. The charge exchange results in a positive space charge region in the n-type semiconductor and a surface charge layer of electrons in the metal. The space charge layers create a potential barrier.

The potential barrier lowers the energy of the electrons in the semiconductor. Because the electron affinity is constant in each material and their difference at the metal-semiconductor interface, the height of the barrier is

$$\Phi_{Bn} = \Phi_m - \chi \tag{2.52}$$

Under thermal equilibrium condition the Fermi level is constant and the built-in voltage is

$$V_{bi} = \Phi_m - \Phi_s \tag{2.53}$$

The space charge region shrinks and grows, if a voltage is applied to the Shockley contact as for a p^+n junction, but an injection of minority charge carriers into the semiconductor bulk under forward bias condition does not occur.

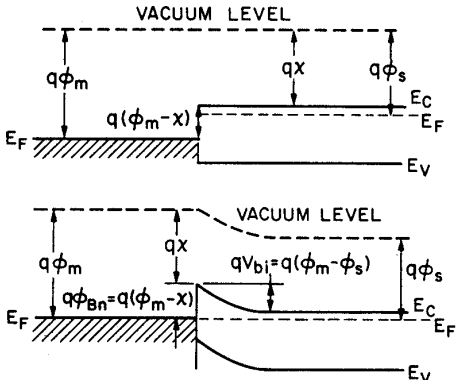

Figure 2.7: *Energy bands of a Shockley contact before and after reaching the thermal equilibrium condition are shown* [Sze85].

2.1.4 Ohmic contact - Back side contact

An ohmic contact is defined as a metal semiconductor contact that has a negligible contact resistance in comparison to the bulk resistance of the semiconductor. The charge transport is furnished by the majority charge carriers of the semiconductor. A metal contact on a highly doped n^+-type semiconductor has this properties, because the barrier width is very narrow, and thus the tunnel rate of majority charge carriers through potential barrier is large [Sze85].

2.2 Manufacturing of the silicon material and processing

Two crystal growth techniques are mainly used to manufacture single-crystal silicon from polycrystalline silicon. The methods, briefly described here, are the Czochralski (CZ) and Floatzone (FZ) techniques. Also it is possible

to growth a silicon layer on single-crystal substrate by deposition of silicon atoms out of a gaseous or liquid phase. This growth technique is referred as epitaxial growing, because the matrix, how to arrange the deposited atoms, is taken from the substrate. A detailed description of the growth techniques can be found in [Mol99].

A contamination of the silicon material during the crystal growth can not be eliminated totally. Oxygen and carbon are the most frequent impurities. During the growth process the silicon material can be deliberately enriched with impurities like oxygen, carbon and nitrogen. The enrichment of silicon with impurities is interesting in the point of view of defect engineering. The introduction of impurities can also be performed after wafer cutting by high temperature diffusion.

2.2.1 Czochralski silicon

The polycrystalline silicon together with the doping impurity is melted in a quartz crucible. A quartz crucible is employed, because the melting point of quartz or fused silica is higher than for silicon. The melting point of silicon is 1420°C. The crucible is surrounded by a graphite suspector. A radio frequency coil is employed to induce currents in the graphite. Due to the power dissipation of the induction currents the crucible is heated. A single-crystal is placed on the surface of the melt and is lifted up. The crystallization at the solid-liquid interface yields a single-crystal with the orientation of the seed. The pulling rate determines the diameter of the crystal. The crystal is grown in an inert atmosphere of nitrogen or argon to have no oxidation of the silicon. Czochralski grown silicon is not defect free. The defects are mainly localized in an annular ring-pattern. The ring is called oxide-induced stacking fault ring (OSF). The position of the OSF ring depends on local growth conditions, e.g. the oxygen concentration, temperature gradient, pulling rate and point defect density [Rae96]. Also during the crystal growth the quartz crucible gradually dissolves, releasing oxygen into the melt. The typical concentration of oxygen in CZ silicon is about $10^{18}\mathrm{cm}^{-3}$. The carbon concentration is about $10^{16}\mathrm{cm}^{-3}$. Thermal donors can be formed during cooling. Thermal donors are multi-oxygen complexes. Due to the contamination with boron from the crucible the available resistivity of CZ wafers is typical less than $100\Omega cm$ for p-type and n-type silicon. Therefore CZ material is not suitable for detector production, which requires high resistivity and defect free silicon.

2.2.2 Floatzone silicon

Defect free and high resistivity single-crystal silicon can be obtained using the FZ technique. The refinement is done by moving a small molten zone along a polycrystalline rod. A RF coil is employed to melt the silicon. As the float zone is moved along the rod, the molten silicon solidifies into crystalline silicon with a high purity. Again a single-crystal seed is used to determine

the orientation of the silicon crystal at the beginning of the refinement. The crystal growth is performed in a inert atmosphere or vacuum to avoid the oxidation of the silicon. Because there is no mechanical contact with the environment, the contamination of the silicon is low. Typical oxygen and carbon concentrations in FZ silicon are less than $10^{16}\,\mathrm{cm}^{-3}$.

The resistivity of the silicon depends on the doping atom concentration in the polycrystalline material. But FZ crystals can also be doped by adding gases like phosphine (PH_3) or diborane (B_2H_6) to the inert gas atmosphere. A similar method to introduce impurities with a high concentration is to flow gases directly on the floating zone. This technique have been used for the production of oxygen enriched silicon, referred as jet-oxygenated silicon. But this method works only, if the crystal diameter is smaller than 2 inches. Another technique is to introduce the impurity species at the beginning of the FZ process, e.g. by soldering a slice of a crystal with a high carbon content between the seed and the silicon rod. Because the initial impurity concentration in the molten zone decreases during moving along the rod, the impurity concentration in the FZ crystal is not constant and shows a gradient. The above techniques have been used for the production of oxygen and carbon enriched silicon.

2.2.3 Epitaxial silicon

This technique is the growth of a silicon layer on a single-crystal silicon substrate. There are many epitaxial growing methods. The most important for silicon device production is the vapor-phase epitaxy (VPE). The silicon atoms are deposited out of a gaseous phase on the substrate. Various silicon sources are used for VPE technique, e.g. silicon tetrachloride. The typical reaction temperature is about 1200° C. The reaction scheme of silicon tetrachloride is

$$SiCl_4(gas) + 2H_2(gas) \longleftrightarrow Si(solid) + 4HCl(gas).$$

and also the competing reaction taking place

$$SiCl_4(gas) + Si(solid) \longleftrightarrow 2SiCl_2(gas).$$

Therefore, if the silicon tetrachloride concentration is too high, etching rather than growth of silicon take place. The dopant impurities are incorporated into the lattice during the growth of the silicon layer. Gaseous phosphine (PH_3) and diborane (B_2H_6) are used as n-type and p-type dopants. Hydrogen gas is employed as diluent to allow the control of the flow rate for the desired doping concentration. During epitaxial growth impurities like oxygen and carbon diffuse from the substrate into the epitaxial layer. A wafer of CZ silicon can be employed as a single-crystal substrate to grow oxygen rich silicon. The commercial available thickness of epitaxial grown silicon layers is less than 5 μm. Therefore epitaxial grown silicon is not used for detector fabrication.

As indicated by the double arrows the reactions also works in the other direction, e.g. a high temperature HCl gas flow can be employed to etch and clean the surfaces of silicon wafers.

2.2.4 Oxygen diffusion

Another way to introduce oxygen into crystalline silicon is to grow a thick thermal oxide layer on wafer surface and to diffuse the oxygen out of the oxide layer into the silicon bulk. The diffusion process is done in a high temperature nitrogen or oxygen atmosphere ($1150-1200^{\circ}$C). The source of oxygen is the silicon-oxide interface. Secondary Ion Mass Spectroscopy (SIMS) measurements show that the oxygen concentration near the surface is higher than in the bulk [Fon00]. The oxygen concentration at a deep greater than 50 μm is constant and in the range from $1-4\cdot10^{17}\mathrm{cm}^{-3}$. For long oxygenation times the oxygen is distributed more homogeneously.

2.2.5 Planar processing

The silicon wafers, which are the starting point for detector fabrication, are obtained by cutting a single-crystal ingot into disks with a thickness of about 300 μm. After cutting the wafers are lapped to the wanted thickness and polished to reduce the surface roughness or the damage of the foregoing steps. The detector structures on silicon wafers are processed in various steps. At the beginning of the processing a thick oxide layer is grown, referred as field oxide. The thick oxide protects the wafer during handling, and later the detector from contamination with impurities from the environment. The oxide acts also as an insulator between the detector structures and eliminate lateral surface currents. Also the interface state density at the oxide-silicon interface is much lower than for an unpassivated silicon surface. The thermal oxidation is performed in an oxygen atmosphere (dry oxidation) or in an oxygen atmosphere with water vapor (wet oxidation). The growth rate in a wet atmosphere is higher than in a dry atmosphere. High quality thermal oxide is grown in a dry atmosphere at a temperature of 1000°C. The growth rate also depends on the orientation of the wafer substrate. Sometimes small quantities of HCl or TCE are added to the oxygen atmosphere to getter transition metals at the wafer surface and to enhance the growth rate. The technology to manufacture detectors on silicon wafers is referred as planar technology.

For the macroscopic and microscopic studies simple p^+n diodes processed by different institutes and companies are used.

The ITE process is described in [Mol99]. The cross section and the top view of a $p^+\,\nu\,n^+$ structure are shown in figure 2.8. The area of the front contact is 0.25 cm^2. The distance between the guard ring and the front contact is 0.1 mm. The width of the guard is 0.2 mm. The diameter of the window in the middle of the front contact is 2 mm. The back contact is furnished by

an aluminium grid. The p^+ and n^+ regions are diffused.

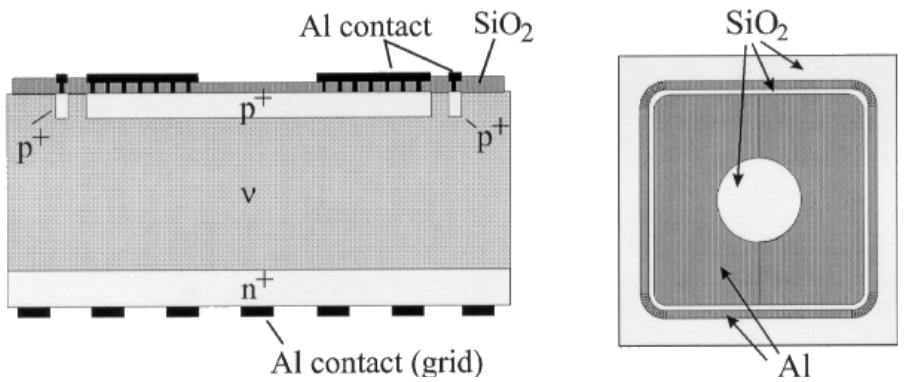

Figure 2.8: *Cross section and top view of a $p^+ \nu\ n^+$ structure are shown* [Mol99].

The same mask is also used for the diodes processed by STMicroelectronics and CiS. SINTEF used a mask with a smaller guard ring. The diodes processed by ELMA have a fine multi-guard ring structure and the back side is full metallized. The area of the front contact is 0.24 cm^2. The test structures are processed together with a large area detector on one wafer. The p^+ and n^+ regions are implanted.

2.3 Operation of silicon detectors

Various types of detectors are used in High Energy Physic (HEP) experiments to detect the secondary particles produced after a collision of high energetic particles. Silicon detectors are used in the inner tracking region of HEP experiments to track the particle traces near the collision point. Silicon detectors are preferred, because of the ability of fine segmentation of p^+n junction structures and the fast collection of the charge generated along the track of an ionising particle. Thus silicon detectors will fullfill the requirements for the next generation of HEP experiments. The only drawback is the radiation damage in the silicon material.

2.3.1 Properties of silicon detectors

The properties of silicon detectors are the depletion voltage, the depletion capacitance, the leakage current and the charge collection efficiency. These parameters are changed after irradiation with high energy particles. The voltage to deplete a detector fully is

$$V_{depl} = \frac{q_0 \cdot N_{eff}}{2\,\epsilon_s} \cdot d^2 \tag{2.54}$$

where d is the thickness of the detector. This can be easily seen from equation 2.35 neglecting the built-in voltage V_{bi} and the depletion zone in the p^+

region. The electric field distribution has a triangular shape. The effective space charge density $q_0 \cdot N_{eff}$ is changed after irradiation with high energy particles. Also the electric field distribution differs from the triangular shape [Cas00]. The capacitance of a fully depleted detector depends only on the geometrical area of the front contact pattern or back contact pattern. The capacitance per area is

$$C_{depl} = \frac{\epsilon_s}{d} \tag{2.55}$$

The reverse capacitance of a not fully depleted detector is inverse proportional to the square root of the applied voltage

$$C_R = C_{depl} \sqrt{\frac{V_{depl}}{V_R}} \tag{2.56}$$

The leakage current of an unirradiated fully depleted detector is mostly small. The leakage current after irradiation with high energy particles is dominated by the volume generation current and is proportional to the particle fluence

$$I_{depl} \propto \Phi_p \tag{2.57}$$

The reverse current of a not fully depleted detector is proportional to the square root of the applied voltage

$$I_R = I_{depl} \sqrt{\frac{V_R}{V_{depl}}} \tag{2.58}$$

Along an ionisation trace of a particle electron-hole (eh) pairs are generated. In the depleted detector volume the eh pairs are separated by the electric field. The collected charge (CC) of an homogeneous ionisation trace in a not fully depleted detector is proportional to the square root of the applied reverse voltage

$$\mathrm{CC} = Q_{depl} \sqrt{\frac{V_R}{V_{depl}}} \tag{2.59}$$

The charge collection efficiency (CCE) of a fully depleted detector is one. After irradiation with high energy particles the CCE decreases, because trapping of electrons and holes occurs. Trapping centers are created due to the radiation damage. The electron and hole trapping after neutron irradiation is investigated in [Bro00].

However, the IV and CV/CC characteristics of irradiated diodes are shown in figure 2.9 and 2.10. They exhibit deviations from the ideal characteristics of unirradiated diodes. The deviations have been not explained yet. A possible explanation are surface effects. Also the value of the depletion voltage depends on the equivalent circuit which is used to describe the device. One is the serial circuit in which the capacitor and the resistor are in series and the other one is the parallel circuit in which the capacitor and the resistor are parallel.

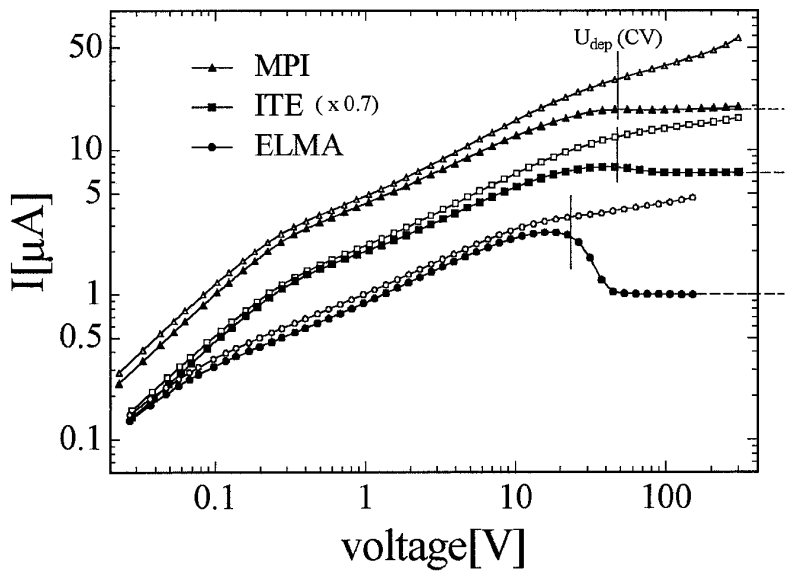

Figure 2.9: *Examples of IV characteristics of irradiated diodes are shown. The filled symbols indicate the measurements with connected guard ring and the open ones without connected guard ring* [Mol99].

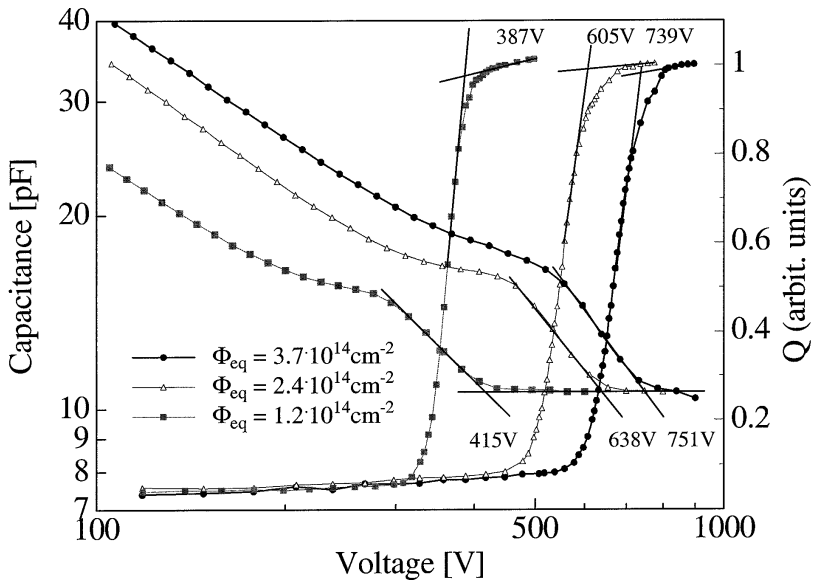

Figure 2.10: *Examples of CV/CC characteristics of irradiated diodes are shown* [Mol00].

Chapter 3

Radiation induced damage in silicon

Radiation damage in silicon detectors can be divided into surface and bulk damage [Lin87]. The degradation of the properties of silicon detectors is mainly due to the bulk damage which is caused by displacements of atoms from their sites in the crystal lattice. A useful quantity to describe the displacement damage is the Non Ionisation Energy Loss (NIEL). The radiation effects produced by different particles with various energies scale in good approximation with the NIEL. The displacement damage after irradiation with high energy particles results in a formation of isolated point defects and clusters of defects. After ^{60}Co γ-photon and high energy electron irradiation only isolated point defect are created. The electrical properties of point defects and clustered defects are different. Also only the kinetic of point defects is influenced by impurities in the silicon material.

3.1 Damage mechanism of particles

A particle passing through a material volume loses its energy in different ways. The coulomb interaction results in an excitation and ionisation of the shell electrons of the atoms constituting the solid medium. Another energy loss mechanism due to coulomb scattering is the deacceleration of a charged particle passing through the electric field of an atomic nucleus. The emission of electromagnetic radiation occurs. Kinetic energy is mainly transferred to an atom of the solid by nuclear scattering. If the transferred energy is high enough, the atom is displaced out of its lattice site. In high energy collision also an excitation of the nucleus take place and the emission of γ-photons and secondary particles occur. Also a fragmentation of the nucleus is possible. The energy loss in a medium is expressed as the energy deposition per unit path length dE/dx. If the energy loss is high, the impinging particle is stopped in the medium. The energy loss is often normalized to the density of the material ρ, referred as stopping power $S = \frac{1}{\rho}\frac{dE}{dx}$.

3.1.1 Surface damage

The coulomb interaction of a charged particle with the shell electrons of an atom transferres kinetic energy to the electrons. If the energy transferred to an electron is larger than its binding energy, a void in one of the bonds between the atoms constituting the solid is left. In the band structure picture an electron is excited from the valence band to the conduction band. This excitation is referred as ionisation. The electron and the hole are mobile in the crystal lattice. The average energy to generate an electron-hole (eh) pair in crystalline silicon is $E_{eh} = 3.6$ eV and in thermally grown silicon oxide $E_{eh} = 17$ eV. In both materials the ionisation energy is larger than energy of the band gap. The remaining energy is dissipated during the thermalisation of the generated eh pairs.

In crystalline silicon the generation of eh pairs produce no damage. The eh pairs recombine in the electrical neutral bulk. In the presence of an electrical field the eh pairs are separated and the charge neutrality is restored by the induced current flowing in the closed electronic circuit.

The generation of eh pairs by ionisation in an oxide layer grown on crystalline silicon changes the properties of the surface due to deep trapping of holes near the silicon-oxide interface and due to the generation of interface states, as shown in figure 3.1. Electrons are not trapped because of the lack of deep electron trapping centers in thermally grown oxide[1]. Because the hole traps are localized near the interface, an electric field in the oxide bulk during irradiation enhances or suppresses the trapping of holes at the interface [Ma89].

The oxide interface is positively charged after radiation with ionising particles. The charge contribution of the interface states depends on the position of the Fermi level at the silicon-oxide interface, which determines the number of occupied interface states [Kuh97]. The positive oxide charge results in an accumulation layer of electrons in n-type silicon and a depletion layer in p-type silicon. If the density of positive oxide charge is high enough, a negative inversion charge layer is build up in p-type silicon. In the case of depletion the interface states act as generation centers and the thermal generated eh pairs contribute to the surface leakage current. If an accumulation charge layer in n-type silicon or an inversion charge layer in p-type silicon exits, no eh generation occurs and the recombination rate of holes via the interface states is high. The accumulation and inversion charge layers present also a conducting channel, if a lateral electric field distribution exists. However, the potential distribution created by multi-guard ring structures results in a complicated behaviour of the silicon-oxide interface after irradiation due to the effects mentioned above. Gate controlled diodes are used for systematic investigations [Wue00]. Also the deviation of the IV characteristic of an inverted diode after charged particle irradiation from the characteristic of an unirradiated diode is assumed to be due to surface effects.

[1] The dielectric material silicon nitride Si_3N_4 contains mainly electron traps.

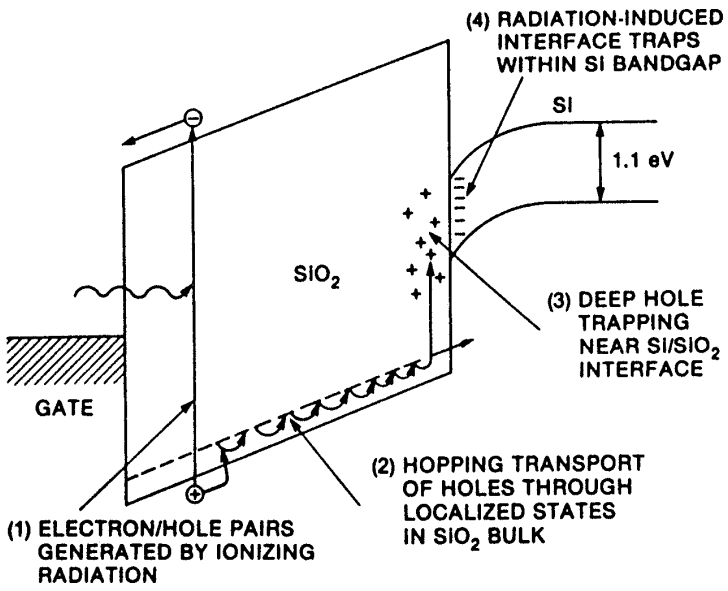

Figure 3.1: *The generation of surface damage at the oxide-silicon interface by ionising radiation in a MOS device* [Gar89].

3.1.2 Bulk damage

The interaction of an impinging particle with the lattice atoms transferres kinetic energy to the atoms and displaces them out of their lattice sites. Such a displaced atom is called Primary Knock on Atom (PKA). The energy spectrum of the produced PKAs depends on the impinging particle type and energy. For further details see chapter 3.2.4. A PKA loses its kinetic energy by further displacements of lattice atoms and ionisation. The energy loss due to ionisation or the electronic stopping power increases with increasing PKA energy.

A recoiled silicon atom with an energy E $>$ 10 keV displaces only a few silicon atoms at the beginning of its stopping range, because the nuclear stopping power is small in comparison to the electronic stopping power [Nor97]. Single interstitial-vacancy pairs, referred as Frenkel pairs, are generated along the track. The kinetic energy transferred to the secondary recoiled silicon atoms is mostly smaller than one keV. Only sometimes the transferred energy is greater than one keV. The threshold energy to create a Frenkel pair is about 20 eV. The nuclear stopping power increases strongly, if the recoil energy is E $<$ 10 keV. Hence the number of displacements per unit path increases. The stopping range is less than a few ten nanometers for silicon recoils with an energy E $<$ 10 keV. Terminal cluster regions are generated. Therefore a high energy PKA produces a collision cascade with terminal clusters. The case of a tree like collision cascade is shown on the left hand side on figure 3.2. The diameter of the terminal clusters is estimated from Transmission Electron Microscopy (TEM) and is in the order of 5 nm [How87]. Also a

time evolution of the cluster damage is observed [Rua83]. The time scale is in the order of 10 s at room temperature. The main number of generated interstitials and vacancies inside a terminal cluster region recombine. A silicon recoil atom that loses an energy of 5−10 keV creates a terminal cluster region containing 100−200 vacancies, if only in vicinity to each other generated vacancy-interstitial pairs recombine, and 10−20 vacancies, if the recombination length is equal to five lattice constants [Mue80]. In conclusion an energy greater than 3 keV is converted into thermal energy neglecting the ionisation energy loss, which is also mainly converted into thermal energy during electron-hole pair recombination. A classical estimation of the energy to melt a silicon sphere with a diameter of 5 nm is about 1.4 keV. Hence the terminal cluster region is overheated immediately after creation and represents a heat spike. After cooling the terminal cluster region is composed of divacancies and may be higher order vacancy complexes. Also higher order interstitial defects are possible. A simplified picture of a collision cascade is shown on the right hand side of figure 3.2, referred as supercluster. The size

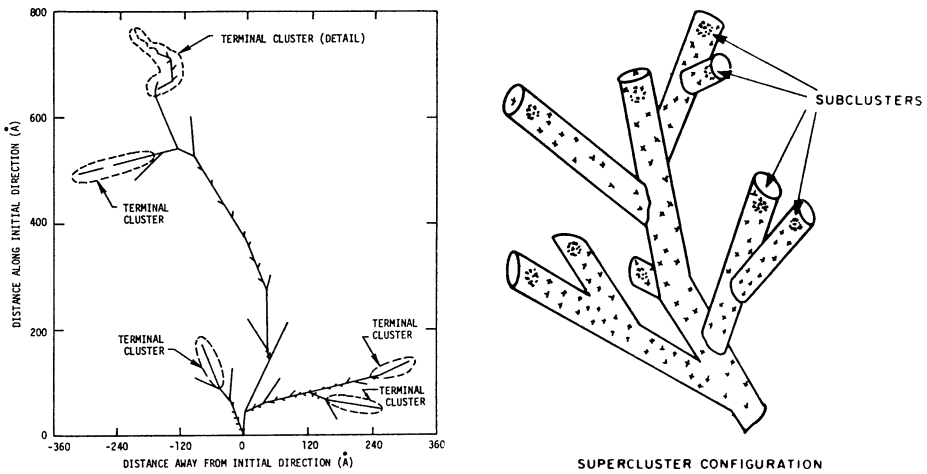

Figure 3.2: *On the left hand side the collision cascade produced by a PKA with an energy of 50 keV is shown* [Lin72]. *The terminal clusters are regions with a high displacement density. The tree like collision cascade is described reasonable by the supercluster model* [Hol70]. *Such a supercluster is shown on the right hand side. The configuration consists of single cylinders which contain the displacements. The crosses represent isolated displacements and the subclusters are equivalent to the terminal clusters.*

of a supercluster increases with increasing PKA energy. The diameter of a supercluster configuration is in the order of the range of the silicon recoil. The diameter of a supercluster created by a 50 keV PKA is about 100 nm. It is assumed that interstitials and vacancies are emitted into the environment

of the cascade damage region and that the defect kinetic inside the collision cascade region and in the environment is important for understanding cluster damage [Wat00]. It should be mentioned that collision cascades created by PKAs with the same energy show variations in their forms [Mue82], but the supercluster model is still valid. Simulations of collision cascades taking into account the fragmentation of the silicon nucleus show also tree like cascades and regions with a high density of defects [Huh00]. The diameter of the regions with a high defect density is in the order of 200 Å.

The electric field inside the terminal clusters due to charged defects plays a role during cluster formation [Zin82]. Ionisation during irradiation can change the charge states of the defects and hence the electric field distribution inside the terminal clusters. An attractive interaction between vacancies over a few lattice constants is also proposed [Bon98].

The collision cascades generated in a silicon crystal by silicon recoils with an energy $0.4-10$ keV is studied in more detail with molecular dynamics (MD) simulation methods [Nor98]. The displacement damage generation on the time scale of femtoseconds is simulated. It is shown that the damage which is created by a silicon recoil with an energy more than 1 keV has the form of a subcascade. The number of displaced atoms increases linearly with the deposited energy due to nuclear scattering processes. The damage can be separated into clusters of different sizes and isolated point defects. The large clusters are vacancy rich. The other damage consisting of point defects and small clusters is interstitial rich. The simulations are done in a cube with a side length of 184 Å for a 10 keV PKA [Nor00].

3.2 Non Ionising Energy Loss

The displacement damage in crystalline silicon can be scaled with the quantity of the Non Ionising Energy Loss (NIEL). The NIEL is the stopping power without the ionisation energy loss of the silicon recoils produced by an impinging particle. The NIEL hypothesis assumes that every macroscopic quantity scales linear with the NIEL. Thus it is useful to express the NIEL of different particles in units of the NIEL of 1 MeV neutrons. As discussed previously the displacement damage generated by a silicon recoil atom depends on its energy. Therefore the use of the NIEL as a quantity to scale the radiation damage between different particles is valid, if the NIEL is mainly due to PKAs with the same energy.

For example the NIEL hypothesis states that the ratio between the NIEL and the volume generation current is independent on the particle type and energy. This is supported by the assumption that mainly clusters are generated after particle irradiation which are responsible for the current generation. In conclusion the NIEL hypothesis applied to the volume generation current is only valid for particles which produce mainly recoils with an energy above a few keV. Therefore the NIEL hypothesis is not applicable for low energy proton, high energy electron and ^{60}Co γ-photon irradiations.

3.2.1 Displacement damage cross section

A particle that transverses a solid medium transferres kinetic energy to the atoms of the medium. This is referred as Kinetic Energy Released to MAtter (KERMA). For a medium with the thickness d the number of scattered particles per unit area and time of an interaction with the total cross section σ_ν is

$$\Delta\phi_p = \phi_p\Big(1 - \exp(-\sigma_\nu n\, d)\Big) \approx \phi_p{\cdot}\sigma_\nu{\cdot}n{\cdot}d \tag{3.1}$$

The density of scattering centers n is equal to the density of medium atoms. The approximation is valid, if $\sigma_\nu \cdot n \cdot d \ll 1$. However, the total cross section of an interaction depends on the energy of the impinging particle E_p and the recoiled atoms have an energy distribution. The function $p(E_p, E_R)dE_R$, which is employed to describe the recoil energy distribution, is the likelihood that the energy of the recoil atom is in the interval $[E_R, E_R + dE_R]$. The maximal energy is transferred to a medium atom after elastic back scattering

$$E_{R,max} = 2Mc^2\,\frac{p^2c^2}{(E_p + Mc^2)^2 - p^2c^2} \tag{3.2}$$

where M is the mass of the medium atom, m the mass of the impinging particle, p the momentum of the impinging particle and $E_p = \sqrt{m^2c^4 + p^2c^2}$ the particle energy[2]. This value is used as an upper limit for the recoil energy. It should be mentioned that the maximal recoil energy after non-elastic scattering is lower. The lower limit for the recoil energy is given by the threshold energy E_d to displace an atom out of its lattice site. As discussed previously, the recoiled atom loses its energy by displacements of atoms and ionisation. The portion of displacement energy loss is given by the Lindhard partition function $P(E_R)$. An analytical expression is given in [Laz87, Wun92]. The kinetic energy released to matter is

$$\text{KERMA} = \phi_p{\cdot}N{\cdot}\,t_{exp}\,\sum_\nu \sigma_\nu \cdot \int_{E_d}^{E_{R,max}} E_R\,P(E_R)\,p_\nu(E_p, E_R)dE_R \tag{3.3}$$

where N is the number of atoms in the medium and t_{exp} the exposure time. The sum includes the different scattering processes. It is more comfortable to define a displacement damage cross section

$$D_p(E_p) = \sum_\nu \sigma_\nu \cdot \int_{E_d}^{E_{R,max}} E_R\,P(E_R)\,p_\nu(E_p, E_R)dE_R \tag{3.4}$$

[2]The angular dependence of the energy of an elastic scattered particle in the Labor system is $E_p'(\theta) =$

$$\frac{E_p^2Mc^2 + E_p(M^2c^4 + m^2c^4) + Mc^2{\cdot}m^2c^4 + Mc^2(E_p^2 - m^2c^4)\cos(\theta)\sqrt{1 - \left(\frac{m}{M}\right)^2\sin^2(\theta)}}{(E_p + Mc^2)^2 - (E_p^2 - m^2c^4)\cos^2(\theta)}$$

The NIEL of a particle is the kinetic energy released to matter per unit path length divided by the density of the medium. The NIEL of one particle is

$$\text{NIEL} = \frac{D_p(E_p)}{M} = \frac{1}{M} \sum_{\nu} \sigma_\nu \cdot \int_{E_d}^{E_{R,max}} E_R \, P(E_R) \, p_\nu(E_p, E_R) dE_R \tag{3.5}$$

where M is the mass of a medium atom.

3.2.2 Hardness factor

It is useful for scaling the displacement damage to compare different irradiation sources in regard of their NIEL. The particle fluence of an irradiation source is related to the fluence of a 1 MeV neutron source Φ_{eq} by the hardness factor

$$\Phi_{eq} = \kappa \cdot \Phi_p \tag{3.6}$$

if the same amount of kinetic energy is released to matter. For calculation of the hardness factor of an irradiation source its particle energy distribution has to be taken into account. The differential energy flux of an irradiation source is

$$\phi_p = \int_E \left(\frac{d\phi_p}{dE_p} \right)_{E_p} dE_p \tag{3.7}$$

where ϕ_p is the particle flux. The particle fluence Φ_p after an exposure time t_{exp} is

$$\Phi_p = \phi_p \cdot t_{exp} \tag{3.8}$$

The hardness factor κ of the source is

$$\kappa = \frac{1}{D_n(1MeV)} \frac{\int_E \left(\frac{d\phi_p}{dE_p} \right)_{E_p} D_p(E_p) \, dE_p}{\int_E \left(\frac{d\phi_p}{dE_p} \right)_{E_p} dE_p} \tag{3.9}$$

where $D_n(E)$ is the displacement damage cross section for neutrons and $D_p(E)$ the displacement damage cross section for the impinging particle. The displacement damage cross section of 1 MeV neutrons is $D_n(1MeV) =$ 95 MeVmb. The displacement damage cross sections of neutrons, protons, pions and electrons for various energies are calculated. The results are shown in figure 3.3.

3.2.3 Experimental determination of the hardness factor

The NIEL hypothesis proposes that every macroscopic quantity scales linear with the NIEL independent on the particle type and energy [Vas97]. Therefore the volume generation current is

$$\frac{I_{vol}}{V} = \alpha \cdot \kappa_{exp} \cdot \Phi_p \tag{3.10}$$

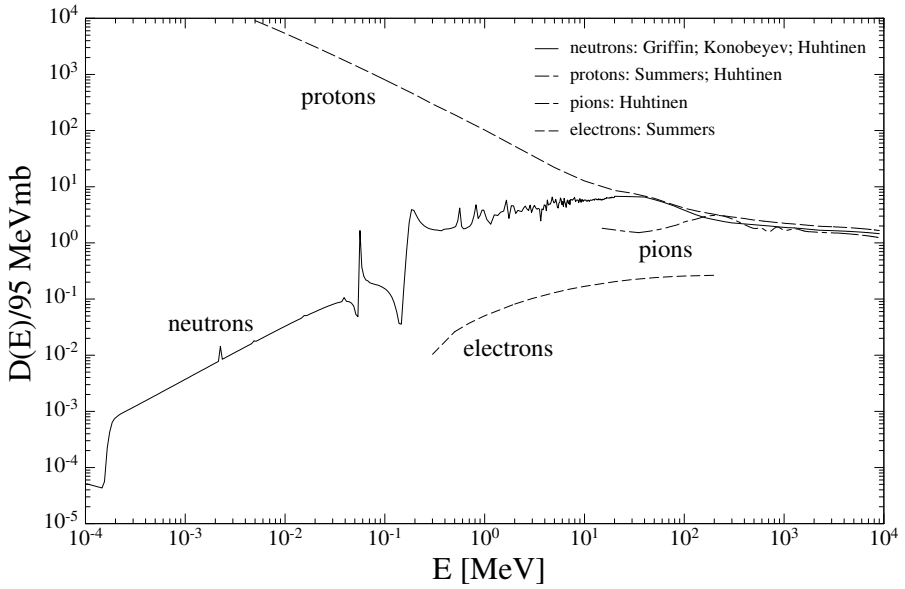

Figure 3.3: *The dependence of the displacement damage cross section of neutrons, protons, pions and electrons in units of the displacement damage cross section of 1 MeV neutrons on the kinetic energy is shown. The normalized displacement damage cross section is equivalent to the hardness factor of a monoenergetic particle source* [Lin99].

where α is the current related damage rate for 1 MeV neutrons. It depends on the annealing state of the radiation damage. Thus a comparison of measured and calculated κ values is possible. The calculated κ values depend appreciably on the Lindhard partition function which separates between displacement and ionising damage. But also the choice of the lower limit of the recoil energy is important, because low energy recoils generate mainly isolated point defects which do no contribute to the current generation. Therefore it is reasonable to introduce an energy threshold E_{th}. Below the threshold only isolated point defects are generated and above only clusters. This energy threshold E_{th} is suggested as a lower limit for the calculation of the displacement damage cross section. The adjustment of the lower limit can also be accomplished by a multiplication of the Lindhard partition function with a unit step function

$$P^*(E_R) = P(E_R) \cdot U(E_R - E_{th}) \tag{3.11}$$

The step of $U(E_R - E_{th})$ can be smooth out to include the continuous transition from isolated point defect generation to cluster generation. The independence of the current related damage rate on the defect distribution in the clusters is assumed. Hence the current related damage rate depends not strongly on the particle type and energy.

High energy electrons and low energy protons are appropriate to investigate the influence of the recoil energy distribution on the radiation damage. The

scattering of these particles is elastic due to the Coulomb interaction. No nuclear scattering occurs. The determination of the threshold energy E_{th} for cluster damage generation is possible. The NIEL or the displacement damage cross section of high energy electrons is calculated employing the relativistic Coulomb scattering cross section and taking into account the nuclear charge distribution. The NIEL of low energy protons is calculated employing the classical Rutherford scattering cross section [Kuh00a].

3.2.4 Particle dependence

For understanding the displacement damage in detail the distribution of recoiled silicon atoms is important. In figure 3.4 the relative displacement damage for silicon recoils produced by different particles are shown. Only elastic scattering (both nuclear and coulomb interaction) has been included. The relative NIEL contribution for recoil energies smaller than 5 keV is negligible for 1 MeV neutrons and the generation of cluster is favoured. Also for charged hadrons a considerable portion of the NIEL is lost by displacements in the energy region E > 5 keV. But the low energy part contributes also significantly to the displacement damage and therefore more isolated displacements are generated.

A short description of the scattering processes and the produced displacement damage for the various particle types and energies is given below.

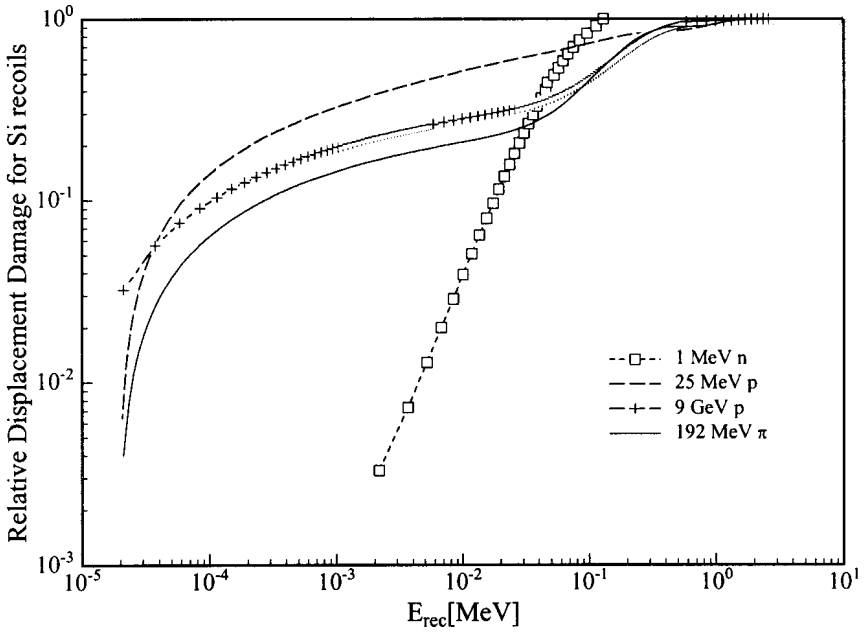

Figure 3.4: *Relative damage efficiency for different particles as function of the recoil energy* [Ros00].

Electrons

The scattering of high energy electrons in a solid medium is due to the electromagnetic interaction between impinging electron and positive charged nucleus. The scattering cross section was first derived in a classical manner by Rutherford. This classical approximation is only valid for low energy electrons. An electron with a kinetic energy of 100 keV has already a velocity of $v/c = 0.55$ and thus the classical approximation is not valid. The relativistic cross section is given by the the Mott scattering cross section. The differential cross section have been expanded in a power series in $Z\alpha$ by McKinley and Feshbach [McK48].

During irradiation of silicon with electrons which have an energy below 1 MeV only isolated displacements are created. If the energy of the electrons is above 1 MeV, the generation of clusters starts. The maximal recoil energy of an elastic scattering process is obtained from Equation 3.2.

Gamma photons

The four interaction processes of photons with matter are photo electrical absorption, Compton and Rayleigh scattering and pair production [Sto70]. The produced electrons and positrons are responsible for the displacement damage.

During irradiation of silicon with ^{60}Co γ-photons, which have an energy of 1.17 and 1.33 MeV, only isolated displacements are created. The displacement damage is produced by the secondary Compton electrons. However, the Compton electrons are mainly generated in the material surrounding the sample. The electrons that incident on the sample have already transversed some material and are slowed down [Sum93].

Protons

The differential cross section for elastic scattering of protons shows no significant difference from Rutherford scattering at energies below 10 MeV

$$\frac{d\sigma_{el}}{d\Omega} = \frac{1}{(4\pi\epsilon_0)^2}\left(\frac{Ze^2}{2mc^2}\right)^2 \frac{1-\beta^2}{\beta^4}\csc^4(\theta/2) \tag{3.12}$$

where $\beta = v/c = pc/E$, p the momentum of the electron, $E = \sqrt{c^2p^2 + m^2c^4}$ the electron energy, θ is the angle between the incident and scattered electron and m the rest mass of the electron. At energies above 10 MeV elastic nuclear scattering is not negligible. The differential cross section is enhanced at certain scattering angles [NIS99]. The total cross section is increased. If the proton energy is greater than 20 MeV, non-elastic scattering starts to contribute to the total cross section. Above 100 MeV non-elastic events begin to dominate the interaction. However, for high energy protons there

are many reaction channels which lead to a variety of secondary reaction products. Also a fragmentation or overall spallation of the nucleus occur.

Protons with energies from several MeV to tens of GeV create cluster damage and isolated displacements. The fraction of isolated displacements increases with decreasing proton energy. However, for high energy protons an excitation and fragmentation of silicon nuclei occur and the displacement damage in the silicon lattice is produced also by secondary charged particles and fragments of the nuclei.

The nuclear reactions induced by protons and neutrons at high energies are practically the same. Thus the displacement damage introduced by non-elastic scattering of high energy protons can be expected to follow the damage of high energy neutrons [Ros00].

192 MeV pions

The interaction of a pion with a silicon nucleus is more complicated than the proton interaction. For π^+ scattering at some energies resonances in the cross section occur. In particular the Δ resonance around 200 MeV kinetic energy leads to a large total cross section [Huh93a]. Also a fragmentation of the nucleus and a spallation of nucleons occur at this energy. The fragmentation of silicon nuclei starts for nuclear excitation energies above 150−200 MeV [Huh93b].

The displacement damage created by 192 MeV π^+ consists of cluster damage and isolated displacements. As for high energy proton irradiations some portion of the displacement damage is produced by fragments of silicon nuclei.

Neutrons

The scattering of neutrons with an energy below 5 MeV is elastic. For neutrons with an energy above 5 MeV inelastic scattering (n,n′) contributes to the total cross section. Also non-elastic scattering processes like the nuclear reactions (n,p) and (n,α) occur [Smi66]. Inelastic neutron scattering always leaves the nucleus in an excited state. Two level with the energies 1.78 MeV and 4.62 MeV are possible below 5 MeV. The emission of a γ-photon with an energy of 1.78 MeV or 2.84 MeV during nuclear decay results in a recoil energy of 61 eV or 154 eV to conserve momentum and energy. This is enough to displace a silicon atom out of its lattice site and to create a Frenkel pair. At neutron energies above 20 MeV heating of the nucleus occurs and neutrons and protons evaporate. Again for neutron energies greater than 100 MeV a fragmentation of the nucleus is possible, because the nuclear excitation energy is large.

For neutrons with a kinetic energy of 5 MeV the ratio of the elastic cross section to the total cross section is $\sigma_{elas}/\sigma_{tot} = 0.67$, ratio of inelastic cross section to the non-elastic cross section is $\sigma_{inel}/\sigma_{nel} = 0.97$ and the sum of

the cross sections of the (n,p) reactions is five times greater than the cross section of the (n,α) reaction [NIS99].

The maximal neutron energy of the two neutron sources employed for the studies is less than 10 MeV. Collision cascade trees with terminal clusters are mainly created by the recoiled silicon atoms. Thus the single displacements are mainly produced in the collision cascades. The maximal energy transferred to silicon atoms due to elastic scattering of 150 eV, 3 keV and 5 MeV neutrons is 20 eV, 400 eV and 671 keV. The scattering of 10 MeV neutron produces also protons and alpha particles. The coulomb interaction of these secondary particles produce isolated displacements.

3.3 Radiation induced defects

The radiation damage after high energy particle irradiation in silicon can be separated into isolated point defects and clusters of defects. Impurities, e.g. oxygen and carbon, are constituents of the point defects. The point defects observed with the DLTS method are the vacancy interstitial-oxygen complex VO_i or A center, the interstitial-carbon atom C_i, the interstitial-carbon substitutional-carbon complex C_iC_s and the interstitial-carbon interstitial-oxygen complex C_iO_i. The clusters consist mainly of divacancies VV. But also the formation of higher order intrinsic defect with a smaller concentration in the cluster regions can not be excluded. Also it is assumed that some part of the deposited energy is converted into elastic energy which results in lattice deformation and strain fields. The electronic bond switching of the divacancy is propose to be prevented by these lattice deformation and strain fields [Sve97]. Deformation and strain fields also changes the configuration switching of the defect C_iC_s at the cluster peripheries. Because of the abnormal behaviour in high energy particle irradiated silicon the divacancy VV and the defect C_iC_s are treated in further detail for understanding the experimental results in chapter 6.

3.3.1 Interstitial-carbon Substitutional-carbon complex

The interstitial-carbon substitutional-carbon C_iC_s has two configurations A and B, as shown on the left hand side of figure 3.5. The configuration A has a C_{1h} point-group symmetry and the mirror plane contains the edges of the ground plane of the cube occupied with atoms and the unoccupied edges of the top plane of the cube. The mirror plane is the (1 1 0) plane in the shown cubic lattice. The 1-fold symmetry axis is perpendicular to the mirror plane. The symmetry axis coincides with the [1 1 0] direction in the cubic lattice. The configuration B has also at low temperatures (T$\approx$1.7 K) a C_{1h} point-group symmetry with the same mirror plane and symmetry axis as the configuration A, as shown on the left hand side of figure 3.5. At higher temperatures (T$\approx$30 K) the silicon atom between the carbon atoms is symmetrical delocalized around the 3-fold symmetry axis in the [$\overline{1}$ 1 1] direction

and hence the symmetry is the higher C_{3v} symmetry[3]. The vertical mirror planes parallel to the 3-fold axis are obtained by rotation of the (1 1 0) plane around this axis. The four <1 1 1> directions, which coincide with the directions of the binding orbitals in a silicon lattice, are equivalent . Thus four different orientations of the defect C_iC_s are possible. A switching between the two configurations is accomplished by the simultaneous movement of the silicon and carbon atom inside the cube volume and a configurational coordinate is introduced as a parameter. Because also the electronic binding configuration is changed, the energies of both configurations are not equal and an energy barrier separates both configurations. The configurational switching is thermally activated. However, the unsaturated orbitals of the carbon and silicon atom in configuration A and of the silicon atom in configuration B can accommodate one additional electron or lose one electron. Therefore a single positive and a single negative charge state together with a neutral charge state exist. The energies of the configurations A and B depend on their charge states. The configurational coordinate energy diagrams are shown on the right hand side of figure 3.5. The configuration with

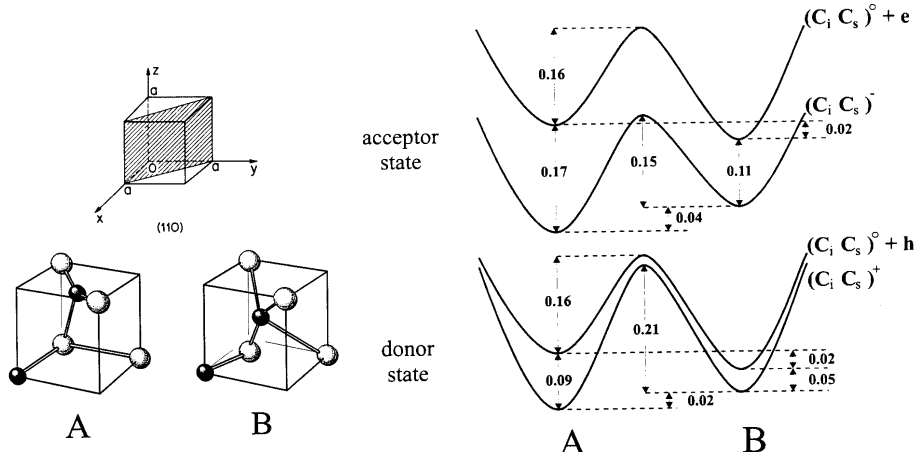

Figure 3.5: *The models for the two configurations of the C_iC_s complex are shown on the left hand side. The black atoms are carbon atoms and the white ones a silicon atoms. The configurational coordinate energy diagrams are shown on the right hand side. The units are eV* [Son90].

the lower energy is preferred in thermal equilibrium. The occupation ratio of the two configurations is given by the Boltzmann factor

$$\frac{n(E_1)}{n(E_2)} = e^{-(E_1-E_2)/k_BT} \tag{3.13}$$

The occupancy of the higher energy state is about 0.3% for $E_1 - E_2 = 0.04$ eV and 5.5% for $E_1 - E_2 = 0.02$ eV at T=80 K. Also vibration modes exist.

[3]The interstitial oxygen is also delocalized [Art97]. In germanium the delocalization is an annulus around the binding direction between two atoms. In silicon the delocalization is centered between two atoms.

The approximation with a harmonic energy potential results in a discrete vibrational energy spectrum $E_n = (n + \frac{1}{2})\hbar\omega$. Also rotational modes exist.

The configurational switching is observed at low temperatures, if a non equilibrium situation is induced. The time constant of the configurational switching is temperature dependent

$$\tau = \tau_0 \cdot e^{\Delta E / k_B T} \tag{3.14}$$

where ΔE is the energy barrier to be overwhelmed for a configurational change. It depends on the charge state of the defect.

3.3.2 Divacancy

The divacancy is created in the silicon lattice by removing two neighbouring atoms. Four different orientations of the divacancy are possible, because the bond directions between the silicon atoms coincide with the <1 1 1> directions. One orientation is shown on the left hand side of figure 3.6. The symmetry of the undistorted divacancy is the D_{3d} point-group symmetry. The 3-fold symmetry axis coincides with the <1 1 1> direction intersecting the voids. The three vertical mirror planes parallel to this rotation axis contain each two silicon atoms: (a a′), (b b′) or (d d′). The two-fold rotation axes, which bisect the 60° angle between two vertical mirror planes and intersect the remaining plane with a 90° angle, are perpendicular to the 3-fold axis. After the Jahn-Teller distortion the symmetry is lowered to the

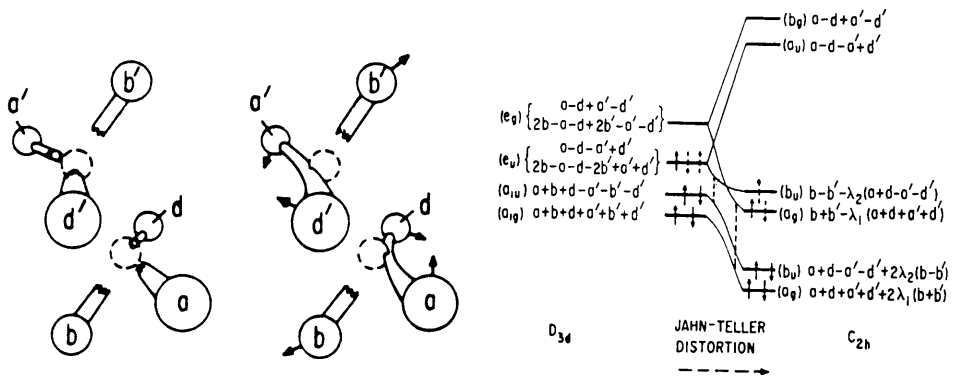

Figure 3.6: *The not distorted divacancy with the D_{3d} symmetry is shown on the left hand side. In the middle the Jahn-Teller distortion is indicated by the arrows at the atoms. The symmetry is lowered to the C_{2h} symmetry. The electronic structure is shown on the right hand side. The energy levels of the orbitals are changed by the Jahn-Teller distortion. The solid arrows denote the electrons, and their spins, for the single positive charge state. The dotted arrows denote the additional electrons in the single negative charge state* [Wat65].

C_{2h} point-group symmetry. The atom groups (a d) and (a′ d′) are paired together by a binding orbital. Between the atoms of the group (b b′) an

extended binding orbital is formed. This binding orbital can accommodate one, two, three or even four electrons presenting the different charge states of the divacancy. The mirror plane of the C_{2h} symmetry containing the atoms of the group (b b′) is equivalent to one of the vertical mirror planes of the D_{3d} symmetry[4] [Lin79]. The atoms of the groups (a d) and (a′ d′) are exchanged after a mirror operation. The 2-fold axis of the C_{2h} symmetry coincides with one of three 2-fold axes of the D_{3d} symmetry. Also the binding orbitals have to be invariant under the mirror and rotation operations, because Electron Paramagnetic Resonance (EPR) is used to determine the symmetry of the defect. The interaction of the electron spins, which have a density distribution, with an external magnetic field is measured. The interaction of the nuclear spins with the electrons spins (Hyperfine interaction) changes energy of the resonance slightly (satellite lines).

The new atomic and electronic configurations after a Jahn-Teller distortion lower the energy of the system by strong mixing of the molecular orbitals as shown on the right hand side of figure 3.6. The molecular orbitals are obtained by a Linear Combination of Atomic Orbitals (LCAO).

But also the groups (a b) and (a′ b′) or the groups (b d) and (b′ d′) can pair together forming a bond. The extended binding orbital is formed between the two remaining atoms. In conclusion a divacancy aligned in one of the <1 1 1> directions has three electronic bond configurations. Hence 4×3 configurations are possible. At low temperatures (T<20 K) the divacancy has a C_{2h} symmetry, because it remains in one configuration. At high temperatures (T>30 K) the electronic bond switching is thermally activated and the fast switching averages the three configurations of the groups (a b c) and (a′ b′ c′) to a single configuration resulting in a D_{3d} symmetry. Actually the atoms of each group are attached to the edges of a single side triangle. The planes of the two triangles are parallel to each other and one of the triangles is rotated by 180° around an axis through the centers of the triangles.

At high temperature the divacancies are orientated randomly in all four <1 1 1> directions. After a stress induced alignment of the divacancies at a low temperature the reorientation in temperature range T $\approx 40-110$ K takes place.

3.4 Electrical properties of defect centers

The macroscopic properties of a semiconductor crystal are changed due to defect centers with energy states in the band gap. The occupancy of isolated point defects is described by the Shockley Read Hall (SRH) statistics [Sho52]. The defect centers capture and emit free charge carriers from/into the conduction and valence band states. A charge transfer between the defect centers does not occur. However, in clusters of divacancies inter-

[4]The mirror plane is slightly tilted, if the atoms of the group (b b′) are moved out of the vertical mirror plane of the D_{3d} symmetry.

centre-charge-transfer is possible and the occupancies of the different charge states of the divacancy differ from the SRH prediction [Gil97].

3.4.1 Capture rate

The rate of capturing a charge carrier occupying a state in the conduction or valence band into a defect state in the band gap is given by

$$R_{n,p} = \sigma_{n,p} \cdot |\vec{v}_{n,p}| \cdot \{p_T, n_T\} \tag{3.15}$$

where $\sigma_{n,p}$ is the electron or hole capture cross section, $\vec{v}_{n,p}$ the velocity vector of the free charge carrier, n_T is the number of occupied defect states per unit volume and thus $p_T = 1 - n_T$ the number of unoccupied defect states per unit volume. Therefore the change of the defect occupancy is

$$\begin{aligned} \frac{d\{n_T, p_T\}}{dt} &= \{p_T, n_T\} \int_E \sigma_{n,p} \, |\vec{v}_{n,p}| \, \{f_{Dirac} \, , [1 - f_{Dirac}]\} \, D_{C,V} \, dE \\ &= \sigma_{n,p} \cdot v_{th,n,p} \cdot \{n, p\} \cdot \{p_T, n_T\} \end{aligned} \tag{3.16}$$

The thermal velocity is obtained by reordering of Eq. 3.16, using Eq. 2.10 and 2.12 and assuming an energy independence of the capture cross section

$$v_{th,n,p} = \frac{\int_E |\vec{v}_{n,p}| \, \{f_{Dirac} \, , [1 - f_{Dirac}]\} \, D_{C,V} \, dE}{\int_E \{f_{Dirac} \, , [1 - f_{Dirac}]\} \, D_{C,V} \, dE} \tag{3.17}$$

The evaluation of integral is done more easily in $\vec{k}$-space.

3.4.2 Isolated point defects - Shockley Read Hall statistics

The following charge transfer processes occur between a defect state in the band gap and the states in the conduction and valence bands

- The capture of electrons from the conduction band: $r_a = c_n \cdot n \cdot p_T$
- The emission of electrons into the conduction band: $r_b = e_n \cdot n_T$
- The capture of holes from the valence band: $r_c = c_p \cdot p \cdot n_T$
- The emission of holes into the valence band: $r_d = e_p \cdot p_T$

where $e_{n,p}$ and $c_{n,p}$ are emission rates and capture coefficients for electrons and holes of the defect center, n_T is the number of occupied defect states per unit volume and $p_T = 1 - n_T$ the number of unoccupied defect states per unit volume and $\{n, p\}$ the density of electrons and holes. The different processes are visualized in figure 3.7. Also the generation of an electron-hole (eh) pair under external illumination is shown. The capture coefficient is the product of capture cross section and thermal velocity

$$c_{n,p} = \sigma_{n,p} \cdot v_{th,n,p} \tag{3.18}$$

The time dependence of the defect occupancy is governed by the differential equation

$$\frac{dn_T}{dt} = r_a - r_b - r_c + r_d \tag{3.19}$$

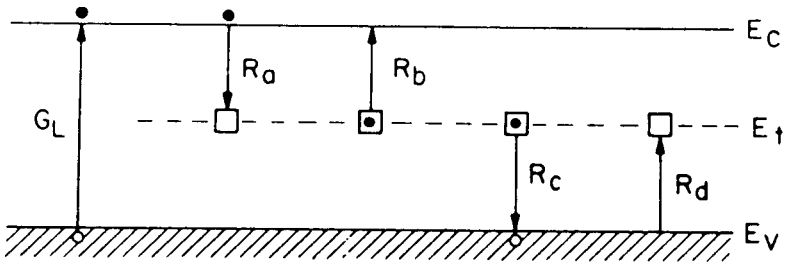

Figure 3.7: *Capture and emission processes of free charge carriers and electron-hole pair generation under external illumination are shown* [Sze85].

Thermal equilibrium occupancy

Under thermal equilibrium condition the defect occupancy and the electron and hole densities are calculated with the Fermi-Dirac function. The Fermi-Dirac function f_{Dirac} can be approximated by an exponential tail above the conduction band edge and also the inverse Fermi-Dirac function $(1 - f_{Dirac})$ below the valence band edge, if $|E_F - E_{C,V}| \gg k_B T$. The numbers of electrons entering and leaving the conduction band via a defect center is assumed be $r_a = r_b$. This assumption is called the principle of detailed balance. It is also used for holes $r_c = r_d$. Employing these assumptions the emission rate is

$$e_{n,p} = c_{n,p} \cdot N_{C,V} \cdot e^{\pm\beta(E_T - E_{C,V})} \tag{3.20}$$

where E_T is the energy of the defect state in the band gap, $E_{C,V}$ the energy of the conduction and valence band edges and $\beta = \frac{1}{k_B T}$. However, the energy needed to excite an electron or hole into a state in the conduction or valence band is correctly interpreted as Gibbs free energy [Eng83]

$$\Delta G_{n,p} = \Delta H_{n,p} - \Delta S_{n,p} \cdot T \tag{3.21}$$

The transition from one charge state to another charge state results in a change of the enthalpy $\Delta H_{n,p}$ and entropy $\Delta S_{n,p}$ of the system. Putting Eq. 3.21 into Eq. 3.20 gives

$$e_{n,p} = X_{n,p} \cdot c_{n,p} \cdot N_{C,V} \cdot e^{-\beta \Delta H_{n,p}} \tag{3.22}$$

The entropy factor is

$$X_{n,p} = e^{\Delta S_{n,p}/k_B} \tag{3.23}$$

The change in the entropy can divided into two additive parts, if the Hamilton operator of the system separates into a part of electronic energy and a part of vibrational energy. A change in the vibration mode and/or a change in the electronic degeneracy after a charge state transition contribute to $\Delta S_{n,p}$. The change of the electronic degeneracy is

$$\Delta S_{n,p\,(elec)} = k_B \cdot \ln\left(\frac{g_1}{g_0}\right) \tag{3.24}$$

where g_0 is the electronic degeneracy of a defect center in a charge state with n electrons and g_1 the degeneracy of a defect center with $n+1$ electrons.

The capture cross section can be temperature dependent. A review of the different temperature dependencies can be found in [Bra79]. Two models are discussed below.

The shifting of the atoms of a defect from their equilibrium positions changes the energy of the defect state in the band gap. The thermal vibrations of the defect atoms around their equilibrium positions are sometimes sufficiently large enough to make a crossing of the defect state with one of the band edges possible. Therefore the probability of capturing a charge carrier is high. In the new charge state the defect atoms are displaced far from their new equilibrium positions. Thus the energy of the defect state immediately after capture is much higher than the equilibrium energy. The resulting violent lattice vibrations are rapidly damped down due to multi phonon emission. At high temperatures the capture cross section has the form [Hen77]

$$\sigma = \sigma_0 \cdot e^{-\beta \Delta E} \tag{3.25}$$

The activation energy in Equation 3.20 increases.

Another model is the cascade capture process. A defect center with a long range attractive Coulomb potential posses a series of excited states. These excited states present various charge carrier distributions inside the defect volume and their extensions are attributed to different cross sections. Near the edge of the band continuum the spacing of the defect levels is much smaller than the energy of the most abundant phonons $k_B T$. Thus the defect states near the band continuum in an energy range of a few $k_B T$ are included into the continuum of band states. Therefore the capture cross section decreases with increasing temperature

$$\sigma = \sigma_0 \cdot T^{-n} \qquad n = 2 \ldots 4 \tag{3.26}$$

This kind of temperature dependence modifies the prefactor in Equation 3.20.

Steady-state occupancy

It is obvious from Eq. 3.20 that the emission rate under thermal equilibrium condition depends not on the Fermi level position and therefore is independent on the electron or hole densities. It is assumed that this relation is also

valid for a variety of steady-state and non steady-state conditions[5]. It is also useful to parameterise the concentration of a charge carrier type under non thermal equilibrium condition by a quasi Fermi level E_F^*

$$\{n,p\} = N_{C,V} \cdot e^{\pm\beta(E_F^* - E_{C,V})} \tag{3.27}$$

if the free charge carrier concentration is dominated by one type of charge carrier. Using the principle of detailed balance the steady-state occupancy of a defect center is

$$F_T = \frac{1}{e^{\pm\beta(E_T - E_F^*)} + 1} \tag{3.28}$$

This is a very convenient way to express the defect occupancy. However, it is often necessary to express the defect occupancy in the following way

$$F_T = \frac{c_n \cdot n + c_p \cdot n_i \cdot e^{\beta(E_i - E_T)}}{c_n \cdot \left(n + n_i \cdot e^{\beta(E_T - E_i)}\right) + c_p \cdot \left(p + n_i \cdot e^{\beta(E_i - E_T)}\right)} \tag{3.29}$$

calculated from Eqs. 3.19 and 3.20 and using the detailed balance conditions. If the free charge carrier densities are $n \ll n_i$ and $p \ll n_i$, Eq. 3.29 reduce to

$$F_T = \left(1 + \frac{c_n}{c_p} \cdot e^{2\beta \cdot (E_T - E_i)}\right)^{-1} \tag{3.30}$$

and with Eqs. 3.20, 2.29 and 2.30 the following form is obtained

$$F_T = \frac{e_p}{e_n + e_p} \quad \text{and} \quad (1 - F_T) = \frac{e_n}{e_n + e_p} \tag{3.31}$$

The effective space charge density $q \cdot N_{eff}$ for defect centers of donor and acceptor type is

$$q \cdot N_{eff} = \sum_j q_j^D \cdot N_{T,j}^D \cdot \left(1 - F(E_{T,j}^D)\right) \; - \sum_j q_j^A \cdot N_{T,j}^A \cdot F(E_{T,j}^A) \tag{3.32}$$

where $q_j^{D,A}$ is the charge accommodated by the defect center j, $N_{T,j}^{D,A}$ the density of the defect center j and $F(E_{T,j}^{D,A})$ the fraction of occupied defect centers j. The indices D and A are for donor and acceptor type. Furthermore the net recombination rate is

$$U = r_a - r_b = \frac{c_n \cdot c_p \cdot N_T \cdot (np - n_i^2)}{c_n \cdot \left(n + n_i \cdot e^{\beta(E_T - E_i)}\right) + c_p \cdot \left(p + n_i \cdot e^{\beta(E_i - E_T)}\right)} \tag{3.33}$$

The generation rate of eh pairs, if the conditions $n \ll n_i$ and $p \ll n_i$ are valid, is

$$G = -U = \frac{n_i}{\tau_g} = \frac{c_n \cdot c_p \cdot N_T \cdot n_i}{c_n \cdot e^{\beta(E_T - E_i)} + c_p \cdot e^{\beta(E_i - E_T)}} \tag{3.34}$$

A comprehensive introduction on the effects of radiation induced defects on the operation properties of silicon detectors is given in [Lut96, Lut99].

[5] The activation energy [Mar81] and the capture cross section [Dus70] can be electric field dependent.

Non steady-state occupancy

The emission rate of a defect center is measured under the condition of negligible free charge carrier concentrations. Hence in Eq. 3.19 the terms r_a and r_c are canceled. Also the emission rate of holes from a defect center with an energy state in the upper half of the band gap is negligible and the emission rate of electrons from a defect center with an energy state in the lower half of the band gap. Hence Eq. 3.19 is governed by the term r_b or r_d. The solution of the differential equation with the condition $\{n_T, p_T\} = N_T$ at $t = 0$ is

$$\{n_T, p_T\} = N_T \cdot e^{-e_{n,p} \cdot t} \tag{3.35}$$

The capture rate of a defect center is determined experimentally by measuring the time dependence of the defect occupancy during the capture of one type of charge carrier. Again the emission rate of holes from a defect center with an energy state in the upper half of the band gap is negligible and the emission rate of electrons from a defect center with an energy state in the lower half of the band gap. Thus in Eq. 3.19 the term r_d or r_b is canceled. The solution of the differential equation with the condition $\{n_T, p_T\} = 0$ at $t = 0$ is

$$\begin{aligned} \{n_T, p_T\} &= \frac{N_T}{1 + \frac{e'_{n,p}}{\{n,p\} c_{n,p}}} \left(1 - e^{-(\{n,p\} c_{n,p} + e'_{n,p}) \cdot t}\right) \\ e'_{n,p} &= e_{n,p} + \{p, n\} \cdot c_{p,n} \end{aligned} \tag{3.36}$$

However, if the free charge carrier concentration is not homogeneous during the capture, the number of occupied/unoccupied defect states per unit volume depends on the space coordinate $\{n_T(x), p_T(x)\}$. The capture kinetic of defect states taken into account the distribution of majority charge carriers in a p^+n junction is discussed in [Pon84]. The deviation from the exponential time dependence of Equation 3.36 is small.

3.4.3 Inter-center-charge-transfer

Isolated defects in the crystal lattice emit and capture free charge carriers. An exchange of charge carriers between two neighbouring defects does not occur. In a cluster of defects the inter-centre-charge-transfer is possible [Wat96]. Clusters of divacancies are generated after high energy particle irradiations. The charge exchange reaction $VV^0 + VV^0 \rightarrow VV^+ + VV^-$ is assumed to occur. The transfer rate depends on the distance between the divacancies or their density in the cluster regions. A high density of divacancies enhance the electron-hole generation rate and the occupancy of the charge state VV^- in a depleted space charge region compared to the SRH prediction. In the case of 1 MeV neutron damage the agreement between the model and data is not satisfactory [Gil97, Mac97a]. The density of divacancies in the cluster regions is estimated from the current related damage rate $\alpha = 1.5 - 5 \cdot 10^{-17}$ A/cm to be $10^{18} - 10^{20}\text{cm}^{-3}$.

3.5 Defect kinetics

Radiation induced defects like the interstitial carbon C_i and the vacancy V migrate at room temperature through the crystal lattice and form defects like VO_i, VP_s, VV, C_iO_i and C_iC_s. The resulting defect complexes are immobile at room temperature as their precursor atoms: interstitial oxygen O_i, substitutional carbon C_s and substitutional phosphorous P_s. The divacancies are mainly localized in the cluster regions after high energy particle irradiations. The defect complexes dissociate like a chemical compound into its components above a certain temperature. The known radiation induced defects dissociate in a temperature range between 100°C and 400°C, as shown in figures 3.8.

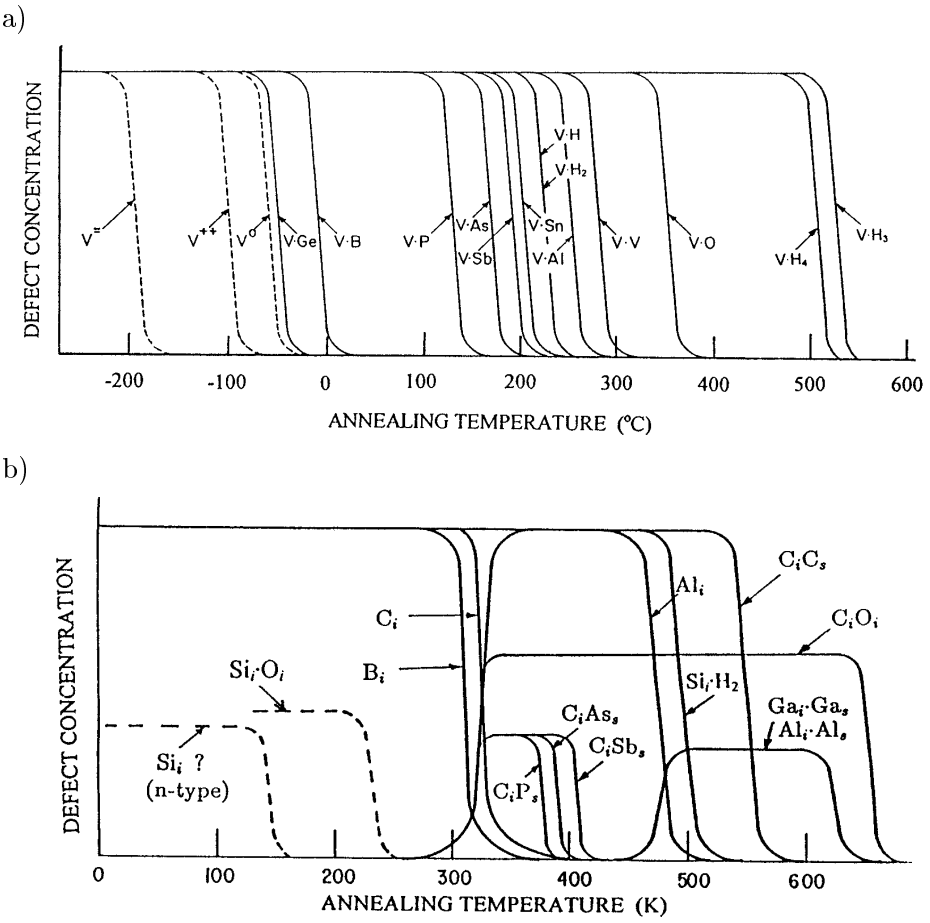

Figure 3.8: *The annealing behaviour of (a) isolated vacancy related defects and (b) isolated interstitial related defects of an isochronal tempering study (15−30 min) is shown* [Wat99].

3.5.1 Defect formation and annealing

During irradiation of crystalline silicon with particles isolated displacements of silicon atoms and regions with a high density of displacements occur. The defect formation and annealing for this two types of displacement damage is different.

Point defect reactions

Primary generated isolated interstitials I and vacancies V migrate at room temperature through the crystal lattice. The interstitials exchange with a substitutional carbon atom

$$I + C_s \rightarrow C_i$$

This reaction is called the Watkins exchange mechanism. The interstitial carbon C_i migrates further through the lattice and is captured at impurity atoms like substitutional carbon C_s, interstitial oxygen O_i or substitutional phosphorous P_s

$$C_i + C_s \rightarrow C_iC_s$$

$$C_i + O_i \rightarrow C_iO_i$$

$$C_i + P_s \rightarrow C_iP_s$$

These defects are also stable and immobile at room temperature as their precursors. The migrating vacancies form vacancy interstitial-oxygen complexes VO_i, divacancies VV and the vacancy substitutional-phosphorous complexes VP_s

$$V + O_i \rightarrow VO_i$$

$$V + V \rightarrow VV$$

$$V + P_s \rightarrow VP_s$$

which are also stable and immobile at room temperature. The generation of divacancies by migrating vacancies is small, because the capture of vacancies at O_i sites is favoured already in standard silicon material. Also the generation of VP_s defects involving phosphorous is negligible in high resistivity n-type silicon in the low fluence range [Mac96]. The generation of a vacancies at the cluster peripheries by the reaction

$$C_i + VV \rightarrow C_s + V$$

is also possible. The defect V_2O is suggested to be of major importance for defect engineering in the high fluence region [Mac97a, Mac97b]

$$V + VO_i \rightarrow V_2O$$

Also other defect complexes like

$$I + C_iO_i \rightarrow C_iO_iI$$

$$I + C_i C_s \rightarrow C_i C_s I$$
$$I + C_i C_s \rightarrow C_i C_s II$$

are produced after high fluence irradiations. The defect $C_i O_i I$ is identified with the 1020 cm^{-1} absorption line in [Dav87]. Silicon interstitials can also reduce defect complexes with vacancies

$$I + VO_i \rightarrow O_i$$
$$I + V_2 O \rightarrow VO_i$$
$$I + VP_s \rightarrow P_s$$

In conclusion four types of defects are generated in a silicon crystal after low fluence irradiations used for DLTS investigations: the vacancy interstitial-oxygen complex VO_i, the interstitial-carbon substitutional-carbon complex $C_i C_s$, the interstitial-carbon and interstitial-oxygen complex $C_i O_i$ and the divacancy VV.

Cluster formation

The silicon interstitials I and vacancies V generated in the terminal cluster regions mainly annihilate because of the high density of the primary defects

$$I + V \rightarrow \emptyset$$

Other possible reactions are the formation of higher order intrinsic defects like the divacancy

$$V + V \rightarrow V_2$$

the trivacancy

$$V + V_2 \rightarrow V_3$$

or even rings of vacancies and higher order interstitial defects like

$$I + I \rightarrow I_2$$
$$I + I_2 \rightarrow I_3$$

and also the reduction of higher order intrinsic defects

$$I + V_2 \rightarrow V$$
$$I + V_3 \rightarrow V_2$$
$$V + I_2 \rightarrow I$$
$$V + I_3 \rightarrow I_2$$

can occur. In the terminal cluster regions impurity atoms have no influence on the defect kinetics, because the mean number of an impurity species like interstitial oxygen or substitutional carbon in the cluster regions is small. Therefore the defects inside the cluster regions are assumed to be intrinsic.

Defect annealing

The initial defect kinetic due to the migration of interstitial carbon is accomplished on time scale of a few days or weeks. The time constant of the C_i annealing depends on the impurity content and temperature. All other isolated radiation induced defects in high resistivity n-type silicon are stable at room temperature, because the defect dissociation starts at temperatures above 100°C. Therefore the macroscopic properties of silicon detectors after ^{60}Co γ-photon irradiation during room temperature annealing do not change [Fei97].

The terminal cluster regions are assumed to consist mainly of divacancies. The activation energies of the diffusion and dissociation processes of the divacancy are to high to allow a dissolution of a cluster of divacancies at room temperature. But elastic energy deposited into strain and deformation fields can be employed to break divacancies inside the cluster regions. Thus a dissociation of divacancies during annealing of the cluster damage at room temperature is possible. A decay of higher order vacancy complexes at room temperature is excluded, because the vacancy aggregates $V_3 ... V_6$ are more stable than the divacancy [Has97]. The most stable complex is the hexagonal ring of vacancies V_6. But the hexagonal ring has also eighteen metastable configurations with appreciable higher energies. The time scale on which the rearrangement to the stable configuration at room temperature occurs is not known. The rearrangement at high temperatures T=1200 K is assumed to be accomplished on the picosecond time scale. The gained energy from rearrangement can be employed to dissociate other vacancy complexes.

However, it is suggested that an agglomeration of defects at the peripheries of the clusters after high energy particle irradiation takes place, which results in an impurity defect shell [Vas82]. The migration and reaction of the defects during annealing in the impurity defect shell is assumed to be different from the reaction kinetics of isolated point defects. Also deformation and strain field can influence the migration of defect species, e.g. interstitial carbon [Zan00].

The microscopic properties and perhaps the annealing behaviour of some defects have an electric field dependence. An applied external bias influences the defect formation and annealing during irradiation of silicon detectors with neutrons and pions [Cin00].

Thermal activated processes

Most of the thermally activated processes like diffusion or defect complex formation or dissociation are described by an Arrhenius relation

$$k = k_0 \cdot e^{-\beta E_B} \tag{3.37}$$

where k is the reaction rate, E_B the energy barrier height to be overwhelmed for a reaction and $k_0 = \delta \cdot k_B T/h$. The value $1/\delta$ is related to the number of

jumps involved in a reaction, k_BT the Boltzmann constant times temperature and h the Planck constant. For a defect decay associated with a single jump $\delta \approx 1$ and for a reaction involving a large number of jumps $\delta \ll 1$. In the case of diffusion $k_0 = D_0 = \alpha \cdot a^2/h\beta$, where α gives the number of jump sites next to the diffusing species and a is the lattice spacing. The energy diagrams of different reaction processes are shown in figure 3.9.

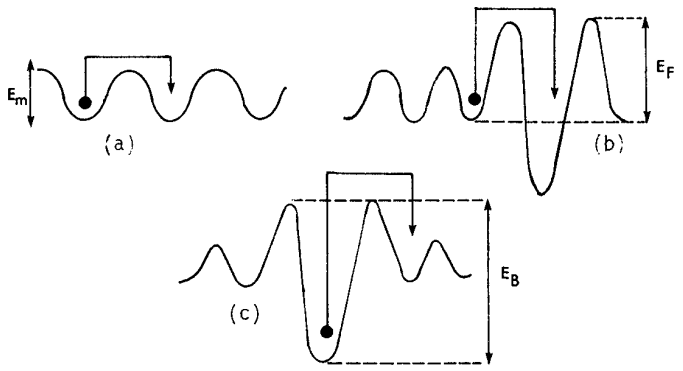

Figure 3.9: *The simplified energy diagrams of (a) defect migration, (b) defect complex formation and (c) defect complex dissociation are shown* [Bou83].

The possible reaction kinetics in particle irradiated silicon detectors, 1^{st} and 2^{nd} order processes, are described in [Mol99]. The rate equation of a reaction of the order j is

$$\frac{d[X]}{dt} = -k \cdot [X]^j \tag{3.38}$$

where $[X]$ is the concentration of the defect species X.

Chapter 4

Experimental Methods

4.1 Material

Various silicon materials have been investigated. The doping impurity is phosphorous and the effective doping concentration is in the range from $N_{eff} = 7 \cdot 10^{11}$ to $3.5 \cdot 10^{13}\text{cm}^{-3}$. This corresponds to a resistivity range from $100\Omega cm$ to $10\text{k}\Omega cm$. The silicon was mainly FZ material. Only one investigated material was CZ material which was employed because of its naturally high oxygen concentration. The oxygen enrichment of the FZ material is done either during the crystal growth process or by high temperature diffusion. The carbon enrichment is done during the growth process. The oxygen concentration is ranging from $[O] < 2 \cdot 10^{14}$ to $9 \cdot 10^{17}\text{cm}^{-3}$ and the carbon concentration is ranging from $[C] < 5 \cdot 10^{15}$ to $3.5 \cdot 10^{16}\text{cm}^{-3}$. The material properties and diode producer are listed in table 4.1. The ITME II and III material is oxygen enriched by a gas jet during the FZ process. The Polovodice II material is carbon enriched. The Wacker II material has a very low oxygen concentration, because the FZ process is done in vacuum. The oxygen and carbon concentrations together with the parameter of the high temperature diffusion process are listed in table 4.2. The depth profile of oxygen and carbon is measured by Secondary Ion Mass Spectroscopy (SIMS). SIMS measurements show mostly a constant oxygen concentration at a depth greater than 50 μm and a higher surface concentration, as shown in figure 4.1. For the SINTEF processed diodes the SIMS results are confirmed by infarot absorption measurements. The higher carbon content of the silicon material diffused in an oxygen atmosphere is due to the use of TCA during the thermal oxidation.

4.2 Irradiations

The radiation damage produced in crystalline silicon depends on the particle type and energy. Thus the irradiations were performed with ^{60}Co γ-photons, low and high energy protons, high energy pions and neutrons to take into

account the particle mixing in the inner detector of HEP experiments.

Table 4.1: *Material properties and diode producer*

Crystal type	Orientation	ρ $[\Omega cm]$	Producer of crystal	Producer of diode	Acronym of material
n-FZ	<111>	120	ITME[a]	ITE[1]	ITME I
n-FZ	<111>	800	ITME	ITE	ITME II
n-FZ	<111>	1.2k	ITME	ITE	ITME III
n-FZ	<111>	2.8k	Polovodice[b]	ITE	Polo I
n-FZ	<111>	1.5k	Polovodice	ITE	Polo II
n-CZ	<111>	100	Polovodice	HH[2]	Polo III
n-FZ	<111>	400	Wacker[c]	ITE	Wacker I
n-FZ	<111>	4k	Wacker	ITE	Wacker II
n-FZ	<111>	6−20k	Wacker	ELMA[3]	Wacker III
n-FZ	<111>	2.0k	Wacker	SINTEF[4]	Wacker IV,V
n-FZ	<100>	2.0k	Wacker	STM[5]	Wacker VI
n-FZ	<111>	2.0k	Wacker	STM	Wacker VII
n-FZ	<111>	4.0k	Wacker	CiS[6]	Wacker VIII
n-FZ	<100>	2.0k	Wacker	STM	Wacker IX
n-FZ	<111>	4.0k	Topsil[d]	SINTEF	Topsil I
n-FZ	<100>	1.5k	Topsil	CiS	Topsil II

a) Institute of Electronic Materials Technology, Warsaw, Poland
b) Polovodice, Prague, Czech Republic
c) Wacker Siltronic, Burghausen, Germany
d) Topsil Semiconductor Materials, Frederissund, Denmark
1) Institute of Electron Technology, Warsaw, Poland
2) II. Inst.f.Exp.physik, University Hamburg, Germany
3) ELMA, Moscow, Russia
4) SINTEF Electronics and Cybernetics, Oslo, Norway
5) ST Microelectronics, Cantania, Italy
6) CiS, Erfurt, Germany

4.2.1 Be(d,n) neutron irradiation

The neutron source of the Physikalisch Technische Bundesanstalt (PTB) at Braunschweig/Germany is a beryllium target that is bombarded with deuterons of an energy of 13.5 MeV. The reaction $^9Be(d,n)^{10}B$ provides a neutron field with a mean energy of 5.3 MeV. The maximal neutron energy is about 10 MeV. The neutron flux is proportional to the deuteron current and depends on the distance from the target. For a deuteron current of 30 μA the neutron flux ranges from about $1 \cdot 10^9$ to $1 \cdot 10^{10}$ cm^{-2}s^{-1} [Mol99]. The flux is determined from an ionisation measurement and the neutron

Table 4.2: *The oxygen and carbon concentrations of the different materials*

Acronym of material	Oxygen enrichment	[O] $10^{16}\mathrm{cm}^{-3}$	[C] $10^{16}\mathrm{cm}^{-3}$	Oxygen diffusion
ITME I	no	< 5	≤ 2	
ITME II	jet-oxygenated	17	< 2	
ITME III	jet-oxygenated	21	1	
Polo I	no	< 5	< 1	
Polo Ia	72h@1150°C in N_2	23	< 1	ITE
Polo II	no	< 5	1.8	
Polo III	no	90	0.5	
Wacker I	no	< 5	< 2	
Wacker II	no	< 0.02	< 3	
Wacker III	no	< 5	< 0.5	
Wacker IVa	72h@1150°C in N_2	14	< 0.63	SINTEF
Wacker Vb	72h@1150°C in O_2	21	1.5	SINTEF
Wacker VIc	30h@1200°C in N_2	26	1.2	STM
Wacker VIIc	30h@1200°C in N_2	36	1.8	STM
Wacker VId	60h@1200°C in N_2	22	0.44	STM
Wacker VIId	60h@1200°C in N_2	57	1.3	STM
Wacker VIII	no	0.9	0.62	
Wacker VIIIe	16h@1150°C in N_2	14	0.47	CiS
Wacker VIIIf	24h@1150°C in N_2	30	0.43	CiS
Wacker IX	no	0.9	< 0.3	
Topsil Ia	72h@1150°C in N_2	14	< 0.63	SINTEF
Topsil Ib	72h@1150°C in O_2	14	0.9	SINTEF
Topsil II	no	2.2	0.56	
Topsil IIg	144h@1200°C in N_2	34	3.5	BNL[1]

1) Brookhaven National Institute, USA

energy spectrum from a time-of-flight measurement. The deuteron current was 3 μA for the low fluence irradiations and 30 μA for the high fluence irradiations. The irradiated sample are listed in table F.1. The equivalent fluence was calculated from the measured particle fluence and the hardness factor. The hardness factor κ depends also on the distance from the target, because the energy distribution of neutrons changes.

4.2.2 Reactor neutron irradiation

The TRIGA Mark II research reactor of the Jožef Stefan Institute at Ljubljana/Slovenia is a light water reactor with solid fuel elements [Cas98]. The neutron energy spectrum has a range from thermal to 10 MeV neutrons.

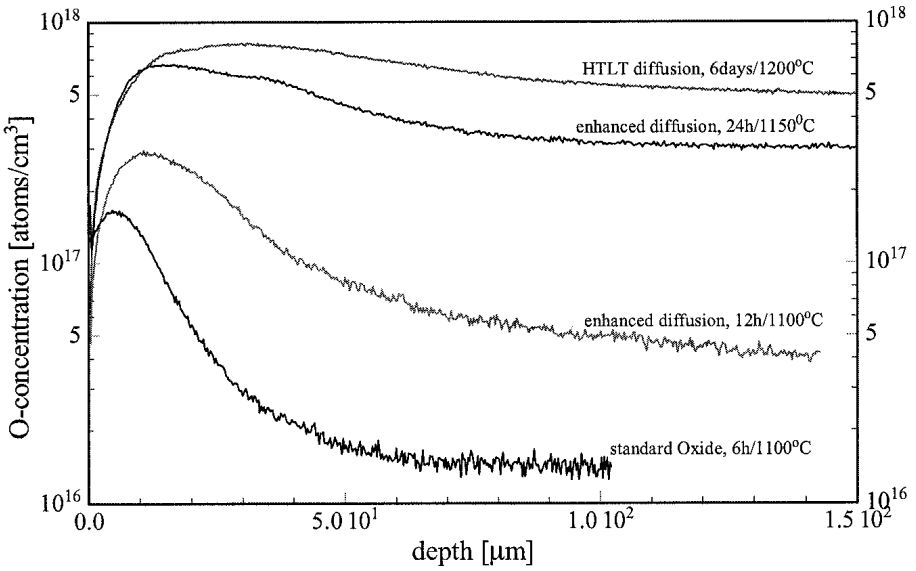

Figure 4.1: *Depth profiles of the oxygen concentration obtained from SIMS measurements on samples oxygenated for different times at different temperatures are shown* [Lin00].

The flux in the reactor core was determined from a measurement of the activity of a gold alloying. The flux is proportional to the reactor power. For the low fluence irradiations the reactor power was 100 W and the neutron flux given in NIEL equivalent of 1 MeV neutrons was $8.8 \cdot 10^8$ cm^{-2}s^{-1}. The hardness factor is estimated to be $\kappa \approx 0.9$. The irradiated samples are listed in table F.1. The equivalent fluence is determined from the volume generation current of a reference diode processed on standard FZ 6-20kΩcm (Wacker III). The reference diodes were irradiated together with the diodes for the DLTS studies. The agreement with the estimated fluences from the neutron flux is better than 10%.

4.2.3 23 GeV proton irradiation

The protons were accelerated to an energy of 23 GeV in the Proton Synchrotron (PS) at CERN. The fluence was monitored with a Secondary Emission Chamber (SEC). The signals from the chamber were counted. The SEC was calibrated with a fluence obtained from an activity measurement of aluminium [Cas98]. The proton beam consists of particle bunches (spills). A particle bunch contains about $5 \cdot 10^{10}$ protons. Therefore 2−4 spills are needed to accumulate the low fluences for the DLTS studies and only a crude estimation of the particle fluence is possible. The equivalent fluence is determined from the volume generation current of a reference diode processed on standard FZ 6-20kΩcm (Wacker III). The reference diodes were irradiated together with the diodes for the DLTS studies. The DLTS diodes were also

sometimes employed for the fluence determination and a good agreement was found with the results from the reference diodes. The deviation is less than 6%. The irradiated samples are listed in table F.2.

4.2.4 27 MeV proton irradiation

The two sample listed in table F.2 were irradiated with 27 MeV protons at Laboratori Nazionali di Legnaro/Italy. The beam current was measured with an array of faraday cups and the particle fluence was calculated from the integrated current [Wys00]. The equivalent fluence was calculated from the measured particle fluence and the hardness factor in [Sum93].

4.2.5 7-10 MeV proton irradiation

The four sample listed in table F.2 were irradiated with 7, 8, 9 and 10 MeV protons. The irradiations were done at Montreal University/Canada. The particle fluences for all irradiations were $5 \cdot 10^{10}$ cm^{-2}. The equivalent fluence was calculated from the particle fluence and the hardness factor in chapter 6.2.1. The hardness factor decreases with increasing proton energy.

4.2.6 192 MeV pion irradiation

The samples listed in table F.2 were irradiated at the Paul Scherrer Institut (PSI) in Villigen/Switzerland. The pions are produced inside a target that is bombarded with protons. The π^+ beam flow was continuous and the energy of the pions was 192 MeV. The flux was about $1.5 \cdot 10^9$ cm^{-2}s^{-1}. The beam intensity was monitored during the irradiation with a Secondary Emission Chamber (SEC). The calibration of the monitoring system is done with a fluence obtained from an activity measurement of aluminium. A measurement of the particle fluence even in the low fluence range was possible. Because the SEC is without a spatial resolution, the error due to fluctuations in the intensity profile of the beam is not excluded. The fluctuations in the calibration factor is shown in figure 4.2. The mean of the calibration factor is $7.31 \cdot 10^6 \pm 4.99 \cdot 10^5$ cm^{-2}cts^{-1}. The equivalent fluence is determined from the volume generation current of a reference diode processed on standard FZ 6-20kΩcm (Wacker III). The reference diodes were irradiated together with the diodes for the DLTS studies. The hardness factors in table F.2 are calculated from the particle and the equivalent fluences. The mean of hardness factor is $\kappa = 1.22 \pm 0.08$.

4.2.7 ^{60}Co γ-photon irradiation

The irradiations were performed at the ^{60}Co source of the Brookhaven National Institut/USA (BNL). The emission of two γ-photons with an energy

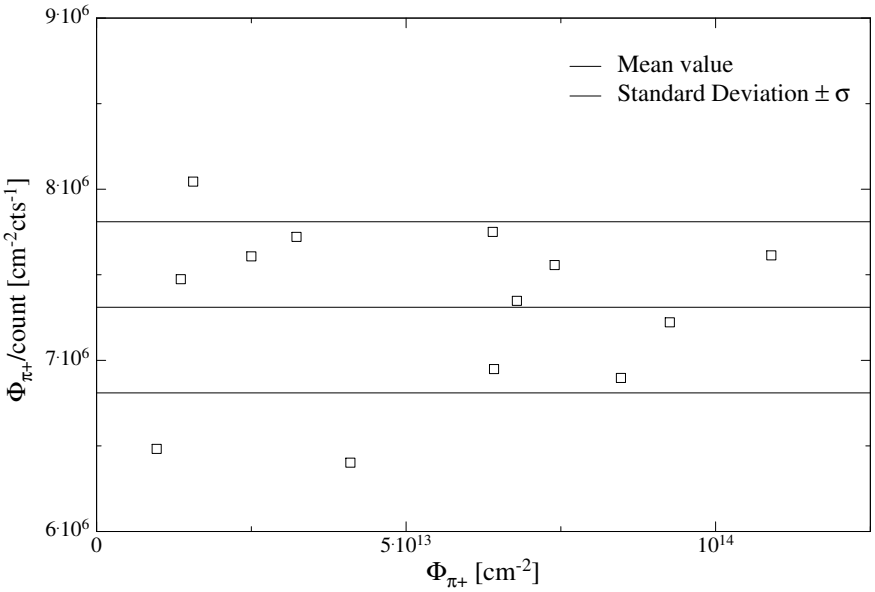

Figure 4.2: *The fluctuations in the calibration factor employed to determine the pion fluence is shown. The fluence obtained from an activity measurement is divided by the number of signals counted during a irradiation (cts). The irradiation source is the pion source at the PSI Villigen.*

of E_1=1.17 MeV and E_2=1.33 MeV occurs per disintegration of a ^{60}Co nucleus. The dose was measured with a silicon diode and the photon fluence is calculated from the dose with the factor

$$\frac{2 \cdot \rho}{E_1 \cdot \mu(E_1) + E_1 \cdot \mu(E_1)} = 1.89 \cdot 10^{15}\ \mathrm{cm}^{-2}\ \mathrm{Mrad}^{-1} \qquad (4.1)$$

where $\mu(E)$ is the absorption coefficient for photons with an energy E and ρ the density of the absorption material [PRD98]. The irradiated samples are listed in table F.3. A hardness factor is not reasonable.

4.3 Macroscopic methods for damage characterisation

A method to characterize the radiation induced damage in silicon is to measure the leakage current and the full depletion voltage of silicon detectors. These macroscopic parameters are obtained from the CV and IV measurements of p^+n diodes processed on the material under study. The fluence dependence and the annealing behaviour of both macroscopic parameters is employed to predict the operation scenarios of future HEP experiments, e.g. ATLAS Pixel Detector.

4.3.1 CV and IV setup

A commercial Prober station from SUESS is used. The Keithley Meter 487 or 6517A are employed as high voltage source and current meter. The maximal voltage supply of the Keithley 487 is 500 V and of the Keithley 6517A is 1000 V. The current limit is 2.5 mA for the 500V source and 1 mA for the 1000V source. The LCR Meter of Hewlett Packard 4263A is

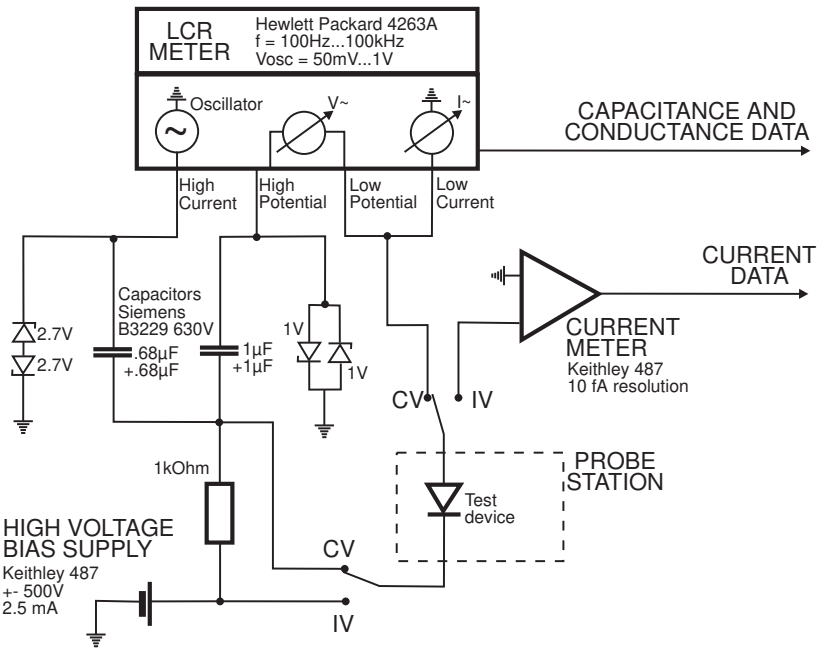

Figure 4.3: *The blockdiagram of the IV/CV measurement circuit is shown* [Fei97].

employed as capacitance meter. The small signal oscillator was operated with a frequency of 10 kHz and the amplitude was 50 mV or 0.5 V. The blockdiagram of the IV/CV measurement circuit is shown in figure 4.3.

4.4 Microscopic methods for damage characterisation

Different methods to characterize the microscopic defect parameters can be used, e.g. Deep Level Transient Spectroscopy (DLTS), Transient Current Technique (TCT) and Thermally Stimulated Current (TSC). The most powerful method is DLTS which allow to determine the defect parameters in a reasonable time. The TSC method allow a fast characterization, but for a determination of all defect parameters also a lot of experimental work is needed [Fei97]. The TCT method can be employed to characterize deep level defects [Ere95].

4.4.1 Deep Level Transient Spectroscopy

The DLTS method is the most developed method to determine the parameters of a defect center: concentration, activation energy and cross section. The exponential time dependence of the emission of charge carriers from a defect center is used. From the temperature dependence of the emission time constant the activation energy and cross section of a defect center is determined. The principle of a DLTS operation cyclus is shown in figure 4.4. The capacitance of a reverse biased p^+n junction is used to measure

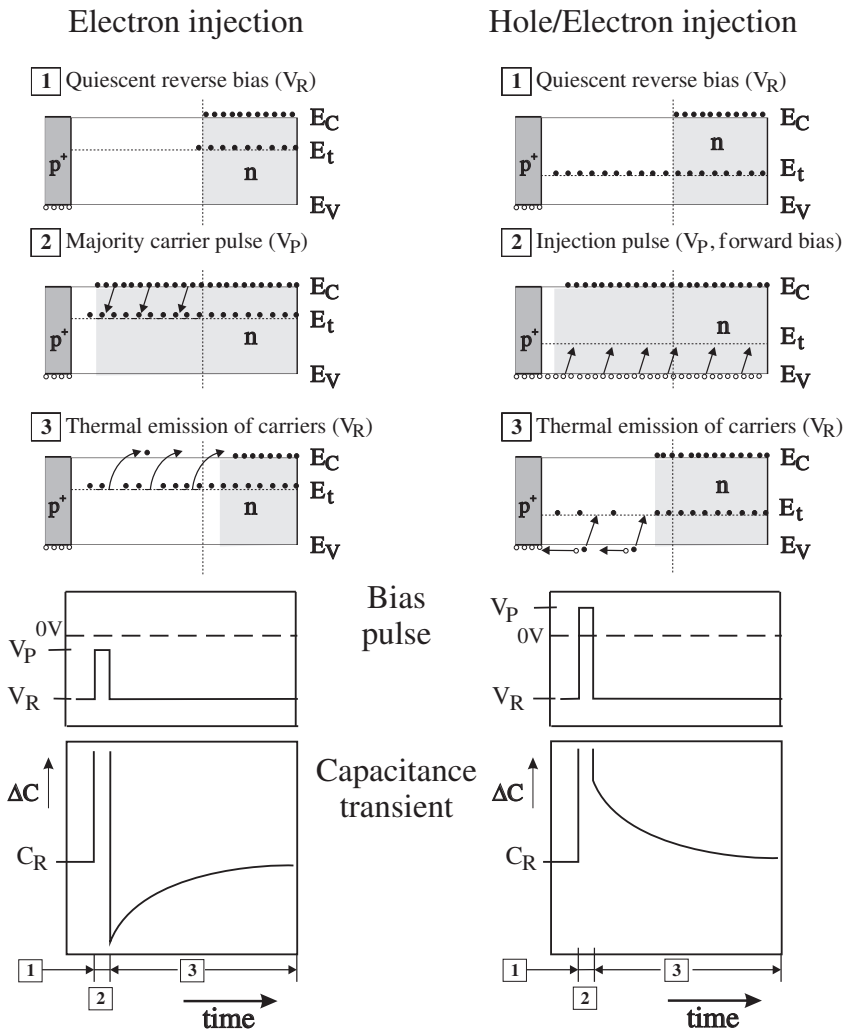

Figure 4.4: *The principle of the DLTS operation cyclus is shown* [Mol99].

the charge carrier emission. The reverse biased capacitance is quiescent, if no emission of charge carriers occur (1). The filling of defect states with majority charge carriers is accomplished by reducing the reverse bias and the filling of defect states with minority charge carriers is accomplished by forward biasing of the p^+n junction (2) or by illumination with light (not shown). The capacitance of the again reverse biased p^+n junction, which

determines the space charge density, depends on the occupancy of the emitting defect center (3). The emission of charge carriers results in a change of the reverse biased capacitance with the same exponential time dependence as the emission. The amplitude of the capacitance transient is proportional to the defect concentration. The sign of the amplitude is negative for majority charge carrier emission and positive for minority charge carrier emission. Because a capacitance transient is measured, this method is referred as capacitance (C-)DLTS. Another way to measure a transient is to keep the capacitance of a reverse biased p^+n junction constant during charge carrier emission. This method is referred as voltage (U-)DLTS or constant capacitance (CC-)DLTS, because a voltage transient is measured and the capacitance is kept constant. The evaluation of the transients is done by weighting with various types of functions. The weighting of transients of different time constants with the function of a double boxcar integrator is shown in figure 4.5. Because the emission time constant depends on the

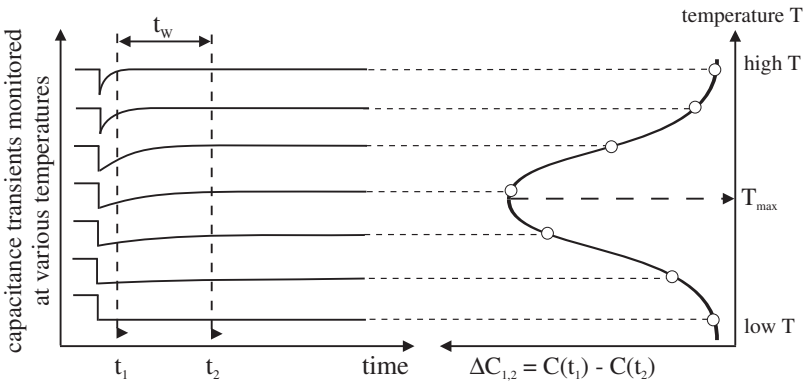

Figure 4.5: *The weighting of transients with the function of a double boxcar integrator is shown* [Mol99].

temperature, the weighted signal has a maximum at a certain temperature. In the employed DLTS system 18 weighting functions are used. Two of the weighting functions are the sine and cosine functions. The obtained coefficients are the Fourier coefficients and the method is referred as Deep Level Transient Fourier Spectroscopy (DLTFS) [Wei91]. Further there is the possibility to determine the capture rate of a defect center by measuring the dependence of the defect occupancy on the filling time. The features of the DLTS method is explained in further detail below.

Principles of the DLTS method

The emission time constant $\tau_{n,p}$ is the reciprocal of the emission coefficient

$$\tau_{n,p} = \frac{1}{e_{n,p}} \tag{4.2}$$

which depends on the temperature. Reordering of Eq. 3.20 and substituting Eq. 3.18 and 4.2 results in

$$\ln(\tau_{n,p} \cdot v_{th,n,p} \cdot N_{C,V}) = \ln(\sigma_{n,p}) \pm \frac{E_{C,V} - E_T}{k_B T} \tag{4.3}$$

where $\sigma_{n,p}$ is the cross section, $v_{th,n,p}$ the thermal velocity, $N_{C,V}$ the effective density of states, $E_{C,V}$ the energy of the conduction and valence band edge and E_T the energy of the defect state. The activation energy is $\pm(E_{C,V} - E_T)$. It is clear that from the slope of a plot of the term on the left hand side of Eq. 4.3 versus the reciprocal of the temperature the activation energy is obtained and from the intersection at 1/T=0 the cross section. This kind of plot is well known as Arrhenius Plot. The following effective masses $m_n^* = m_{th,n}^* = 1.08\, m_e$ and $m_p^* = m_{th,p}^* = 0.558\, m_e$ are used. The factors to calculate the cross sections employing the effective masses compiled in [Gre90] are listed in appendix A.

The emission time constant is obtained from the time dependence of the reverse biased capacitance. The effective space charge density is

$$q \cdot N_{eff}(t) = q \cdot (N_{eff,0} \mp N_T(t)) \tag{4.4}$$

where $N_{eff,0}$ is the effective doping concentration after emission of all captured charge carriers and $N_T(t)$ the concentration of occupied states. The sign is negative, if majority charge carriers are emitted, and positive, if minority charge carriers are emitted. Equation 2.40 of the reverse biased capacitance can be expanded into a Taylor series, if the defect concentration is $N_T/N_{eff,0} \ll 1$

$$C_R(t) \approx \sqrt{\frac{q\,\epsilon_s N_{eff,0}}{2(V_R + V_{bi})}} \cdot \left(1 \mp \frac{1}{2}\frac{N_T(t)}{N_{eff,0}}\right) \tag{4.5}$$

The time dependence of the reverse biased capacitance is obtained from Eq. 4.5 and 3.35

$$\frac{\Delta C(t)}{C_R} = \frac{C_R(t) - C_R}{C_R} = \mp\frac{1}{2} \cdot \frac{N_T}{N_{eff,0}} \cdot \exp\left(-\frac{t}{\tau_{n,p}}\right) \tag{4.6}$$

$$C_R = \sqrt{\frac{q\,\epsilon_s N_{eff,0}}{2(V_R + V_{bi})}} \tag{4.7}$$

where C_R is the reverse biased capacitance after emission of all captured charge carriers or the quiescent capacitance. Equation 4.6 shows that the time dependence of the capacitance signal is described by the same time constant as the charge carrier emission. Therefore it is possible to determine the emission time constant from the capacitance transient. Equation 4.6 is valid for a homogeneous defect concentration. Note that the contribution of occupied defect states to the capacitance signal depends on their position in the space charge region. The contribution of defect centers near the p^+ region to the capacitance signal is small [Bra79].

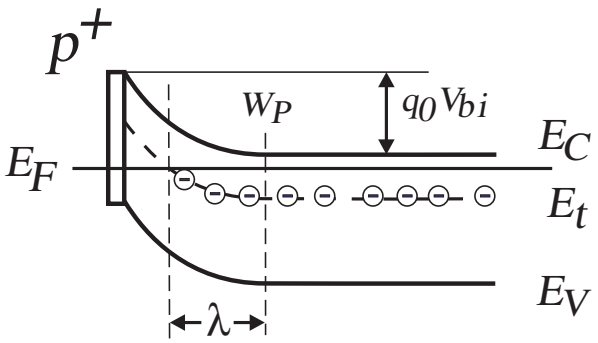

Figure 4.6: *The band bending diagram of a zero biased p^+n junction is shown. Also the effect of the transition region λ is included* [Mol99].

Before each transient measurement the defect states must to be filled with charge carriers. This is accomplished by reducing the applied reverse bias and thus the width of the depletion zone. Free charge carriers are swept into the previous depleted space charge region. The empty defect states are filled by capturing free charge carriers. The capture process is described by Eq. 3.36. During filling a small depletion layer at the p^+ region is left, even if the applied bias is zero. Also the effect that the free charge carrier concentration decreases not abrupt at the edge of the space charge region has to be taken into account. An exponential decrease of the free charge carrier concentration into the depleted zone is a good approximation. The penetration depth is equal to the Debye length $L_D = \sqrt{\epsilon_s/(q\,n_0\,\beta)}$. This results in a transition region between the edge of the space charge layer and the depleted zone, in which the defect states are occupied under thermal equilibrium condition, as shown in figure 4.6. The length of the transition region is

$$\lambda = \sqrt{\frac{2\epsilon_s(E_F - E_T)}{q^2\,n_0}} \tag{4.8}$$

where n_0 is the free charge carrier concentration in the electrical neutral bulk. From a detailed analysis regarding both effects the concentration of a defect center filled with majority charge carriers is

$$\begin{aligned} \frac{N_T}{N_{eff,0}} &= \left\{\left(1+\frac{\Delta C}{C_R}\right)^{-2} - 1\right\} \\ &\times \left\{\left(1+\frac{\Delta C}{C_R}\right)^{-2} - \left(\frac{C_R}{C_P}\right)^2 + \frac{2\lambda}{\epsilon_s}\left(\frac{C_R^2}{C_P} - C_R\right)\right\}^{-1} \end{aligned} \tag{4.9}$$

where ΔC is the capacitance amplitude at $t = 0$ and C_P the pulse or filling capacitance. An approximation of Eq. 4.9 for $\Delta C/C_R \ll 1$ is

$$\frac{N_T}{N_{eff,0}} = -2\,\frac{\Delta C}{C_R}\left\{1 - \left(\frac{C_R}{C_P}\right)^2 + \frac{2\lambda}{\epsilon_s}\left(\frac{C_R^2}{C_P} - C_R\right)\right\}^{-1} \tag{4.10}$$

This approximation is used to calculate the concentration of defect centers filled with electrons in n-type semiconductors. The defect states are located

in the upper half of the band gap, because the electron emission dominates for these defect centers during depletion of free charge carriers.

The hole emission dominates for defect states in the lower half of the band gap during depletion of free charge carriers. Defect centers can be filled with minority charge carriers by biasing the p^+n junction in forward direction or by generation of electron-hole (eh) pairs at the back side of the diode. For both methods of filling there is no transition region and no depleted layer during filling and therefore the concentration of a defect center filled with minority charge carriers is

$$\frac{N_T}{N_{eff,0}} = \left\{ \left(1 + \frac{\Delta C}{C_R} \right)^2 - 1 \right\} \tag{4.11}$$

If the applied forward bias is more than 15 $k_B T/q$ the high injection condition is reached and the concentrations of both types of charge carriers are $n \approx p$ in the n-type bulk of a p^+n junction [Mol58]. If eh pairs are generated in the n-type bulk near the back contact, e.g. due to backside illumination with infrared light, the eh pairs diffuse through the electrical neutral bulk to the depleted zone. Only the minority charge carriers drift through the electric field zone. The majority charge carriers are repelled. The occupancy of a defect center after long filling pulses is obtained from Equation 3.36 neglecting emission processes

$$\frac{\{n_T, p_T\}}{N_T} = \left(1 + \frac{\{p, n\} c_{p,n}}{\{n, p\} c_{n,p}} \right)^{-1} \tag{4.12}$$

where n and p are the free charge carrier concentrations and $c_{n,p} = \sigma_{n,p} \cdot v_{th,n,p}$ the capture coefficients.

Transient Evaluation

The measured capacitance transients have the following form

$$f(t) \equiv C(t) = \Delta C \cdot \exp\left(-\frac{t + t_0}{\tau} \right) + C_R \tag{4.13}$$

where t_0 is difference between the start of the emission process and the begin of the transient measurement. The two parameters of the transient signal $f(t)$ are the emission time constant τ, which is temperature dependent, and the capacitance amplitude ΔC[1]. The measured transients are weighted with various types of functions to determine the amplitude and the time constant. A coefficient is defined by the functional

$$S_W(f) = \frac{2}{T_W} \int_0^{T_W} f(t) \cdot W(t)\ dt \tag{4.14}$$

with the restriction

[1] The time delay t_0 is included in the measured capacitance amplitude ΔC_0

$$f(t) = \Delta C \cdot \exp\left(-\frac{t + t_0}{\tau} \right) = \Delta C_0 \cdot \exp\left(-\frac{t}{\tau} \right)$$

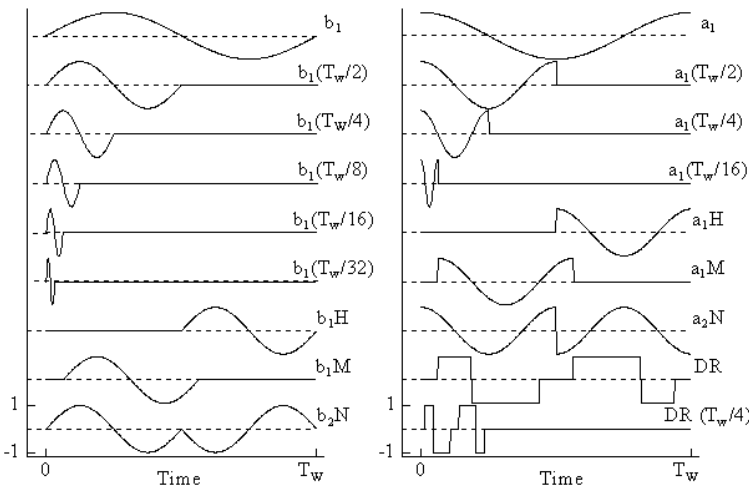

Figure 4.7: *The set of 18 weighting functions to evaluate the transients is shown* [Mol99].

$$S_W(f(t)=1) = \frac{2}{T_W}\int_0^{T_W} W(t)\ dt = 0 \tag{4.15}$$

where $W(t)$ is a weighting function and the upper integration limit T_W is equal to the duration or the time window of the transient measurement. The used set of weighting functions is shown in figure 4.7. It is clear that the conditions

$$\begin{aligned} \lim_{\tau\to 0} S_W(f_\tau) &= 0 \\ \lim_{\tau\to +\infty} S_W(f_\tau) &= 0 \end{aligned} \tag{4.16}$$

are satisfied. It is reasonable to choose only weighting functions for which $S_W(f_\tau)$ has a single maximum. If the harmonic functions $\sin(n\omega t)$ and $\cos(n\omega t)$ with $\omega = 2\pi/T_W$ are employed as weighting functions, the Fourier coefficients are obtained

$$a_n = \frac{2}{T_W}\int_0^{T_W} f(t)\cdot\cos(n\omega t)\ dt \tag{4.17}$$

$$b_n = \frac{2}{T_W}\int_0^{T_W} f(t)\cdot\sin(n\omega t)\ dt \tag{4.18}$$

An analytical evaluation of the integrals gives

$$\begin{aligned} a_0 &= \frac{2\Delta C_0}{T_W}\exp(-t_0/\tau)[1-\exp(-T_W/\tau)]\tau + 2C_R \\ a_n &= \frac{2\Delta C_0}{T_W}\exp(-t_0/\tau)[1-\exp(-T_W/\tau)]\frac{1/\tau}{1/\tau^2+n^2\omega^2} \\ b_n &= \frac{2\Delta C_0}{T_W}\exp(-t_0/\tau)[1-\exp(-T_W/\tau)]\frac{n\omega}{1/\tau^2+n^2\omega^2} \end{aligned} \tag{4.19}$$

The emission time constant τ can be calculated in three different ways from these coefficients [Wei91]

$$\begin{aligned} \tau(a_n, a_k) &= \frac{1}{\omega}\sqrt{\frac{a_n - a_k}{k^2 a_k - n^2 a_n}} \\ \tau(b_n, b_k) &= \frac{1}{\omega}\sqrt{\frac{kb_n - nb_k}{k^2 nb_k - n^2 kb_n}} \\ \tau(a_n, b_n) &= \frac{1}{n\omega} \cdot \frac{b_n}{a_n} \end{aligned} \tag{4.20}$$

The goal of this method is that many τ values are obtained in the temperature range, in which capacitance transients due to charge carrier emission from the defect center are measured. However, the method works only well, if the measured capacitance transient has a high S/N ratio and is an ideal exponential transient [Mol99]. It is more accurate to use only the maximum values of various coefficients at a certain temperature. Because the magnitude of $S_W(f)$ is proportional to the amplitude ΔC and $S_W(f)$ has a single maximum at a certain τ value, from each coefficient maximum a set $\{\tau, \Delta C, T\}$ is obtained. Often the capacitance transient at one temperature is measured with different time window T_W and a set $\{\tau, \Delta C, T\}$ is obtained for each time window. An example of this maxima evaluation to determine the temperature dependence of the emission time constant is shown in figure 4.8. This method is used to evaluate the measured DLTS spectra.

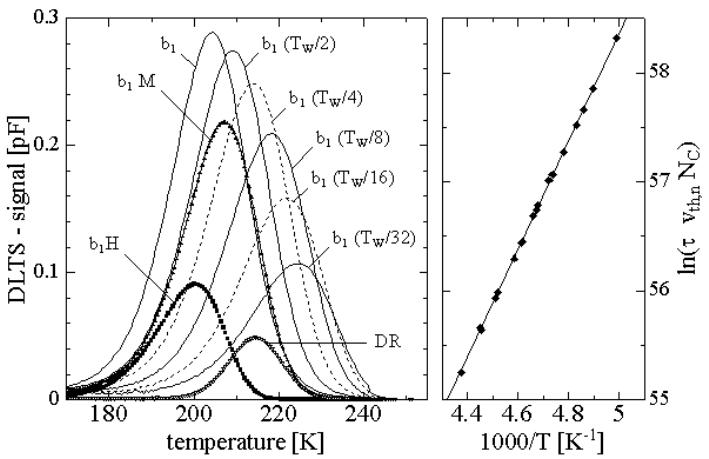

Figure 4.8: *On the left hand side the values of various coefficients are plotted versus the temperature (DLTS spectra). On the right hand side a Arrhenius Plot is shown. The temperature dependence of the emission time constant τ is determined from the maxima of the coefficients. The transition $VV^{-/0}$ is measured* [Mol99].

The Full Width at Half Maximum (FWHM) of a coefficient plotted versus the temperature depends on the used weighting function. Therefore the

resolution or the separation of defect states with small differences in their energy levels or emission rates $e_{n,p}(T)$ is determined by the used weighting function. However, weighting functions, that allow a high resolution, are more sensitive to the S/N ratio of the transient signal. Only transient signals with a high S/N ratio allow a separation of defect states with small differences in their emission rates [Ist97].

Signal Processing

Fourier Transformation Often it is more convenient to represent the time dependence of a periodic signal $f(t) = f(t+T)$ with a frequency $\omega_0 = 2\pi/T$ as a superposition of an infinite number of harmonic functions

$$f(t) = \sum_{n=0}^{+\infty} a_n \cos(n\omega_0 t) + \sum_{n=1}^{+\infty} b_n \sin(n\omega_0 t) \tag{4.21}$$

where a_n and b_n are the Fourier coefficients. The coefficients can be calculated, if the time dependence of the signal $f(t)$ is known. For a non periodic signal the frequency space is a continuum, because $T \to \infty$ and thus $\omega_0 \to 0$. It is more convenient to express the harmonic functions with the complex exponential function and one obtains

$$f(t) = \frac{1}{2\pi} \int_{-\infty}^{+\infty} F(\omega) \exp(i\omega t)\, d\omega \tag{4.22}$$

and the complex amplitude function $F(\omega)$ is obtained from calculating the integral

$$F(\omega) = \int_{-\infty}^{+\infty} f(t) \exp(-i\omega t)\, dt \tag{4.23}$$

Equation 4.23 is called the Fourier transformation. A Fourier transformation is possible for a large set of functions. Equation 4.22 is called the inverse Fourier transformation.

Discrete Fourier Transformation For a measured signal only a discrete Fourier transformation is possible, because the signal is measured only at a finite number of time points t_k. The discrete Fourier transformation is defined by

$$F_D(\omega) = \sum_{k=0}^{n} f(t_k) \exp(-i\omega t_k) \tag{4.24}$$

Equation 4.24 is expressed in the following form by using the delta function

$$F_D(\omega) = \sum_{k=0}^{n} \int_{t_0}^{t_n} f(t)\, \delta(t - t_k)\, \exp(-i\omega t)\, dt \tag{4.25}$$

The delta function $\delta(t)$ is also a superposition of an infinite number of complex exponential functions

$$\delta(t - t_k) = \frac{1}{2\pi} \int_{-\infty}^{+\infty} \exp(i\omega(t - t_k))\, d\omega \tag{4.26}$$

Substituting Eq. 4.26 into Eq. 4.25 and performing the integration over the variable t results in

$$F_D(\omega) = \frac{1}{2\pi} \sum_{k=0}^{n} \int_{-\infty}^{+\infty} F(\omega - \omega') \exp(-i\omega' t_k)\, d\omega' \tag{4.27}$$

If the signal is sampled over the time interval T_W with a constant sampling rate $1/\Delta t = n/T_W$ and the integration is divided into equal intervals with the length of the sampling frequency

$$\omega_s = 2\pi/\Delta t \tag{4.28}$$

Equation 4.27 is simplified to

$$F_D(\omega) = \frac{1}{2\pi} \sum_{k=0}^{n} \sum_{m=-\infty}^{+\infty} \int_{-\omega_s/2}^{+\omega_s/2} F(\omega - \omega' - m\omega_s) \exp\left(-\frac{2\pi i \omega' k}{\omega_s}\right) d\omega' \tag{4.29}$$

Exchanging the sum over the index k and the integration over the variable ω' in Eq. 4.29 gives

$$F_D(\omega) = \frac{1}{2\pi} \sum_{m=-\infty}^{+\infty} \int_{-\omega_s/2}^{+\omega_s/2} F(\omega - \omega' + m\,\omega_s)\; s\left(\frac{\omega'}{\omega_s}\right) d\omega' \tag{4.30}$$

where $s(x)$ is the abbreviation of the following sum

$$\begin{aligned} s(x) &= \sum_{k=0}^{n} \exp(-2\pi i x k) \\ &= \sum_{k=0}^{n} \cos(2\pi x k) - i \sum_{k=0}^{n} \sin(2\pi x k) \end{aligned} \tag{4.31}$$

If the finite summation is replaced by an infinite one, $s(x)$ is a periodic array of delta functions

$$s_\infty(x) = \sum_{k=-\infty}^{+\infty} \exp(2\pi i x k) = \sum_{k=-\infty}^{+\infty} \delta(x - k) \tag{4.32}$$

The sum $s(x)$ for $x \in [0, 1]$ is calculated numerical for $n = 128$, $n = 256$, $n = 512$ and $n = 1024$. The results are shown in figure 4.9. The function $s(x)$ is averaged over small intervals of the length 0.01, because $s(x)$ is rapidly oscillating. For the later analysis this averaging does not matter, because $F(\omega)$ is mostly a slowly varying function and the oscillation are averaged to zero. The results show that the real part of the finite sum $s(x)$ can be approximated by a delta function and the small imaginary part is negligible. If $s(x)$ in Eq. 4.30 is substituted by a delta function, the integration over the variable ω' can be performed

$$F_D(\omega) = \frac{1}{\Delta t} \sum_{m=-\infty}^{+\infty} F(\omega + m\,\omega_s) \tag{4.33}$$

This result shows that the Fourier spectra of a non-digitized and digitized signal are not identical.

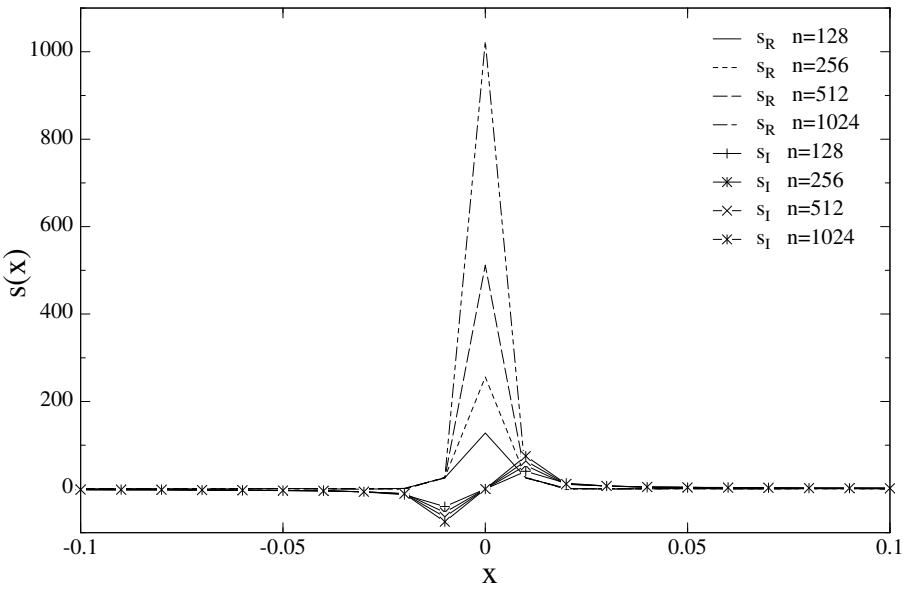

Figure 4.9: *The sum $s(x)$ is calculated numerical for $n = 128$, $n = 256$, $n = 512$ and $n = 1024$. The symmetric real part of $s(x)$ has a maximum at $x = 0$. The height of the maximum is equal to n. The imaginary part of $s(x)$ is asymmetric and the extrema are smaller in comparison to the real part.*

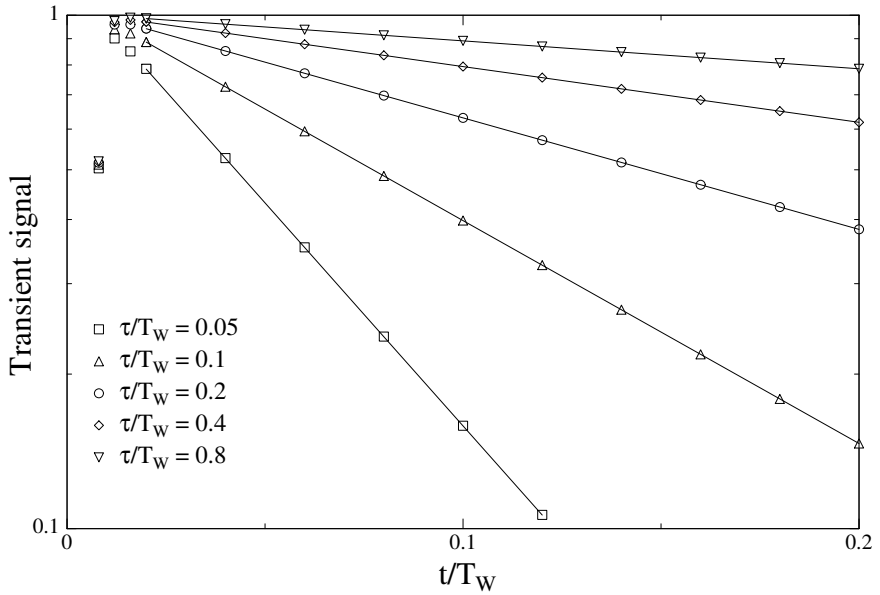

Figure 4.10: *The response of an 8^{th} order Bessel filter to exponential transients of different time constants is shown (symbols). The number of sampling points is $n = 512$. The cutoff frequency is $\omega_g = \omega_N/4$. No deviation from delayed exponential transients (lines) is seen.*

Sampling theorem The amplitude of the discrete Fourier transformation $F_D(\omega)$ in the interval $[-\omega_s/2, +\omega_s/2]$ is multiple reproduced on the rest of the frequency spectrum, because it can be seen from Eq. 4.33 immediately

$$F_D(\omega) = \frac{1}{\Delta t}\ F_D(\omega + m\,\omega_s) \tag{4.34}$$

The Fourier transformation $F_D(\omega)$ of a discrete signal, which is restricted in the frequency interval $[-\omega_s/2, +\omega_s/2]$, is in very good approximation equal to the Fourier transformation $F(\omega)$ of the corresponding continuous signal. In other words no information is lost, if a signal, which is restricted in the frequency interval $[-\omega_s/2, +\omega_s/2]$, is digitized with a higher sampling rate than $\omega_s/2\pi$. The half of the sampling frequency is the well known Nyquist frequency

$$\omega_N = \omega_s/2 \tag{4.35}$$

The folding in the spectrum of a digitized signal with frequencies higher than ω_N is called the Aliasing effect. If the time constant of an exponential transient is calculated from the Fourier coefficients, this effect has to be taken into account. Hence the high frequency components of an exponential transient must be suppressed with a low pass filter.

Signal filtering A filter, which modifies the frequency spectrum of a signal, can be described by an amplitude response function

$$H(\omega) = |H(\omega)| \cdot \exp(i\varphi(\omega)) \tag{4.36}$$

The filtered signal is obtained from

$$g(t) = \frac{1}{2\pi}\int_{-\infty}^{+\infty} G(\omega)\exp(i\omega t)d\omega$$

$$\text{with} \quad G(\omega) = H(\omega)\cdot F(\omega) \tag{4.37}$$

The absolute value of $H(\omega)$ for an ideal low pass filter with the cutoff frequency ω_g is $|H(\omega)| = 1$ for $\omega \le \omega_g$ and $|H(\omega)| = 0$ for $\omega > \omega_g$. The phase shift $\varphi(\omega) = 0$ is frequency independent. The signal processed by an ideal low pass filter is

$$g_{ideal}(t) = \frac{1}{2\pi}\int_{-\omega_g}^{+\omega_g} F(\omega)\exp(i\omega t)d\omega \tag{4.38}$$

The group delay of a filter, which is used to describe the time delay of a filtered signal, is

$$T_{gr}(\Omega) = -\frac{1}{2\pi}\ \frac{d\varphi}{d\Omega}$$

$$\text{with} \quad \Omega = \frac{\omega}{\omega_g} \tag{4.39}$$

Thus for an ideal low pass filter the group delay is $T_{gr} = 0$ and the filtered signal is not delayed. For a Bessel filter the phase shift increases linear with

increasing frequency for $\Omega \leq 1$ and hence the group delay T_{gr} is constant. The signal filtered by a Bessel filter is delayed

$$g_{Bessel}(t) \approx g_{ideal}(t - t_{gr}) \tag{4.40}$$

and the delay time is

$$t_{gr} = \frac{2\pi \cdot T_{gr}}{\omega_g} \tag{4.41}$$

Bessel filters are often employed, because a filtered step-like signal is only delayed and not strongly distorted.

The transient signals are filtered in the used DLTS system by an 8^{th} order Bessel filter with a cutoff frequency $\omega_g = \omega_N/4$ to avoid the Aliasing effect in the evaluation of the Fourier coefficients. The response of an 8^{th} order Bessel filter to exponential transients is shown in figure 4.10. The group delay of an 8^{th} order Bessel filter is $T_{gr} = 0.506$ [Tie93]. A deviation from an exponential transient shifted with the group delay time is not visible. The shown examples are equivalent to $n = 128 \cdot k$ and ω_N/k, because in the integral of the inverse Fourier transformation only the quotients n/k and τ/T_W occur.

Error estimation

The concentration of a defect center filled with majority charge carriers is calculated from Equation 4.10. The widths of the space charge regions are calculated from the measured capacitances, thus Eq. 4.10 can be rewritten into

$$N_T = 2\ N_{eff,0}\ \frac{W_R' - W_R}{W_R'} \left\{ 1 - \left(\frac{W_P}{W_R}\right)^2 + \frac{2\lambda}{W_P} \left(\left(\frac{W_P}{W_R}\right)^2 - \frac{W_P}{W_R} \right) \right\}^{-1} \tag{4.42}$$

where W_R' is the width of the space charge region, if all defect centers are occupied. The error estimation of the defect concentration is obtained from the Gaussian law of error propagation

$$\frac{\delta N_T}{N_T} = \sqrt{ \left(\frac{\delta \left(\frac{W_R' - W_R}{W_R'} \right)}{\frac{W_R' - W_R}{W_R'}} \right)^2 + \left(\frac{\left(2\frac{W_P}{W_R} - \frac{2\lambda}{W_P} \left(2\frac{W_P}{W_R} - 1 \right) \right) \delta \left(\frac{W_P}{W_R} \right)}{1 - \left(\frac{W_P}{W_R} \right)^2 + \frac{2\lambda}{W_P} \left(\left(\frac{W_P}{W_R} \right)^2 - \frac{W_P}{W_R} \right)} \right)^2 } \tag{4.43}$$

for the variables

$$\frac{W_R - W_R'}{W_R'} = \frac{\Delta C}{C_R} \tag{4.44}$$

and

$$\frac{W_P}{W_R} = \frac{C_R}{C_P} \tag{4.45}$$

Equation 4.43 has a pole at

$$\frac{\lambda}{W_P} = \frac{1}{2} \left(1 + \frac{W_R}{W_P} \right) \tag{4.46}$$

and hence the error in the defect concentration is infinite, if Equation 4.46 is valid. The error in the first variable is

$$\delta\left(\frac{W_R - W_R'}{W_R'}\right) = \frac{W_R - W_R'}{W_R'}\sqrt{\left(\frac{\delta(\Delta C)}{\Delta C}\right)^2 + \left(\frac{\delta C_R}{C_R}\right)^2} \tag{4.47}$$

The error in the capacitance per area is

$$\frac{\delta C}{C} = \sqrt{\left(\frac{\delta C_{meas}}{C_{meas}}\right)^2 + \left(\frac{\delta A}{A}\right)^2} \tag{4.48}$$

where C_{meas} is the measured capacitance and A the area of the depletion zone under the p^+n junction which is increased due to the lateral extension of the electric field zone. Because the ratio of two capacitances with about the same lateral extension of the depletion zone is calculated in Eq. 4.44, the error is mainly determined by the error in the capacitance measurement. The accuracy of the capacitance meter is about 0.1% [Boo88]. Both capacitances C_R and ΔC are measured in the 30 pF range with a compensation capacitance. The error in C_R is estimated to be between 1% and 5% due to the compensation capacitance. Also a plot of the reverse biased capacitance versus the temperature indicate an error of that magnitude. The error in $\delta(\Delta C)/\Delta C \leq 1\%$ due to the accuracy of the capacitance meter is small in comparison to the error due to the evaluation of ΔC from the capacitance transient employing various weighting functions (Maxima evaluation). The error is estimated from plots of ΔC versus the temperature to be around 10%.

The error in the second variable is mainly determined by the lateral extension of the depletion zone

$$\begin{aligned}\delta\left(\frac{W_P}{W_R}\right) &= \frac{W_P}{W_R}\cdot\sqrt{\left(\frac{\delta C_R}{C_R}\right)^2 + \left(\frac{\delta C_P}{C_P}\right)^2} \\ &\approx \frac{W_P}{W_R}\cdot\frac{\delta C_R}{C_R} \approx \frac{W_P}{W_R}\cdot\frac{\delta A}{A}\end{aligned} \tag{4.49}$$

The error is estimated to be around 10% [Mol99].

It is assumed that the relative errors in both variables are equal to make a crude error estimation possible. The error in each variable is 10%. The relative error in the defect concentration is shown in figure 4.11. The error is plotted versus the ratio W_R/W_P, which is equal to $(V_R/V_{bi}+1)^{-1/2}$ for $V_P =$ 0 V. If V_R=10 V and V_{bi}=0.42−1.25 V, the ratio W_R/W_P is in the range from 3 to 5. The effect of the transition region is included in the parameter λ/W_P. The dependence of the error $\delta N_T/N_T$ on $\lambda/W_P \in [0.01, 0.75]$ is weak for $W_R/W_P > 3$. The error is dominated by the error in the first variable $\Delta C/C_R$.

Further the error in $N_{eff,0}$ is included with

$$\delta\left(\frac{N_T}{N_{eff,0}}\right) = \frac{N_T}{N_{eff,0}}\cdot\sqrt{\left(\frac{\delta N_{eff,0}}{N_{eff,0}}\right)^2 + \left(\frac{\delta N_T}{N_T}\right)^2} \tag{4.50}$$

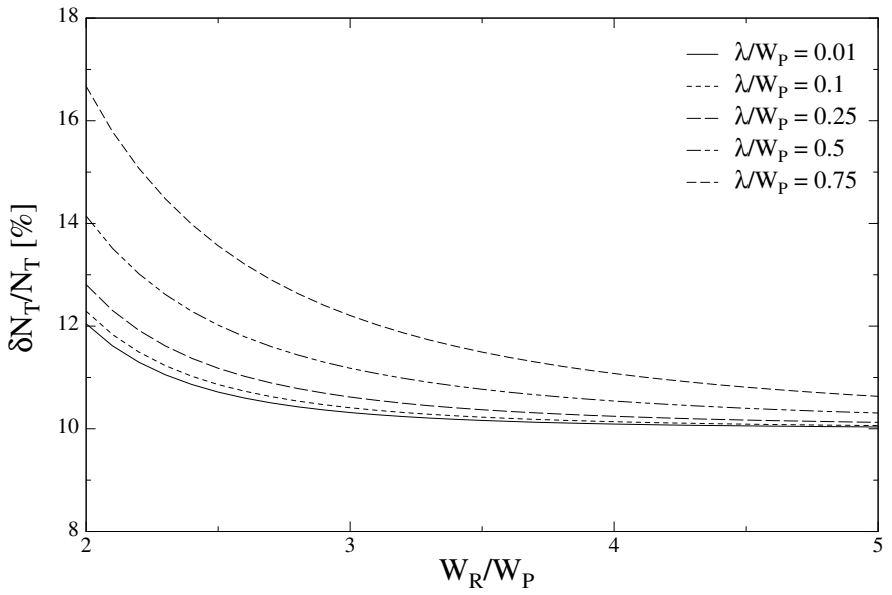

Figure 4.11: *The relative error in the defect concentration is shown. For further details see text.*

The effective doping concentration $N_{eff,0}$ is determined from the slope of a $1/C^2$-V plot. Differentiating Eq. 2.41 and reordering yields

$$N_{eff,0} = \frac{2}{q \cdot \epsilon_s} \left(\frac{d(1/C^2)}{dV} \right)^{-1} \tag{4.51}$$

The method of linear regression is employed to determine the slope of the $1/C^2$-V plot. It is assumed that during the CV measurement all defect centers are unoccupied. The linear regression is reduced to two points for an error estimation. Equation 4.51 is simplified to

$$N_{eff,0} = \frac{2}{q \cdot \epsilon_s} \cdot \frac{V_R - V_P}{1/C_R^2 - 1/C_P^2} \tag{4.52}$$

Only regarding the error due to the lateral extension of the depletion zone - all other errors are much smaller - the error in $N_{eff,0}$ is

$$\frac{\delta N_{eff,0}}{N_{eff,0}} \approx \frac{2}{1 - (C_R/C_P)^2} \cdot \frac{\delta C_R}{C_R} \approx 2 \frac{\delta A}{A} \tag{4.53}$$

The error is estimated to be around 20%. The error in the concentration of a defect center filled with majority charge carriers is around 23% for $\delta(\Delta C/C_R)/(\Delta C/C_R) = \delta A/A = 10\%$, $W_R/W_P \in [3,5]$ and $\lambda/W_P = 0.75$. The error is dominated by the error in $N_{eff,0}$ which is due to the lateral extension of the depletion region. However, more points are used for the linear regression and the error is reduced. The error in the concentration of a defect center filled with minority charge carriers is dominated also by the

error in $N_{eff,0}$. But also other not explained features in the DLTS spectrum may enhance the error.

From an Arrhenius plot the activation energy and cross section of a defect center is determined. The method of linear regression is applied to determine the slope and intersection. For the error estimation a two point Arrhenius plot is used

$$\frac{\ln \tau_1 - \ln \tau_2}{1/(k_B T_1) - 1/(k_B T_2)} = \pm (E_{C,V} - E_T) \tag{4.54}$$

where the temperatures are $T_1 < T_2$. The temperatures T_1 and T_2 determine the temperature range in which the emission time constants τ_1 and τ_2 are obtained from the DLTS spectra. Neglecting the error in the emission time constant and regarding only the error in the temperature, the error in the activation energy is

$$\frac{\delta(E_{C,V} - E_T)}{E_{C,V} - E_T} = \sqrt{\left(\frac{1}{1 - T_1/T_2}\frac{\delta T_1}{T_1}\right)^2 + \left(\frac{1}{T_2/T_1 - 1}\frac{\delta T_2}{T_2}\right)^2} \tag{4.55}$$

The relative error in the temperature is nearly constant $\delta T/T \approx 0.5\%$ during temperature ramping and Eq. 4.55 is simplified to

$$\frac{\delta(E_{C,V} - E_T)}{E_{C,V} - E_T} = \frac{\sqrt{T_2^2 + T_1^2}}{T_2 - T_1} \cdot \frac{\delta T}{T} \tag{4.56}$$

The calculated errors are in the range from 3% to 4% for the various radiation induced defects in appendix B. The error in the cross section due to the accuracy of the temperature measurement is obtained from keeping the slope of the Arrhenius plot constant and shifting the reciprocal temperature scale with $\delta T/T^2$

$$\ln\left(1 + \frac{\delta\sigma}{\sigma}\right) = \pm \frac{E_{C,V} - E_T}{k_B T} \cdot \frac{\delta T}{T} \tag{4.57}$$

where the temperature T is the mean of T_1 and T_2. The cross section is changed by a factor $0.85-1.15$. But the main error is correlated with the error in the slope of the Arrhenius plot. The error is

$$\ln\left(1 + \frac{\delta\sigma}{\sigma}\right) = \pm \frac{E_{C,V} - E_T}{k_B T} \cdot \frac{\delta(E_{C,V} - E_T)}{E_{C,V} - E_T} \tag{4.58}$$

The cross section is changed by factor greater than two. However, because more points are employed for the linear regression, the error in the activation energy and cross section is reduced. But still the error in the cross section is more than a factor $10-100$ larger than the error in the activation energy.

4.4.2 DLTS setup

The DLTS system consists of a cooling system, a temperature controller, a capacitance meter, an analog low pass Bessel filter, a transient recorder,

a data processing unit and a PC to control the measurement, to store and to evaluate the data. The optical illumination of the sample was furnished with an infrared LED or a 670 nm laser diode. The blockdiagram of the DLTS system is shown in figure 4.12. The digital data acquisition system

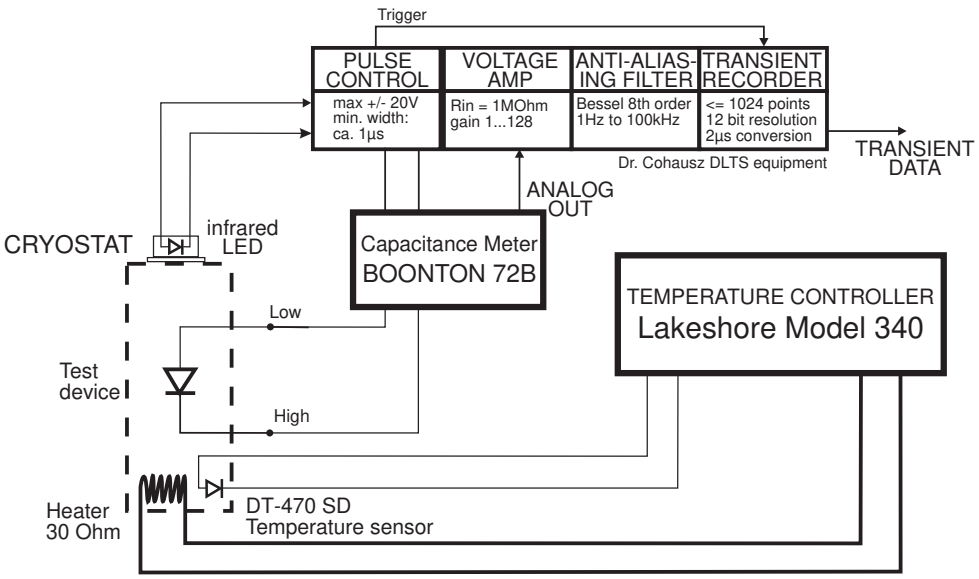

Figure 4.12: *The blockdiagram of the DLTS system is shown* [Mol99].

and software package was developed by the Halbleitermesstechnik GmbH in Moosburg. An overview of the components is given below for understanding the functionality of the system.

Cooling system

A closed cycle two-stage helium refrigerator from CTI-Cryogenics Model 22C combined with a hot stage offers the possibility to cool a test device to a temperature between 20 K and 450 K. The temperature range from 30 K to 280 K was used. The hot stage is shown in figure 4.13. The helium gas of high purity with a pressure of 1800 kPa is expanded inside a tower and therefore the temperature of the helium gas is lowered to about $10-20$ K. The temperature of the helium gas depends on its purity and pressure. Hence an absorber is employed in the closed helium gas cycle to keep the helium gas clean. The resistance of the heater is 30 Ω.

Temperature controller

A silicon diode DT-470 SD is used to measure the temperature near the sample. A constant current is sustained through the diode. The measured voltage across the diode depends on the temperature and is converted by the temperature controller into a temperature value. The current flow through the heater is supplied by one of the outputs of the controller to kept the

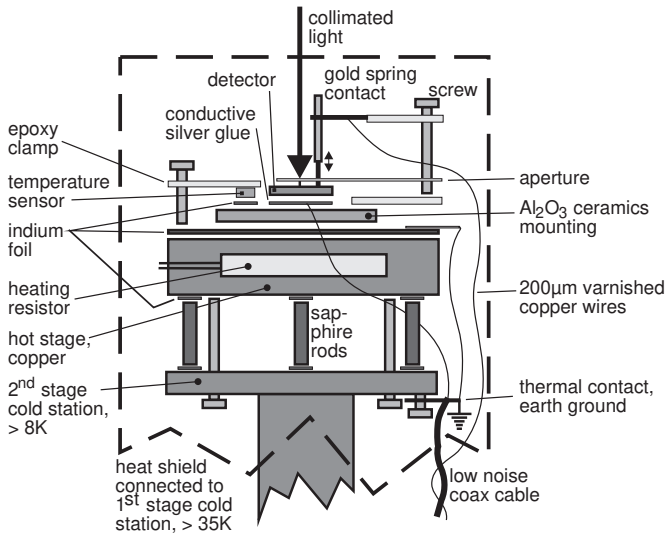

Figure 4.13: *The hot stage of the DLTS system is shown* [Fei97].

temperature constant or to ramp the temperature. The temperature set point is one of the control parameters. The PID control parameters are chosen to optimize the relaxation time and the temperature overshot after increase of the value of the temperature set point. The maximum heating power was 30 W.

Capacitance meter

The capacitance meter measures the small signal capacitance of a test device

$$C = \frac{\delta Q}{\delta V} \tag{4.59}$$

The amplitude of the AC signal is 15 mV (R.M.S.) and the frequency 1 MHz. An external voltage source is employed to apply a DC voltage to the test device. Further the meter has the possibility to measure the difference between two capacitances. The schematic circuit diagram is shown in figure 4.14. A transformer divides the RF signal of the oscillator into two signals with 180° phase shift. The resonance frequency of the RCL series circuit is equal to the oscillator frequency

$$\omega_r = \frac{1}{\sqrt{LC}} \tag{4.60}$$

and therefore the impedance of the series circuit is $Z = R$. Another parameter of the series circuit is the quality

$$Q = \frac{\omega_r L}{R} = \frac{1}{\omega_r \, CR} \tag{4.61}$$

A series circuit of low quality is used to avoid a change in the impedance caused by instabilities in oscillator frequency or changes in L and C. The

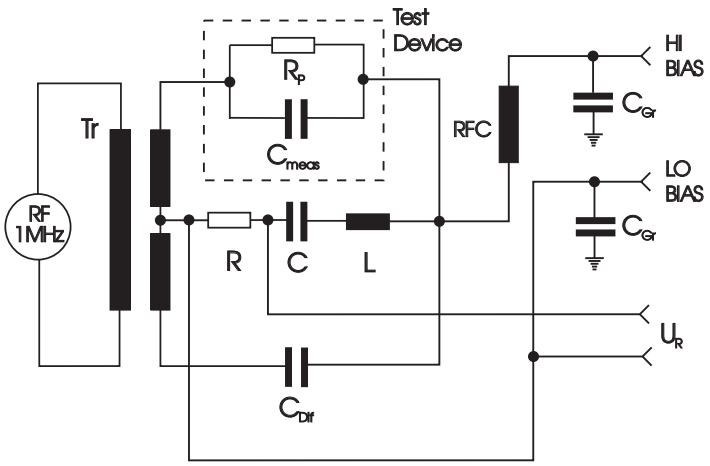

Figure 4.14: *The schematic circuit of the capacitance meter is shown.*

capacitance of the series circuit avoids a short cut of the external DC voltage source at the Hi Bias and Lo Bias connectors across the low ohmic resistor R. The capacitors C_{Gr} are employed to make the potential at the Hi Bias and Lo Bias connectors equal to common ground for the RF signal. The RF Coil is used to avoid a short cut of the RF signal to common ground. The ratio between U_R, the voltage across the resistor R, and U_{osc}, the oscillator amplitude, is

$$\frac{U_R}{U_{osc}} = \frac{i\,\omega_r\,R\,(C_{meas} - C_{Dif}) + \frac{R}{R_P}}{1 + i\,\omega_r\,R\,(C_{meas} + C_{Dif}) + \frac{R}{R_P}} \tag{4.62}$$

For $R/R_P \ll 1$ the absolute value of U_R/U_{osc} is

$$\left|\frac{U_R}{U_{osc}}\right| = \frac{\omega_r\,R\,(C_{meas} - C_{Dif})}{\sqrt{1 + \cot^2\varphi}} \tag{4.63}$$

where φ is the phase shift between U_R and U_{osc}

$$\cot\varphi = \omega_r\,R\,(C_{meas} + C_{Dif}) \tag{4.64}$$

Hence the absolute value $|U_R/U_{osc}|$ is proportional to the capacitance difference. The range of the capacitance meter is determined by the resistor R.

Transient recording and analysis

The transient signal is amplified and filtered by an 8^{th} order low pass Bessel filter and is digitized by an 12bit ADC. The conversion time of the ADC is 2 μs, the number of sample points 512. The durations of the transient recordings or the time windows were 19.97 ms, 199.94 ms and 2.00 s. The time delay between the end of the filling pulse and the start of the transient recording was 5.19 ms for the 19.97 ms time window, 6.64 ms for the 199.94

ms time window and 19.53 ms for the 2.00 s time window, because the recovery time of the capacitance meter was set to $t_0 = 5$ ms. The transients were averaged to enhance the S/N ratio. The measuring time for the 19.97 ms and 199.94 ms time windows was 4 s and 10 s for the 2.00 s time window. The duration of the filling pulse was 100 ms. An external data processing unit was employed for the weighting of the transients. The obtained datas were stored and analyzed on a PC.

The reverse bias was 10 V and during filling with majority charge carriers a voltage pulse of 0 V was applied to the diode. During the filling with minority charge carriers the diode was biased in forward direction. The applied voltage was -3 V. Optical filling with minority charge carriers is furnished by back side illumination of the diode with an infrared LED. Also front side illumination with a 670 nm laser diode is used to fill defects with majority charge carriers.

Mounting and electrical connections

For the mounting of the sample inside the cryostat a ceramic with a high thermal conductivity was used. An indium layer provides a good thermal contact between the ceramic and the cooling plate. A small piece of indium foil was also used to have a good thermal contact between the temperature sensor and the ceramic. The sample was glued on the ceramic. The ceramic has a conductive gold alloy pattern on its surface. A special silver glue (Emetron 200) which cures at room temperature was used. Also the electrical contact on the top side of the sample was furnished with silver glue. A thin wire was employed to bond the top side of the sample with a metal pattern on the ceramic. The silver glue contacts work well in the used temperature range 30−280 K. Other contacts inside the cryostat and on the ceramic were soldered. The wires for all connections are copper wires with a varnish isolation. The wire from the back contact has an additional plastic isolation surrounded by a braided copper shield (low noise coaxial cable). Around the braided copper shield the wire from the front contact is winded. The braided copper shield is connected to common ground as all metal parts of the cryostat. The outer conductors (shielding) of the coaxial cables which are used for the connection outside the cryostat are also connected to common ground. The low bias potential of the voltage source is set to the potential of common ground.

Optical illumination

The commercial IR emitter Model OD-50L is an infrared LED with a high power output [Opt00]. The peak emission wavelength is 880 nm and the spectral bandwidth at 50% is 80 nm. The infrared light emitting diode is enclosed in a TO-39 hermetic package which was mounted on the radiation shield inside the cryostat. The forward current through the LED was 500 mA at room temperature. An one transistor switch was used to pulse the

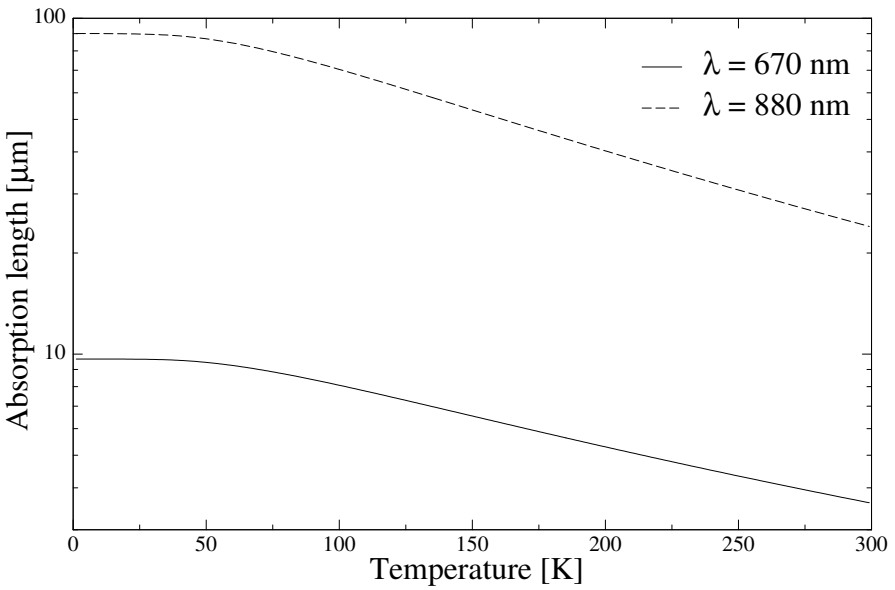

Figure 4.15: *The absorption length of 670 nm and 880 nm monochromatic light in crystalline silicon is shown* [Bue94].

LED with the TTL-like signal from the driver of the DLTS system. The rise and fall time of the LED is 0.7 μs. The LED operated in the employed temperature range 30−280 K. The distance of the LED above the sample was about 4 cm to assure an illumination of the whole sample area 7x7 mm^2. The photo current through the reverse biased sample at room temperature was in the range from 1 to 2 mA. The photo current slightly increases with decreasing temperature.

A 670 nm laser diode mounted outside the cryostat was employed for front side illumination. The driver of the DLTS system is employed to pulse the laser diode. The photo current through the reverse biased sample at room temperature was in the range from 0.60 to 0.75 mA. The photo current at T=85 K was between 0.40 and 0.45 mA.

The dependence of the absorption length of monochromatic light in crystalline silicon on the temperature is shown in figure 4.15. A semiempirical description of the absorption coefficient is used [Bue94].

Chapter 5

Macroscopic studies

The measured macroscopic parameters of silicon detectors are the leakage current and the full depletion voltage. Both parameters are changed after irradiation with high energy particles. Macroscopic results have shown that an oxygen enrichment of standard FZ increases the radiation tolerance of silicon detectors after charged particle irradiations [Ruz99a]. The results presented in this chapter are collected from the working groups of the ROSE collaboration. Mainly the results of the groups in Hamburg and CERN are presented [Mol99, Lin00].

5.1 Volume generation current

The volume generation current of an irradiated diode is proportional to the particle fluence. The proportional constant or the current related damage rate is independent on the material type, but depends on the particle type. The annealing of the current related damage rate at different temperatures is shown in figure 5.1. The current related damage rate is $\alpha_{80/60} = 4.01 \cdot 10^{-17}$ A/cm after a tempering of 80 min at 60°C and $\alpha_{4/80} = 4.56 \cdot 10^{-17}$ A/cm after a tempering of 4 min at 80°C.

The volume generation current already dominates the reverse current after particle irradiations with small fluences used for the DLTS studies. For high energy particle irradiations the NIEL hypothesis is valid and the measured leakage current can be employed to determine the equivalent fluence. For further details see chapter 3.2.3.

5.2 Effective doping concentration

The change in the full depletion voltage results from a decrease of the effective space charge density $q \cdot N_{eff}$ due to radiation induced defects. For n-type silicon the initial effective space charge density is positive. The change of the effective doping concentration with the fluence as its annealing behaviour is

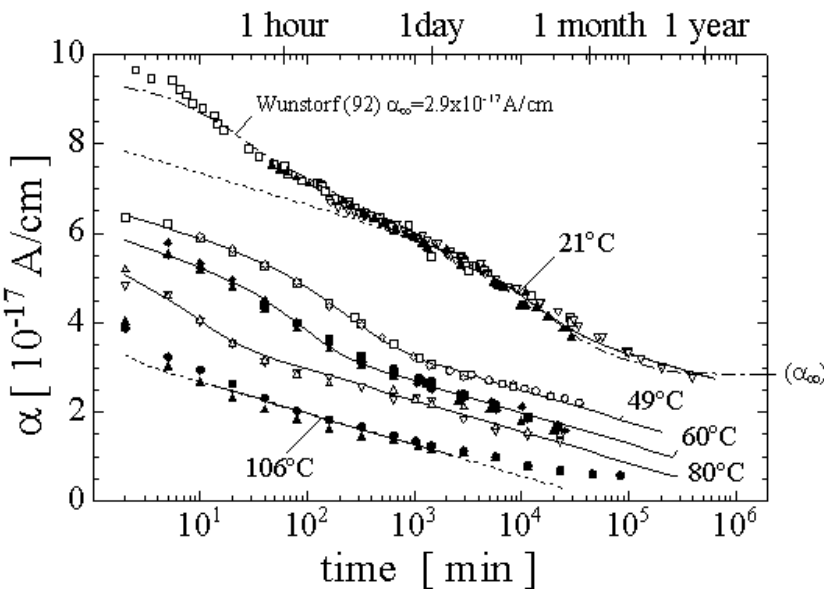

Figure 5.1: *The annealing of the current related damage rate at different temperatures after neutron irradiation is shown* [Mol99].

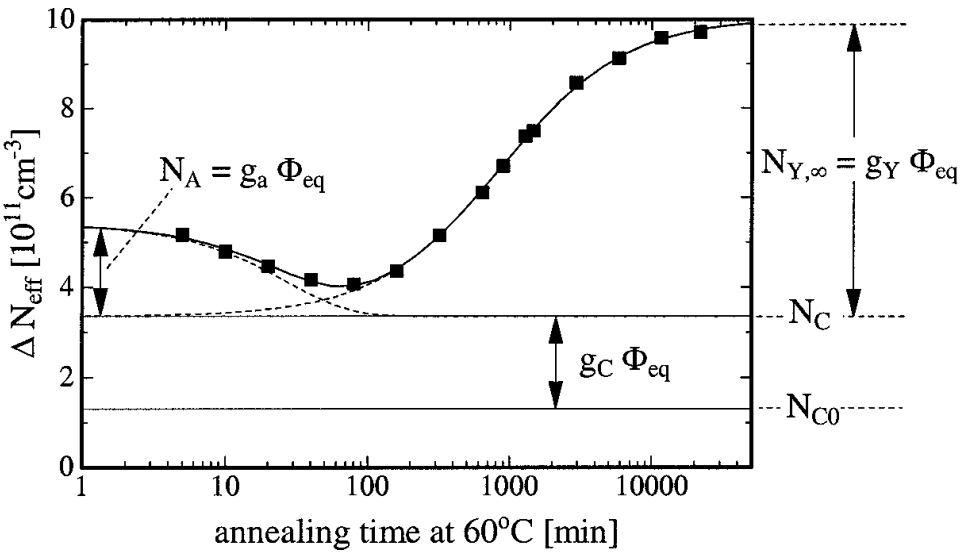

Figure 5.2: *The annealing of ΔN_{eff} at 60°C after neutron irradiation is shown. The three different components are used to describe the radiation damage: beneficial annealing, stable damage and reverse annealing* [Mol99].

described by three components

$$\begin{aligned} \Delta N_{eff}(\Phi_{eq}, t) &= N_{eff,0} - N_{eff}(\Phi_{eq}, t) \\ &= N_A(\Phi_{eq}, t) + N_C(\Phi_{eq}) + N_Y(\Phi_{eq}, t) \end{aligned} \tag{5.1}$$

where $N_{eff,0}$ is the initial doping concentration. Two of three components are time dependent. The annealing behaviour of ΔN_{eff} is shown in figure 5.2.

The component which anneals out in a short time is named beneficial annealing, because ΔN_{eff} decreases. The underlying reaction kinetic is given by exponential decays with different time constants

$$N_A(t) = \sum_i N_{a,i} \exp\left(-\frac{t}{\tau_{a,i}}\right) \tag{5.2}$$

The time constants $\tau_{a,i}$ are temperature dependent. The amplitudes of the beneficial annealing $N_{a,i}$ scale linear with the fluence for neutron irradiation. The introduction rate and the time constant of the beneficial annealing at 60°C are independent on the material type after neutron irradiation.

The component with a long term annealing behaviour is named reverse annealing, because ΔN_{eff} increases. The reverse annealing process is described well by a second order reaction kinetic

$$N_Y(t) = N_{Y,\infty}\left(1 - \frac{1}{1 + t/\tau_y}\right) \tag{5.3}$$

But the time constant τ_y shows no fluence dependence as expected for a 2^{nd} order process. The time constant is temperature dependent. The time constant shows fluctuations not correlated with the oxygen concentration for neutron irradiation. But for 23 GeV proton irradiation the time constant is larger in oxygen enriched silicon than in standard silicon. The amplitude of the reverse annealing scales linear with the fluence for neutron irradiation. The introduction rate of the reverse annealing is by a factor two smaller in CZ silicon with an oxygen concentration $[O] = 9 \cdot 10^{17}\text{cm}^{-3}$ in comparison to other materials with $[O] < 2 \cdot 10^{17}\text{cm}^{-3}$ after neutron irradiation. A dependence on the oxygen concentration is already seen after 23 GeV proton irradiation in silicon materials with $[O] < 2 \cdot 10^{17}\text{cm}^{-3}$. The amplitude of the reverse annealing in 23 GeV proton irradiated diffusion oxygenated (DO)FZ samples is reduced at high fluences in comparison to standard FZ. The fluence dependence of the amplitude of the reverse annealing after irradiation with 23 GeV protons is shown in figure 5.3.

The third component depends only on the fluence and exhibit no annealing

$$N_C = N_{C0}\left[1 - \exp(-c \cdot \Phi_{eq})\right] + g_c \cdot \Phi_{eq} \tag{5.4}$$

This component is called stable damage. The first term describes the so called donor removal and the second term the creation of acceptor like defects

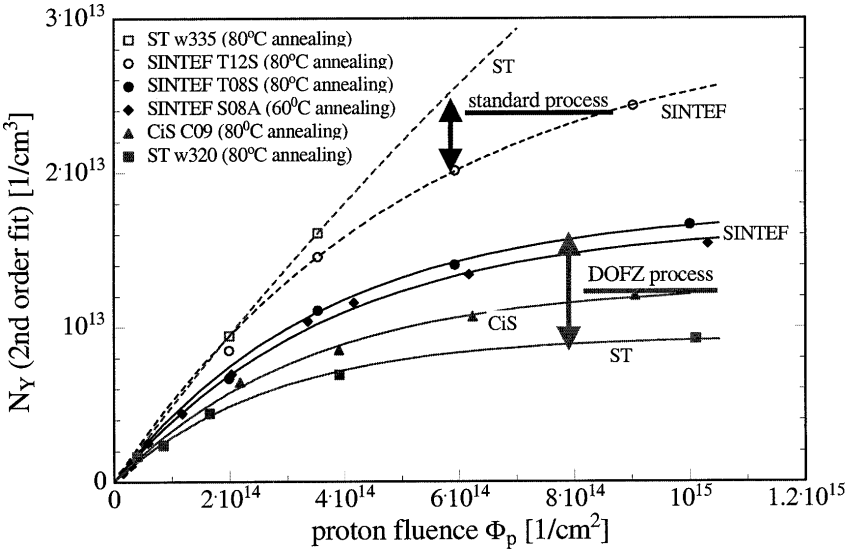

Figure 5.3: *The fluence dependence of the amplitude of the reverse annealing after 23 GeV proton irradiation is shown* [Lin00].

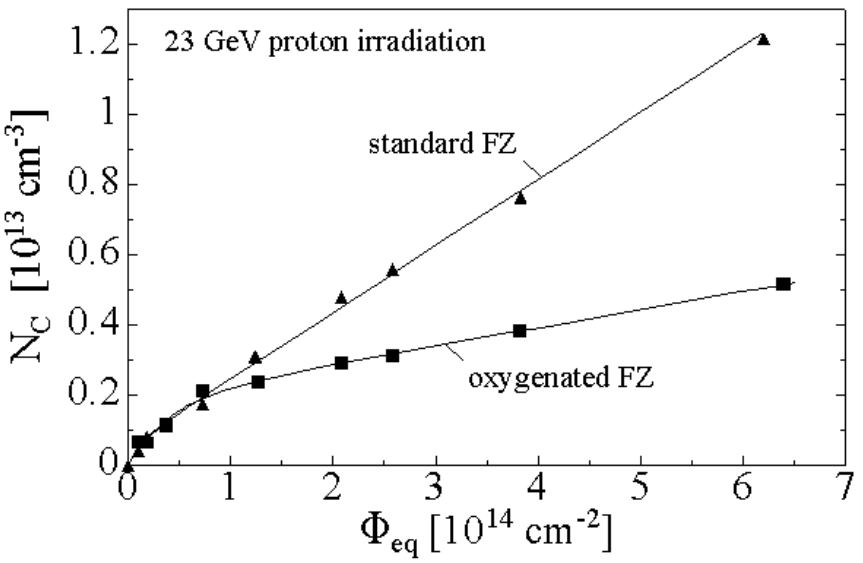

Figure 5.4: *The fluence dependence of the stable damage after 23 GeV proton irradiation is shown* [Mol99].

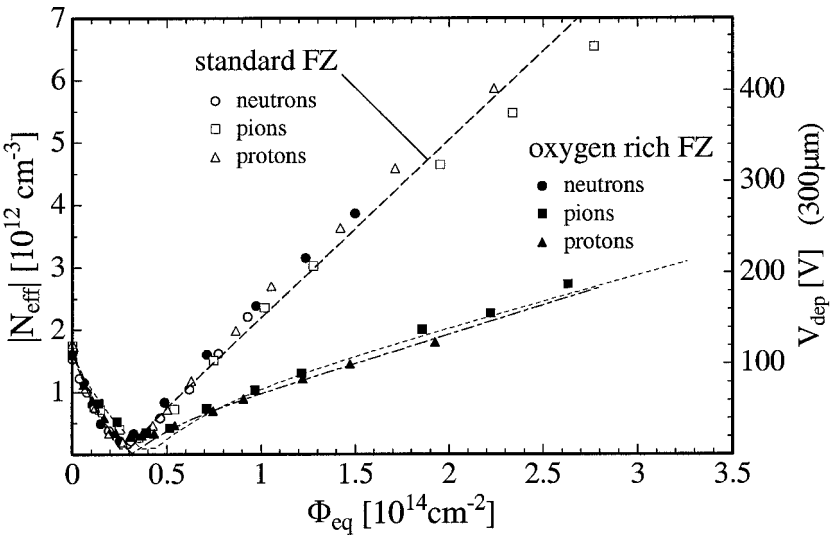

Figure 5.5: *Results of the radiation scenarios employed to characterize the radiation tolerance of different materials are shown. The change of the effective space charge density of standard and oxygen enriched FZ samples irradiated with reactor neutrons, 23 GeV protons and 192 MeV pions are shown* [Ros00].

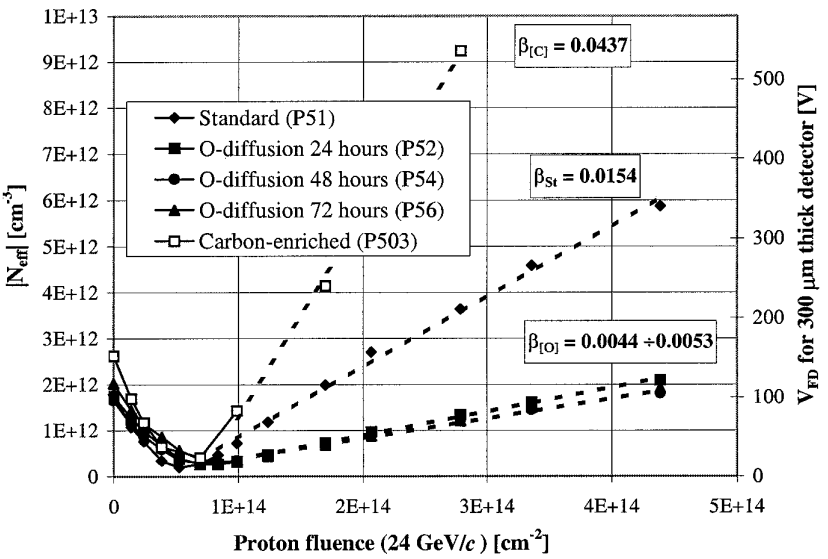

Figure 5.6: *Results of the radiation scenarios employed to characterize the radiation tolerance of different materials are shown. The change of the effective space charge density of standard, oxygen and carbon enriched FZ samples irradiated with 23 GeV protons are shown* [Ros00].

(a)

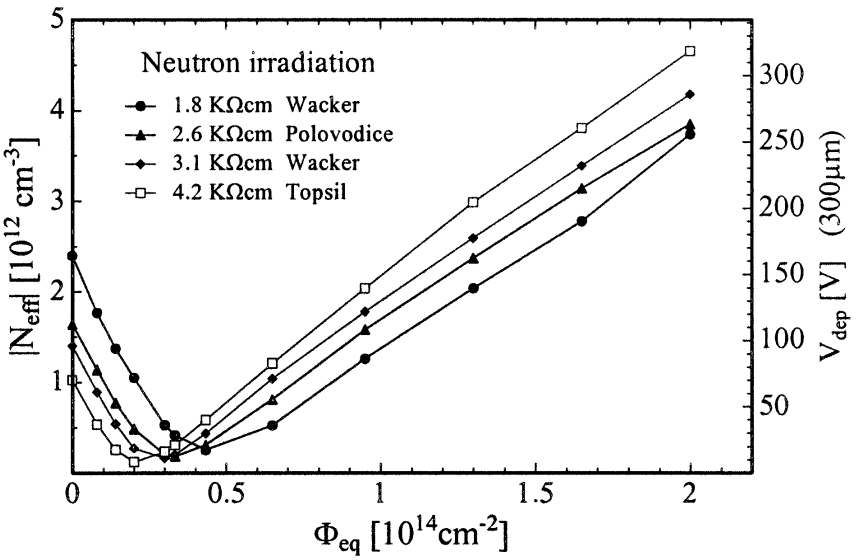

(b)

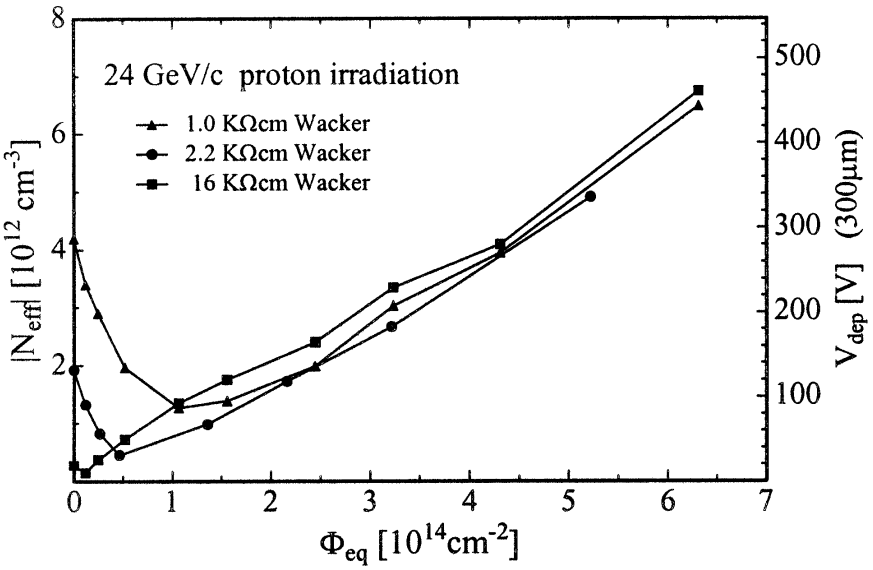

Figure 5.7: *Results of the radiation scenarios employed to characterize the radiation tolerance of different materials are shown. Oxygen enriched FZ samples with different resistivities were irradiated. The change of the effective space charge density of (a) samples irradiated with reactor neutrons and (b) of samples irradiated with 23 GeV protons are shown* [Ros00].

with the introduction rate g_c. The ratio $N_{C0}/N_{eff,0}$ depends on the particle and material type. In neutron irradiated CZ silicon $N_{C0}/N_{eff,0} \approx 0.10$ is by a factor $5-9$ smaller in comparison to other materials with an oxygen concentration $[O] < 2 \cdot 10^{17}\text{cm}^{-3}$. The donor removal is incomplete after neutron irradiation. The donor removal is always complete after 23 GeV proton irradiation. The introduction rate of the stable acceptor damage g_c is about the same in neutron and 23 GeV proton irradiated standard FZ samples. The fluence dependence of the stable damage after irradiation with 23 GeV protons is shown in figure 5.4. In oxygen enriched FZ samples the introduction rate of the stable acceptor damage is reduced by a factor 4 after 23 GeV proton irradiation, but not after neutron irradiation.

A radiation scenario is often used to characterize the radiation tolerance of different materials. Samples of various materials are irradiated in steps and tempered for 4 min at 80°C after each irradiation step. The heat treatment accomplishes the benifical annealing of the radiation damage. The initial part of the radiation scenario is determined mainly by the donor removal and the final part at high fluences is determined by the stable acceptor damage and the damage due the reverse annealing. The reverse annealing may be suppressed in oxygen rich silicon. The slope $\beta = \Delta N_{eff}/\Phi_{eq}$ of the final part is used as a parameter to characterize the radiation hardness of the silicon material. The benifical effect of oxygen after charged particle irradiation is shown in figure 5.5. The detrimental effect of carbon after charged particle irradiation is shown in figure 5.6. The final part of the curves at high fluences indicates the benifical effect of oxygen and detrimental effect of carbon. Neutron irradiated samples of carbon enriched FZ do not show this detrimental effect. The β values of various silicon materials are listed in [Ruz99b]. Radiation scenarios with 16, 21 and 27 MeV protons show that the mean value of β is reduced only by 35% in jet oxygenated FZ in comparison to standard FZ [Bis00, Wys00]. Thus the decrease in the final slope is less pronounced in comparison to 23 GeV proton irradiation. However, the β value in both standard and jet oxygenated FZ samples depends on the kinetic energy for 16, 21 and 27 MeV proton irradiations.

The effect of incomplete and complete donor removal after reactor neutron and 23 GeV proton irradiation is shown in figure 5.7. The initial part of the curves is described mainly by the donor removal. The shifting of the curves indicates that only a fraction of the initial donor concentration is removed after neutron irradiation. The final part of the curves can be linear extrapolated. The intersection at $\Phi_{eq} = 0$ is equal to $N_{eff,0} - N_{C0}$. Oxygen enriched silicon is employed to reduce the fluctuations in the slope of the curves at high fluences.

Chapter 6

Microscopic studies

The microscopic properties of radiation induced defects in crystalline silicon are relevant to understand the macroscopic damage effects in silicon detectors. Not only the electrical properties which determine the charge states of the defects in the space charge region of a fully depleted detector are needed, but also a detailed understanding of the defect formation and annealing. The DLTS study in this chapter indicates that both isolated point defects and clusters of defects are formed after particle irradiation. The annealing of the various radiation induced defects after particle irradiation supplies further information about the radiation damage and its influence on the macroscopic properties. But it is difficult to understand the microscopic properties of clustered defects and their influence on the macroscopic properties. The influence of isolated point defects on macroscopic properties are much better understood. The impurities oxygen and carbon influence the defect kinetic of the isolated point defects. Thus defect engineering is possible. The results are useful to understand the improvement of radiation tolerance of silicon detectors due to oxygen enrichment.

6.1 Process induced defects

Not only during particle irradiation defects are induced into the silicon material, also during processing of the wafers defects are induced. The defect states are caused either by metal impurities which are diffused into the silicon crystal during a high temperature step [Gra95] or by the residual damage of an ion implantation processing step [Ben97]. Also process induced defects are thermal donors which are multi oxygen complexes or Si_yO_x clusters [Shi94]. DLTS studies show that the concentration of processed induced defects is sometimes in the order of the radiation induced defects. The quality of the processing line can change with time and is not the same for different manufacturers. The DLTS signals are labeled with the letters E and H to distinguish between electron or hole emission from a defect center. It should be mentioned that not all investigated materials are listed in table 4.1.

The carbon enriched FZ 1.5kΩcm (Polo II) is processed by ITE. The DLTS spectra are shown in figure 6.1a. One defect state in the upper half of the band gap and two in the lower half of the band gap are detected. Two different filling methods are used to fill the defects with holes: Applying a forward bias to the junction or illuminating the back side of the sample with an infrared LED. The ratio of the free charge carrier concentrations is $n/p \approx 1$ for the case of forward injection and $n/p \ll 1$ for the case of back side illumination. Thus defect centers with $\sigma_n/\sigma_p \gg 1$ are not filled with holes during forward injection. The defect centers H1 and H2 are filled during back side illumination. The FZ 2.8kΩcm (Polo I) is oxygenated and processed by ITE. The high temperature oxygen diffusion is performed for 24h, 48h and 72h at 1200°C in a nitrogen atmosphere. The DLTS spectra are shown in figure 6.1b. The concentrations of the two defects H1 and H2 in the lower half of the band gap are not correlated with the time of the oxygen diffusion. A deep profile measurement shows that the defect centers H1 and H2 are located near the p^+ region. The spatial extension is about 50 μm. The defect center E1 is also found, but the concentration is very small. In the oxygen lean FZ 4kΩcm (Wacker II) processed by ITE more defect states are detected. The DLTS spectrum of electron emission is shown in figure 6.1c. A possible explanation is that interstitial oxygen acts as a getter site for metal impurities [Shi94]. The not gettered metal impurities are detected with the DLTS method and the gettered metal impurities are not detected.

The FZ 2kΩcm (Wacker IVa & Vb) oxygenated and processed by SINTEF have nearly no process induced defects. The high temperature oxygen diffusion is performed for 72h at 1150°C in a nitrogen and oxygen atmosphere. The DLTS spectra are shown in figure 6.1d. Only a broad signal is detected. The filling with holes is furnished by back side illumination. Nearly no difference is seen between both oxygenation processes.

The FZ 1kΩcm oxygenated and processed by ST Microelectronics has nearly no process induced defects. The high temperature oxygen diffusion is performed for 60h at 1200°C in a nitrogen atmosphere. The DLTS spectra are shown in figure 6.1e. The filling with holes is furnished by back side illumination. The signal at T=50 K is associated with the electron emission from shallow thermal donor states. The thermal donors are generated due to wrong quenching or cooling from a high temperature step in oxygen rich silicon [Mol99].

The FZ 4kΩcm (Wacker VIII) processed by CiS has one process induced defect H2 in the lower half of the band gap. The material is not oxygen enriched. The DLTS spectra are shown in figure 6.1f. The filling with holes is furnished by back side illumination.

The FZ 1.5kΩcm oxygenated by BNL and processed by CiS (Topsil IIg) has one process induced defect in the lower half of the band gap H2. The defect is also present in other materials processed by CiS. But also defect states in the upper half of the band gap are detected. The high temperature oxygen diffusion is performed for 144h at 1200°C in a nitrogen atmosphere.

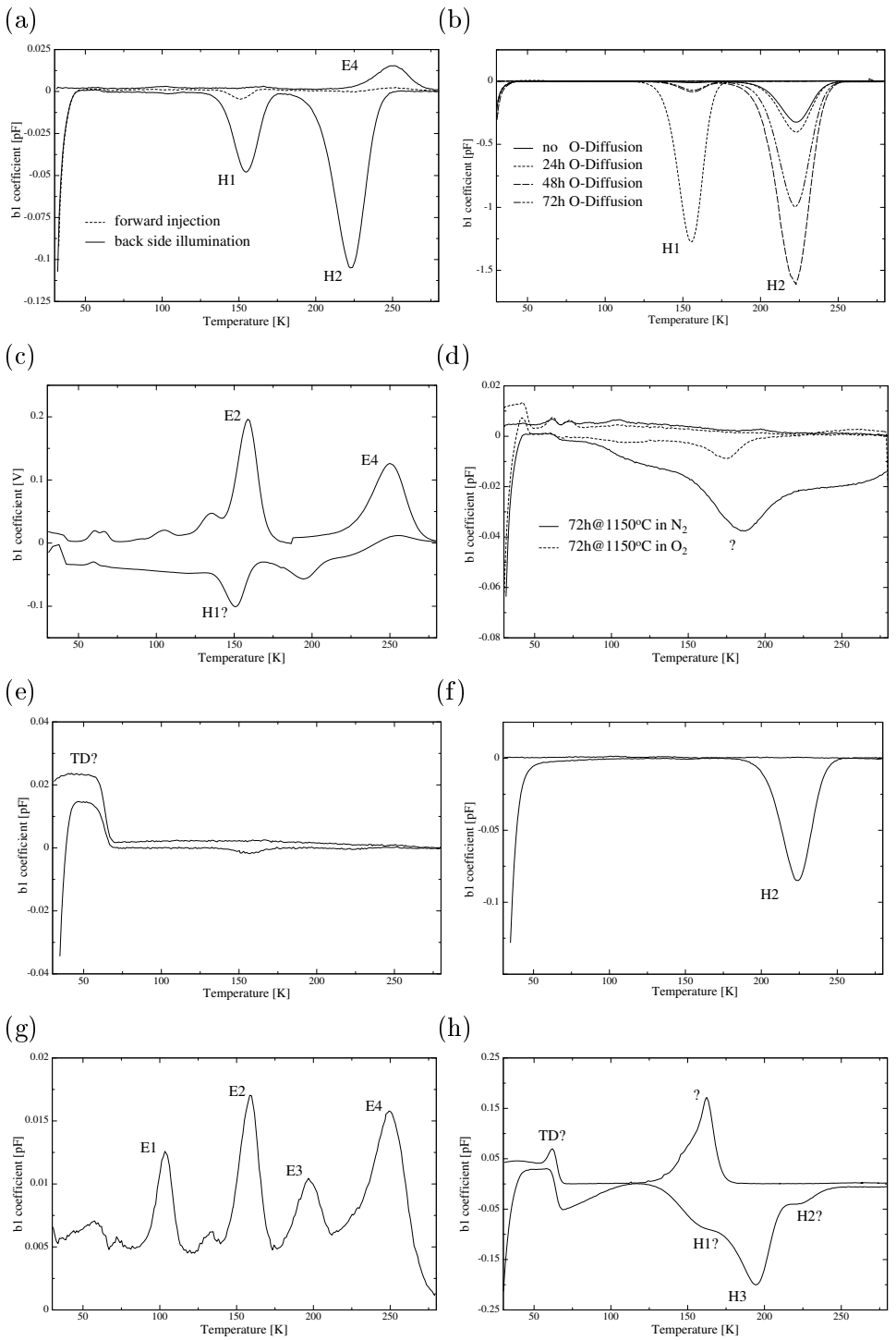

Figure 6.1: *The DLTS spectra of unirradiated samples oxygenated and processed by different manufacturers are shown: (a-c) ITE, (d) SINTEF, (e) ST Microelectronics, (f) CiS, (g) BNL/CiS and (h) BNL/ITE. For further details see text.*

Table 6.1: *The activation energies and cross sections of the process induced defects, a possible identification and the processor are listed.*

Defect	E_T [eV]	σ_T [10^{-15} cm^2]	Identification	Processor
E1	0.20	≈ 1	–	BNL
E2	0.36	≈ 30	–	ITE,BNL
E3	0.44	≈ 15	–	BNL
E4	0.56	≈ 9	Au_s	ITE,BNL
H1	0.32	≈ 4	Cr_iAu_s	ITE
H2	0.47	≈ 3	Cr_iAl_s	ITE,CiS
H3	0.42	≈ 5	–	BNL

The DLTS spectrum of electron emission is shown in figure 6.1g. Because of the low concentrations a determination of the defect parameters was only possible for four defect states and the error in the cross sections is large. The defects are suggested to be caused by metal impurities introduced during the high temperature oxygenation. Another FZ 1kΩcm material is oxygenated by BNL and processed by ITE. The high temperature oxygen diffusion is performed for 216h at 1200°C in a oxygen atmosphere. The DLTS spectra are shown in figure 6.1h. The determination of the emission parameters is done only for the defect state H3. The filling with holes is furnished by back side illumination.

The activation energies and cross sections of the various process induced defects and a possible identification are listed in table 6.1. The factors to calculate the cross sections employing the effective masses compiled in [Gre90] are listed in the appendix A. The defect state H1 is identified with the complex Cr_iAu_s and the defect state H2 with the complex Cr_iAl_s. The defect state E1 is identified with substitutional gold Au_s [Gra95]. The metal impurities introduced during the ITE process are assumed to be chromium, aluminium and gold. The metal impurities introduced during the CiS process are assumed to be chromium and aluminium.

6.2 Introduction rates of radiation induced defects

In this section the introduction rates of radiation induced defects are compiled. The DLTS method is employed to determine the concentrations of the radiation induced defects. The DLTS spectrum of a neutron irradiated sample of FZ 120Ωcm (ITME I) is shown in figure 6.2. The chemical symbols of the various radiation induced defects are assigned to the DLTS peaks. Because the DLTS spectrum of electron emission is shown, only the defect states in the upper half of the band gap are seen. During isothermal tempering the concentration of the radiation induced defects increases or decreases, referred as annealing. The concentration of C_i decreases. The

concentration of the defects VO_i and C_iC_s increases. The DLTS signals of both defects coincide. The electron emission of C_iC_s in the configuration A is detected. The concentration of the divacancy in the single negative charge state VV^- decreases, but the concentration of the divacancy in the double negative charge $VV^=$ increases. Some unknown defects contribute to the DLTS signal $VV^{-/0}$+?. The defect C_iO_i has an energy state in the lower half of the band gap and is not seen. Also the defect C_i has a second energy state in the lower half of the band gap. The emission parameters of the radiation induced defects are listed in table B.1. The introduction rates of the various radiation induced defects are calculated from the defect concentration and equivalent fluence. The determination of the equivalent fluence is described in chapter 4.2. The introduction rates depend on particle and material type. Also the time constant of the annealing of C_i depends on the oxygen and carbon concentrations.

The irradiated samples were tempered to avoid any errors in the defect concentrations due to different annealing stages after irradiation. The samples irradiated with particles were heated for 80 min at 60°C with the exception of the 7-10 MeV proton irradiated samples which were heated for 4 min at 80°C. Sometimes an additional storage at room temperature was needed to finish the annealing of C_i. The ^{60}Co γ-photon irradiated samples were stored for a few month at room temperature to reduce the oxide damage.

6.2.1 Particle and material dependence

The samples of the jet oxygenated FZ 800/1.2kΩcm (ITME II & III) were irradiated with neutrons, protons and pions. The DLTS spectra of the electron and hole emission from the defect centers are shown in figure 6.3. The symbols of the radiation induced defects are assigned to the peaks in the DLTS spectra. The annealing of C_i is already finished in the oxygen rich silicon material. The introduction rates of the defects VO_i + C_iC_s and C_iO_i depend on the particle type and are higher for charged particle irradiations, as shown in figure 6.4. Also a dependence on the proton energy is seen. The introduction rate of the $VV^{-/0}$+? is nearly independent on the particle type. The introduction rate of $VV^{=/-}$ depends on the particle

Table 6.2: *Introduction rates of radiation induced defects for different particles in jet-oxygenated FZ 800/1.2kΩcm samples are listed.*

Particle type	g(VO_i) [cm^{-1}]	g(C_iC_s) [cm^{-1}]	g(C_iO_i) [cm^{-1}]	g($VV^{-/0}$+?) [cm^{-1}]	Σ g_{point} [cm^{-1}]
p^+ 27 MeV	1.36	0.43	2.34	1.26	4.13
p^+ 23 GeV	0.82	0.53	1.95	1.35	3.30
π^+ 192 MeV	0.67	0.67	1.83	1.30	3.17
n Be(d,n)	≈0.10	≈0.72	1.14	1.38	1.96

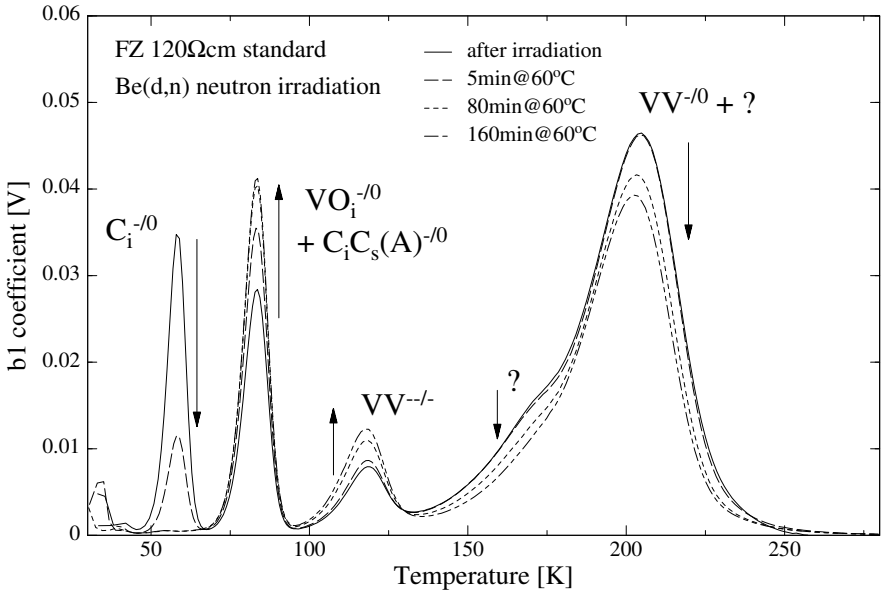

Figure 6.2: *DLTS spectra of a FZ 120Ωcm sample irradiated with Be(d,n) neutrons is shown. The annealing of the various defects in the upper half of the band gap is shown.*

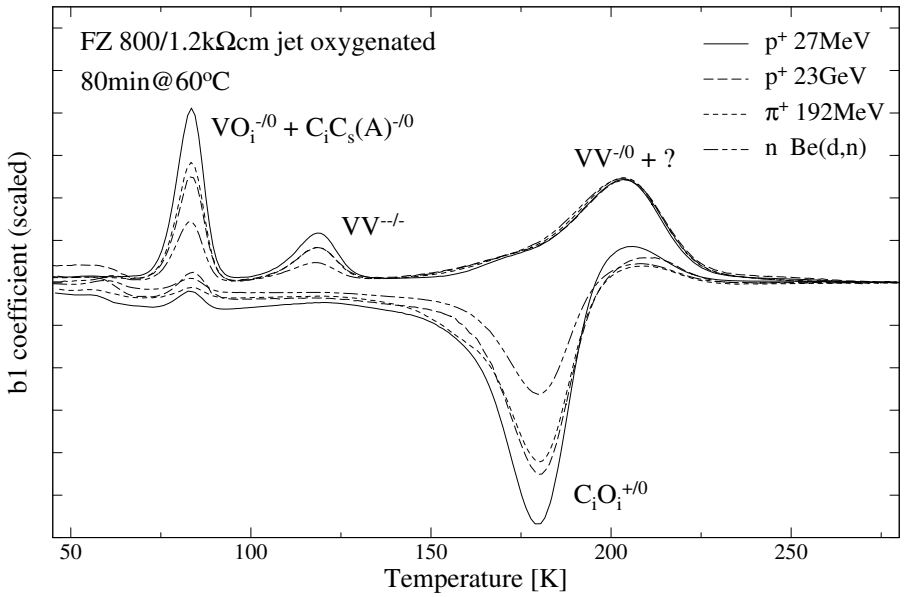

Figure 6.3: *DLTS spectra of jet-oxygenated FZ 800/1.2kΩcm samples irradiated with different particles are shown. The DLTS signals are scaled to have a coincidence of the signals $VV^{-/0}$+?.*

type. The introduction rates of radiation induced defects are summarized in table 6.2 and also the sum of the introduction rates of the defects VO_i, C_iC_s and C_iO_i is calculated, named $\Sigma\ g_{point}$. A capture measurement was used to separate the defects VO_i and C_iC_s. This method works only well for low energetic particle irradiations. An optical capture measurement on an Be(d,n) neutron irradiated sample is used to estimate the introduction rate g(VO_i) < 0.20 cm^{-1}. For further details see chapter 6.3.

The impurity defects VO_i, C_iC_s and C_iO_i are isolated point defects in the crystal lattice, because their emission parameter are not changed. The higher introduction rates of point defects for charged particle irradiations can be explained with the enhancement of the small energy transfer to PKAs due to coulomb scattering. PKAs with an energy of few times the threshold energy to displace a silicon atom produce only single displacements. PKAs with an higher energy create terminal clusters and collision cascade regions with terminal clusters. For further details see chapter 3.1.2.

The introduction rate of g($VV^{-/0}$+?) is particle independent. This suggests that the divacancies are mainly located in the terminal clusters which are generated at the end of a displacement track of an recoiled silicon atom. The main portion of the PKA energy goes into the terminal cluster generation. Because for the high energy particle irradiation the volume generation current is employed to determine the equivalent fluence, it is assumed that the damage in the terminal clusters is responsible for current generation. The particle independence of the shape of the DLTS signal $VV^{-/0}$+? also supports this assumption, because the independence suggests that the radiation damage in the terminal clusters and at their peripheries is identical. The ratio of the concentrations of two charge states of the divacancy $[VV^{=/-}]/[VV^{-/0}+?]$ depends on the particle type and energy, as shown in figure 6.5. This ratio is smaller for neutron irradiation than for charged particle irradiations. It is assumed that the electronic band structure in the terminal cluster regions is bent. Therefore at low temperatures only a fraction of the divacancies in the terminal clusters is occupied with two electrons. The properties of the divacancy in particle irradiated samples is discussed in more detail in chapter 6.4.5.

The samples of the FZ 2kΩcm (Wacker IX) were irradiated with 7-10 MeV protons. The displacement damage cross sections were calculated taking into account only Rutherford scattering. For further details see chapter 3.2. Also the dependence of the proton energy on the penetration depth is taken into account. The dependence of the projected range on the proton energy is used to calculate the dependence of the proton energy on the penetration depth [PRD98]. The thickness of the silicon layer in which the displacement damage occurs is set equal to the width of the space charge region W $\approx$ 70 μm. The hardness factors for the 7-10 MeV protons and the χ^2 value for $\overline{g(VV^{-/0}+?)} = 1.48$ are calculated for various threshold energies. The results are shown in figure 6.6. The introduction rate g($VV^{-/0}$+?) is by a factor $\alpha_{4/80}/\alpha_{80/60} = 1.14$ higher due to the different fractions of annealed

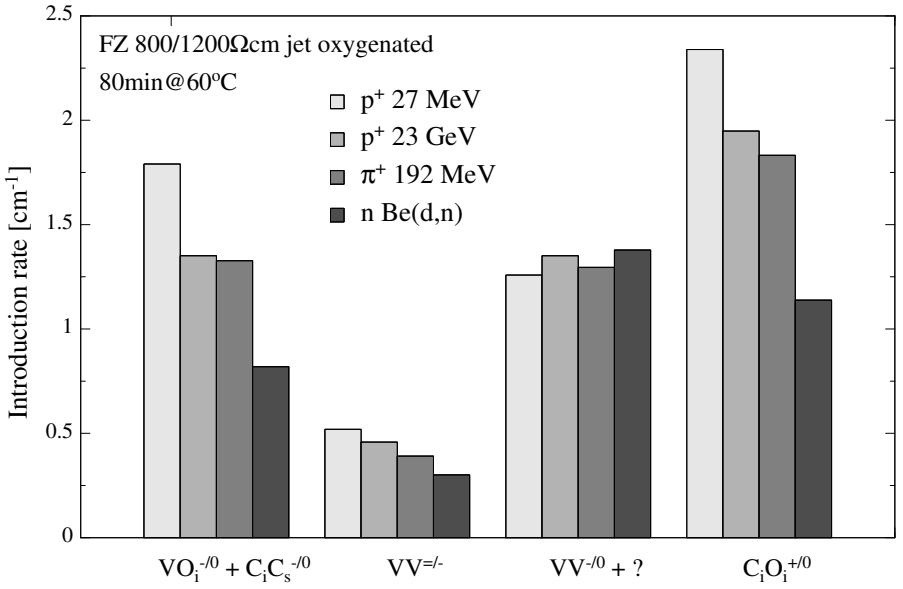

Figure 6.4: *The introduction rates of radiation induced defects in jet-oxygenated FZ 800/1.2kΩcm samples irradiated with different particles are shown.*

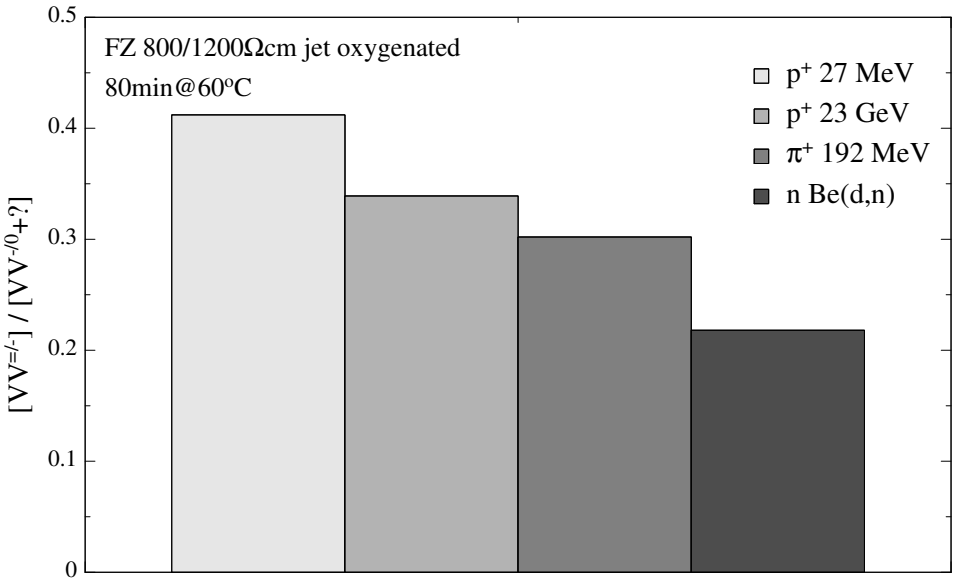

Figure 6.5: *The ratio of the defect concentrations of the two charge states of the divacancy in jet-oxygenated FZ 800/1.2kΩcm samples irradiated with different particles are shown.*

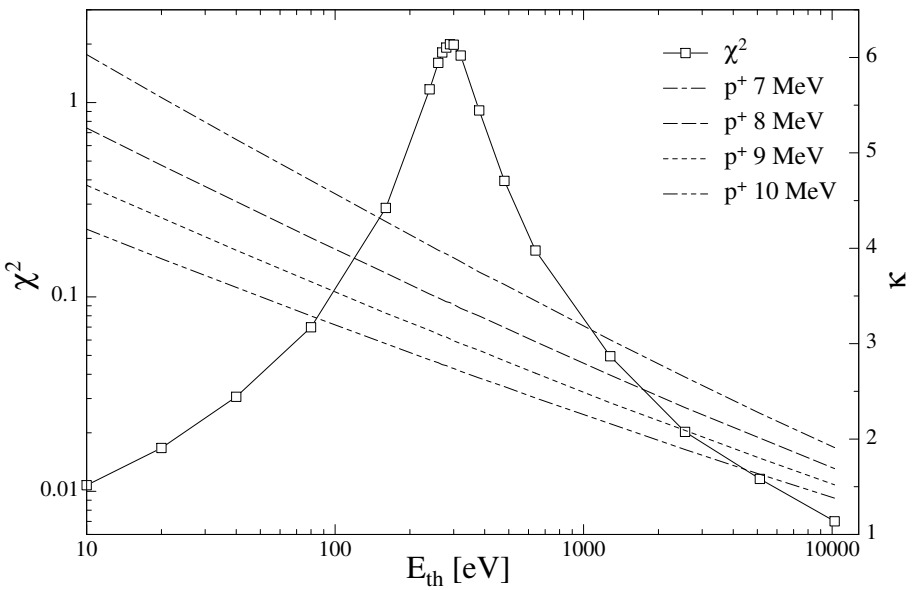

Figure 6.6: *The dependence of the χ^2 value and the hardness factors κ on the threshold energy for cluster generation E_{th} is shown.*

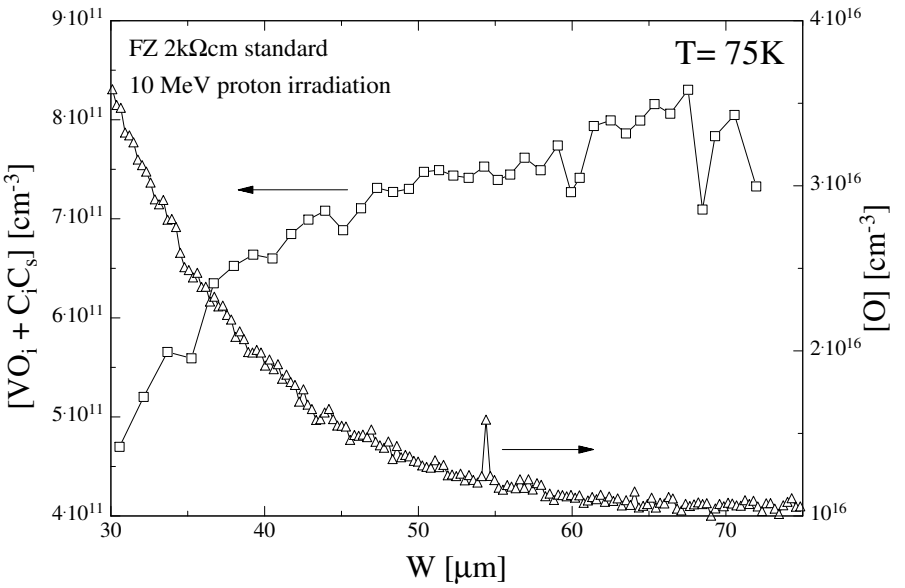

Figure 6.7: *The concentration profiles of $[VO_i + C_iC_s]$ and $[O]$ near the surface in the sample of FZ 2kΩcm irradiated with 10 MeV protons are shown.*

divacancies after a heat treatment for 4 min at 80°C and a heat treatment for 80 min at 60°C. The error in the defect concentrations due to the inhomogeneous defect distribution is neglected. The threshold energy $E_{th} \approx 300$ eV obtained from the maximum value of χ^2 is proposed to be the energy at which a recoiled silicon atom starts to create a terminal cluster. The corresponding κ values are listed in table F.2. The introduction rates are listed in table 6.3.

In the tables 6.2 and 6.3 the sum of the introduction rates of the point defects $\Sigma\ g_{point}$ for various particles and energies are listed. As discussed previously more isolated displacements occurs during low energy proton irradiations. However, the ratio shows nearly no dependence on the energy for the 7-10 MeV protons. A comparison of the introduction rates of the various point defects is not possible, because the oxygen and carbon content of both materials is different. The concentration of the defects $VO_i + C_iC_s$ decreases with increasing oxygen concentration. The concentration profile of $VO_i + C_iC_s$ near the surface in the 10 MeV proton irradiated sample of FZ 2kΩcm (Wacker IX) together with oxygen concentration profile is shown in figure 6.7. The oxygen concentration profile is obtained from a SIMS measurement of a sample from the same wafer. The carbon concentration is below the detection limit, but SIMS measurements of other samples suggest that the carbon concentration is homogeneous near the surface. The material dependence is discussed in more detail in the following paragraphs.

In figure 6.8 the material dependence after Be(d,n) neutron irradiation is shown. The results from the samples of FZ 400Ωcm (Wacker I), FZ 120Ωcm (ITME I), jet oxygenated FZ 800Ωcm (ITME II) and CZ 100Ωcm (Polo III) are shown. Only the sample of FZ 120Ωcm have a higher introduction rate of the defects $VO_i + C_iC_s$.

The material dependence after 23 GeV proton and 192 MeV pion irradiation is shown in figure 6.9. The results from the samples of jet oxygenated FZ 800Ωcm (ITME II), FZ 400Ωcm (Wacker I), 120Ωcm (ITME I) and carbon enriched FZ 1.5kΩcm (Polo II) are shown. The introduction rate of the impurity defects $VO_i + C_iC_s$ is suppressed and the introduction rate of the defect C_iO_i is enhanced in jet oxygenated FZ 800Ωcm, while in carbon enriched FZ 1.5kΩcm the generation of the impurity defects $VO_i + C_iC_s$ is enhanced and generation of the defect C_iO_i is suppressed. Again the sum of the introduction rates of the defects $VO_i + C_iC_s$ is higher in the sample of FZ 120Ωcm, but the generation of C_iO_i is not suppressed. The samples of FZ 400Ωcm were irradiated with both types of particles and the introduction rates are the same, hence it is assumed that 23 GeV protons and 192 MeV pions generate the identical damage in the crystal lattice.

The material dependence is explained with sharing of mobile interstitial carbon atoms at O_i and C_s sites. However, the introduction rate of the defect C_iO_i in the sample of FZ 120Ωcm is conflicting. It should be lower, but the listed impurity concentrations in table 4.2 exclude further conclusions and perhaps are not correct and complete. The introduction rate g($VV^{-/0}$+?)

is independent on the material type. This confirms the assumption that the divacancies are created mainly in the terminal clusters with dimensions less than $\sqrt[3]{1/N_{Imp}} = 100$ Å for $N_{Imp} = 10^{18}$ cm^{-3}.

The same result is also observed after irradiation with reactor neutrons in jet oxygenated FZ 800/1.2kΩcm (ITME II&III) and carbon enriched FZ 1.5kΩcm (Polo II). However, the introduction rate g($VV^{-/0}$+?) ≈ 1.00 cm^{-1} is too small in comparison to other particles.

The results from the various standard FZ materials which are oxygenated and processed by different manufacturers are listed in table 6.4. The oxygen enrichment was done by high temperature diffusion (DOFZ). The samples were irradiated with 23 GeV protons. The results from the samples of FZ 2kΩcm (Wacker IVa & Vb) and FZ 4kΩcm (Topsil Ia & Ib) oxygenated and processed by SINTEF are listed in the first block. The results from the samples of FZ 2kΩcm (Wacker VIIc, VIc, VIId & VId) oxygenated and processed by ST Microelectronics are listed in the second block. The results from the samples of FZ 4kΩcm (Wacker VIII, VIIIe & VIIIf) and of FZ 1.5kΩcm (Topsil IIg) oxygenated and processed by Cis and BNL/CiS are listed in the third block. The sample with the lowest oxygen concentration was processed on not oxygenated FZ 4kΩcm. The annealing of C_i was accomplished during an additional storage at room temperature for 7 days. All other materials are oxygenated and the annealing of C_i is finished after a tempering for 80 min at 60°C.

The sum of the introduction rates of point defects of the four samples in each block depends not on the oxygen and carbon concentrations. These defects are generated by mobile carbon interstitials and vacancies. Thus the introduction rate of the defects C_i and V depends mainly on the particle type and not on the impurity content.

The sum of the introduction rates of the point defects, the introduction rate of the cluster defects and the ratio between both for the different particles are listed in table 6.5. The listed introduction rates correspond to an annealing state reached after 80 min tempering at 60°C. The sum of the introduction rates of point defects is particle dependent. The introduction rate g($VV^{-/0}$+?) is particle independent with exception for the reactor neutrons. However, the ratios for the two neutron irradiations are equal.

6.2.2 ^{60}Co γ-photon irradiation

The samples of oxygen lean FZ 4kΩcm (Wacker II), FZ 10kΩcm (Wacker III), FZ 400Ωcm (Wacker I), jet oxygenated FZ 800Ωcm (ITME II), CZ 100Ωcm (Polo III) were irradiated with ^{60}Co γ-photons. The DLTS spectra of a sample of FZ 400Ωcm is shown in figure 6.10. The introduction rates of the radiation induced defects are listed in table 6.6. The introduction rate of C_iO_i in the oxygen lean FZ 4kΩcm samples is not known, because the DLTS signal of a process induced defect coincides with the signal of C_iO_i. The introduction rate is assumed to be zero because of the low oxygen con-

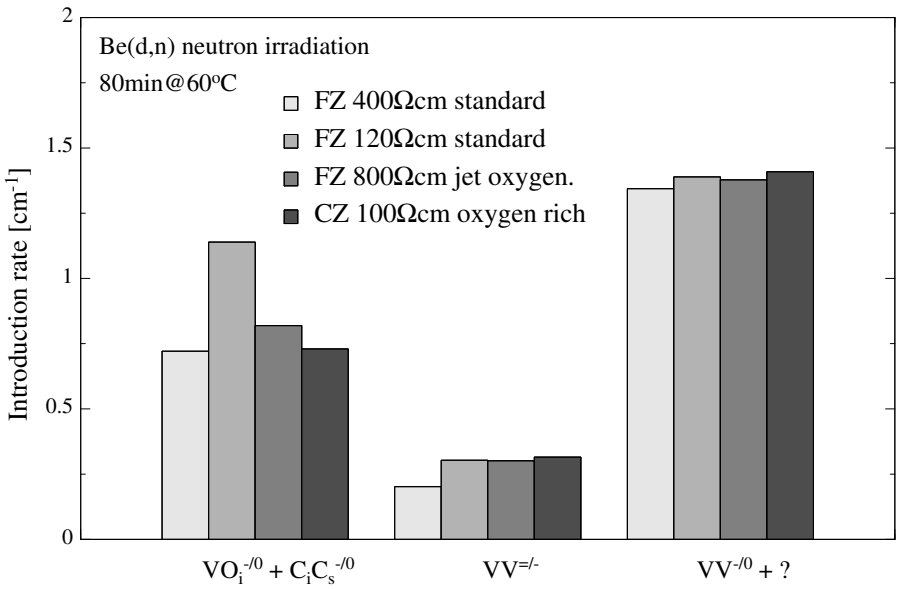

Figure 6.8: *The introduction rates of radiation induced defects in samples of different FZ/CZ materials irradiated with Be(d,n) neutrons are shown.*

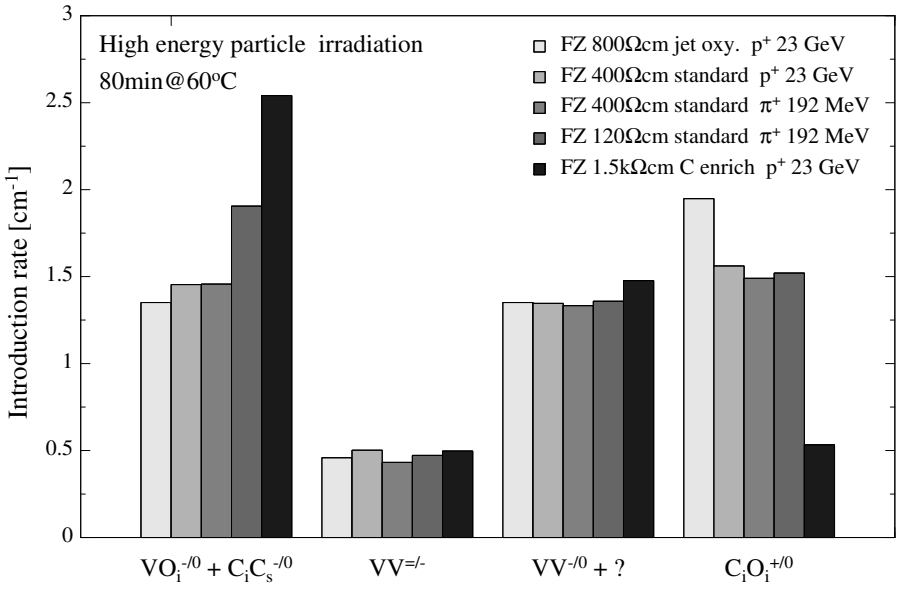

Figure 6.9: *The introduction rates of radiation induced defects in samples of different FZ materials irradiated with 23 GeV protons and 192 MeV pions are shown.*

Table 6.3: *Introduction rates of radiation induced defects after 7-10 MeV proton irradiation in the FZ 2kΩcm samples are listed.*

Particle type	g(VO_i) [cm^{-1}]	g(C_iC_s) [cm^{-1}]	g(C_iO_i) [cm^{-1}]	g($VV^{-/0}$+?) [cm^{-1}]	Σ g_{point} [cm^{-1}]
p^+ 7 MeV	–	–	2.72	1.44	–
p^+ 8 MeV	2.76	0.75	2.97	1.44	6.49
p^+ 9 MeV	2.94	0.94	2.87	1.57	6.74
p^+ 10 MeV	2.95	0.82	2.80	1.50	6.56

Table 6.4: *Introduction rates of radiation induced defects after 23 GeV proton irradiation in the FZ material oxygenated and processed by different manufacturers are listed.*

[O]	[C]	g(VO_i)	g(C_iC_s)	g(C_iO_i)	g($VV^{-/0}$+?)	Σ g_{point}
10^{16} [cm^{-3}]		[cm^{-1}]	[cm^{-1}]	[cm^{-1}]	[cm^{-1}]	[cm^{-1}]
14	<0.63	0.63	0.51	1.84	1.26	2.98
21	1.5	0.73	0.63	2.01	1.38	3.37
14	<0.63	0.70	0.51	2.05	1.21	3.26
14	9.0	0.70	0.59	2.19	1.35	3.48
36	1.8	0.78	0.36	1.63	1.17	2.77
26	1.2	0.77	0.43	1.72	1.28	2.92
57	1.3	0.72	0.40	1.59	1.15	2.71
22	0.44	0.75	0.43	1.72	1.27	2.90
0.9	0.62	1.15	1.06	1.30	1.32	3.51
14	0.47	0.95	0.60	2.12	1.41	3.67
30	0.43	0.78	0.48	2.16	1.37	3.42
34	3.5	0.84	0.70	1.96	1.45	3.58

Table 6.5: *Sum of the introduction rates of the point defects, the introduction rate of the cluster defects and the ratio between both introduction rates for the different particles are listed. The mean values from all irradiated sample are calculated.*

Particle type	Σ g_{point} [cm^{-1}]	g($VV^{-/0}$+?) [cm^{-1}]	Σ g_{point}/ g($VV^{-/0}$+?)
p^+ 7-10 MeV	6.52	1.31	3.87
p^+ 27 MeV	4.14	1.26	3.36
p^+ 23 GeV	3.26	1.32	2.46
π^+ 192 MeV	3.23	1.32	2.46
n Be(d,n)	1.82	1.30	1.43
n reactor	1.50	1.03	1.45

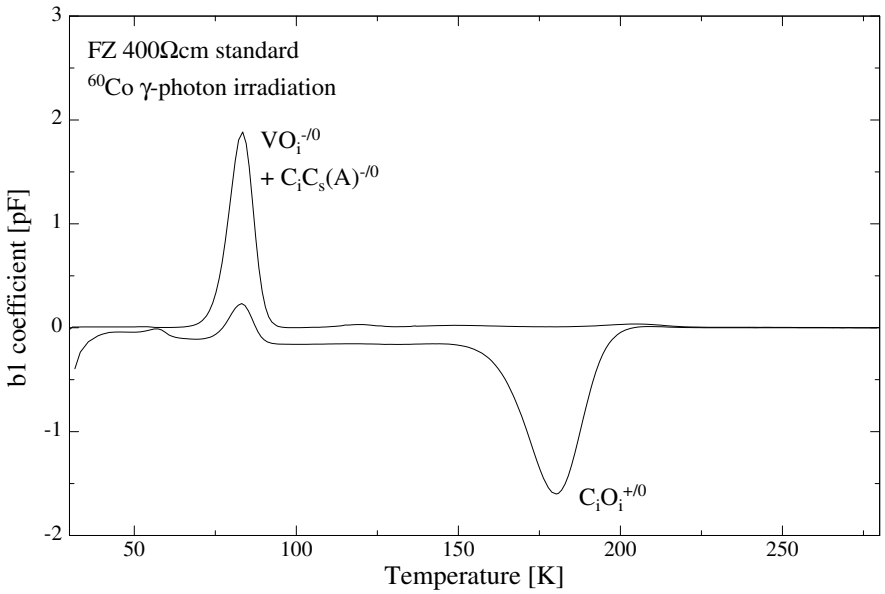

Figure 6.10: *DLTS spectra of a FZ 400Ωcm sample irradiated with ^{60}Co γ-photons are shown. The DLTS signals due to the two negative charge states of the divacancy are very small.*

centration in the material. Also the activation energies of the two negative charge states of the divacancy are different compared to the other materials.

The activation energy of the single negative charge state of the divacancy decreases with increasing electric field strength. This is the well known Pool Frenkel effect [Mar81]. Also the cross section of this defect state decreases with increasing electric field strength [Dus70]. These effects were measured in a sample of FZ 10kΩ*cm* at two different reverse biases $V_R = 5$ and 10 V.

All radiation induced defects are distributed homogeneously in the sample volume after ^{60}Co γ-photon irradiation. The introduction rates of the de-

Table 6.6: *Introduction rates of radiation induced defects after ^{60}Co γ-photon irradiation in different FZ/CZ materials. The mean values from all irradiated sample are calculated.*

$[O]$	$[C]$	g(VO_i)	g(C_iC_s)	g(C_iO_i)	g($VV^{=/-}/VV^{-/0}$)
10^{16} [cm^{-3}]		[cm^{-1}]	[cm^{-1}]	[cm^{-1}]	[cm^{-1}]
<0.02	<3	$7.59 \cdot 10^{-5}$	$2.72 \cdot 10^{-4}$	≈ 0	$1.80/1.14 \cdot 10^{-4}$
<5	<0.5	$2.47 \cdot 10^{-4}$	$1.02 \cdot 10^{-4}$	$1.15 \cdot 10^{-4}$	$10.0/8.07 \cdot 10^{-6}$
<5	<2	$3.74 \cdot 10^{-4}$	$1.86 \cdot 10^{-5}$	$2.86 \cdot 10^{-4}$	$6.48/7.83 \cdot 10^{-6}$
17	<2	$3.72 \cdot 10^{-4}$	$8.49 \cdot 10^{-6}$	$3.25 \cdot 10^{-4}$	$5.99/7.25 \cdot 10^{-6}$
90	0.5	$3.54 \cdot 10^{-4}$	$7.08 \cdot 10^{-7}$	–	$6.65/4.27 \cdot 10^{-6}$

fects VO_i, C_iC_s and C_iO_i depends on the oxygen and carbon concentrations. The introduction rate of the divacancies is only higher in the samples of the oxygen lean material, because the mean free path length of vacancies is large and vacancies generated in different collision events can capture each other. In the other materials divacancies are produced mainly by the capture of two vacancies created in the same collision event [Sve92]. The concentrations of the two charge states of divacancy are not the same. This is in contradiction to previous results [Mol97]. The baseline shifts in the DLTS spectra makes an accurate determination of small defect concentrations impossible. Sometimes only broad DLTS signals are observed. The defect parameters of the defect centers $VO_i + C_iC_s$ and C_iO_i are more reliable due to the larger concentrations. An capture measurement is employed to separate the defects VO_i and C_iC_s. Further details are given in chapter 6.3. A detailed discussion of the material dependence is not possible, because mostly the upper limits of the impurity concentrations are known.

The discussion of the various ratios between the concentrations of the radiation induced defects is done in chapter 6.4.

6.3 Capture measurements

In this section the capture measurements on the radiation induced point defects VO_i, C_iC_s, C_i and C_iO_i and the cluster defect VV are presented. The DLTS method is used to determine the capture rate of VO_i, C_i, C_iO_i and VV and the time constant of the configurational switching of C_iC_s. For further details see chapter 3.3. Both time constants depend on the particle and material type. The experimental results are useful to understand the primary displacement damage in crystalline silicon and the secondary defect kinetic with the impurity atoms oxygen and carbon.

Different methods are employed to inject free charge carriers into the depleted space charge region of a reverse biased p^+n junction. The filling of defects with majority charge carriers is furnished by reducing the reverse bias. Also front side illumination with a 670 nm laser diode is employed to create a small density of majority charge carriers in the space charge region. The filling of defects with minority charge carriers is furnished by forward biasing or back side illumination with an infrared LED ($\lambda_{max} = 880$ nm). A change of the applied bias is referred as electrical filling and the illumination of the sample as optical filling. The evaluation of the capture measurements is described in further detail in the appendices C and D.

The particle irradiated samples were heated for 80 min at 60°C or for 4 min at 80°C. If the C_i annealing was not finished, the samples were stored at room temperature for a few days or weeks. For some samples the tempering time period at 60°C or 80°C was longer. The ^{60}Co γ-photon irradiated samples were stored at room temperature for a few month to reduce the oxide damage.

6.3.1 Electrical filling of VO_i and C_iC_s

The filling characteristics $VO_i^0 \rightarrow VO_i^-$ and $C_iC_s^0 \rightarrow C_iC_s^-$ in the samples of FZ 10kΩcm (Wacker III) and oxygen lean FZ 4kΩcm (Wacker II) after ^{60}Co γ-photon irradiation are shown in figure 6.11 and 6.12. Also the theoretical predictions of the filling characteristics are shown. A separation of the signals of the two defect centers VO_i and C_iC_s is possible. All states of the defect center VO_i are already occupied with majority charge carriers for short filling pulses. The capture time constant of the defect center VO_i is between 10$-$15 μs for the two samples. The configurational switching of the defect $C_iC_s^-(B) \rightarrow C_iC_s^-(A)$ is observed for filling pulses with a longer duration. The signal of C_iC_s in the configuration B is not detected, because of its short emission time constant at T=70$-$90 K. Only the portion of C_iC_s in the configuration A is observed. The observed configuration change is described by an exponential time dependence. After electron emission C_iC_s changes again its configuration $A \rightarrow B$ in the depleted space charge region and the configuration B capture majority charge carriers during the next filling cycle.

The capture measurements of the sample of FZ 2kΩcm (Wacker IX) irradiated with 10 MeV protons reveal a slight deviation of the capture characteristic of VO_i from the prediction with a constant capture rate of 0.25 μs^{-1}, as shown in figure 6.13. The configurational switching of C_iC_s is described well by the prediction.

In the sample of FZ 120Ωcm (ITME I) irradiated with Be(d,n) neutrons the capture rate of the defect VO_i is not constant, as shown in figure 6.14. The configurational switching of C_iC_s is described reasonable by the prediction. The filling characteristics depend not on the annealing state of the radiation damage.

The filling characteristic of the defects VO_i and C_iC_s after Be(d,n) neutron irradiation depends on the oxygen concentration, as shown in figure 6.15. In the sample of standard FZ 2.8kΩcm (Polo I) the deviation of the filling characteristic from the prediction is small. But in the sample of oxygen enriched FZ 2.8kΩcm (Polo Ia) the filling characteristic is not described by the prediction.

The particle dependence of the filling characteristics of the defects VO_i and C_iC_s in the samples of jet oxygenated FZ 800/1.2$k\Omega cm$ (ITME II & III) are shown in figure 6.16. The filling characteristics of the samples irradiated with various particles deviate from the filling characteristic of the ^{60}Co γ-photon irradiated sample. This effect is mostly pronounced after neutron irradiation. However, a separation of the two defect centers is still possible with exception for the neutron irradiated sample. The ratio g(C_iC_s)/g(VO_i) is small in the ^{60}Co γ-photon irradiated sample and large in the neutron irradiated sample. For the charged particle irradiated samples the estimated ratio is between these two values. Nearly the same filling behaviour is also observed in the samples of FZ 400Ωcm (Wacker I). The filling characteristics

of the samples of FZ 10kΩcm (Wacker III) with [O]/[C] ≈ 1 are shown in figure 6.17. The slope of the initial capture characteristic indicates that the capture rate of VO_i in the neutron irradiated sample is smaller than in the 23 GeV proton irradiated sample. Also the filling characteristic of C_iC_s is more stretched after reactor neutron irradiation.

The filling characteristics of the defects VO_i and C_iC_s in the samples of carbon enriched FZ 1.5kΩcm (Polo II) after 23 GeV proton and reactor neutron irradiation are shown in figure 6.18. The capture rate of VO_i is constant and the configurational switching of C_iC_s is described well by the prediction.

The results of the capture measurements indicate that the filling behaviour of the defects VO_i and C_iC_s in some materials after particle irradiation is changed due to the cluster damage.

The following model is proposed to explain the experimental results. The primary displacement damage in crystalline silicon is different for various particles. For further details see chapters 3.1.2 and 3.2.4. The size of the collision cascade trees and the number of terminal clusters increases with increasing PKA energy. The displacement damage occurs mainly in the terminal cluster regions. It is assumed that the mobility of silicon interstitials is much higher than the mobility of vacancies and hence after the initial annihilation the left interstitials are diluted in the sample volume. The silicon interstitials exchange with substitutional carbon atoms. The density of vacancies in the terminal clusters is high and the generation of divacancies is favored. No generation of VO_i occurs in the terminal cluster regions. Isolated vacancies generated by PKAs with energies less than the threshold energy for cluster generation $E_{th} = 300$ eV are more responsible for the generation of VO_i. Thus the introduction rate of VO_i is higher for charged particles. Only if the PKA energy is greater than 10 keV as for neutron irradiations, the generation of vacancies due to single displacements in the collision cascade regions and perhaps due to escaping from the terminal cluster regions is dominating. The migrating vacancies are captured at the nearest O_i sites. Further it is assumed that the migration of carbon interstitials is influenced by strain and deformation fields originating from the terminal clusters [Zan00]. Therefore the C_i migrate in direction to the terminal clusters. No capture at O_i and C_s sites occurs on the way to the terminal clusters, because the mean free path length of C_i is assumed to be large even in the oxygen and carbon rich silicon. The final migration of C_i is constricted in the environment of the terminal clusters. The migration volume decreases with increasing defect density in the terminal clusters, because the strength of the strain and deformation fields increases. The defect density in the terminal clusters is particle dependent. For further details see chapter 6.4.5. The migrating C_i are captured mainly at O_i and C_s sites in the environment of the terminal clusters. In oxygen and carbon lean silicon migrating C_i are also captured at VV sites at the peripheries of the terminal clusters. The released vacancies are captured at O_i sites outside

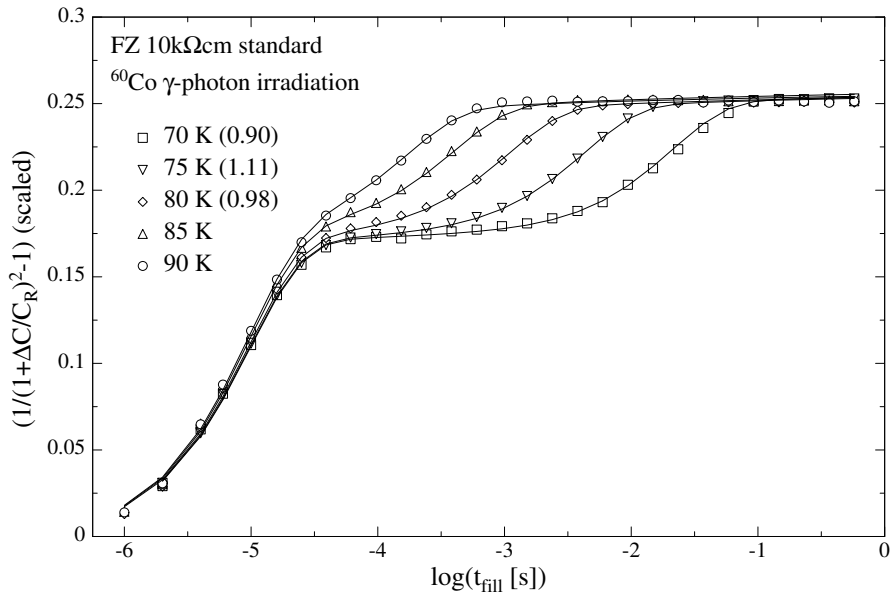

Figure 6.11: *The electrical filling characteristics of the defects VO_i and C_iC_s in a sample of FZ 10kΩcm after ^{60}Co γ-photon irradiation at different temperatures are shown (symbols). The signals are scaled with the factors in the parentheses. Also the theoretical predictions of the filling characteristics are shown (lines).*

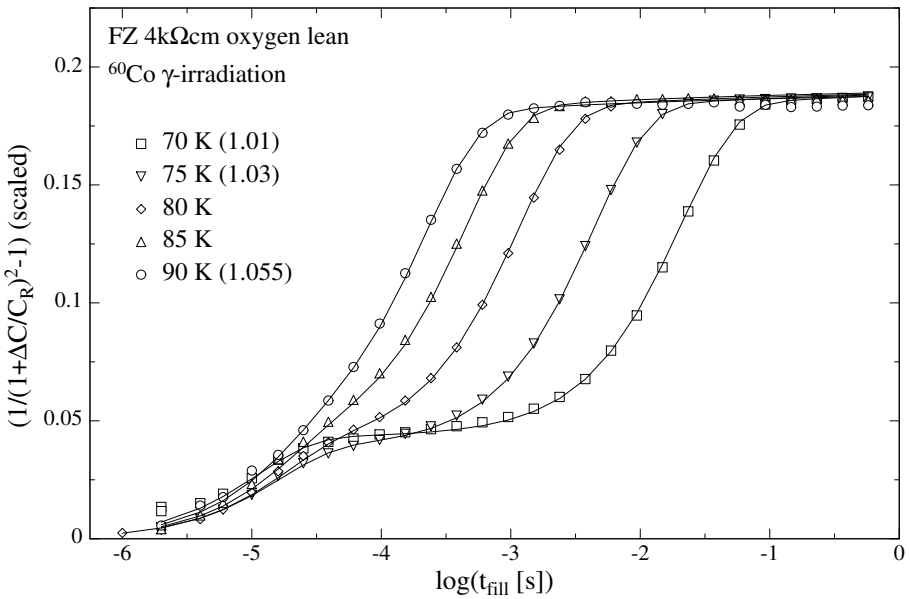

Figure 6.12: *The electrical filling characteristics of the defects VO_i and C_iC_s in a sample of oxygen lean FZ 4kΩcm after ^{60}Co γ-photon irradiation at different temperatures are shown (symbols). The signals are scaled with the factors in the parentheses. Also the theoretical predictions of the filling characteristics are shown (lines).*

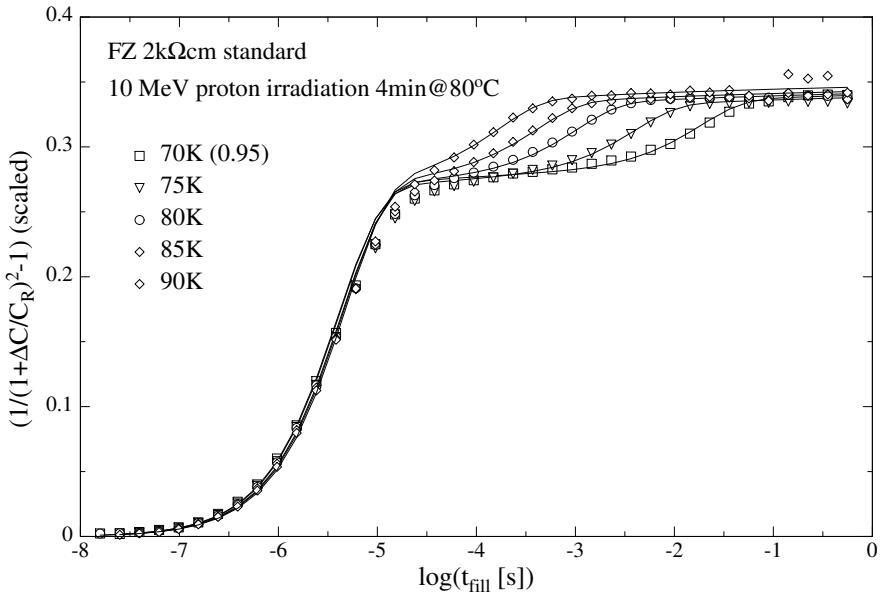

Figure 6.13: *The electrical filling characteristics of the defects VO_i and C_iC_s in a sample of FZ 2kΩcm after 10 MeV proton irradiation at different temperatures are shown (symbols). The signals are scaled with the factors in the parentheses. Also the theoretical predictions of the filling characteristics are shown (lines).*

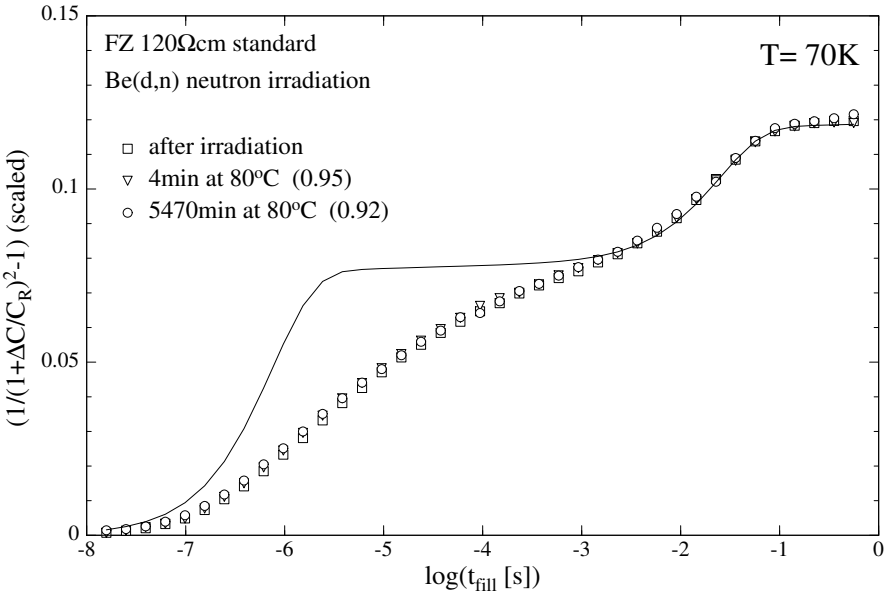

Figure 6.14: *The electrical filling characteristics of the defects VO_i and C_iC_s in a sample of FZ 120Ωcm after Be(d,n) neutron irradiation are shown (symbols). The signals are scaled with the factors in the parentheses. Also the theoretical prediction of the filling characteristic is shown (line).*

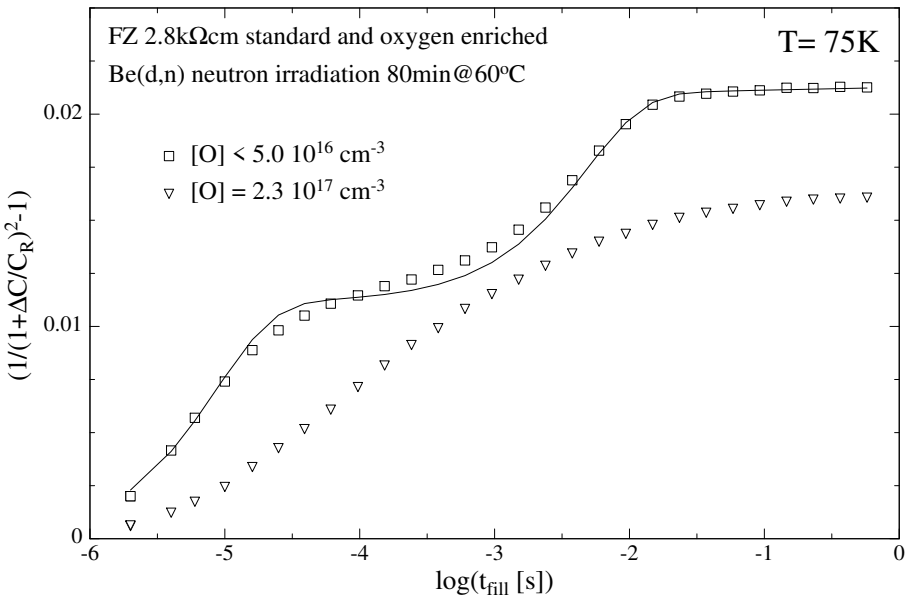

Figure 6.15: *The electrical filling characteristics of the defects VO_i and C_iC_s in a samples of standard and oxygen enriched FZ 2.8kΩcm after Be(d,n) neutron irradiation are shown (symbols). Also the theoretical prediction of the filling characteristic is shown (line).*

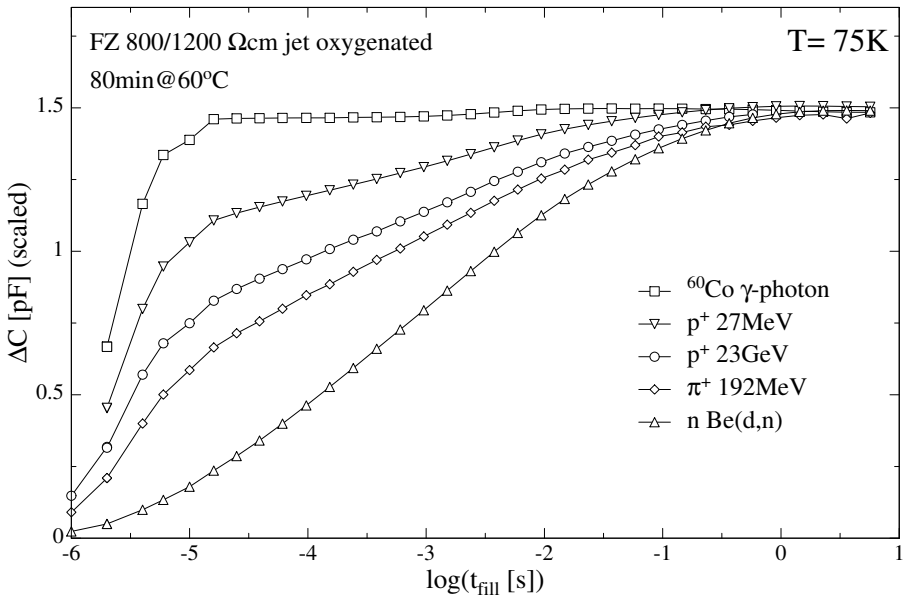

Figure 6.16: *The electrical filling characteristics of the defects VO_i and C_iC_s in samples of jet oxygenated FZ 800/1.2kΩcm after irradiation with ^{60}Co γ-photons and various particles are shown. The amplitudes are scaled.*

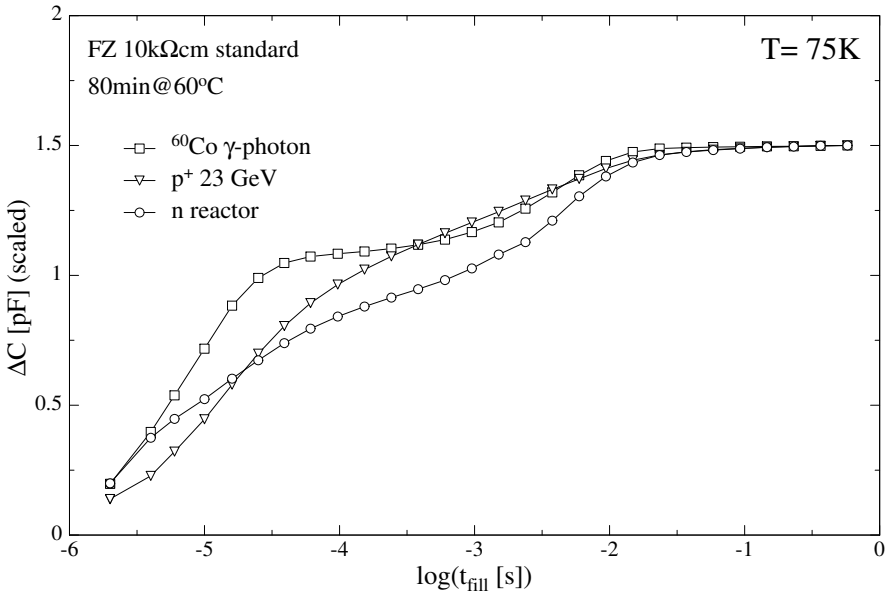

Figure 6.17: *The electrical filling characteristics of the defects VO_i and C_iC_s in samples of FZ 10kΩcm after irradiation with ^{60}Co γ-photons and various particles are shown. The amplitudes are scaled.*

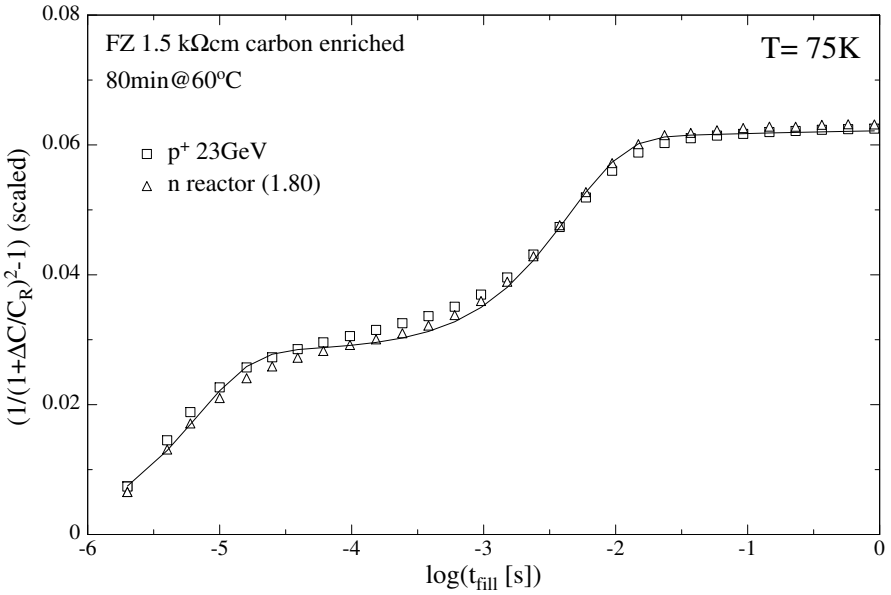

Figure 6.18: *The electrical filling characteristics of the defects VO_i and C_iC_s in samples of carbon enriched FZ 1.5kΩcm after 23 GeV proton and reactor neutron irradiation are shown (symbols). The signal is scaled with the factor in the parenthesis. Also the theoretical prediction of the filling characteristic is shown (line).*

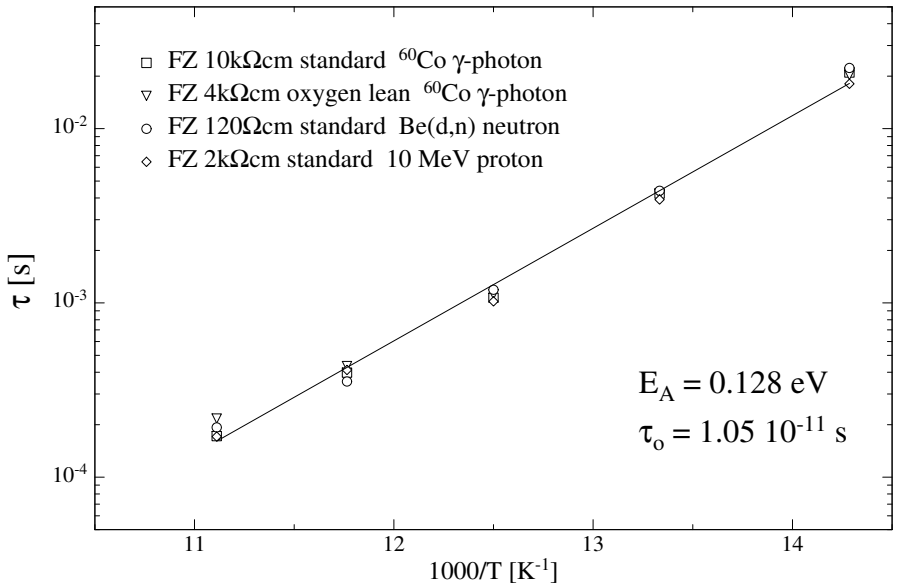

Figure 6.19: *The temperature dependence of the time constant of the configurational switching of C_iC_s measured in various samples is shown.*

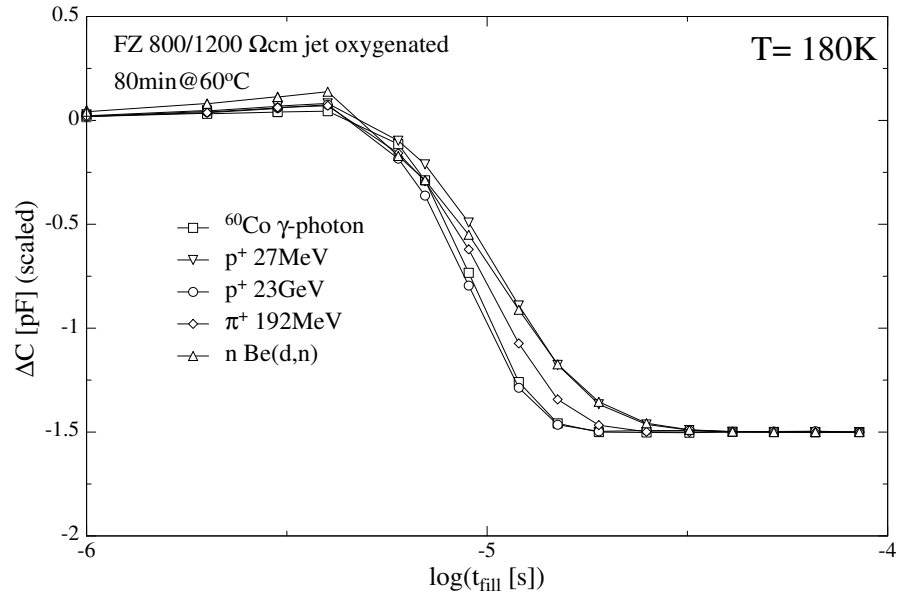

Figure 6.20: *The electrical filling characteristics of the defect C_iO_i in samples of jet oxygenated FZ 800/1.2kΩcm after irradiation with ^{60}Co γ-photons and various particles are shown. The amplitudes are scaled.*

the environment of the terminal clusters. The other migrating C_i are captured at the new C_s sites. Thus an envelope of C_iC_s defects around the terminal clusters is created. The configurational switching of C_iC_s in the envelope is changed by strain and deformation fields. Also a positive space charge region surrounding the negative charged terminal clusters is assumed [Gos59]. Therefore the capture rate of VO_i defects near the terminal clusters is decreased due to the smaller concentration of majority charge carriers.

After 10 MeV proton irradiation of FZ 2kΩcm (Wacker IX) most of the defects VO_i are distributed homogeneously in the sample volume. The capture rate of VO_i is only slightly decreased due the depletion zone surrounding the terminal clusters. The final migration volume of C_i is large, because the defect density in the terminal clusters is small. Thus the C_iC_s centers are created mainly in the environment of the terminal clusters and not at the peripheries and the configurational switching of C_iC_s is not changed by strain and deformations field.

After Be(d,n) neutron irradiation of FZ 120Ωcm (ITME I) the defects VO_i are distributed inside and near the cascade damage regions. Thus the capture rate is strongly decreased due the depletion zone surrounding the terminal clusters. The extension of the depletion regions depends not on the annealing state of the terminal cluster damage. The final migration volume of C_i is smaller in comparison to 10 MeV proton irradiation. The configurational switching of C_iC_s is not changed by strain and deformations fields, because the C_i is captured at C_s sites located in the environment of the terminal clusters due to the high carbon content of the material.

After Be(d,n) neutron irradiation of standard FZ 2.8KΩcm (Polo I) with a low oxygen concentration the defects VO_i are created in a greater distance from the cascade damage regions, because the mean free path length of V is large. Also the defects C_iC_s are distributed in the environment of the terminal clusters. Thus the capture rate of VO_i and the configurational switching of C_iC_s is not changed by the cluster damage. In oxygen enriched FZ 2.8KΩcm (Polo Ia) the vacancies are captured at O_i sites inside and near the cascade damage regions, because the mean free path length of V is small. Therefore the depletion regions surrounding the terminal clusters reduce the capture rate. The distribution of C_iC_s is assumed to be similar to the distribution in the not oxygen enriched FZ 2.8KΩcm, but the introduction rate g(C_iC_s) is smaller due to the higher oxygen concentration.

After ^{60}Co γ-photon irradiation of jet oxygenated FZ 800Ωcm (ITME II) the mobile vacancies are captured at O_i sites. The defects VO_i are distributed homogeneously in the sample volume as their precursors O_i. Also the mobile C_i are captured mainly at O_i sites. Thus the generation of C_iC_s is strongly suppressed. The defects C_iC_s are distributed homogeneously in the sample volume as their precursors C_s. After particle irradiation of jet oxygenated FZ 800/1.2kΩcm (ITME II & III) the migration of C_i is constricted in the environment of the terminal clusters. The final migration volume decreases with increasing defect density in the terminal clusters. Because the number

of interstitial oxygen atoms O_i decreases with a decreasing migration volume, the generation of C_iC_s is mostly enhanced after neutron irradiation and the generation of C_iO_i is mostly suppressed. The introduction rates are listed in table 6.2.

The same behaviour is also observed after particle irradiation of FZ 10kΩcm (Wacker III). Because more single displacements occur during 23 GeV proton irradiation in comparison to reactor neutron irradiation, the fraction of VO_i defects generated homogeneously in the sample volume is larger after 23 GeV proton irradiation compared to reactor neutron irradiation. Also the extension of the depletion region surrounding a terminal cluster is smaller after 23 GeV proton irradiation in comparison to reactor neutron irradiation. Thus the capture rate of VO_i is less reduced after 23 GeV proton irradiation. Also the configurational switching of C_iC_s is changed after reactor neutron irradiation, because the C_iC_s defects are generated mainly at the terminal cluster peripheries. Again the ratio $g(C_iC_s)/g(VO_i)$ is larger in the neutron irradiated sample compared to the 23 GeV proton irradiated sample, because the final migration volume decreases and the number of isolated displacements is smaller.

After 23 GeV proton and reactor neutron irradiation of carbon enriched FZ 1.5kΩcm (Polo II) the defects VO_i are distributed far away from the cascade damage regions or terminal clusters, because the oxygen concentration in the material is low. Because of the high carbon concentration all C_i are captured at C_s sites in the environment of the terminal clusters and not at peripheries of the terminal clusters.

6.3.2 Configurational switching of C_iC_s

The temperature dependence of the time constant of the configurational switching of C_iC_s is studied in the four samples for which the filling characteristics are not stretched. The results are shown in figure 6.19. The temperature dependence of the configurational change $B \rightarrow A$ of $C_iC_s^-$ is described by Equation 3.14. The temperature dependence of the configurational switching after neutron irradiation is also investigated in [Mol99]. The coincidence with shown results is in good agreement.

6.3.3 Electrical filling of C_iO_i

The filling characteristic $C_iO_i^0 \rightarrow C_iO_i^-$ during forward injection is independent on the particle type in the samples of jet oxygenated FZ 800/1.2k Ωcm (ITME II & III) and no significant difference is seen in comparison to the ^{60}Co γ-photon irradiated sample, as shown in figure 6.20. It is assumed that the C_iO_i centers are distributed in the environment of the terminal clusters. The extension of the environment depends on the particle type, as discussed previously. Because the concentration of electrons and holes $n/p \approx 1$ under high injection condition is much higher than majority charge

carrier concentration under thermal equilibrium condition $n \gg n_0$, charged defects in the terminal clusters do not change the concentration of the free charge carriers in the environment. Thus the capture rate is not changed.

6.3.4 Electrical filling of VV

The cross sections of the neutral charge state of the divacancy $VV^0 \rightarrow VV^-$ in ^{60}Co γ-photon irradiated samples of oxygen rich CZ 100Ωcm (Polo III), FZ 10kΩcm (Wacker III) and oxygen lean FZ 4kΩcm (Wacker II) are listed in table 6.7. The effective masses compiled in [Gre90] are employed. The capture characteristics are described well by the theoretical prediction with

Table 6.7: *The capture time constants and cross sections of the neutral charge state of isolated divacancies are listed. Also the cross sections obtained from the DLTS spectra and the ratio between both are listed. The electrical filling was performed at T=205 K.*

Material type	τ_c [μs]	σ_c [10^{-15}cm^2]	σ_T [10^{-15}cm^2]	σ_c/σ_T
CZ 100Ωcm oxy. rich	0.542	3.36	0.78	4.31
FZ 10kΩcm standard	31.4	3.80	1.06	3.58
FZ 4kΩcm oxy. lean	13.3	5.84	9.2	0.63

a constant capture rate. The capture cross section σ_c is nearly independent on the material type, but the cross section obtained from the DLTS spectra σ_T is material dependent. This effect can be explained with an electric field dependence of the cross section [Dus70]. But the ratio is not always $\sigma_c/\sigma_T > 1$. An electric field dependence of the activation energy and the cross section is also mentioned in chapter 6.2.2.

Capture characteristics of the neutral charge state of the divacancy $VV^0 \rightarrow VV^-$ after particle irradiation in various samples are shown in figure 6.21a. The samples are described in more detail in table 6.8. The time scale is shifted with $\log(N_{eff}/10^{12}\text{cm}^{-3})$ to take into account the different majority charge carrier concentrations under thermal equilibrium condition. This

Table 6.8: *The samples, in which the electrical capture characteristics of the divacancy were measured, are listed.*

Material type	Particle type	Tempering period	$[VV^{=/-}]/[VV^{-/0}+?]$
FZ 2kΩcm standard	p^+ 10 MeV	4min@80°C	0.48
FZ 800Ωcm jet oxyg.	π^+ 192 MeV	1280min@60°C	0.42
FZ 120Ωcm standard	n Be(d,n)	5470min@80°C	0.44
FZ 1.5kΩcm C enrich.	n reactor	80min@60°C	0.14

results in a coincidence of the capture characteristics. The capture characteristics exhibit a large deviation from the prediction of a capture characteristic with a constant capture rate (τ_c=10 μs). A dependence on the impurity content, particle type and annealing state is not seen. This suggests that the electron concentration in the terminal cluster regions is reduced due to negative charged divacancies. The bending of the electronic bandstructure is determined by the distributions of divacancies in the terminal cluster regions.

The predictions of capture characteristics assuming a Gaussian distribution of divacancies in the terminal clusters are also shown in figure 6.21a. The capture rate is not constant and depends only slightly on the number of divacancies in the terminal clusters. The width of the Gaussian distribution is L_0 = 10 nm and the number of divacancies M = 5 and 9. The capture cross section is $\sigma_c = 3 \cdot 10^{-15}\text{cm}^2$. The effective doping concentration is $N_{eff} = 10^{12}\text{cm}^{-3}$. The deviation from the prediction of the capture characteristic with a constant capture rate decreases with decreasing numbers of divacancies. Also the predicted capture characteristics for a Gaussian distribution of divacancies are nearly independent on the effective doping concentration in the range from 10^{12} to 10^{13}cm^{-3} [Kuh00b]. For the details to calculate the capture characteristics see appendix E.

The capture characteristics of the single negative charge state of the divacancy $VV^- \rightarrow VV^=$ measured in the same samples are shown in figure 6.21b. The time scale is not shifted, because a shifting with $\log(N_{eff}/10^{12}\text{cm}^{-3})$ does not result in a coincidence of the capture characteristics. The capture characteristics exhibit also a large deviation from the prediction of a capture characteristic with a constant capture rate (τ_c=200 μs). A dependence on particle type and annealing state is seen. The samples of jet oxygenated FZ 800Ωcm (ITME II) and of FZ 120Ωcm (ITME I) were tempered for longer periods. Thus the radiation damage is in its final stable annealing state. The ratios $[VV^{=/-}]/[VV^{-/0}+?]$ are nearly identical. Also the capture characteristics coincide. Therefore it is assumed that the terminal cluster damage created by irradiations with Be(d,n) neutrons and 192 MeV pions is not very different. The terminal cluster damage in the samples of FZ 2kΩcm (Wacker IX) and of carbon enriched FZ 1.5kΩcm (Polo II) is also annealed to about the same state. But the ratios $[VV^{=/-}]/[VV^{-/0}+?]$ are different and the capture characteristics do not coincide. Thus the terminal cluster damage generated by 10 MeV protons and reactor neutrons is different. The capture measurements also indicate that after long term annealing the terminal cluster damage will not be in the the same state. A detailed study of the particle dependence and annealing behaviour of the capture characteristics of the neutral and single negative charge states of the divacancy is needed for better understanding of the cluster damage.

Also the predictions of capture characteristics assuming a Gaussian distribution of divacancies in the terminal clusters with the same parameters as above are shown in figure 6.21b. The capture cross section is σ_c =

(a)

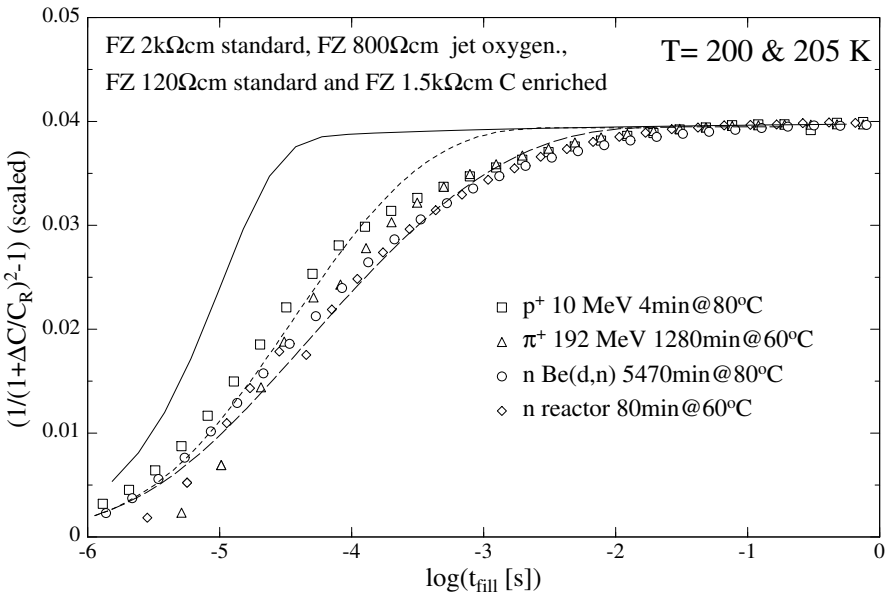

(b)

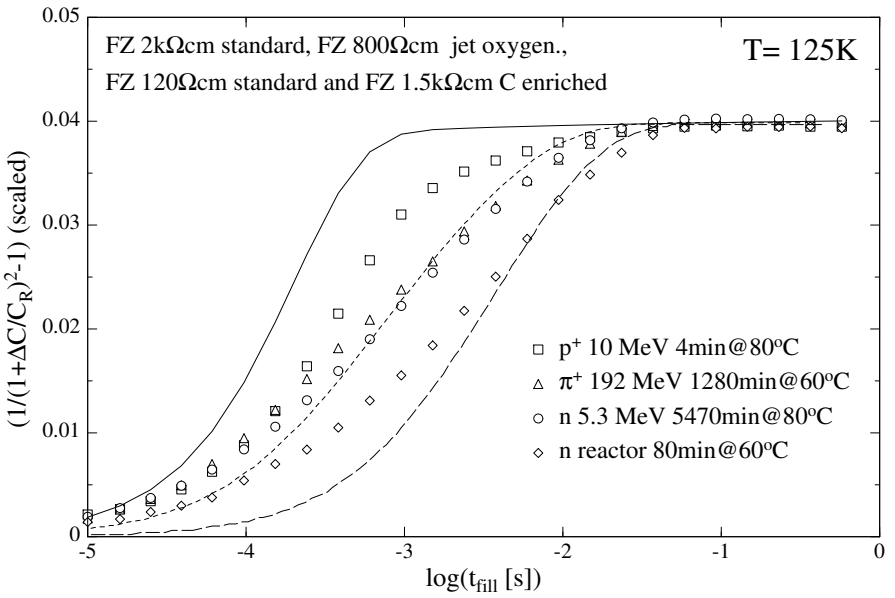

Figure 6.21: *The electrical filling characteristics of (a) the divacancy in the neutral charge state and (b) in the single negative charge state in various samples after particle irradiation are shown (symbols). The theoretical predictions of the capture characteristic with a constant capture rate (line) and with a not constant capture rate (dotted lines) are shown. For further details see text. The signals are scaled.*

$5 \cdot 10^{-15}\text{cm}^2$. The dependence of the capture rate on the number of divacancies in the terminal cluster is more pronounced. The deviation from the predictions of the capture characteristic with a constant capture rate decreases with decreasing numbers of divacancies in the terminal clusters. However, the assumption of a Gaussian distribution of divacancies seem to be reasonable [Vas86].

6.3.5 Electrical filling of C_i

The capture characteristics $C_i^0 \rightarrow C_i^-$ in a 23 GeV proton irradiated sample of FZ 4kΩcm (Wacker VIII) are shown in figure 6.22. The sample was tempered for 80 min at 60°C and further annealed for 5.3 days at room temperature. The capture rate is not constant during filling. This effect is independent on the concentration of C_i. The assumptions, that the mobile interstitial carbon atoms are localized in the environments of the terminal clusters and that the depletion regions surrounding the terminal clusters reduce the majority charge carrier density during electrical filling, are confirmed. For further details see chapter 6.3.1. The same effect was observed in 23 GeV proton irradiated samples of FZ 1.5kΩcm (Topsil II) and FZ 10kΩcm (Wacker III) and in a Be(d,n) neutron irradiated sample of FZ 120Ωcm (ITME I). Only a slight deviation from the theoretical prediction is visible in 7-10 MeV proton irradiated samples of FZ 2kΩcm (Wacker IX). The capture characteristic of the 10 MeV proton irradiated sample is shown in figure 6.23. The effect is less pronounced, because the carbon interstitials are assumed to be distributed in a larger volume surrounding the terminal clusters and the extension of the depletion region is smaller due to the smaller defect density in the terminal clusters.

6.3.6 Optical filling of C_i and C_iO_i

The capture characteristics $C_i^0 \rightarrow C_i^+$ and $C_iO_i^0 \rightarrow C_iO_i^+$ in a sample of FZ 4kΩcm (Wacker VIII) after 23 GeV proton irradiation are shown figure 6.24 and 6.25. The samples were tempered for 80 min at 60°C and further annealed for 3.7 days at room temperature. The defect centers are filled during back side illumination with an infrared LED. The theoretical prediction of a capture characteristic with a constant capture rate describes not the measured capture characteristic. The capture rate in the space charge region of a reverse biased p^+n junction is space dependent, because the hole density is inhomogeneous. The free hole density distribution in the space charge region is calculated assuming a constant drift current and a linear electric field distribution. The theoretical prediction of a capture characteristic with the previous assumptions describes the optical capture characteristic well. For further details see appendix D. The optical capture characteristics are independent on the impurity content and on the particle type. During filling at temperatures T=145 K and 180 K an appreciable fraction of the divacancies in the terminal clusters is in the single negative charge state, because

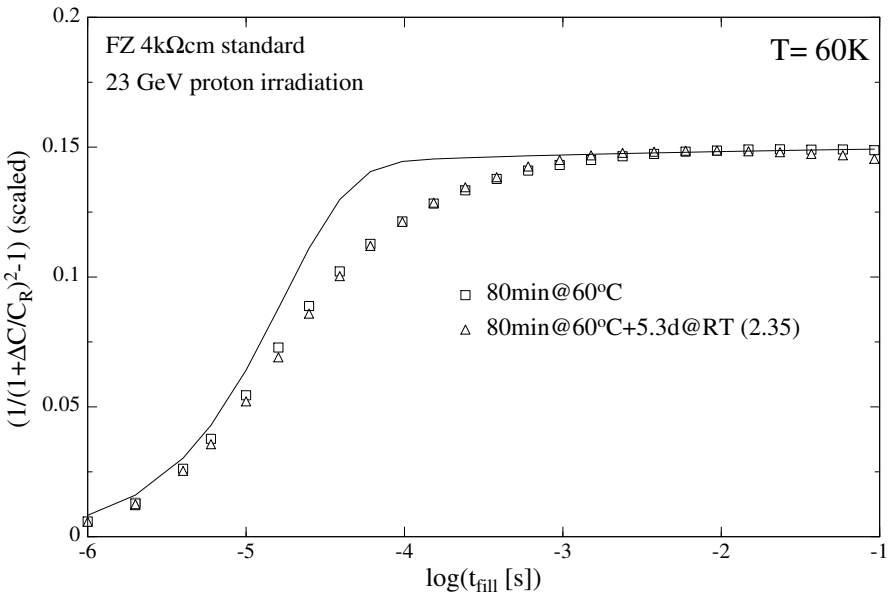

Figure 6.22: *The electrical filling characteristics of the defect C_i in a sample of FZ 4kΩcm after irradiation with 23 GeV protons at two annealing states are shown (symbols). The signal is scaled with the factor in the parenthesis. Also the theoretical prediction of the capture characteristics is shown (line).*

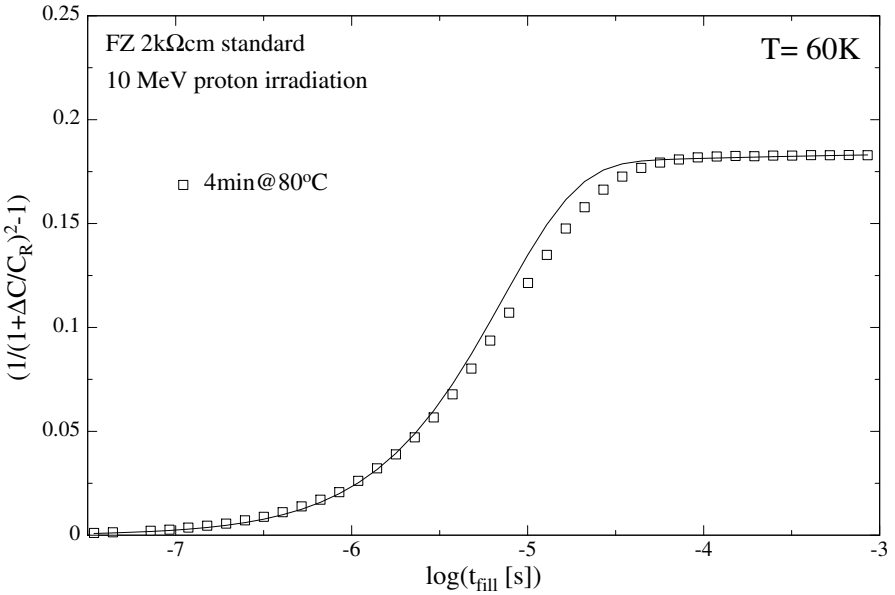

Figure 6.23: *The electrical filling characteristics of the defect C_i in a sample of FZ 2kΩcm after irradiation with 10 MeV protons is shown (symbols). Also the theoretical prediction of the capture characteristic is shown (line).*

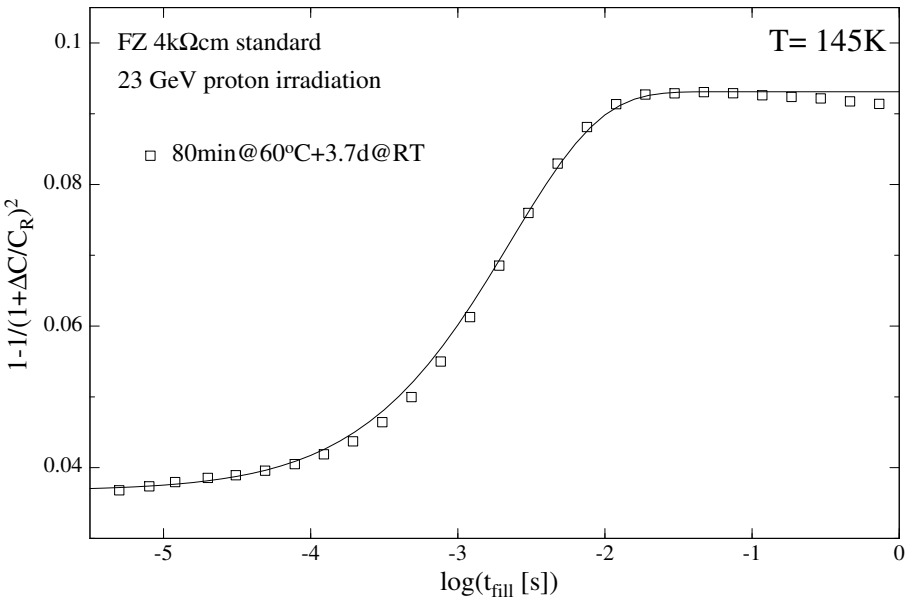

Figure 6.24: *The optical filling characteristic of the defect C_i in a sample of FZ 4kΩcm after irradiation with 23 GeV protons is shown (symbols). Also the theoretical prediction of the capture characteristic is shown (line).*

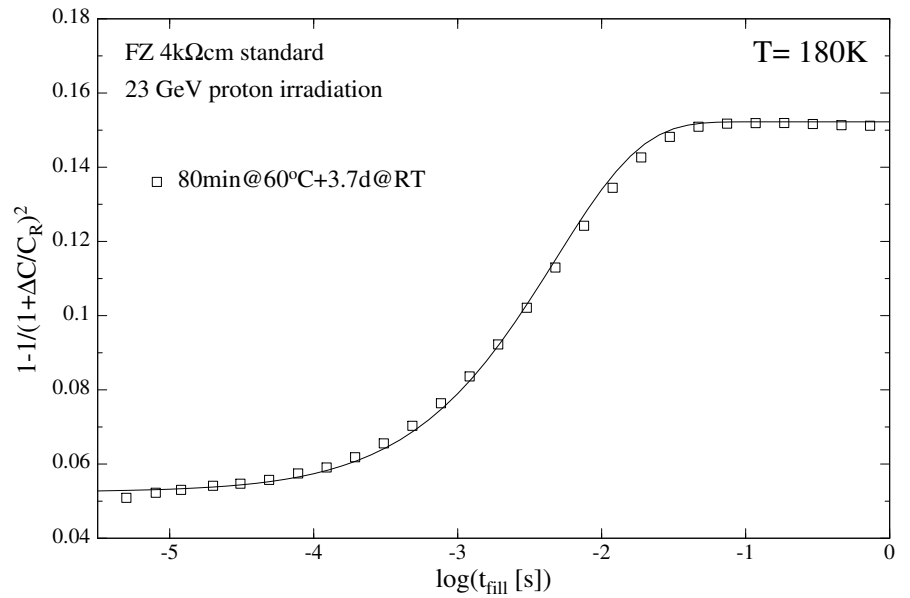

Figure 6.25: *The optical filling characteristic of the defect C_iO_i in a sample of FZ 4kΩcm after irradiation with 23 GeV protons is shown (symbols). Also the theoretical prediction of the capture characteristic is shown (line).*

Table 6.9: *The capture cross sections obtained from optical capture characteristics and from DLTS spectra are listed. The capture measurements of C_i were performed at T=145 K and of C_iO_i at T=180 K.*

Material type	Particle type	Defect center	σ_c	σ_T	σ_c/σ_T
			$[10^{-16}\mathrm{cm}^2]$		
FZ 4kΩcm standard	p^+ 23 GeV	C_i	14.5	17.7	0.82
FZ 4kΩcm standard	p^+ 23 GeV	C_iO_i	3.61	3.38	1.07
FZ 2kΩcm O enrich	n reactor	C_iO_i	3.23	3.49	0.93
FZ 4kΩcm O enrich	p^+ 23 GeV	C_iO_i	3.40	2.08	1.63
FZ 2kΩcm standard	p^+ 7 MeV	C_i	15.5	13.3	1.17
FZ 2kΩcm standard	p^+ 7 MeV	C_iO_i	2.35	2.59	0.91
FZ 2kΩcm standard	p^+ 8 MeV	C_i	15.0	15.0	1.00
FZ 2kΩcm standard	p^+ 8 MeV	C_iO_i	2.26	2.61	0.87
FZ 2kΩcm standard	p^+ 9 MeV	C_i	16.5	14.0	1.18
FZ 2kΩcm standard	p^+ 9 MeV	C_iO_i	2.85	3.10	0.92
FZ 2kΩcm standard	p^+ 10 MeV	C_i	13.8	16.5	0.84
FZ 2kΩcm standard	p^+ 10 MeV	C_iO_i	2.06	2.85	0.72

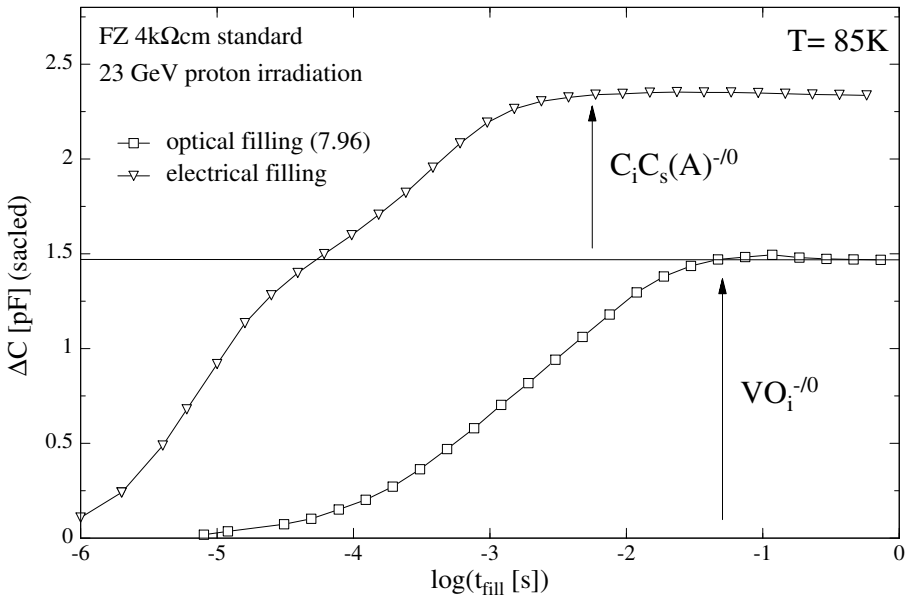

Figure 6.26: *The optical and electrical filling characteristics of the defect VO_i in a sample of FZ 4kΩcm after irradiation with 23 GeV protons are shown. The amplitude of the optical capture characteristic is scaled with the factor in the parenthesis. Front side illumination only fill the defect VO_i.*

the applied bias before the filling was $V_R = 0$ V, and also other radiation induced defects in the environment of the terminal clusters can change the effective space charge density after low fluence irradiation. But the capture rate is not changed due to hole density variations in the environment of the terminal clusters. The cross sections σ_c from the optical capture characteristics together with the cross sections σ_T from the DLTS spectra of samples of FZ 4kΩcm (Wacker VIII), oxygen enriched FZ 2kΩcm (Wacker IVa), oxygen enriched FZ 4kΩcm (Topsil Ia) and FZ 2kΩcm (Wacker IX) are listed in table 6.9. The hole mobility from [Fei97] and the effective masses from [Gre90] are used. The agreement between the cross sections is good.

6.3.7 Optical filling of VO_i

The filling characteristics $VO_i^0 \rightarrow VO_i^-$ in the sample of FZ 4kΩcm (Wacker VIII) after 23 GeV proton irradiation are shown in figure 6.26. Two different filling methods are employed. The centers VO_i are filled during reducing the reverse bias or during front side illumination with a 670 nm laser diode. The amplitude of the optical capture characteristic is multiplied with a factor to take into account the restricted filling under the area of the optical window. The factor is equal to the ratio between the area of the optical window and the area of the p^+ region. After this correction the signals associated with VO_i are equal. The position of the quasi Fermi level exclude an occupation of the carbon complex C_iC_s in the configuration B. The electron density near the p^+ region was $n_0 = 1.75 \cdot 10^9 \mathrm{cm}^{-3}$ and hence $E^*_{F,n} = 0.158$ eV. The configuration B has an energy level 0.11 eV below the conduction band [Son90]. The theoretical prediction of the capture characteristic with the assumptions made in appendix D does not described the measured capture characteristic because of the inhomogeneous intensity profile of the laser light spot.

6.4 Ratios of defect concentrations

For further understanding of the defect generation and kinetic in crystalline silicon the ratios of the concentrations of the radiation induced defects VO_i, VV, C_iO_i and C_iC_s are discussed. The following ratios are employed.

$$\mathrm{R1} = \frac{[VO_i] + 2\,[VV]}{[C_iC_s] + [C_iO_i]} = \frac{[V_{mig}] + [V_{clus}]}{[I_{mig}]} = \frac{\Sigma\,[V]}{[I_{mig}]} \tag{6.1}$$

is the ratio between the concentrations of defects generated by vacancies and silicon interstitials. The migrating vacancies V_{mig} generate mainly VO_i, the generation of VP_s is negligible. The vacancies generated in the terminal clusters V_{clus} form mainly divacancies. Higher order vacancy complexes are not taken into account. The migrating silicon interstitials I_{mig} exchange with substitutional carbon atoms. The migrating carbon interstitials C_i

form the defects C_iC_s and C_iO_i at C_s and O_i sites.

$$\mathrm{R2} = \frac{[VO_i]}{[C_iC_s] + [C_iO_i]} = \frac{[V_{mig}]}{[I_{mig}]} \tag{6.2}$$

is the ratio between the concentrations of defects generated by migrating vacancies and silicon interstitials.

$$\mathrm{R3} = \frac{[VO_i]}{2\,[VV]} = \frac{[V_{mig}]}{[V_{clus}]} \tag{6.3}$$

is the ratio between the concentrations of defects generated by migrating vacancies and vacancies generated in the terminal clusters.

$$\mathrm{R4} = \frac{[C_iO_i]}{[C_iC_s]} \propto \frac{[O_i]}{[C_s]} \tag{6.4}$$

is the ratio between the concentrations of defects generated by the capture of C_i at O_i sites and C_i at C_s sites. The ratio R4 is proportional to the ratio between the interstitial oxygen concentration and the substitutional carbon concentration, if no exhaustion of O_i and C_s sites occur. The proportional constant Γ is the ratio between the capture radii

$$\Gamma = \frac{R_c(C_iO_i)}{R_c(C_iC_s)} \quad \text{for} \quad \begin{cases} [C_iO_i] \ll [O_i] \\ [C_iC_s] \ll [C_s] \\ [C_iO_i] + [C_iC_s] \ll [C_s] \end{cases} \tag{6.5}$$

The ratio of the capture radii is $1/\Gamma \approx 3.10$ [Mac96].

In the following sections the dependence of the ratios R1, R2, R3 and R4 on the particle and material type is discussed. The particle dependence of the ratio between the concentrations of the two negative charge states of the divacancy $[VV^{=/0}]/[VV^{-/0}]$ is discussed in a separate section.

6.4.1 ^{60}Co γ-photon irradiation

The samples of oxygen lean FZ 4kΩcm (Wacker II), FZ 10kΩcm (Wacker III), FZ 400Ωcm (Wacker I), jet oxygenated FZ 800Ωcm (ITME II), CZ 100Ωcm (Polo III) were irradiated with ^{60}Co γ-photons. The radiation induced defects are distributed homogeneously in the sample volume. The ratios of the defect concentrations are listed in table 6.10. The ratio R1 is always greater than one. The previous result of R_1=1 is not confirmed [Mol97]. Therefore a portion of the primary generated silicon interstitials is lost. The leak of silicon interstitials after γ-photon irradiation is explained with annihilation of silicon interstitials at the sample surface. The surface annihilation velocity depends on the sample geometry which is the same for all samples. The fluctuations in R1 are due to the error in the measured defect concentrations. No values of the surface annihilation velocity for silicon interstitials are known. Also no theoretical model exists to describe the recombination of VI pairs during irradiation [Dav87].

Table 6.10: *Ratios of radiation induced defects after ^{60}Co γ-photon irradiation in various silicon materials.*

$[O]$	$[C]$	R1	R2	R3	R4
10^{16} [cm^{-3}]		$\Sigma[V]/[I_{mig}]$	$[V_{mig}]/[I_{mig}]$	$[V_{mig}]/[V_{clus}]$	$\propto [O_i]/[C_s]$
<0.02	<3	1.34	0.28	0.26	≈0
<5	<0.5	1.22	1.14	13.67	1.13
<5	<2	1.27	1.23	26.14	15.38
17	<2	1.16	1.12	28.10	38.28
90	0.5	–	–	32.42	–

The ratio R2 is only appreciably smaller than R1 in the samples of oxygen lean FZ 4kΩcm. In the other samples the ratios are more identical. As discussed in chapter 6.2.2 the migrating vacancies are captured mainly at O_i sites in standard and oxygen rich silicon. The capture of two vacancies generated in different collision events occurs only in oxygen lean silicon.

The ratio R3 is proportional to $g(V)/g(VV)$. The mean value of R3 $\approx$ 29 for the samples of standard FZ 400Ωcm, jet oxygenated FZ 800Ωcm and CZ 100Ωcm in which the divacancies are only generated in primary collision events. Thus g(V)/g(VV) $\approx$ 60 for ^{60}Co γ-photon irradiations and is 6$-$7 times larger in comparison to 2 MeV electron irradiations [Dav87, Sve92].

The ratio R4 depends on the oxygen and carbon concentrations. The ratio $[O_i]/[C_s]$ can be estimated according to Eq. 6.4 and 6.5. But a comparison with the results of SIMS measurements is not possible, because mostly the upper limits of the concentrations are known. If the oxygen and carbon concentrations in the two jet oxygenated FZ 800/1.2kΩcm (ITME II & III) materials are assumed to be identical, the ratio $[O]/[C]$ obtained from SIMS measurements is about 20 and hence six times smaller than the ratio $[O_i]/[C_s] \approx 120$ obtained from DLTS measurements.

6.4.2 Particle dependence

The ratios obtained form samples of jet oxygenated FZ 800/1.2kΩcm (ITME II & III) irradiated with ^{60}Co γ-photons and different particles are listed in table 6.11. As discussed in chapter 6.3.1 the silicon interstitials left after immediate annihilation in the terminal cluster regions dilute homogeneously in the sample volume. The left vacancies in the terminal clusters form divacancies and perhaps higher order vacancy complexes.

The ratio R1 is particle independent and greater than one. Therefore a portion of the primary generated silicon interstitials annihilate at the surface as discussed in the previous section. The generation of higher order interstitial complexes in the terminal cluster regions after particle irradiation can not be excluded, because the ratio R1 is larger after particle irradiation com-

Table 6.11: *Ratios of radiation induced defects in samples of jet oxygenated FZ 800/1.2kΩcm irradiated with ^{60}Co γ-photons and different particles are listed.*

Particle type	R1 $\Sigma[V]/[I_{mig}]$	R2 $[V_{mig}]/[I_{mig}]$	R3 $[V_{mig}]/[V_{clus}]$	R4 $\propto [O_i]/[C_s]$
^{60}Co γ-photons	1.16	1.12	28.1	38.3
p^+ 27 MeV	1.40	0.49	0.53	5.44
p^+ 23 GeV	1.42	0.33	0.30	3.68
π^+ 192 MeV	1.31	0.27	0.26	2.73
n Be(d,n)	≈1.54	≈0.05	≈0.04	≈1.58

pared to ^{60}Co γ-photon irradiation. But the ratio R1 for the ^{60}Co γ-photon irradiated samples also fluctuates in this range. The particle independence of R1 suggests that the ratio between generated and annihilated silicon interstitials per unit time is constant or the surface annihilation rate of silicon interstitials is proportional to the generation rate of silicon interstitials.

In the ^{60}Co γ-irradiated sample the ratio R2 is close to R1, because no clusters are created and the generation of divacancies is negligible in oxygen rich silicon. The deviation of the ratio R2 from R1 is large after neutron irradiation, because mainly terminal clusters are produced.

The ratio R2 is particle dependent. The generation of migrating vacancies compared to the generation of migrating silicon interstitials is strongly suppressed during neutron irradiation, because the migrating vacancies are generated mainly due to single displacements in the collision cascade regions and the migrating silicon interstitials are generated mainly in the terminal clusters from which they escape. During charged particle irradiation the generation of migrating vacancies is enhanced, because more single displacements of silicon atoms occur. The ratio between displacements generated outside and in the terminal cluster regions depends on the particle type.

The ratio R3 is particle dependent. The ratio R3 indicates that during neutron irradiation most of the vacancies are generated in terminal cluster regions. The fraction of isolated vacancies generated in the collision cascade regions or perhaps escaped from the terminal cluster regions is small. The enhancement of the generation of migrating vacancies during charged particle irradiation increases the ratio R3.

The ratio R4 is particle dependent. The ratio R4 is smaller for the particle irradiated samples compared to the ^{60}Co γ-photon irradiated sample. The ratio R4 is lowest for neutron irradiation, because the generation of C_iO_i is strongly suppressed compared to the generation of C_iC_s. This is explained with the constriction of the migration of carbon interstitials in the environment of the terminal clusters. For further details see chapter 6.3.1. The

ratio R4 decreases with the decreasing migration volume. An exhaustion of O_i and C_s sites is assumed to occur in the environment of the terminal clusters. New C_s sites can be created by the capture of C_i at VV sites at the terminal cluster peripheries.

6.4.3 Material dependence

The ratios of the defect concentrations obtained from samples of various standard FZ materials which are oxygenated and processed by different manufacturers are listed in table 6.12. The oxygen enrichment was done by high temperature diffusion (DOFZ). The samples were irradiated with 23 GeV protons. The results from the samples of FZ 2kΩcm (Wacker IVa & Vb) and FZ 4kΩcm (Topsil Ia & Ib) oxygenated and processed by SINTEF are listed in the first block. The results from the samples of FZ 2kΩcm (Wacker VIIc, VIc, VIId & VId) oxygenated and processed by ST Microelectronics are listed in the second block. The results from the samples of FZ 4kΩcm (Wacker VIII, VIIIe, VIIIf & Topsil IIg) oxygenated and processed by BNL/CiS are listed in the third block. The sample with the lowest oxygen concentration was processed on standard FZ 4kΩcm which was not oxygenated. The annealing of C_i was accomplished during an additional storage at room temperature for 7 days. All other materials are oxygenated and the annealing of C_i is finished after a tempering period for 80 min at 60°C.

The ratios R1, R2 and R3 are nearly independent on the oxygen and carbon concentrations in each block. The difference between the blocks is assumed

Table 6.12: *Ratios of radiation induced defects in samples of various materials oxygenated and processed by different manufacturers are listed. The samples were irradiated with 23 GeV protons*

$[O]$	$[C]$	R1	R2	R3	R4
10^{16}	[cm^{-3}]	$\Sigma[V]/[I_{mig}]$	$[V_{mig}]/[I_{mig}]$	$[V_{mig}]/[V_{clus}]$	$\propto [O_i]/[C_s]$
14	<0.63	1.34	0.27	0.25	3.61
21	1.5	1.32	0.28	0.26	3.19
14	<0.63	1.22	0.27	0.29	4.02
14	0.9	1.22	0.25	0.26	3.71
36	1.8	1.57	0.39	0.33	4.53
26	1.2	1.55	0.36	0.30	4.00
57	1.3	1.52	0.36	0.31	3.98
22	0.44	1.53	0.35	0.30	4.00
0.9	0.62	1.61	0.49	0.43	1.23
14	0.47	1.39	0.35	0.34	3.53
30	0.43	1.33	0.29	0.28	4.50
34	3.5	1.41	0.32	0.29	2.80

to be due to the experimental accuracy. The ratios R1, R2 and R3 for the sample with the lowest oxygen concentration in the third block are slightly larger, because the generation of VO_i is enhanced due to capture of C_i at VV sites during annealing at room temperature. The mean ratios from all samples are $R1 = 1.42 \pm 0.14$, $R2 = 0.33 \pm 0.07$ and $R3 = 0.30 \pm 0.05$.

The independence of R1 on the material type confirms that the leak of silicon interstitials is due to surface annihilation of silicon interstitials or higher order interstitial complexes in the terminal clusters. However, the higher order interstitial complexes could also be higher order carbon complexes, e.g. C_iO_iI, C_iC_sI and C_iC_sII, which are not detected with the DLTS method [Dav87]. The higher order carbon complexes are suggested to be formed in environment of the terminal clusters. Because the ratio R2 is independent on the material type after low fluence irradiations used for the DLTS studies, the generation of higher order carbon complexes is excluded. Only C_iO_i and C_iC_s defects are generated.

The ratio R3 is independent on the oxygen concentration. Therefore migrating vacancies are not attracted by the terminal clusters and the generation of VO_i is not restricted in the environment of the terminal clusters.

The ratio R4 depends on the ratio $[O]/[C]$, as shown in figure 6.27a. However, the value of R4 saturates for $[O]/[C] > 20$. The dependence of the introduction rates g(C_iO_i) and g(C_iC_s) on the ratio $[O]/[C]$ is shown in figure 6.27b. The introduction rates g(C_iO_i) and g(C_iC_s) depend not on the ratio $[O]/[C]$ with the exception of the not oxygen enriched sample with $[O]/[C] = 1.45$. This suggests that for $[O]/[C] > 20$ no exhaustion of O_i sites in the environment of the terminal clusters occurs and C_s sites are generated at the terminal cluster peripheries by the capture of C_i at VV sites. Other migrating C_i are captured mainly at these new C_s sites. The C_iC_s defects envelope the terminal cluster regions. The details of the reaction kinetics in the environment of the terminal clusters are not understood.

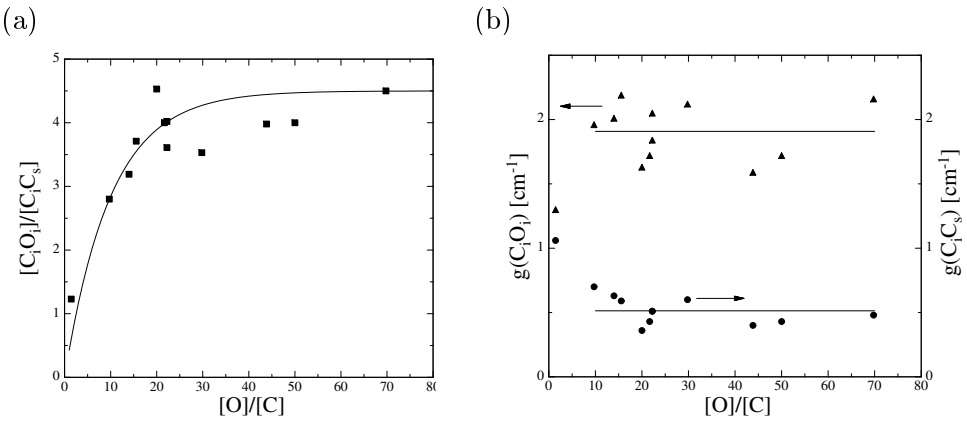

Figure 6.27: *The dependence of (a) the ratio $[C_iO_i]/[C_iC_s]$ and of (b) the introduction rates g(C_iO_i) and g(C_iC_s) on the ratio $[O]/[C]$ are shown. The exponential curve and the lines are shown to guide the eye.*

6.4.4 Low energy protons

The ratios of 8-10 MeV proton irradiated samples of standard FZ 2kΩcm (Wacker IX) are listed in table 6.13. As discussed in the previous section the dependence of the ratios R1, R2 and R3 on the oxygen and carbon concentrations is weak. Therefore a comparison with the ratios in the tables 6.11 and 6.12 is possible. But the ratio R4 depends on particle and material type.

The particle independence of R1 is confirmed. Thus the explanation for the leak of silicon interstitials due to surface annihilation of silicon interstitials is supported, because the generation rate of higher order interstitial complexes for low energy protons is assumed to be different compared to other particles. Capture characteristics indicate that the terminal cluster damage created by 10 MeV protons is different compared to the terminal cluster damage created by the other particles. For further details see chapter 6.3.4.

The ratios R2 and R3 indicate that more migrating vacancies are generated and the fraction of vacancies generated in the terminal clusters is smaller.

A discussion of the ratio R4 is not possible. The results of ^{60}Co γ-photon irradiated samples of the same material are needed.

Table 6.13: *Ratios of radiation induced defects in 8-10 MeV proton irradiated samples of standard FZ 2kΩcm are listed.*

Particle type	R1 $\Sigma[V]/[I_{mig}]$	R2 $[V_{mig}]/[I_{mig}]$	R3 $[V_{mig}]/[V_{clus}]$	R4 $\propto [O_i]/[C_s]$
p^+ 8 MeV	1.51	0.74	0.96	3.95
p^+ 9 MeV	1.60	0.77	0.93	3.06
p^+ 10 MeV	1.65	0.82	0.98	3.43

6.4.5 Ratio $[VV^{=/-}]/[VV^{-/0}]$

The measured ratio $[VV^{=/-}]/[VV^{-/0}+?]$ is particle dependent. No dependence on the concentrations of oxygen and carbon is observed. Also the ratio is independent on the effective doping concentration. For further details see chapter 6.2.1.

The ratio $[VV^{=/-}]/[VV^{-/0}+?]$ is less than one after particle irradiation. Thus the fraction of divacancies occupied with two electrons at T=125 K is smaller than the fraction of divacancies occupied with one electron at T=200 K under thermal equilibrium condition. The electronic band structure is bent in the terminal cluster regions. The shape of the bending depends on the defect distribution in the terminal clusters which is particle dependent. Because no dependence on the impurity content is observed, it is assumed that the terminal clusters consist of higher order vacancy, mainly

divacancies, and perhaps higher order interstitial complexes.

The electronic band structure is calculated with the assumption of a Gaussian distribution of divacancies in the clusters and a homogeneous distribution of the shallow doping impurities [Vas86]. The majority charge carriers are electrons. The generation of higher order vacancy or interstitial complexes in the terminal clusters is neglected. The contribution of charged impurity defects to the positive space charge in the regions surrounding the negative charged terminal clusters is neglected, because their concentrations are assumed to be much smaller than the doping concentration after low fluence irradiations used for the DLTS studies. For further details see appendix E. The calculated ratios $[VV^{=/-}]/[VV^{-/0}]$ for various ratios M/L_0 are shown in figure 6.28. M is the number of divacancies in a cluster and L_0 is the width of the Gaussian distribution. The concentration $[VV^{=/-}]$ is obtained from a simulation at T=125 K and the concentration $[VV^{-/0}]$ is obtained from a simulation at T=200 K. The ratio $[VV^{=/-}]/[VV^{-/0}]$ decreases with increasing ratio M/L_0. The ratio $[VV^{=/-}]/[VV^{-/0}]$ depends on the effective doping concentration, because the distance of the Fermi level from the conduction band edge decreases with increasing concentration of free electrons in the conduction band. Hence the number of divacancies in the double negative charge state at T=125 K increases with increasing effective doping concentration.

The following parameters are used in the simulations. The introduction rate

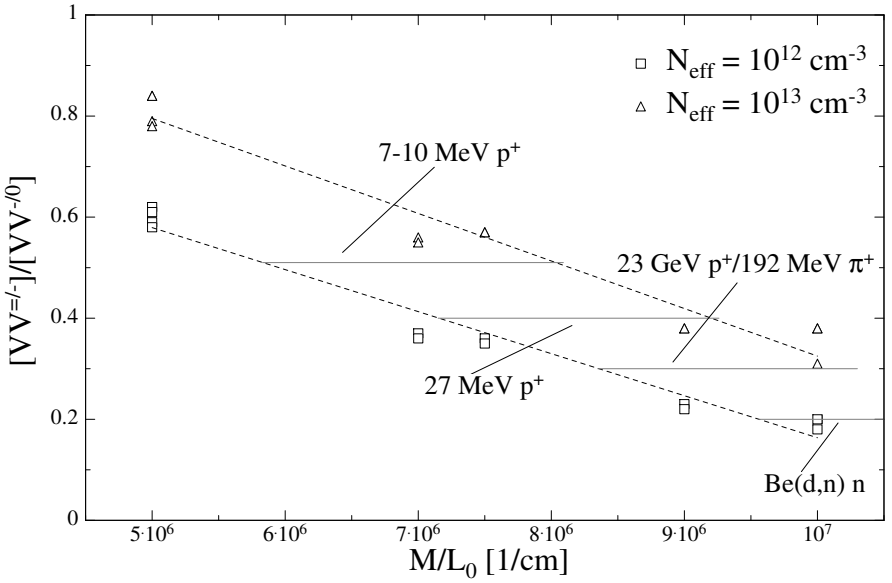

Figure 6.28: *The dependence of* $[VV^{=/-}]/[VV^{-/0}]$ *on the ratio* M/L_0 *for two effective doping concentrations are shown (symbols). For further details see text. The experimental values of* $[VV^{=/-}]/[VV^{-/0}+?]$ *for different particles are indicated by horizontal lines. Also the linear regressions of the data points are shown (dotted lines).*

of divacancies is g(VV) = 1.33 cm^{-1}. The fluences are $\Phi_{eq} = 10^{10}$ & $10^{11}cm^{-2}$ for $N_{eff} = 10^{12}cm^{-3}$ and Φ_{eq}=10^{11} & $10^{12}cm^{-2}$ for $N_{eff} = 10^{13}cm^{-3}$. The number of divacancies in a cluster are $M = 5$ for L_0=$5 \cdot 10^{-7}$cm, $M = 5$, 7 & 9 for $L_0 = 10^{-6}$cm and $M = 50$, 75 & 100 for $L_0 = 10^{-5}$cm. Thus eighteen data points are shown.

The dimension of a terminal cluster is about 10 nm. For further details see chapter 3.1.2. For $L_0 = 10^{-6}$ cm the number of divacancies in a terminal cluster is M=5−8 for 7-10 MeV proton irradiation, M=7−9 for 27 MeV proton irradiation, M=8−10 for 23 GeV proton/192 MeV pion irradiation and M=10−11 for Be(d,n) neutron irradiation. Therefore the concentration of divacancies in the center of the terminal clusters is in the range $[VV]_{cor} \approx 9 \cdot 10^{17}$ to $2 \cdot 10^{18}cm^{-3}$ and inter-center-charge-transfer is possible. But the change in the occupancies due to inter-center-charge-transfer is small under thermal equilibrium condition.

However, the dependence of the ratio $[VV^{=/-}]/[VV^{-/0}]$ on the effective doping concentration is not confirmed by the DLTS studies. Results from samples of FZ 2kΩcm (Wacker IVa) and FZ 10kΩcm (Wacker III) irradiated with reactor neutrons indicate that the ratio $[VV^{=/-}]/[VV^{-/0}+?]$ depends slightly on the effective doping concentration. It is suggested that the density of divacancies in the terminal clusters after reactor neutron irradiation is larger than after Be(d,n) neutron irradiation. Therefore the effect is more pronounced. A clear dependence of g($VV^{-/0}$+?) on the effective doping concentration is observed in samples of FZ 800Ωcm (ITME II), FZ 2kΩcm (Wacker IVa) and FZ 10kΩcm (Wacker III) after 23 GeV proton and reactor neutron irradiation. Simulation results also show a decrease of $[VV^{-/0}]/[VV]$ with decreasing effective doping concentration [Kuh00b].

The assumption of a Gaussian distribution of divacancies in the terminal clusters explains the experimental results reasonable. The core of a terminal cluster may consist of higher order vacancy and interstitial complexes or may be a disordered region. If the defect concentration is homogeneous in the terminal cluster core, the core is neutral and the Fermi level is pinned to the energy level of the defect with the largest concentration. However, no simulations are done.

6.5 Annealing studies

Annealing studies are performed at 60°C to agitate the defect kinetics. Sometimes also an additional tempering for 1280 min at 100°C is used. The DLTS spectra of an annealing study are shown in figure 6.29. The sample of oxygen rich CZ 100Ωcm (Polo III) was irradiated with Be(d,n) neutrons. The concentration of the point defects $VO_i + C_iC_s$ (E2) increases and the concentration of the cluster defects VV+? (E4, E4a & E4b) decreases. The increase of the signal $VV^{=/-}$ (E3) is explained with a decrease of the defect density in the terminal clusters. The annealing of the cluster defects VV+? occurs on the long term scale. After a tempering for about 640 min at 60°C

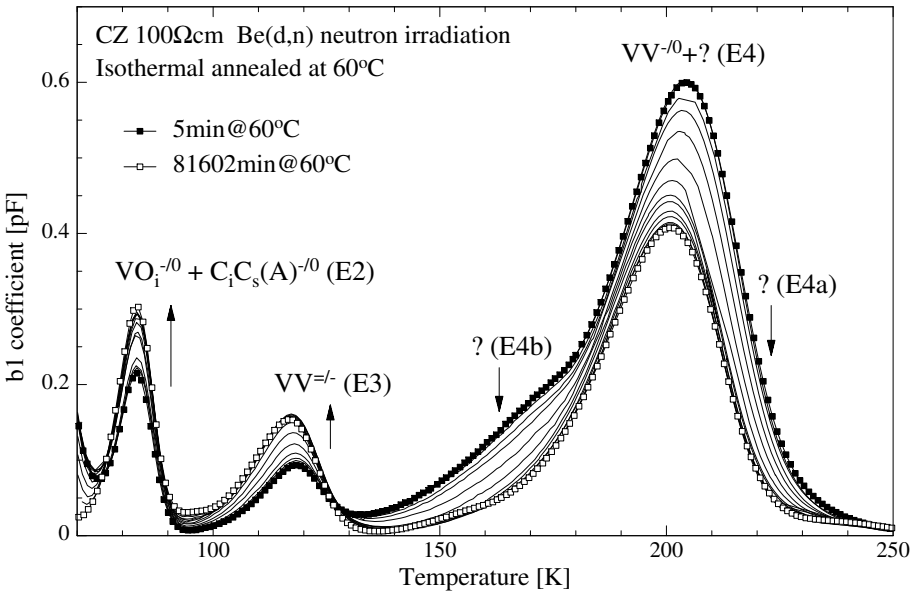

Figure 6.29: *DLTS spectra of a CZ 100Ωcm sample are shown. The signals $VO_i^{-/0} + C_iC_s(A)^{-/0}$ (E2) and $VV^{=/-}$ (E3) increase during annealing. On the left hand and right hand side of the signal $VV^{-/0}$+? (E4) the decreasing signals E4a and E4b are visible.*

the ratio $[VV^{=/-}]/[VV^{-/0}+?]$ is constant. The annealing of C_i which occurs on short term scale is shown in figure 6.2. In the sample of standard FZ 120Ωcm (ITME I) the annealing of C_i is finished after a tempering period for less than 10 min at 60°C. In the samples of standard FZ 4kΩcm (Wacker VIII) and FZ 2kΩcm (Wacker IX) the annealing of C_i is not accomplished after a tempering period for 80 min at 60°C or 4 min at 80°C. The annealing of C_i is finished during storage at room temperature for about one week.

6.5.1 Annealing of C_i

The annealing of interstitial carbon was not finished in the 23 GeV proton irradiated sample of FZ 4kΩcm (Wacker VIII) after the tempering period for 80 min at 60°C. An increase of the signal amplitudes of both defects VO_i and C_iC_s during room annealing is observed, as shown in figure 6.30. The C_i are captured at C_s and O_i sites in the environment of the terminal clusters and also capturing at divacancy sites at the peripheries of the terminal clusters occurs. For further details see chapter 3.5.1. The vacancies are released from the terminal cluster regions and are captured at O_i sites. This assumption is confirmed by the independence of the sum of the point defect concentrations during room temperature annealing, as shown in figure 6.31. The same annealing behaviour is observed in 7-10 MeV proton irradiated samples of FZ 2kΩcm (Wacker IX).

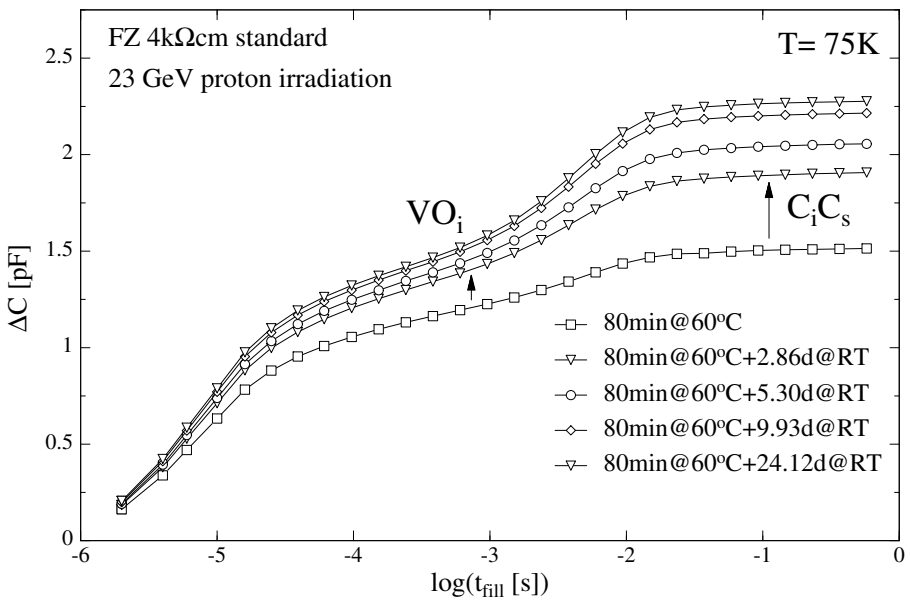

Figure 6.30: *The electrical filling characteristics of the defects VO_i and C_iC_s in a 23 GeV proton irradiated sample of FZ 4kΩcm at different annealing states are shown. The signal amplitudes of VO_i and C_iC_s increase.*

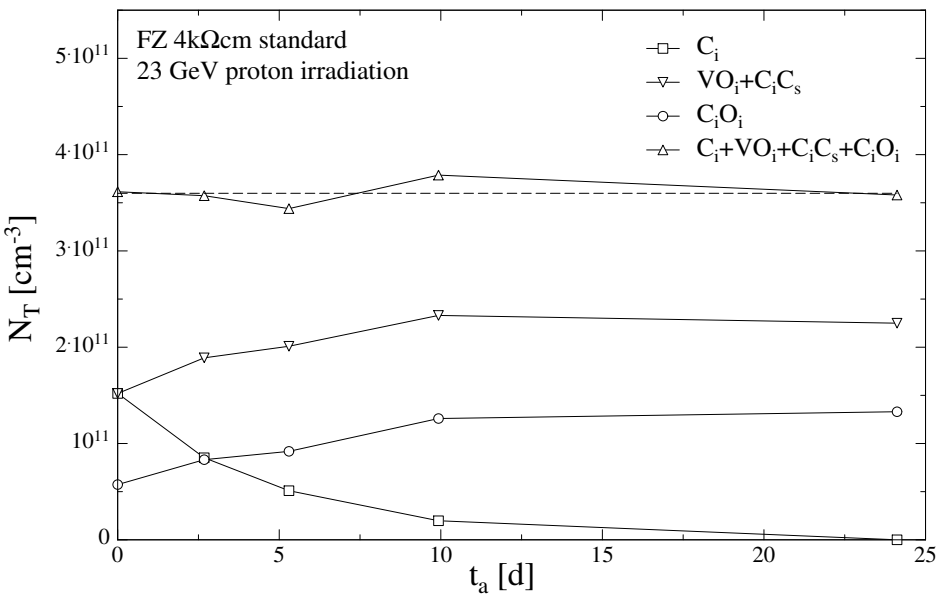

Figure 6.31: *The concentrations of the point defects during room temperature annealing in a sample of FZ 4kΩcm irradiated with 23 GeV protons are shown. Before room temperature annealing the sample was tempered for 80 min at 60° C.*

6.5.2 Annealing of $VO_i + C_iC_s$

A neutron irradiated sample of jet oxygenated FZ 800Ωcm (ITME II) was first isothermal annealed to 2560 min at 60°C and then tempered for 1280 min at 100°C. The DLTS spectra are shown in figure 6.32. The C_i annealing is already finished after a tempering period for 80 min at 60°C. The signal C_iO_i is constant. Thus a release of silicon or carbon interstitials from the terminal cluster regions is excluded. An increase of the signal $VO_i + C_iC_s$ and a decrease of the signal $VV+?$ is observed. Because the oxygen concentration is more than four orders of magnitude higher than the phosphorous concentration, the generation of VP_s defects is negligible and a decay of VP_s during the 100°C tempering can be excluded. However, it is assumed that divacancies in the terminal clusters are less stable and dissociate into single vacancies at lower temperatures as isolated divacancies. It is suggested that the elastic energy deposited in strain and deformation fields is employed to break divacancies. Also higher order vacancy complexes can release energy due to configurational changes. For further details see chapter 3.5.1. But the sum of the defect concentrations $[VO_i + C_iC_s] + 2 \cdot [VV+?]$ is not constant during annealing. However, the determination of the concentration of divacancies from the signal $VV^{-/0}+?$ is not very reliable. This item is discussed in more detail in chapter 6.5.3.

In figure 6.33 the dependence of the introduction rate g$(VO_i + C_iC_s)$ and the ratio $[VV^{=/-}]/[VV^{-/0}+?]$ in a neutron irradiated sample of CZ 100Ωcm (Polo III) on the tempering time at 60°C are shown. Both parameters are constant for tempering times $t_a > 640$ min. This indicates that the annealing of the terminal cluster damage is accomplished on this time scale.

6.5.3 Annealing of $VV+?$

The DLTS signals of the cluster defects $VV+?$ are simulated. The signals of the two negative charge states of the divacancy are calculated assuming an exponential density distribution of energy states due to lattice deformations. The b1 coefficient is obtained from

$$b_1(E_T, T) = \int_0^{+\infty} b_1(T, E_T + \text{sign} \cdot E) \cdot D(E)\ dE \tag{6.6}$$

If the sign is positive, the energy states are distributed in direction to the conduction band edge, and if the sign is negative, the energy states are distributed in direction to the valence band edge. The density function is

$$D(E) = \frac{\exp(-E/\Delta E)}{\Delta E} \tag{6.7}$$

The ratio $\Delta E/E_T$=0.04 is held constant. Only the activation energies and the amplitudes are adjusted to have a coincidence of the signals. The Gaussian-Laguerre quadrature formula (n=4) is employed to calculate the integral [Kry62]. The DLTS spectra of different annealing states together

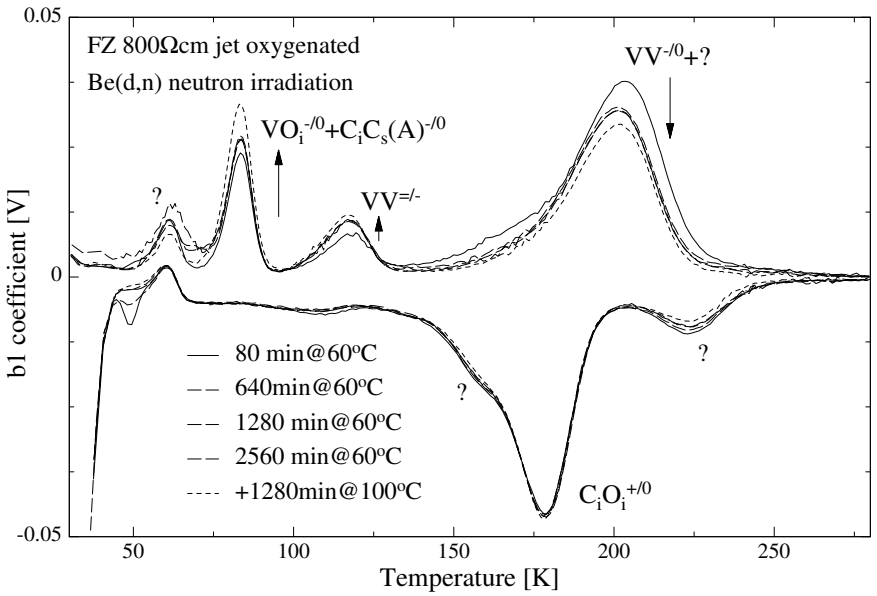

Figure 6.32: *The DLTS spectra of five different annealing states are shown. A change in the signals of the defects VO_i+C_iC_s and VV+? is observed. No change in the signal of the defect C_iO_i is seen. The defect centers are filled with minority charge carriers generated optically at the back side of the sample. The various process induced defects are labeled with question marks.*

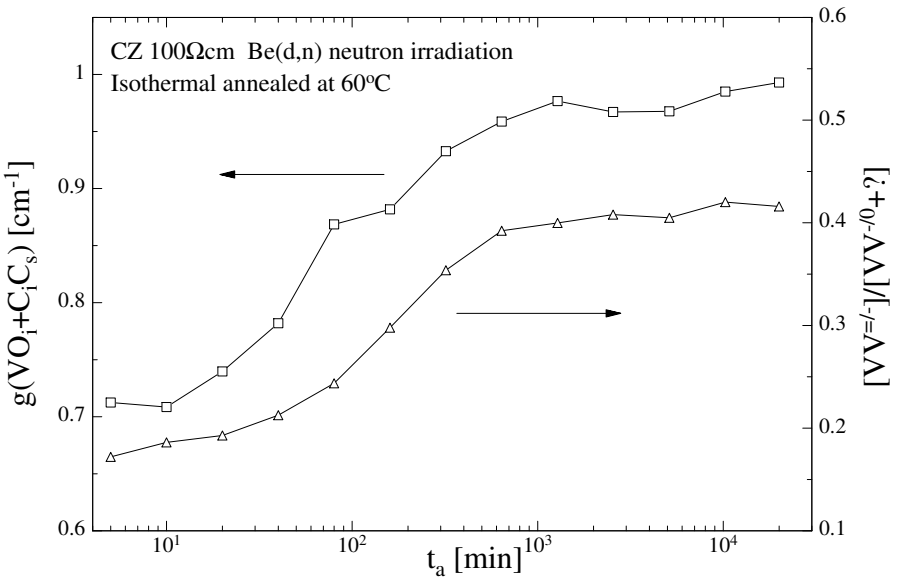

Figure 6.33: *The dependence of the introduction rate $g(VO_i + C_iC_s)$ and the ratio $[VV^{=/-}]/[VV^{-/0}+?]$ on the tempering time at 60° C are shown. For tempering times $t_a > 640$ min both parameters are constant.*

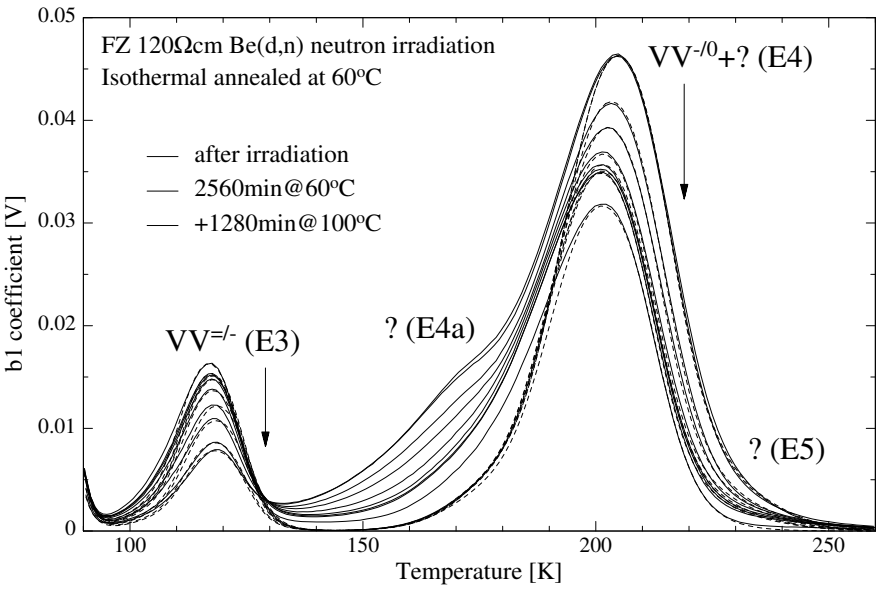

Figure 6.34: *The DLTS spectra of different annealing states (lines) and the simulations (dotted lines) are shown. The DLTS signals of the two negative charge states of the divacancy are simulated with an exponential density distribution of energy states.*

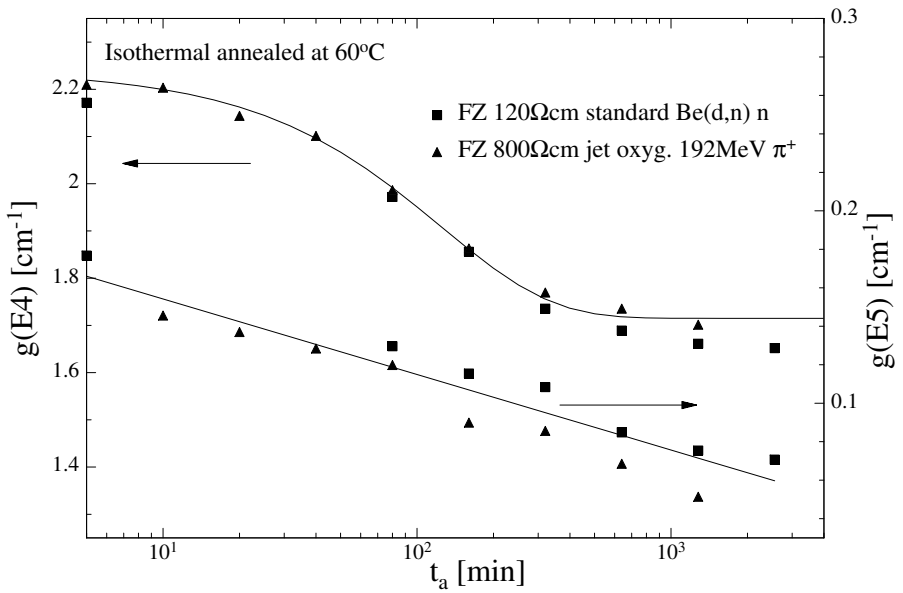

Figure 6.35: *The introduction rates of the cluster defects $VV^{-/0}$+? (E4) and ? (E5) are shown (symbols). The time dependence of g(E4) is exponential and of g(E5) logarithmic (lines).*

Table 6.14: *The parameters of the simulation for the annealing state 80 min at 60°C are listed. The effective masses are* $m_n^* = m_{th,n}^* = 1.08\, m_e$.

Defect	E_T [eV]	sign	ΔE [eV]	$\sigma_T[10^{-15}\mathrm{cm}^2]$	ΔU [V]
$VV^=$ (E3)	0.2515	+	0.01006	5.000	0.0550
VV^-+? (E4)	0.4340	+	0.01736	2.000	0.2125
? (E5)	0.5000	−	0.02000	20.00	0.0138

with the simulations are shown in figure 6.34. The sample of FZ 120Ωcm (ITME I) was first isothermal annealed to 2560 min at 60°C and then tempered for 1280 min at 100°C. The right hand side of the signal $VV^{-/0}$+? (E4), named E4b, is described reasonably by the simulation. The left hand side of the signal, named E4a, is not described by the simulation. The signal E4a is attributed to an additional density distribution of energy states which is not included in the simulation. The defect for these energy states is not known. The deviation on the left hand side decreases during annealing. Another deep defect center with a density distribution of energy states is needed to simulate the right hand tail of the signal E4, named E5. The signal E5 is totally annealed out after the tempering period at 100°C. The simulated signal $VV^{=/-}$ (E3) shows a deviation on the left side hand from the measured signal. The parameters of the simulation for the annealing state 80min at 60°C are listed in table 6.14. The activation energies of the two negative charge states of the divacancy slightly decrease during annealing. The relaxation of the lattice deformations during annealing changes the activation energies. The amplitudes of the signals E4 and E5 decrease during annealing. The dependence of introduction rates of E4 and E5 on the tempering time are shown in figure 6.35. The datas are obtained from a sample of FZ 120Ωcm (ITME I) irradiated with Be(d,n) neutrons and from a sample of jet oxygenated FZ 800Ωcm (ITME II) irradiated with 192 MeV pions. The time dependence of g(E4) is exponential $A \cdot \exp(-t_a/\tau) + B$ with A=0.525 cm^{-1}, B=1.715 cm^{-1} and τ=125 min. The obtained introduction rate g($VV^{-/0}$+?) is higher than the introduction rate obtained from the DLTS spectra using the maxima evaluation. The time dependence of g(E5) is logarithmic $a + b \cdot \ln(t_a/t_0)$ with a=0.193 cm^{-1}, b=0.017 cm^{-1} and $t_0 = 1$ min. The correlation coefficient is $r^2 = 0.897$. In the sample of jet oxygenated FZ 800Ωcm the signal E5 is not simulated as good as in the sample of FZ 120Ωcm, because the process induced defect (Au_s) is suggested to contribute to the signal.

The annealing of the signals E4a and E4b is also studied by subtracting two interpolated DLTS spectra of different annealing states from each other. The difference DLTS spectra of the Be(d,n) neutron irradiated sample of FZ 120Ωcm (ITME I) are shown in figure 6.36. Two decreasing signals are seen, also named E4a and E4b. The difference spectra indicate that the annealing of the signals E4a and E4b is finished after a tempering period for 640 min at

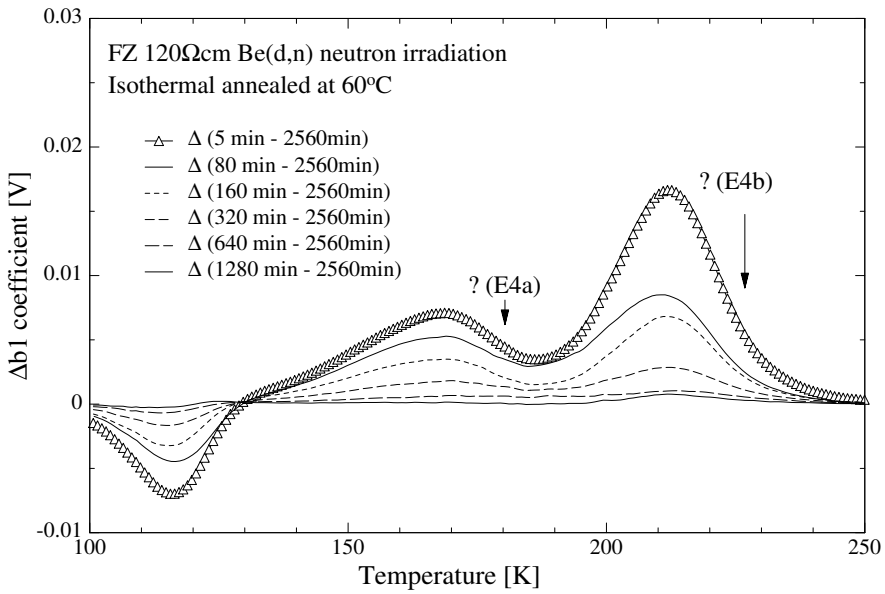

Figure 6.36: *The difference of interpolated DLTS spectra of two different annealing states are shown. The signals E4a and E4b are not visible for tempering times $t_a > 640$ min at 60° C.*

60° C. The emission parameters of the signal E4b obtained from 32 difference DLTS spectra[1] are $E_T = 0.459 \pm 0.013$ eV and $\sigma_T = 4.50 \pm 4.26 \cdot 10^{-15}\text{cm}^2$. The signal E4a is assumed to be caused by a distribution of energy states around 0.36 eV.

The localization of the defects causing the signals E4a, (E4b) and E5 is assumed to be in the terminal cluster regions, because the signals are only observed after particle irradiation.

6.5.4 Annealing of $[VV^{=/-}]/[VV^{-/0}+?]$

The annealing of the ratio $[VV^{=/-}]/[VV^{-/0}+?]$ in the sample of CZ $100\Omega cm$ (Polo III) is shown in figure 6.33. The difference in the concentrations of the two negative charge states of the divacancy is explained with the bending of the electronic band structure in the terminal cluster regions. Only a fraction of the divacancies are occupied with two electrons at low temperatures. The results of calculations assuming a Gaussian distribution of divacancies in the terminal clusters is presented in chapter 6.4.5. The ratio $[VV^{=/-}]/[VV^{-/0}]$ increases with decreasing concentration of divacancies in the terminal clusters. Because the capture characteristic $VV^0 \rightarrow VV^-$ is independent on the annealing state, as shown in figure 6.21a, it is assumed that the distribution of free electrons and the distribution of divacancies

[1] Because the samples were glued with the front side on the ceramic, an accurate determination of the defect concentrations was not possible, but the evaluation of the Arhennius plots.

in the terminal clusters is not strongly changed during annealing. Hence only the number of divacancies in the terminal clusters during annealing decreases.

6.6 Correlation with macroscopic results

The correlation of the experimental results of the microscopic defect studies with the results of the macroscopic studies is discussed. However, only the exponential part of the annealing of the leakage current can be explained with the annealing of a defect localized in the terminal cluster regions.

6.6.1 Volume generation current

The isothermal annealing of the current related damage rate α after Be(d,n) neutron irradiation correlates with the annealing of the defect E4b in the sample of CZ $100\Omega cm$ (Polo III), as shown in figure 6.37. The emission

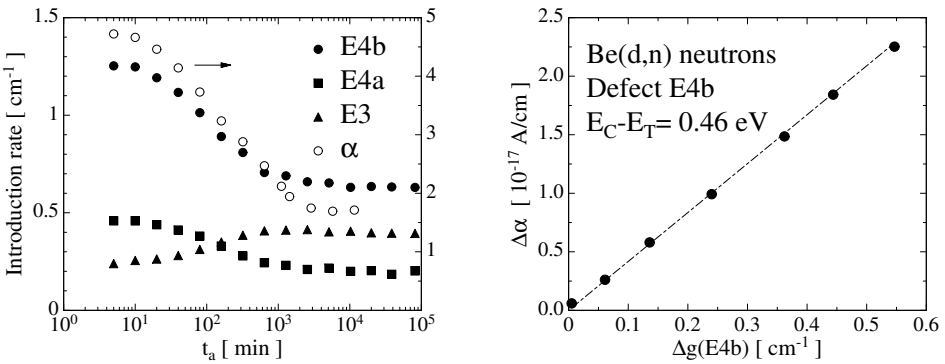

Figure 6.37: *The annealing of the defect concentrations and of the current related damage rate at 60° C are shown on the left hand side. The correlation between the change of the introduction rate $\Delta g(E4b)$ and the current related damage rate $\Delta\alpha$ is shown on the right hand side* [Fre99].

parameters of the defect E4b are E_T=0.46 eV and σ_n=$5\cdot10^{-15}$cm^2. The hole cross section is not known. But the amplitude of the exponential annealing of the current related damage rate is employed to calculate the hole cross section $\sigma_p \approx 3\cdot10^{-13}$cm^2 [Mol99]. The current related damage rate is related to the defect parameters by

$$\alpha = q_0 \cdot \frac{e_n \cdot e_p}{e_n + e_p} \cdot \frac{N_T}{\Phi_{eq}} \tag{6.8}$$

Equations 3.34, 3.31, 2.47 and 3.10 are used. A coulomb attractive center has a cross section in this order

$$\sigma_{coul} = \frac{q^4 \cdot \pi}{(8 \cdot \pi \cdot \epsilon_s \cdot k_B \cdot T)^2} = 1.80 \cdot 10^{-13}\ \mathrm{cm}^2 \tag{6.9}$$

However, it is not known, if the signal E4b is due to the emission from a single energy level in the band gap or due to lattice deformation and strain fields. For further details see chapter 6.5.3.

However, the enhanced generation rate of electron-hole (eh) pairs in the space charge region can also be explained with the inter-centre-charge-transfer between the different charge states of the divacancies in the terminal clusters [Mac97a]. The current per unit volume in the clusters J_{vol}^{clus} is approximated with

$$J_{vol}^{clus} = J_{vol,0}^{clus} \cdot (N_T\,[\mathrm{cm}^{-3}])^{\nu} \tag{6.10}$$

where $J_{vol,0}^{clus} = 4.82 \cdot 10^{-35}$ A/cm^3 and ν=1.915. The current related damage rate for a Gaussian distribution of divacancies is

$$\alpha = J_{vol,0}^{clus} \cdot g_{clus} \cdot L_0^3 \cdot \left(\frac{\pi}{\nu}\right)^{3/2} \cdot \left(\frac{M}{\pi^{3/2} L_0^3\,[\mathrm{cm}]}\right)^{\nu} \tag{6.11}$$

where M is the number of divacancies in a cluster, L_0 the width of the Gaussian distribution and g_{clus}=g(VV)/M the introduction rate of clusters. The number of clusters during annealing is constant. For M=10, L_0=10^{-6} cm and g(VV) = 2.00 cm^{-1} the current related damage rate is $\alpha = 1.83 \cdot 10^{-18}$ A/cm and hence much smaller than the measured current related damage rate $\alpha = 4.01 \cdot 10^{-17}$ A/cm after a tempering period for 80 min at $60°C$. However, the isothermal annealing of the signal $VV^{-/0}$+? (E4) has about the same time constant τ=125 min as the annealing of the exponential part of the current related damage rate. The concentration of E4 is reduced to 75% of its initial value during annealing.

The long term annealing of the volume generation current is logarithmic. The time dependence of the current related damage rate during tempering at 60°C is [Mol99]

$$\alpha(t) = \alpha_1 \cdot \exp(-t/\tau) + (\alpha_0 - \beta \cdot \ln(t/t_0)) \tag{6.12}$$

The parameters are $\alpha_1 = 1.21 \cdot 10^{-17}$ A/cm, τ = 93 min, $\alpha_0 = 6.03 \cdot 10^{-17}$ A/cm, $\beta = 0.40 \cdot 10^{-17}$ A/cm and t_0 = 1 min. Assuming that the short term annealing of the volume generation current is correlated with the concentration of E4 it is possible to separate the stable part of the current related damage rate α_0 into a portion due to the stable terminal cluster damage on the long term scale α_1^* and a portion due to the logarithmic annealing of an unknown defect species α_0^*

$$\alpha(t) = \alpha_1^* + \alpha_1 \cdot \exp(-t/\tau) + (\alpha_0^* - \beta \cdot \ln(t/t_0)) \tag{6.13}$$

The new parameters are $\alpha_1^* = 3.63 \cdot 10^{-17}$ A/cm and $\alpha_0^* = 2.40 \cdot 10^{-17}$ A/cm. The ratio is $\alpha_0^*/\beta = 6$. A correlation with the logarithmic annealing of the signal E5 is not possible, because the ratio is a/b=11.2. The signal E5 is assumed to be caused by an exponential distribution of energy states to the middle of the band gap. For further details see chapter 6.5.3. However, another not detected defect species is needed to explain the logarithmic annealing of the current related damage rate.

6.6.2 Effective space charge density

The benifical or short term annealing of the effective space charge density can be explained with the decrease of the concentration of the single negative charged divacancies in the terminal clusters. The occupancy of the single negative charge state of the divacancy is not zero in the space space region due to the inter-centre-charge-transfer. The occupancies of the four charge states of the divacancy depend on the density of divacancies in the terminal clusters, as shown in figure 6.38. But the time constant of the short term annealing τ=19 min is about six times smaller than the time constant of the annealing of g($VV^{-/0}$+?) which is assumed to be proportional to the mean density of divacancies in the terminal clusters. Also the estimated introduction rate of the short term annealing $g_a \approx g(VV^{-/0}+?) \cdot 10^{-3}$=1 − $2 \cdot 10^{-3}\mathrm{cm}^{-1}$ is one order of magnitude too small. Therefore other defects in the terminal clusters or in their environments are assumed to contribute to the negative space charge density that anneals out on the short term scale.

However, on the long term scale the inter-centre-charge-transfer rate is constant and the remaining fraction of divacancies in the single negative charge state contributes to the stable acceptor damage. Also the defect V_2O is suggested to contribute to the stable acceptor damage. This defect is assumed to contribute mainly to the effective space charge density after type inversion in ^{60}Co γ-photon irradiated samples. It is proposed that the defect V_2O has an acceptor state near the middle of the band gap (E_T=0.50 eV). The contributions of the different radiation induced defects to the effective space charge density after ^{60}Co γ-photon irradiation are shown in figure 6.39. However, the defect V_2O is only identified in a EPR study [Lee76]. The introduction rate of V_2O is too low for detection with the DLTS method.

The defect V_2O is used to explain the radiation hardness of oxygen enriched silicon. The generation of V_2O in silicon with a high oxygen content is suppressed, because the condition $[O_i] \gg [VO_i]$ is valid in a large fluence range. Thus migrating vacancies are captured mainly at O_i sites even for high fluence irradiations. But also the carbon content of the silicon is important, because the C_s sites are sinks for silicon interstitials. Therefore the reaction rate of V_2O with silicon interstitials decreases with increasing carbon concentration. In chapter 6.3.1 it is proposed that the vacancies during neutron irradiation are generated mainly in the cascade damage regions and not homogeneously. Hence the generation of V_2O occurs near the cascade damage region and an exhaustion of O_i sites is assumed to occur. The independence of the stable acceptor damage after neutron irradiation on the oxygen concentration also confirms this assumption. An overlap of the cascade damage regions is excluded for the fluences used in the macroscopic studies, because the overlap of the cascade damage regions occurs at a equivalent fluence $\Phi_{eq} = N_{clus}\, M/(g(VV)\, V_{clus}) \approx 4 \cdot 10^{16}\mathrm{cm}^{-2}$, if the diameter of the cascade damage regions is about 100 nm, the number of divacancies in a terminal cluster region M = 10 and the number of terminal clusters in cascade damage region N_{clus} = 3. During 23 GeV proton irradiation the

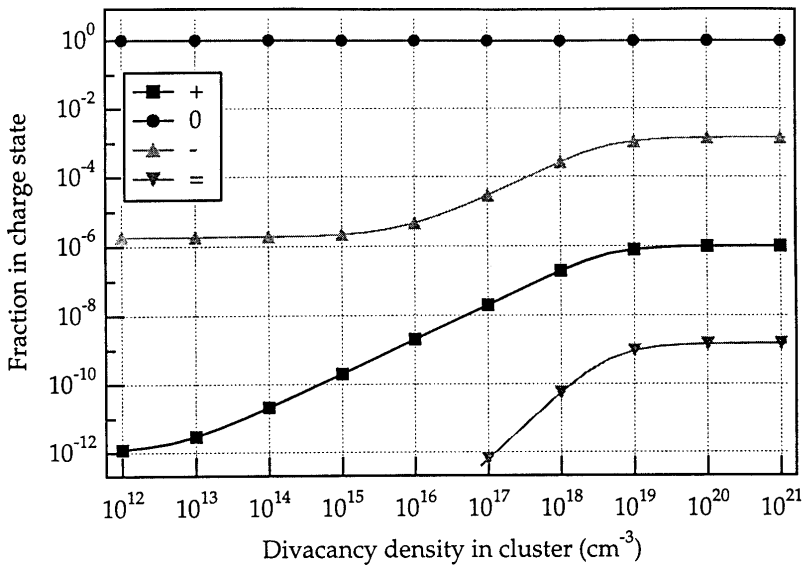

Figure 6.38: *The dependence of the fraction of divacancies in each charge state on the density of divacancies in the clusters are shown* [Mac97a].

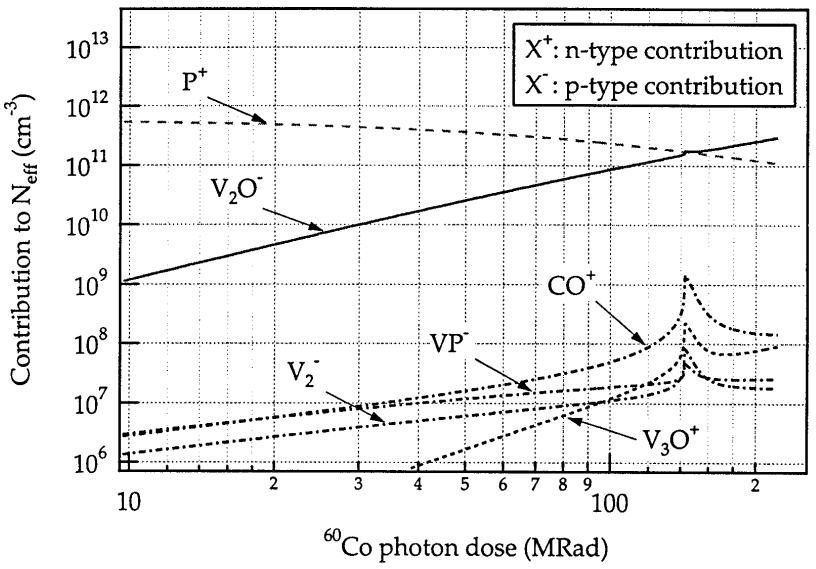

Figure 6.39: *The predicted contributions of the different radiation induced defects to the effective space charge density for ^{60}Co γ-photon irradiation are shown* [Mac97a].

generation of vacancies is more homogeneous and a dependence of the stable acceptor damage on the oxygen concentration is observed. As discussed previously also the single negative charged divacancies in the terminal clusters contribute to the stable acceptor damage. After 23 GeV proton irradiation the contribution of the negative charged divacancies to the stable acceptor damage is smaller in comparison to neutron irradiation, because the defect density in the terminal clusters is lower after 23 GeV proton irradiation compared to neutron irradiation. The particle dependence of the contributions of V_2O and negative charged divacancies to the stable acceptor damage is not known.

The donor removal after $^{6}0$Co γ-photon and particle irradiations in phosphorous doped silicon is assumed to be due to creation of VP_s defects which remove the phosphorous atoms. The generation of VP_s depends on the ratio R2 $\propto$ g(V_{mig})/g(I_{mig}), because the electrical deactivated phosphorous atoms are reactivated by the capture of silicon interstitials at VP_s sites. The donor removal is incomplete after neutron irradiation, because the ratio g(V_{mig})/g(I_{mig}) is small. It is assumed that for high fluence neutron irradiations the concentration of VP_s saturates, because the generation rate of VP_s is equal to the annihilation rate of VP_s with silicon interstitials. The silicon interstitials are assumed to be distributed homogeneously in the sample volume. Also the donor removal is only suppressed in oxygen rich CZ silicon after neutron irradiation. This confirms the assumption that the defects VP_s and the vacancy oxygen complexes VO_i and V_2O are produced near the cascade damage regions and an exhaustion of O_i sites occurs. During 23 GeV proton irradiation the homogeneous generation of vacancies due to single displacements is enhanced. Therefore the distribution of VP_s defects is more homogeneous. No saturation of the concentration of VP_s occurs, because the ratio g(V_{mig})/g(I_{mig}) is larger in comparison to neutron irradiation. Hence the donor removal is complete.

The reverse or long term annealing of the effective space charge density is only observed after particle irradiation. The radiation induced defects after low fluence irradiation in the environment of the terminal clusters, e.g. C_iC_s and C_iO_i, do not change the effective space charge density. It is assumed that higher order defects in the environment of the terminal clusters change the effective space charge density. Thus the reverse annealing of the effective space charge density occurs only after a high fluence particle irradiation. An agglomeration of higher order defects with carbon atoms in the environment of the terminal clusters is assumed, because the carbon interstitials, which are generated homogeneously in the sample volume due to the exchange of silicon interstitials with substitutional carbon atoms, are attracted by the terminal cluster regions. Also an attachment of silicon interstitials to carbon defects is proposed [Dav87]. The concentration of carbon defects in the environment of terminal clusters is high. It is assumed that the carbon defects, which envelope the terminal clusters after high fluence irradiation, are instable and a complex reaction scheme involving decays and formation of higher order carbon complexes occur. Also the evaporation of vacancies

during long term annealing from the clusters is suggested to play a role. The extension of the environment or the final migration volume of C_i depends on the particle type. In chapter 6.3.1 it is suggested that the extension of the environment after 23 GeV proton irradiation is larger than after neutron irradiation. Therefore the defect generation in the environment is more affected by the impurity content after 23 GeV proton irradiation than after neutron irradiation. This assumption is confirmed by the dependence of the amplitude of the reverse annealing on the oxygen concentration for 23 GeV proton irradiation and weak dependence of the amplitude of the reverse annealing on the oxygen concentration for neutron irradiation. The defect generation in the environment of the terminal clusters after neutron irradiation depends only on the oxygen concentration, if the concentration is in the order of 10^{18} cm^{-3}, e.g. oxygen in CZ silicon.

Chapter 7

Summary

In this thesis the microscopic properties of the radiation induced defects vacancy interstitial-oxygen VO_i, divacancy VV, interstitial carbon C_i, interstitial-carbon substitutional-carbon C_iC_s and interstitial-carbon interstitial-oxygen C_iO_i after low fluence irradiations were investigated with the DLTS method. The concentration of the radiation induced defects is below the effective doping concentration. The emission of charge carriers from the defect states and the capture of charge carriers into the defect states is used to determine the defect parameters. From the temperature dependence of the emission rate the activation energies and cross sections of the defect states are obtained. From the filling characteristics the capture rate of the defects VO_i, VV, C_i and C_iO_i and the time constant of the configurational switching of C_iC_s is determined.

Various materials with different oxygen and carbon concentrations were employed. The effective doping concentration of the n-type FZ and CZ silicon is $N_{eff} = 7 \cdot 10^{11} - 3.5 \cdot 10^{13}\text{cm}^{-3}$. The doping impurity is phosphorous. The oxygen concentration is ranging from $[O] < 2 \cdot 10^{14}$ to $9 \cdot 10^{17}\text{cm}^{-3}$ and the carbon concentration is ranging from $[C] < 5 \cdot 10^{15}$ to $3.5 \cdot 10^{16}\text{cm}^{-3}$. The oxygen and carbon concentrations were obtained from SIMS profiles at a depth greater than 50 μm. The oxygen concentration in diffusion oxygenated silicon wafers is higher at the surface. The irradiations were performed with reactor neutrons, Be(d,n) neutrons, 23 GeV protons, 192 MeV pions (π^+), 27 MeV protons, 7-10 MeV protons and ^{60}Co γ-photons. The average energy of the Be(d,n) neutrons is 5.3 MeV.

The equivalent fluence is used to calculate the introduction rates of the radiation induced defects. For the high energy particle irradiations the NIEL hypothesis is valid and the volume generation current is used to determine the equivalent fluence for the 23 GeV proton, 192 MeV pion and neutron irradiations. The cluster damage is responsible for the current generation. The NIEL hypothesis is not valid for low energy proton irradiations. The measured particle fluences and the calculated hardness factors are employed to determine the equivalent fluences.

The microscopic properties of the radiation induced defects are useful to understand the primary generation of the radiation damage, the displacement of silicon atoms out of their lattice sites, and the reaction of the primary defects silicon interstitials and vacancies with the impurities in the silicon material.

The radiation induced defects change the macroscopic parameters of silicon detectors, the leakage current and the full depletion voltage. The leakage current is proportional to the particle fluence. The proportional constant is the current related damage rate. The full depletion voltage depends on the effective space charge density.

The introduction rates of the impurity defects VO_i, C_iC_s and C_iO_i depend on the oxygen and carbon concentrations. After ^{60}Co γ-photon irradiation the introduction rates of the impurity defects are much higher than the introduction rate of the divacancies. Only in oxygen lean silicon the introduction rates are in the same order of magnitude. The introduction rate of divacancies depends not on the impurity content for standard and oxygen rich silicon.

During ^{60}Co γ-photon irradiation only isolated single displacements of silicon atoms occur. Thus silicon interstitial and vacancy pairs are created. The silicon interstitials exchange with substitutional carbon atoms and mobile carbon interstitials are generated. The vacancies are captured at O_i sites and the carbon interstitials are captured at O_i and C_s sites. Thus the impurity defects VO_i, C_iC_s and C_iO_i are formed. The ratio of the capture radii is estimated to be $R_c(C_iO_i)/R_c(C_iC_s) \approx 1/19$ and is six times smaller than the value from literature. The introduction rate of divacancies is only higher in the samples of the oxygen lean silicon, because the mean free path length of vacancies is large and vacancies generated in different collision events can capture each other. In the other materials divacancies are produced mainly by the capture of two vacancies created in the same collision event. The ratio $g(V)/g(VV) \approx 60$ is 6−7 times larger compared to 2 MeV electron irradiations. All defects are distributed homogeneously in the sample volume.

The impurity defects VO_i, C_iC_s and C_iO_i are also isolated point defects after particle irradiation, because their emission parameter are not changed. The sum of the introduction rates of point defects Σg_{point} is 6.5 cm^{-1} for 7-10 MeV proton, 4.1 cm^{-1} for 27 MeV proton, 3.3 cm^{-1} for 23 GeV proton, 3.2 cm^{-1} for 192 MeV pion, 1.8 cm^{-1} for Be(d,n) neutron and 1.5 cm^{-1} for reactor neutron irradiation. The introduction rate of the cluster defects VV+? is independent on the material type. The introduction rate is $g(VV^{-/0}+?) \approx 1.3$ cm^{-1} after 27 MeV proton, 23 GeV proton, 192 MeV pion and Be(d,n) neutron irradiation. However, the introduction rate $g(VV^{-/0}+?) \approx 1.0$ cm^{-1} after reactor neutron irradiation is lower. The shape of the signal $VV^{-/0}$+? is also particle independent. Thus the cluster damage generated by these particles is nearly identical.

The energy distribution of the primary recoiled silicon atoms or Primary

Knock on Atoms (PKAs) depends on the particle type. During neutron irradiation mainly PKAs with an energy E > 10 keV are generated and collision cascades with terminal clusters are produced. The terminal clusters are dense displacement regions. Because the mobility of silicon interstitials is much higher than the mobility of vacancies, the silicon interstitials are diluted after initial annihilation in the sample volume. The left vacancies form mainly divacancies in the terminal clusters. Thus the generation rate of divacancies is much higher for neutron irradiation in comparison to ^{60}Co γ-photon irradiation. The threshold energy at which a recoiled silicon atom starts to create a clusters is estimated to be $E_{th} \approx 300$ eV. The density of divacancies in the terminal clusters depends on the particle type.

During irradiation with charged particles more isolated single displacements are produced by low energy PKAs due to Coulomb scattering. This is the main difference between radiation damage after charged particle irradiation and neutron irradiation.

The leak of silicon interstitial related defects occurs after particle and ^{60}Co γ-photon irradiations. Because the silicon interstitials are distributed homogeneously in the sample volume during particle and ^{60}Co γ-photon irradiation, the surface annihilation of silicon interstitials is a possible explanation. However, the generation of higher order interstitial defects in the cluster regions can not be excluded.

The capture rate of defects in the environment of the terminal clusters is reduced due to a depletion region surrounding the negative charged terminal cluster regions. In oxygen enriched silicon the capture rate of VO_i after neutron irradiation is reduced, because the migrating vacancies are captured at O_i sites near the collision cascade regions. In not oxygen enriched silicon the capture rate of VO_i is constant, because the migrating vacancies are captured at O_i sites in a greater distance from the collision cascade regions. During charged particle irradiation the vacancies are generated more homogeneously in the sample volume. Thus the capture rate of VO_i is constant. Also the extension of the depletion region decreases with decreasing defect density in the clusters.

The capture characteristics of C_i indicate that the final migration of C_i occurs in the environment of the terminal clusters. Strain and deformation fields originating from the terminal clusters influence the migration of C_i. The carbon interstitials are attracted by the terminal clusters. It is assumed that no capture of C_i at O_i and C_s sites occur during migration to the terminal clusters. The extension of the final migration volume of C_i decreases with increasing strength of strain and deformation fields, which increase with the defect density in the terminal clusters. The carbon interstitials are captured at O_i and C_s sites in the environment of the terminal clusters. Also new C_s sites are generated at the terminal cluster peripheries by the capture of C_i at VV sites. The released vacancies are captured at O_i sites outside the environment. The concentrations of the defects VO_i, C_iC_s and C_iO_i increase during annealing of C_i. The sum of the four point

defect concentrations is constant. The generation of VO_i and C_iC_s is lower and the generation of C_iO_i is higher in oxygen enriched silicon compared to standard silicon. The sum of the introduction rates of point defects depends not on the oxygen and carbon content of the material. The introduction rates g(C_iC_s) and g(C_iO_i) depend on the ratio $[O]/[C]$ for 23 GeV proton irradiation and saturate for $[O]/[C] > 20$. This suggests that in oxygen enriched silicon no exhaustion of O_i sites in the environment of the terminal clusters occurs and C_s sites are generated at the terminal cluster peripheries. The other migrating C_i are captured mainly at these new C_s sites. The C_iC_s defects envelope the terminal cluster regions. The configurational switching of C_iC_s at the terminal cluster peripheries is changed. In carbon enriched FZ the C_iC_s defects are created in the environment of the terminal clusters after reactor neutron and 23 GeV proton irradiations and the configurational switching of C_iC_s is not changed. The defect kinetic of C_i after particle irradiation is different from the defect kinetic after ^{60}Co γ-photon irradiation. The details of the reaction kinetics in the environment of the terminal clusters are not understood. The annealing of C_i occurs on the short term scale and the time constant depends on the oxygen and carbon concentrations.

The ratio $[VV^{=/-}]/[VV^{-/0}+?]$ depends on the particle type. Simulations with the assumption of a Gaussian distribution of divacancies indicate that the ratio $[VV^{=/-}]/[VV^{-/0}]$ decreases with increasing ratio M/L_0, where M is the number of divacancies in a cluster and L_0 the width of the Gaussian distribution. For L_0=10 nm the number of divacancies in a cluster is M=5−8 for low energy proton irradiation and M=10−11 for neutron irradiation. Thus the concentration of divacancies in the center of the clusters is $[VV]_{cor} \approx 9 \cdot 10^{17} - 2 \cdot 10^{18}\text{cm}^{-3}$ and inter-center-charge-transfer is possible. The capture characteristics of the neutral and single negative charge states of the divacancy are reasonably described by the predicted capture characteristics assuming a Gaussian distribution of divacancies.

The annealing of the cluster damage occurs on the long term scale. The number of divacancies in the terminal clusters decreases during annealing. The elastic energy deposited into strain and deformation fields or the energy from the rearrangement of higher order vacancy complexes V_3...V_6 can be employed to break divacancies inside the cluster regions. A release of vacancies during cluster damage annealing is observed, but no release of silicon interstitials.

The broad signal $VV^{-/0}+?$ (E4) after particle irradiation indicates that also other cluster defects are generated. The subtraction of two DLTS spectra of different annealing states suggests that a broad signal E4a on the left hand side and a signal E4b on the right hand side of the signal $VV^{-/0}+?$ anneal out. The signal E4a is assumed to be caused by a distribution of energy states around 0.36 eV. The defect parameters of E4b are $E_T = 0.459 \pm 0.013$ eV and $\sigma_T = 4.50 \pm 4.26 \cdot 10^{-15}\text{cm}^2$. A correlation between the exponential annealing of the current related damage rate and E4b is possible. The hole

cross section is estimated to be $3 \cdot 10^{-13}\text{cm}^2$. A coulomb attractive center has a cross section in this order. However, it is not known, if the signal E4b is due to the emission from a single energy level in the band gap or due to lattice deformation and strain fields.

The time constant of the exponential annealing of the signal $VV^{-/0}$+? is τ=125 min and hence in the order of the time constant of the exponential annealing of the current related damage rate. Thus a correlation with the exponential annealing of the current related damage rate is possible. The electron-hole generation is enhanced in the terminal clusters due to inter-centre-charge-transfer between the different charge states of the divacancies. The exponential annealing of the current related damage rate can be explained with the decrease of the inter-centre-charge-transfer rate, but the estimated current related damage rate for a Gaussian distribution of divacancies with M=10 and L_0=10 nm is more than one order of magnitude too low.

A correlation between the logarithmic annealing of the current related damage rate and the signal E5 is not possible. The signal E5 is assumed to be caused by an exponential distribution of energy states to the middle of the band gap. However, another not detected defect species is needed to explain the logarithmic annealing of the current related damage rate.

The benifical or short term annealing of the effective space charge density can be explained with the decrease of the concentration of single negative charged divacancies in the terminal clusters. The occupancy of the single negative charge state of the divacancy is about 1/1000 in the space space region due to inter-centre-charge-transfer. But the time constant of the short term annealing τ=19 min is about six times smaller than the time constant of the annealing of g($VV^{-/0}$+?). Also the estimated introduction rate of the short term annealing $g_a \approx 1 - 2 \cdot 10^{-3}\text{cm}^{-1}$ is one order of magnitude too small. Therefore other defects in the terminal clusters or in their environments are assumed to contribute to the negative space charge density that anneals out on the short term scale. However, on the long term scale the inter-centre-charge-transfer rate is constant and the remaining fraction of divacancies in the single negative charge state contributes to the stable acceptor damage. Also the defect V_2O is suggested to contribute to the stable acceptor damage. It is proposed that the defect V_2O has an acceptor state near the middle of the band gap. After ^{60}Co γ-photon irradiation the stable acceptor damage is mainly due to the generation of V_2O. The particle dependence of the contributions of V_2O and negative charged divacancies to the stable acceptor damage is not known.

The donor removal after ^{60}Co γ-photon and particle irradiation in phosphorous doped silicon is assumed to be due to the creation of VP_s defects which remove the phosphorous atoms. The generation of VP_s depends on the ratio g(V_{mig})/g(I_{mig}), because the electrical deactivated phosphorous atoms are reactivated by the capture of silicon interstitials at VP_s sites. The donor removal is incomplete after neutron irradiation, because the ra-

tio $g(V_{mig})/g(I_{mig})$ is small. It is assumed that for high fluence neutron irradiations the concentration of VP_s saturates, because the generation rate of VP_s is equal to the annihilation rate of VP_s. Also the fraction of removed donors after neutron irradiation is only lower in oxygen rich CZ silicon. This confirms the assumption that the generation of VP_s defects and vacancy-oxygen complexes VO_i and V_2O occurs near the cascade damage regions and an exhaustion of O_i sites occurs. No saturation of the concentration of VP_s occurs during 23 GeV proton irradiation, because the ratio $g(V_{mig})/g(I_{mig})$ is larger in comparison to neutron irradiation. Also the vacancies are generated more homogeneously in the sample volume. Hence the donor removal is complete after 23 GeV proton irradiation.

The reverse or long term annealing of the effective space charge density is only observed after particle irradiation. It is assumed that higher order carbon defects in the environment of the terminal clusters change the effective space charge density. The extension of the environment after 23 GeV proton irradiation is larger than after neutron irradiation. Therefore the defect generation in the environment is more affected by the impurity content after 23 GeV proton irradiation compared to neutron irradiation. This assumption is confirmed by the dependence of the amplitude of the reverse annealing on the oxygen concentration for 23 GeV proton irradiations and the weak dependence of the amplitude of the reverse annealing on the oxygen concentration for neutron irradiations.

The radiation hardness of oxygen enriched silicon after charged particle irradiation is related to the higher introduction rates of point defects, because only the defect kinetic of point defects is influenced by the impurities oxygen and carbon. The defect V_2O is assumed to be responsible for the higher radiation tolerance of oxygen enriched silicon. The generation of V_2O in silicon with a high oxygen content is suppressed, because the condition $[O_i] \gg [VO_i]$ is valid in a large fluence range. During neutron irradiation the vacancies are created in the cascade collision regions and the migrating vacancies are captured at O_i sites near the cascade collision regions. An exhaustion of O_i sites is assumed to occur and no beneficial effect of oxygen is seen. During charged particle irradiation the migrating vacancies are created more homogeneously in the sample volume. Therefore no exhaustion of O_i sites occur and the generation of V_2O is suppressed in oxygen enriched silicon. But also the carbon content of the silicon is important, because the C_s sites are sinks for silicon interstitials. Therefore the reaction rate of V_2O with silicon interstitials decreases with increasing carbon concentration. Hence carbon rich silicon is less radiation hard.

Appendix A

Properties of crystalline silicon

The temperature dependence of the intrinsic carrier concentration, the effective densities of states, the energy of the band gap and the effective masses for crystalline silicon are reviewed and compiled in [Gre90]. The intrinsic carrier concentrations, the effective densities of states and the energies of the band gap in the temperature range 4.2−500 K are listed in table A.1. An

Table A.1: *The intrinsic carrier concentration, the effective densities of states and the energy of the band gap of crystalline silicon are listed.*

T [K]	n_i [cm^{-3}]	N_C [cm^{-3}]	N_V [cm^{-3}]	E_g [eV]
4.2	–	$4.55 \cdot 10^{16}$	$1.87 \cdot 10^{16}$	1.1700
50	$1.64 \cdot 10^{-41}$	$1.87 \cdot 10^{18}$	$9.78 \cdot 10^{17}$	1.1690
100	$1.95 \cdot 10^{-11}$	$5.31 \cdot 10^{18}$	$3.66 \cdot 10^{18}$	1.1649
150	$3.16 \cdot 10^{-1}$	$9.81 \cdot 10^{18}$	$8.16 \cdot 10^{18}$	1.1579
200	$5.03 \cdot 10^{4}$	$1.52 \cdot 10^{19}$	$1.43 \cdot 10^{19}$	1.1483
250	$7.59 \cdot 10^{7}$	$2.15 \cdot 10^{19}$	$2.20 \cdot 10^{19}$	1.1367
300	$1.07 \cdot 10^{10}$	$2.86 \cdot 10^{19}$	$3.10 \cdot 10^{19}$	1.1242
350	$3.92 \cdot 10^{11}$	$3.65 \cdot 10^{19}$	$4.13 \cdot 10^{19}$	1.1104
400	$6.00 \cdot 10^{12}$	$4.51 \cdot 10^{19}$	$5.26 \cdot 10^{19}$	1.0968
450	$5.11 \cdot 10^{13}$	$5.43 \cdot 10^{19}$	$6.49 \cdot 10^{19}$	1.0832
500	$2.89 \cdot 10^{14}$	$6.46 \cdot 10^{19}$	$7.81 \cdot 10^{19}$	1.0695

empirical formula for the intrinsic carrier concentration in the temperature range 275−375 K can be found in [Spr91]

$$n_i = 9.15 \cdot 10^{19}\ \text{cm}^{-3} \left(\frac{T}{300\text{K}}\right)^2 \exp\left(-\frac{6880\text{K}}{T}\right) \tag{A.1}$$

The effective densities of states can be described by the expressions [Gre90]

$$N_C = 2.86 \cdot 10^{19}\ \mathrm{cm}^{-3} \left(\frac{T}{300\mathrm{K}}\right)^{1.58} \tag{A.2}$$

and

$$N_V = 3.10 \cdot 10^{19}\ \mathrm{cm}^{-3} \left(\frac{T}{300\mathrm{K}}\right)^{1.85} \tag{A.3}$$

A formula for the temperature dependence of the energy band gap is obtained from [Bue94]

$$E_g\ [\mathrm{eV}] = 1.16 - 7.021 \cdot 10^{-4}\ \frac{T^2[\mathrm{K}]}{1108 + T[\mathrm{K}]} \tag{A.4}$$

The values of the effectives masses are needed to calculate the cross section from the intersection of an Arrhenius Plot. Often the temperature dependence of the effective masses is ignored and the effective mass of state density $m^*_{n,p}$ and the effective thermal mass $m^*_{th,n,p}$ are equal. The DLTS software employs the following values for the effective masses $m^*_{DLTS,n} = 1.08\, m_e$ and $m^*_{DLTS,p} = 0.558\, m_e$. The electron rest mass is $m_e = 9.1095 \cdot 10^{-31}$ kg. The cross section must be corrected with

$$\frac{\sigma_{n,p}}{\sigma_T} = m^*_{DLTS,n,p} \cdot \frac{(m^*_{th,n,p})^{1/2}}{(m^*_{p,n})^{3/2}} \tag{A.5}$$

The effective masses and the correction factors in the temperature range 4.2−500 K are listed in table A.2.

Table A.2: *The effective masses and the correction factors, if the effective masses $m^*_{DLTS,n} = 1.08\, m_e$ and $m^*_{DLTS,p} = 0.558\, m_e$ are used to calculate the cross section, are listed.*

T [K]	m^*_n/m_e	m^*_p/m_e	$m^*_{th,n}/m_e$	$m^*_{th,p}/m_e$	σ_n/σ_T	σ_p/σ_T
4.2	1.06	0.59	0.27	0.37	0.514	0.749
50	1.06	0.69	0.27	0.39	0.514	0.608
100	1.06	0.83	0.27	0.41	0.514	0.473
150	1.07	0.95	0.27	0.42	0.507	0.391
200	1.08	1.03	0.27	0.41	0.500	0.342
250	1.08	1.10	0.27	0.41	0.500	0.310
300	1.09	1.15	0.28	0.41	0.502	0.290
350	1.10	1.19	0.28	0.40	0.495	0.272
400	1.11	1.23	0.28	0.40	0.489	0.259
450	1.12	1.29	0.28	0.40	0.482	0.241
500	1.13	1.29	0.28	0.39	0.476	0.238

Appendix B

Emission parameters of radiation induced defects

The emission parameters of the radiation induced defects in various charge states obtained from the DLTS studies are listed in table B.1. The effective masses $m^*_{DLTS,n} = 1.08\,m_e$ and $m^*_{DLTS,p} = 0.558\,m_e$ are employed to calculate the cross sections. The cross sections have to be multiplied with the correction factors in table A.2.

Table B.1: *The activation energies and cross sections of the radiation induced defects in various charge states are listed. The effective masses* $m^*_{DLTS,n} = 1.08\,m_e$ *and* $m^*_{DLTS,p} = 0.558\,m_e$ *are employed to calculate the cross sections. Also the temperature ranges in which the emission parameters are determined are listed.*

Defect/Charge state	E_T [eV]	σ_T [10^{-15} cm^2]	T_{Range} [K]
Particle irradiation			
$C_i^{-/0}$	0.11	≈ 2	55−65
$VO_i^{-/0} + C_iC_s(A)^{-/0}$	0.17	≈ 10	75−95
$VV^{=/-}$	0.25	≈ 20	105−135
$VV^{-/0}$+?	0.42	≈ 2	185−230
$C_iC_s(A)^{+/0}$	0.10	≈ 10	45−55
$VV^{+/0}$	0.20	≈ 0.5	95−120
$C_i^{+/0}$	0.29	≈ 5	125−155
$C_iO_i^{+/0}$	0.36	≈ 1	160−205
^{60}Co γ-photon irradiation			
$VO_i^{-/0} + C_iC_s(A)^{-/0}$	0.17	≈ 10	75−95
$VV^{=/-}$	0.25	≈ 5	105−135
$VV^{-/0}$	0.42	≈ 1	185−230
$C_iO_i^{+/0}$	0.36	≈ 1	160−205

Appendix C

Majority charge carrier capture characteristic

In the article of Pons the voltage signal of a capture measurement is calculated from the integral [Pon84]

$$\Delta V = -\frac{q_0}{\epsilon_s} \int_0^{W_R} N_T(x,t)\, x\, dx \tag{C.1}$$

where W_R is the width of the space charge region and $N_T(x,t)$ the space and time dependent defect concentration. The voltage signal (CC-DLTS) is converted into a capacitance signal (C-DLTS) using Eq. 2.40

$$\Delta V = q_0 \frac{\overline{N_{eff}}}{2} \frac{W_R^2}{\epsilon_s} \left(1 - \frac{1}{\left(1 + \frac{\Delta C}{C_R}\right)^2} \right) \tag{C.2}$$

where $\overline{N_{eff}}$ is the mean value of the effective doping concentration. Therefore the term in the parenthesis on the right hand side is employed as the signal for the capture measurements.

The calculations in the article are not correct. A wrong approximation of the integral

$$\Psi(\nu, \nu_0) = \int_\nu^{\nu_0} \frac{d\nu}{2\nu \sqrt{\nu - 1 - \ln(\nu)}} \tag{C.3}$$

is used. The function in the integrand

$$g(\nu) = 2\nu \sqrt{\nu - 1 - \ln(\nu)} \tag{C.4}$$

can be approximated by

$$g(\nu) = 2\nu \sqrt{-1 - \ln(\nu)} \qquad \text{for } \nu < 0.285 \tag{C.5}$$

$$g(\nu) = \sqrt{2}\,(\nu - \nu^2) \qquad \text{for } \nu > 0.285 \tag{C.6}$$

Hence the integral C.3 is for $\nu < 0.285$

$$\begin{aligned}\Psi(\nu,\nu_0) &= \sqrt{-1-\ln(\nu)} - \sqrt{-1-\ln(0.285)} \\ &+ \frac{1}{\sqrt{2}}\Big(\ln(\nu_0) - \ln(1-\nu_0)\Big) \\ &- \frac{1}{\sqrt{2}}\Big(\ln(0.285) - \ln(0.715)\Big) \end{aligned} \tag{C.7}$$

and for $\nu > 0.285$

$$\Psi(\nu,\nu_0) = \frac{1}{\sqrt{2}}\Big(\ln(\nu_0) - \ln(1-\nu_0) - \ln(\nu) + \ln(1-\nu)\Big) \tag{C.8}$$

The numerical calculated integral C.3 for $\nu_0 = 0.95$ together with the approximations C.7 and C.8 are shown in figure C.1. The integral is divergent

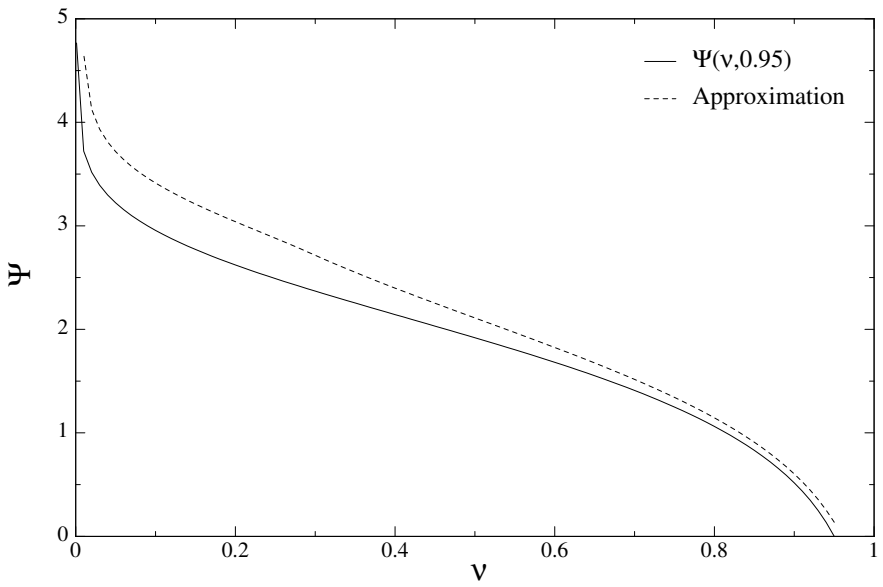

Figure C.1: *The numerical calculated integral* $\Psi(\nu, 0.95)$ *together with the approximation are shown.*

for $\nu \to 0$ and also for $\nu_0 \to 1$. The parameter ν_0, if a p^+n junction is employed for the capture measurement, is

$$\nu_0 = \frac{n}{N_{eff}} \tag{C.9}$$

where n is the free charge carrier concentration of electrons in the n-type bulk under thermal equilibrium condition and N_{eff} the effective doping concentration obtained from a CV measurement. It is assumed that in the temperature range in which the emission of a defect center is measured all states of the center are unoccupied during the CV measurement. All deeper defect centers are assumed to be occupied with majority charge carriers in

the electrical neutral bulk and also in the space charge region, because the emission rate is much lower than the capture rate and the emission time is longer than the measuring time. All shallower defect centers are assumed to be unoccupied in the electrical neutral bulk and in the space charge region, because the emission rate is much higher than the capture rate and emission time is shorter than the measuring time. The shallow doping impurity atoms are always totally ionized in the employed temperature range. Therefore the free electron concentration normalized to the effective space charge density is

$$\begin{aligned}
\frac{n}{N_{eff}} &= \frac{1}{2}\left(1 - \frac{N_T}{N_{eff}} - \frac{N_C}{N_{eff}}\, e^{-\frac{E_C - E_T}{k_B T}}\right) \\
&+ \frac{1}{2}\sqrt{\left(1 - \frac{N_T}{N_{eff}} - \frac{N_C}{N_{eff}}\, e^{-\frac{E_C - E_T}{k_B T}}\right)^2 + \frac{4\, N_C}{N_{eff}}\, e^{-\frac{E_C - E_T}{k_B T}}} \\
&\approx \frac{N_{eff} - N_T}{N_{eff}} \qquad \text{(C.10)}
\end{aligned}$$

Appendix D

Minority charge carrier capture characteristic

The time dependence of the concentration of unoccupied defect states in the lower half of the band gap, taking into account the capture and emission of holes, is

$$p_T(t) = \frac{N_T}{1 + \frac{e_p}{c_p p}} \left(1 - \exp\left(-(c_p\, p + e_p) \cdot t\right) \right) \tag{D.1}$$

where N_T is the defect concentration, e_p the hole emission rate, c_p the hole capture coefficient, p the free charge carrier density of holes. The electric field in the space charge region of a p^+n junction has a triangle shape

$$E(x) = E_{max} \cdot \left(1 - \frac{x}{W_R} \right) \tag{D.2}$$

$$E_{max} = \frac{2 \cdot (V_R + V_{bi})}{W_R} \tag{D.3}$$

where V_R is the applied reverse bias, V_{bi} the built-in voltage and W_R the width of the space charge region. The photo current of holes J_{ph} is proposed to be constant through the space charge region

$$J_{ph} = q_0 \cdot p(x) \cdot \mu_p \cdot E(x) = const. \tag{D.4}$$

where q_0 is the charge of a hole and μ_p the mobility of holes. If the density of injected charge carriers is small in comparison to the space charge density, the space dependence of the hole concentration is

$$p(x) = \frac{p_0}{1 - \frac{x}{W_R}} \tag{D.5}$$

$$p_0 = \frac{J_{ph} \cdot W_R}{2 \cdot q_0 \cdot \mu_p \cdot (V_R + V_{bi})} \tag{D.6}$$

Therefore the voltage signal of a capture measurement is calculated from

$$\Delta V = -\frac{q_0}{\epsilon_s} \cdot N_T \int_0^{W_R} \frac{1 - \exp\left(- \left(\frac{1}{\tau_{c,p} \cdot \left(1 - \frac{x}{W_R}\right)} + e_p \right) t \right)}{1 + e_p \cdot \tau_{c,p} \left(1 - \frac{x}{W_R}\right)} \, x \, dx \qquad \text{(D.7)}$$

with

$$\tau_{c,p} = \frac{1}{c_p \cdot p_0} \qquad \text{(D.8)}$$

where $\tau_{c,p}$ is the hole capture time constant at the p^+ boundary of the space charge region. The evaluation of the integral and converting the voltage signal into a capacitance signal results in

$$1 - \frac{1}{\left(1 + \frac{\Delta C}{C_R}\right)^2} = 2 \, \frac{N_T}{N_{eff}} \qquad \text{(D.9)}$$

$$\times \left\{ \frac{1 + e_p \cdot \tau_{c,p}}{(e_p \cdot \tau_{c,p})^2} \cdot \ln(1 + e_p \cdot \tau_{c,p}) - \frac{1}{e_p \cdot \tau_{c,p}} - \frac{1 + e_p \cdot \tau_{c,p}}{(e_p \cdot \tau_{c,p})^2} \cdot \exp(-e_p \cdot t) \cdot E_1\left(\frac{t}{\tau_{c,p}}\right) \right.$$

$$\left. + \frac{1}{e_p \cdot \tau_{c,p}} \cdot \exp(-e_p \cdot t) \cdot E_2\left(\frac{t}{\tau_{c,p}}\right) + \frac{1 + e_p \cdot \tau_{c,p}}{(e_p \cdot \tau_{c,p})^2} \cdot \Gamma_0\left(\frac{t}{\tau_{c,p}}(1 + e_p \cdot \tau_{c,p})\right) \right\}$$

where

$$E_n(z) = \int_1^\infty \frac{e^{-z \cdot t}}{t^n} dt \qquad \text{(D.10)}$$

is the integral exponential function and

$$\Gamma_n(z) = \int_z^\infty t^{n-1} e^{-t} dt \qquad \text{(D.11)}$$

is the gamma function.

Appendix E

Divacancy cluster with a Gaussian distribution

The calculation of the potential energy distribution in a divacancy cluster with a Gaussian distribution in n-type silicon and the calculation of the capture characteristic are described in detail.

Potential energy distribution

The density distribution of divacancies in a cluster is assumed to be

$$N_{VV}(r) = \frac{M}{\pi^{3/2}\, L_0^3} \cdot \exp\left(-\frac{r^2}{L_0^2}\right) \tag{E.1}$$

where M is the number of divacancies in a cluster and L_0 the width of the Gaussian distribution. It is assumed that the clusters are distributed homogeneously in the sample volume and that in a sphere with the radius

$$r_{max} = \sqrt[3]{\frac{3 \cdot M}{4\pi \cdot g(VV) \cdot \Phi_{eq}}} \tag{E.2}$$

surrounding a cluster the condition of charge neutrality is valid. The occupancies of the charge states of the divacancy depend on the distance of the Fermi level from the conduction band edge. The bending of the electronic band structure increases the distance of the Fermi level from the conduction band edge. The band bending energy is maximal in the cluster center and is not zero at the boundary of the sphere with the radius r_{max}. The distribution of the potential energy is spherical symmetric, because the Gaussian distribution depends only on the radius r. The occupancies of the neutral, single and double negative charge states under thermal equilibrium condition are obtained from [Sho57]. The charge density at the radius r is

$$q_0 \cdot \rho(r) = q_0 \cdot \left[N_D - n - \frac{M}{\pi^{3/2} L_0^3} \cdot \exp\left(-\frac{r^2}{L_0^2}\right) \cdot (F^- + 2 \cdot F^=)\right] \tag{E.3}$$

$$n = n_0 \cdot \exp(-\beta \cdot \psi) \tag{E.4}$$

$$F^- = \frac{f_1}{1 + f_1 + f_1 \cdot f_2} \tag{E.5}$$

$$F^= = \frac{1}{1 + f_1 + f_1 \cdot f_2} \tag{E.6}$$

$$F^0 = \frac{f_1 \cdot f_2}{1 + f_1 + f_1 \cdot f_2} \tag{E.7}$$

$$f_1 = \frac{N_C}{n_0} \cdot \exp(-\beta \cdot (E_1 - \psi)) \tag{E.8}$$

$$f_2 = \frac{N_C}{n_0} \cdot \exp(-\beta \cdot (E_2 - \psi)) \tag{E.9}$$

where ψ is the increase of the distance of the Fermi level from the conduction band edge, n the free electron concentration, n_0 the free electron concentration without divacancy clusters, the ionisation energies of the double and single negative charge states of the divacancy are E_1=0.250 eV and E_2=0.420 eV. If the generation of defects outside the clusters is neglected, the free electron concentration without divacancy clusters is equal to the shallow doping impurity concentration N_D. It is more convenient to express the densities in units of N_D, the energies in units of $1/\beta = k_B T$ and the lengths in units of $r_o = \sqrt{\epsilon_s/(q^2 \beta N_D)}$.

The spherical symmetric charge distribution is approximated by a multi shell distribution. The charge density in each shell is homogeneous. The difference between the radii of two succeeding spherical surfaces is constant. The employed number of shells is ten thousands. The potential energy at each spherical surface is calculated iteratively with

$$\Psi(r_{n+1}) = \frac{q_0 \cdot \rho(r_{n+1})}{6\,\epsilon_s} \left(r_{n+1}^2 + 2\frac{r_n^3}{r_{n+1}} - 3\,r_n^2 \right) - E_n \left(\frac{r_n^2}{r_{n+1}} - r_n \right) + \Psi(r_n) \tag{E.10}$$

$$E(r_n) = \frac{q}{3\,\epsilon_s} \cdot \frac{1}{r_n^2} \sum_{i=1}^{n} \rho(r_i) \cdot (r_i^3 - r_{i-1}^3) \tag{E.11}$$

It is more convenient to express the electric field strength in units of $E_o = q_0 N_D r_o/(\epsilon_s)$. The radius of the smallest sphere is r_0=0. The electric field is zero at r_0=0. The charge density $q_0 \cdot \rho(r_1)$ is calculated with Equation E.3 for a start value ψ_0. The band bending energy ψ and the electric field E at the radius r_1 is calculated with Equations E.10 and E.11. With $\psi(r_1)$ the charge density $q_0 \cdot \rho(r_2)$ is calculated and etc. The start value ψ_0 is varied to obtain charge neutrality

$$\sum_i \rho(r_i) \cdot (r_i^3 - r_{i-1}^3) = 0 \tag{E.12}$$

The algorithmus is written in the C programing language [Bor00].

Capture characteristic

The rate equations which describe the time dependence of the occupancies of the neutral, single and double negative charge states of the divacancy are

$$\frac{dF^{=}}{dt} = v_{th,n} \cdot \sigma_1 \cdot (n\,F^{-} - n_1\,F^{=}) \tag{E.13}$$

$$\frac{dF^{-}}{dt} = v_{th,n} \cdot \sigma_2 \cdot (n\,F^{0} - n_2\,F^{-}) \tag{E.14}$$

$$F^{0} + F^{-} + F^{=} = 1 \tag{E.15}$$

$$n = n_0 \cdot \exp(-\beta \cdot \psi) \tag{E.16}$$

$$n_1 = n_0 \cdot \exp(\beta \cdot (E_F - E_1)) \tag{E.17}$$

$$n_2 = n_0 \cdot \exp(\beta \cdot (E_F - E_2)) \tag{E.18}$$

where n is the free electron concentration which depends on the band bending energy ψ, n_0 the free electron concentration without divacancy clusters, E_F the energy of the Fermi level, E_1 and E_2 the energies of the double and single negative charge states of the divacancy and σ_1 and σ_2 the capture cross sections. However, the analytical solution of the coupled differential equations is a long expression and the numerical solution by multiplying the rate equations with a finite element Δt works only for very small time steps. But the coupling between the two differential equations is weak. Thus only Equation E.13 is used to calculate the capture characteristic $VV^{-} \rightarrow VV^{=}$ at T=125 K and Equation E.14 to calculate the capture characteristic $VV^{0} \rightarrow VV^{-}$ at T=200 K[1]. Each differential equation is solved analytically. All divacancies are in the single negative charge state at the beginning of the capture process $VV^{-} \rightarrow VV^{=}$ and all divacancies are in the neutral charge state at the beginning of the capture process $VV^{0} \rightarrow VV^{-}$. The potential energy distribution is calculated with the known occupancies of the different charge states. The value of the potential energy in the cluster center is varied to obtain charge neutrality. For further details see previous section. Thus the distribution of free electrons is obtained. The change of the occupancies after the time step Δt is calculated with the analytical solution of the proper differential equation. The initial time steps are in the order of the dielectric time constant

$$\tau_{dielec} = \frac{\epsilon_s}{q_0 \cdot n_0 \cdot \mu_n} \tag{E.19}$$

where μ_n is the mobility of electrons. Again the potential energy distribution is calculated and with the new electron distribution the change of the occupancies after another time step Δt is calculated. The width of the time steps increases logarithmical. The algorithmus is repeated until the change in the concentrations of the two charge states is negligible. The potential energy distribution of the steady state coincides with the one obtained under thermal equilibrium condition.

[1] A comparison between capture characteristics taking into account all three charge states with capture characteristics taken into account only the neutral and single charge states of the divacancy at T=200 K indicates nearly no deviations.

Appendix F

Irradiated samples

Table F.1: *Neutron irradiated samples*

Sample	Material	$N_{eff}[10^{12}\mathrm{cm}^{-3}]$	$\Phi_{eq}[10^{10}\mathrm{cm}^{-2}]$	κ	Period
Samples irradiated with Be(d,n) neutrons					
PI5177	Polo I	2.26	5.88	1.50	3/98
PI5716	Polo Ia	2.02	5.88	1.50	3/98
963G02	Polo III	35.0	58.5	1.45	4/97
II02A2	ITME I	35.9	108	1.50	1/98
II02A7	ITME I	37.3	293	1.47	1/98
IICA02	ITME II	7.10	6.08	1.50	3/98
IICA04	ITME II	6.41	24.6	1.46	3/98
IICA14	ITME II	6.30	125	1.48	3/98
WI3239	Wacker I	12.8	6.08	1.50	3/98
WI3262	Wacker I	12.3	12.5	1.48	3/98
Samples irradiated with reactor neutrons					
IIKA24	ITME II	6.45	22.0	0.90	4/99
I20304	ITME III	3.85	9.58	0.90	11/98
I20305	ITME III	-	4.78	0.90	11/98
P50320	Polo II	3.53	4.87	0.90	11/98
P50323	Polo II	3.18	9.74	0.90	11/98
609201	Wacker III	0.774	5.89	0.90	11/98
605107	Wacker III	0.793	6.48	0.90	4/99
605101	Wacker III	0.714	10.7	0.90	4/99
WI3203	Wacker I	12.5	37.2	0.90	4/99
S05A01	Wacker IVa	2.83	6.48	0.90	4/99
S05A04	Wacker IVa	2.74	10.7	0.90	4/99

Table F.2: *Charged particle irradiated samples*

Sample	Material	$N_{eff}[10^{12}\mathrm{cm}^{-3}]$	$\Phi_{eq}[10^{10}\mathrm{cm}^{-2}]$	κ	Period
Samples irradiated with 23 GeV protons					
IIEA05	ITME II	5.69	7.70	-	11/98
P50319	Polo II	2.79	6.14	-	11/98
WI3420	Wacker I	12.5	7.43	-	11/98
715603	Wacker III	0.734	7.81	-	11/98
607316	Wacker III	0.522	10.6	-	9/99
S08A11	Wacker IVa	1.99	7.55	-	5/99
S22A01	Wacker Vb	2.96	7.20	-	5/99
S32A17	Topsil Ia	1.33	7.71	-	5/99
S36A13	Topsil Ib	1.32	7.11	-	5/99
W32015	Wacker VIc	2.31	2.60	-	9/99
W31611	Wacker VIIc	2.31	2.60	-	9/99
W31910	Wacker VId	2.23	2.60	-	9/99
W30913	Wacker VIId	2.60	2.60	-	9/99
C06080	Wacker VIII	1.70	10.2	-	9/99
C09077	Wacker VIIIe	1.46	10.0	-	9/99
C13090	Wacker VIIIf	1.49	10.2	-	9/99
C03006	Topsil II	3.31	9.55	-	9/99
C02054	Topsil IIg	4.10	9.55	-	9/99
Samples irradiated with 27 MeV protons					
IIEA26	ITME II	6.53	53.0	2.41	2/99
IIEA13	ITME II	6.01	96.4	2.41	2/99
Samples irradiated with 7-10 MeV protons					
W33439	Wacker IX	2.25	27.2	3.90	2/00
W33422	Wacker IX	2.19	23.7	3.41	2/00
W33412	Wacker IX	2.37	21.1	3.03	2/00
W33402	Wacker IX	2.26	19.0	2.74	2/00
Samples irradiated with 192 MeV pions					
II05A1	ITME I	35.7	148	1.32	12/98
IIKA18	ITME II	6.00	37.3	1.24	12/98
I20311	ITME III	3.71	13.1	1.18	12/98
WI3244	Wacker I	11.4	48.4	1.15	12/98

Table F.3: *^{60}Co γ-photon irradiated samples*

Sample	Material	$N_{eff}[10^{12}\mathrm{cm}^{-3}]$	$\Phi_\gamma[10^{14}\mathrm{cm}^{-2}]$	Period
Samples irradiated with ^{60}Co γ-photons				
IIGA26	ITME II	6.49	9.51	9/98
IIGA25	ITME II	6.63	19.0	9/98
963G36	Polo III	34.6	73.3	9/98
963G32	Polo III	35.2	190	9/98
WI3437	Wacker I	12.7	9.51	9/98
WI3451	Wacker I	12.6	73.3	9/98
WI3417	Wacker I	11.7	1120	9/98
WI04A2	Wacker II	1.48	3.87	9/98
WI05A1	Wacker II	1.27	9.51	9/98
606606	Wacker III	0.837	3.87	9/98
606609	Wacker III	1.00	9.51	9/98
606611	Wacker III	1.03	73.3	9/98

List of Figures

1.1 Expected damage of the ATLAS experiment 2

2.1 Diamond crystal structure and sp^3-hybrid 4
2.2 Energy band structure and first Brillouin zone 5
2.3 Phonon dispersion spectrum 6
2.4 Schematic band with impurities 9
2.5 Formation of pn junction 11
2.6 Biased pn junction 15
2.7 Shockley contact 17
2.8 Cross section $p^+ \nu n^+$ structure 21
2.9 IV characteristics 23
2.10 CV and CC characteristics 23

3.1 Surface damage 26
3.2 Collision cascade damage 27
3.3 Displacement damage cross section 31
3.4 Relative damage efficiency for different particles 32
3.5 Configurations of C_iC_s 36
3.6 Divacancy and Jahn-Teller distortion 37
3.7 Capture and emission processes 40
3.8 Dissociation of radiation induced defects 44
3.9 Energy diagrams of different reaction processes 48

4.1 SIMS measurement 52
4.2 Calibration factor - 192 MeV pion irradiation 54
4.3 Blockdiagram of the IV/CV setup 55
4.4 DLTS operation cyclus 56
4.5 Weighting of transients with a boxcar integrator 57

4.6 Transition region 59
4.7 Weighting functions 61
4.8 DLTS spectra and Arrhenius Plot 62
4.9 Approximation of the Delta function 65
4.10 Transient Response of 8^{th} order Bessel filter 65
4.11 Error in the defect concentration 69
4.12 Blockdiagram of the DLTS setup 71
4.13 Hot stage of the DLTS setup 72
4.14 Schematic circuit of the capacitance meter 73
4.15 Absorption length 75

5.1 Annealing of the leakage current 77
5.2 Annealing of the effective doping concentration 77
5.3 Reverse annealing - 23 GeV protons 79
5.4 Stable damage - 23 GeV protons 79
5.5 Radiation scenario - Charged particles 80
5.6 Radiation scenario - Oxygen and carbon 80
5.7 Radiation scenario - Donor removal 81

6.1 DLTS spectra - Process induced defects 85
6.2 DLTS spectrum - standard FZ 88
6.3 DLTS spectra - Particle dependence 88
6.4 Introduction rates - Particle dependence 90
6.5 Ratio - Negative charge states VV 90
6.6 Threshold energy of cluster formation 91
6.7 Concentration profile $VO_i + C_iC_s$ 91
6.8 Introduction rates - Material dependence 94
6.9 Introduction rates - 23 GeV protons/192 MeV pions 94
6.10 DLTS spectrum - ^{60}Co γ-photons 96
6.11 Electrical filling $VO_i + C_iC_s$ - ^{60}Co γ-photons 100
6.12 Electrical filling $VO_i + C_iC_s$ - ^{60}Co γ-photons 100
6.13 Electrical filling $VO_i + C_iC_s$ - 10 MeV protons 101
6.14 Electrical filling $VO_i + C_iC_s$ - Be(d,n) neutrons 101
6.15 Electrical filling $VO_i + C_iC_s$ - Oxygen dependence 102
6.16 Electrical filling $VO_i + C_iC_s$ - Particle dependence I 102
6.17 Electrical filling $VO_i + C_iC_s$ - Particle dependence II 103

6.18 Electrical filling $VO_i + C_iC_s$ - Carbon enriched FZ 103
6.19 Configurational switching of C_iC_s 104
6.20 Electrical filling C_iO_i - Particle dependence 104
6.21 Electrical filling VV - Particle dependence 109
6.22 Electrical filling C_i - 23 GeV proton 111
6.23 Electrical filling C_i - 10 MeV proton 111
6.24 Optical filling C_i - 23 GeV proton 112
6.25 Optical filling C_iO_i - 23 GeV proton 112
6.26 Electrical/Optical filling $VO_i + C_iC_s$ - 23 GeV proton 113
6.27 Ratio R4 - Material dependence 119
6.28 Simulation - Negative charge states VV 121
6.29 DLTS spectra - Annealing I 123
6.30 $VO_i + C_iC_s$ - Annealing 124
6.31 Isolated point defects - Annealing 124
6.32 DLTS spectra - Annealing II 126
6.33 Introduction rates - Annealing 126
6.34 DLTS spectra/Simulations VV 127
6.35 Introduction rates of cluster defects E4 and E5 127
6.36 Difference DLTS spectra $VV^{-/0}$+? 129
6.37 Annealing of E4b and α 130
6.38 Inter-center-charge-transfer 133
6.39 Simulated defect generation - ^{60}Co γ-photons 133

C.1 Integral $\Psi(\nu, 0.95)$ and approximation 146

List of Tables

4.1 Material properties 50
4.2 Material processing and impurity concentrations 51

6.1 Process induced defects 86
6.2 Introduction rates - Particle dependence 87
6.3 Introduction rates - 7-10 MeV protons 95
6.4 Introduction rates - 23 GeV protons 95
6.5 Introduction rates - Point/Cluster defects 95
6.6 Introduction rates - ^{60}Co γ-photons 96
6.7 Cross section - Neutral charge state VV 107
6.8 Sample description - Capture measurement VV 107
6.9 Cross section - C_i and C_iO_i 113
6.10 Ratios - ^{60}Co γ-photons 116
6.11 Ratios - Particle dependence 117
6.12 Ratios - 23 GeV protons 118
6.13 Ratios - 8-10 MeV protons 120
6.14 Simulation parameters - Cluster defects $VV+?$ 128

A.1 Properties silicon I 142
A.2 Properties silicon II 143

B.1 Radiation induced defects 144

F.1 Neutron irradiated samples 153
F.2 Charged particle irradiated samples 154
F.3 ^{60}Co γ-photon irradiated samples 155

Bibliography

[Art97] E. Artacho et al.: *Interstitial oxygen in germanium and silicon* Phys. Rev. B **56** (7) 3820 (1997)

[Ash76] N.W. Ashcroft and N.D. Mermin : *Solid state physics* Harcourt Brace College Publishers ISBN 0-03-049346-3 (1976)

[Ben97] J.L. Benton et al.: *Evolution from point to extended defects in ion implanted silicon* J. Appl. Phys. **82** (1) 120 (1997)

[Bis00] D. Bisello et al.: *Radiation damage of standard and oxygenated silicon diodes by 16, 21 and 27 MeV protons* 5^{th} ROSE Workshop RD48, March 2000

[Bon98] A. Bongiorno et al.: *Interaction between a monovacancy and a vacancy cluster in silicon* Phys. Rev. B **57** (15) 8767 (1998)

[Boo88] Instruction Manual Model 72B Capacitance Meter 7/88

[Bor00] Borland Homepage http://www.borland.com/

[Bou83] J. Bourgoin and M. Lannoo: *Solid-State sciences 35: Point defects in semiconductors II* Springer-Verlag Berlin ISBN 3-540-11515-3 (1983)

[Bra79] P. Bräunlich: *Topics in Applied Physics Volume 37: Thermally stimulated relaxation in solids* Springer-Verlag Berlin ISBN 3-540-09595-0 (1979)

[Bro00] T.J. Brodbeck et al.: *A new method of carrier trapping time measurement* to be published (2000)

[Bue94] K. Buecher et al.: *Absorption coefficient of silicon: An assessment of measurements and the simulation of temperature variation* J. Appl. Phys. **75** (2) 1127 (1994)

[Cas98] G. Casse: *The effect of hadron irradiation on the electrical properties of particle detectors made from various silicon materials* Ph.D. thesis, Universite Joseph Fourier - Grenoble 1 (1998)

[Cas00] G. Casse et al.: *Analysis of transient response of LED-illuminated diodes under heavy radiation damage* Nucl. Instr. and Meth. A **443** 148 (2000)

[Cin00] V. Cindro et al. *Bias-dependent radiation damage in high-resistivity silicon diodes irradiated with heavy charge particles* Nucl. Instr. and Meth. A **450** 288 (2000)

[Dav87] G. Davies: *A model for radiation damage effects in carbon-doped crystalline silicon* Semicond. Sci. Technol. **2** (8) 524 (1987)

[Dus70] G.A. Dussel et al.: *Field-Enhanced Ionization* Phys. stat. sol. **39** 375 (1970)

[Eng83] O. Engström et al.: *Energy concepts of insulator-semiconductor interface traps* J. Appl. Phys. **54** (9) 5240 (1983)

[Ere95] V. Eremin et al.: *Trapping induced N_{eff} and electrical field transformation at different temperatures in neutron irradiated high resistivity silicon detectors* Nucl. Instr. and Meth. A **360** 458 (1995)

[Fei97] H. Feick: *Radiation tolerance of silicon particle detectors for high-energy physics experiments* Ph.D. thesis, University of Hamburg (1997)

[Fon00] L. Fonseca et al.: *Silicon wafer oxygenation from SiO_2 layers for radiation hard detectors* Technical Report ROSE/TN/2000-1, CERN (2000)

[Fre99] E. Fretwurst et al.: *Relation between microscopic defects and macroscopic changes in silicon detector properties after hadron irradiation* 1^{st} ENDEASD Workshop, Santorini (Greece) April 1999

[Gar89] J.M. McGarrity et al.: *Ionizing Radiation Effects in MOS Devices* Springer Series in Materials Science 13: Semiconductor Silicon, Editors: G.C. Harbeke and M.J. Schulz, Springer-Verlag Berlin Heidelberg (1989)

[Gil97] K. Gill et al.: *Bulk damage effects in irradiated silicon detectors due to clustered divacancies* J. Appl. Phys. **82** (1) 126 (1997) and Erratum J. Appl. Phys. **85** (11) 7990 (1999)

[Gos59] B.R. Gossik: *Disordered regions in semiconductors bombarded by fast neutrons* J. Appl. Phys. **30** (8) 1214 (1959)

[Gra95] K. Graff: *Metal impurities in silicon-device fabrication* Springer Series in Materials Science 24 Springer-Verlag Berlin Heidelberg ISBN 3-540-58317-3 (1995)

[Gre90] M.A. Green: *Intrinsic concentration, effective densities of states, and effective mass in silicon* J. Appl. Phys. **67** (6) 2944 (1990)

[Has97] J.L. Hastings et al.: *Vacancy aggregates in silicon* Phys. Rev. B **56** (16) 10215 (1997)

[Hen77] C. H. Henry et al.: *Nonradiative capture and recombination by multiphonon emission in GaAs and GaP* Phys. Rev. B **15** (2) 989 (1977)

[Hol70] R.R Holmes: *Carrier removal in neutron irradiated silicon* IEEE NS-**17** (6) 137 (1970)

[How87] L.M. Howe et al. *Heavy ion damage in silicon and germanium* Nucl. Instr. and Meth. B **19/20** 61 (1987)

[Huh93a] M. Huhtinen et al.: *Pion induced displacement damage in silicon devices* Nucl. Instr. and Meth. A **335** 580 (1993)

[Huh93b] M. Huhtinen et al.: *Estimation of pion induced displacement damage in silicon* University of Helsinki, Finland (1993)

[Huh00] M. Huhtinen: *Hadron Interactions in Si* 5^{th} ROSE Workshop RD48, March 2000

[Iba93] H. Ibach and H. Lüth: *Festkörperphysik* Springer Verlag ISBN 3-540-52193-3 (1993)

[Ist97] A.A. Istratov: *New correlation procedure for the improvement of resolution of deep level transient spectroscopy of semiconductors* J. Appl. Phys. **82** (6) 2965 (1997)

[Kit93] C. Kittel: *Einührung in die Festkörperphysik* Oldenbourg Verlag ISBN 3-486-22716-5 (1993)

[Kuh97] M. Kuhnke: *Untersuchung von Defekten in MOS-Dioden nach Schädigung mit 20 keV Elektronen* Diploma thesis, University of Hamburg (1997)

[Kuh00a] M. Kuhnke: http://sesam.desy.de/ kuhnke/

[Kuh00b] M. Kuhnke et al.: *Comparison of microscopic properties of clustered divacancies in n-type silicon with DLTS results* 6^{th} ROSE Workshop RD48, October 2000

[Kry62] V.I. Krylov: *Approximate calculation of integrals* Maximillan, New York (1962)

[Laz87] M.S. Lazo et al. *Radiation damage analysis of State-of-the-Art Microelectronics* Space Nuclear Power Systems 1986 edited by M.S. El-Genk and M.D. Hoover Orbit Book Company (1987)

[Lee76] Y.H. Lee et al.: *EPR studies of defects in electron irradiated silicon: A triplet state of oxygen.vacancy complexes* Phys. Rev. B **13** (6) 2653 (1976)

[Lin72] V.A.J van Lint et al.: *Energy dependence of displacement effects in semiconductors* IEEE NS-**19** (6) 181 (1972)

[Lin79] R.H. van der Linde et al.: *Reorientations of divancancies in silicon* Inst. Phys. Conf. Ser. No. **46** 242 (1979)

[Lin87] V.A.J van Lint: *The physics of radiation damage in particle detectors* Nucl. Instr. and Meth. A **253** 453 (1987)

[Lin99] G. Lindstroem et al.: *Radiation hardness of silicon detectors - a challenge from high-energy physics* Nucl. Instr. and Meth. A **426** 1 (1999)

[Lin00] G. Lindstroem et al.: *Radiation hard silicon detectors - development by the RD48 (ROSE) collaboration* - Technical note ROSE/TN/2000-03 and ROSE/TN/2000-06 to be published

[Lut96] G. Lutz: *Effects of deep level defects in semiconductor detectors* Nucl. Instr. and Meth. A **377** 234 (1996)

[Lut99] G. Lutz: *Semiconductor radiation detectors* Springer-Verlag Berlin ISBN 3-540-64859-3 (1999)

[Ma89] T.P Ma and P.V. Dressendorfer: *Ionizing radiation effects in MOS devices and circuits* Verlag Wiley&Sons ISBN 0471-84893-X (1989)

[Mac96] B.C. MacEvoy et al.: *Defect evolution in irradiated silicon detector material* Nucl. Instr. and Meth. A **374** 12 (1996)

[Mac97a] B.C. MacEvoy: *Defect kinetics in silicon detector material for applications at the Large Hadron Collider* Ph.D. thesis, Imperial College London (1997)

[Mac97b] B.C. MacEvoy et al.: *Defect engineering radiation tolerant silicon detectors* Solid State Phenomena Vols. 57-58 221 (1997)

[Mad81] F.L. Madarasz et al.: *Effective masses for nonparabolic bands in p-type silicon* J. Appl. Phys. **52** (7) 4646 (1981)

[Mar81] P.A. Martin et al.: *Electric field enhanced emission from non-Coulombic traps in semiconductors* J. Appl. Phys. **52** (12) 7409 (1981)

[McK48] W.A. McKinley et al.: *The coulomb scattering of relativistic electrons by nuclei* Phys. Rev. **74** (12) 1759 (1948)

[Mol58] J.L. Moll: *The evolution of the theory for the voltage characteristic of P-N junctions* Proc. IRE **46** 1076 (1958)

[Mol97] E. Moll et al.: *Comparison of defects produced by fast neutrons and ^{60}Co-gammas in high-resistivity silicon detectors using deep-level transient specroscopy* Nucl. Instr. and Meth. A **388** 335 (1997)

[Mol99] M. Moll: *Radiation damage in silicon particle detectors* Ph.D. thesis, University of Hamburg (1999)

[Mol00] M. Moll: *ROSE Contribution to the LEB Workshop* 6^{th} ROSE Workshop RD48, October 2000

[Mue80] G.P. Mueller et al.: *Simulations of cascade damage in silicon* IEEE NS-**27** (6) 1474 (1980)

[Mue82] G.P. Mueller et al.: *The structure of displacement cascades in silicon* IEEE NS-**29** (6) 1493 (1982)

[NIS99] T-2 Nuclear Information Service, Los Alamos: http://t2.lanl.gov/

[Nor97] K. Nordlund: http://www.helsinki.fi/ knordlun/work.html

[Nor98] K. Nordlund et al.: *Defect production in collision cascade in elemental semiconductors and fcc metals* Phys. Rev. B **57** (13) 7556 (1998)

[Nor00] K. Nordlund: Private communication June 2000

[Opt00] OPTO DIODE CORP., California/USA: http://www.optodiode.com/

[Pon84] D. Pons: *Accurate determination of the free carrier capture kinetics of deep traps by space-charge methods* J. Appl. Phys. **55** (10) 3644 (1984)

[PRD98] Physical Reference Data: http://physics.nist.gov/PhysRefData/contents.html

[Rae96] J. Raebiger et al.: *Carrier lifetime and x-ray imaging correlations of an oxide-induced stacking fault ring and its gettering behavior in Czochralski silicon* Appl. Phys. Lett. **69** (20) 3037 (1996)

[Ros00] ROSE Collaboration: 3^{rd} *RD48 Status Report* CERN/LHCC 2000-009 LEB Status/RD48

[Rua83] M.O. Ruault et al. *Transmission electron microscopy study on ion implantation induced Si amorphization* Nucl. Instr. and Meth. **209/210** 351 (1983)

[Ruz99a] A. Ruzin et al.: *Radiation effects in silicon detectors processed on carbon and oxygen rich substrates* Technical Report ROSE/TN/99-5, CERN (1999)

[Ruz99b] A. Ruzin et al.: *Radiation hardness of silicon detectors processed on various oxygen-enriched wafers*
ROSE Meeting RD48, June 1999

[Shi94] F. Shimura: *Oxygen in silicon* Semiconductors and Semimetals Vol. 42, Academic Press INC., ISBN 0-12-752142-9 (1994)

[Sho52] W. Shockley et al.: *Statistics of the recombinations of holes and electrons* Phys. Rev. **87** (5) 835 (1952)

[Sho57] W. Shockley et al.: *Statistics of the charge distribution for a localized flaw in a semiconductor* Phys. Rev. **107** (2) 392 (1957)

[Smi66] E.C. Smith et al.: *Theoretical and experimental determination of the neutron energy deposition in silicon* IEEE NS-**13** (6) 11 (1966)

[Son90] L.W. Song et al.: *Bistable interstitial-carbon substitutional -carbon pair in silicon* Phys. Rev. B **42** (9) 5765 (1990)

[Spr91] A.B. Sproul et al.: *Improved value for the silicon intrinsic carrier concentration from 275 to 375K* J. Appl. Phys. **70** (2) 846 (1991)

[Sto70] E. Storm et al.: *Photon cross sections from 1 keV to 100 MeV for the elements Z=1 to Z=100* Nuclear Data Tables A **7** 565 (1970)

[Sum93] G.P. Summers et al.: *Damage correlations in semiconductors exposed to gamma, electron and proton radiations* IEEE NS-**40** (6) 1372 (1993)

[Sve92] B.G. Svensson et al.: *Generation of divacancies in silicon by MeV electrons: Dose rate dependence and influence of Sn and P* J. Appl. Phys. **72** (12) 5616 (1992)

[Sve97] B.G. Svensson et al.: *Generation of vacancy-type point defects in single collison cascades during swift-ion bombardment of silicon* Phys. Rev. B **55** (16) 10498 (1997)

[Sze81] S.M. Sze: *Physics of Semiconductor Devices* John Wiley & Sons, Inc. ISBN 0-471-05661-8 (1981)

[Sze85] S.M. Sze: *Semiconductor devices Physics and Technology* John Wiley & Sons, Inc. ISBN 0-471-83704-0 (1985)

[Tie93] U. Tietze and C. Schenk: *Halbleiter-Schaltungstechnik* Springer-Verlag Berlin ISBN 3-540-56184-6 (1993)

[Vas82] A.V. Vasil'ev et al.: *Capacitance spectroscopy investigation of defects formed in n-type silicon by neutron irradiation* Sov. Phys. Semicond. **16** (11) 1279 (1982)

[Vas86] A.V. Vasil'ev et al.: *Divacancy levels in the band gap of silicon* Sov. Phys. Semicond. **20** (4) 465 (1986)

[Vas97] A. Vasilescu: *The NIEL scaling hypothesis applied to neutron spectra of irradiation facilities and in the ATLAS and CMS SCT* Technical Report ROSE/TN/97-2, CERN (1997)

[Wat65] G.D. Watkins et al.: *Defects in Irradiated Silicon: Electron Paramagnetic Resonance of the Divacancy* Phys. Rev. **138** (2A) 543 (1965)

[Wat96] S.J. Watts et al.: *A new model for generation and recombination in silicon depletion regions after neutron irradiation* IEEE NS-**43** 2587 (1996)

[Wat99] G.D. Watkins: *Intrinsic Defects in silicon* 1^{st} ENDEASD Workshop, Santorini (Greece) April 1999

[Wat00] S.J. Watts et al.: *Why does NIEL work usually* 5^{th} ROSE Workshop RD48, March 2000

[Wei91] S. Weiss: *Halbleiteruntersuchungen mit dem DLTFS-(Deep-Level Transient Fourier Spectroscopy-) Verfahren* Ph.D. thesis, University of Kassel (Gesamthochschule) (1991)

[Wue00] J. Wuestenfeld: *Radiation induced surface effects of segmented silicon detectors* Seminar Solid State Detectors, Univ. Hamburg, December 2000

[Wun92] R. Wunstorf: *Systematische Untersuchungen zur Strahlenresistenz von Silizium-Detektoren für die Verwendung in Hochenergiephysik-Experimenten* Ph.D. thesis, University of Hamburg (1992)

[Wys00] J. Wyss et al.: *Observation of an energy dependence of the radiation damage on standard and oxygenated silicon diodes by 16, 21 and 27 MeV protons* Technical Report ROSE/TN/2000-7, CERN (2000) to be published in Nucl. Instr. and Meth. A

[Zan00] K. Zankel: *Can cluster physics shed some light on the puzzle of our experimental findings with energetic particles?* 5^{th} ROSE Workshop RD48, March 2000

[Zin82] V.F. Zinchenko et al.: *Investigation of the kinetics of defect formation in neutron-bombarded silicon with allowance for the self-consistent electric field* Sov. Phys. Tech. Phys. **27** (8) 990 (1982)

Acknowledgements

First of all I like to express my thanks to Prof. Dr. Dr. h.c. Gunnar Lindström, Dr. Eckhart Fretwurst and Dr. Michael Moll for supervising this thesis and their advices.

I am greatful to all members of the *Nukleare Messtechnik* for the cooperation and friendly working atmosphere. The technical stuff of the group are Dipl. Ing. Uwe Pein, Peter Buhmann and Christa Nickel. The secretary is Petra Hendrikman Verstegen. I also like to thank Prof. Dr. Robert Klanner for supporting our group and all other people who stayed in the laboratory building during my work on this thesis.

I like to thank all the people that provided irradiation facilities or irradiated samples: R. Böttger, H.J. Brede and H. Klein (PTB Braunschweig), V. Cindro and M. Mikuz (Ljubljana), G. Casse, M. Glaser, F. Lemeilleur, A. Ruzin and A. Zanet (CERN), K. Gabathuler (PSI Villigen), D. Bisello, J. Wyss (Legnaro), Z. Li (BNL) and P. Roy (Montreal).

I wish to thank all members of the ROSE collaboration for the interesting workshops and for bringing together results and ideas.

Finally, I like to thank Ioanna Pintilie for joining me during the work in the laboratory and Gianluigi Casse for helping me during the irradiations at CERN.